Anisotropy, focal mechanisms, and state of stress in an oilfield: Passive seismic monitoring in Oman

Abdullah Said Saleh Al-Anboori

Submitted in accordance with the requirements for the degree of Ph.D.

The University of Leeds

School of Earth and Environment

October 2005

This thesis is dedicated to my mother, father & wife,

may almighty Allah reward-you for everything

Acknowledgments

" Have we not made the earth an expanse and mountains stakes" *The Holy Quran*

To Allah belongs the praise in the first and in the last. I praise Him as one who acknowledges His Perfection. Oh my lord open for me my chest and ease my task.

Mike Kendall, my supervisor, was really the driving force for my research. Without his help, this piece of work would never have been possible. His enthusiasm towards the project, patience with my silly questions, critical advice, guidance throughout my PhD even when he moved to Bristol and his smiley face every time I pop in to see him are greatly appreciated.

I am also grateful to Mirko van der Baan for acting as a local supervisor after Mike left and for his help and many comments. Many thanks to Rob Jones and Dan Raymer for supplying the data, installing XMETAL software here in Leeds and their tremendous help in how to use it. Thanks to Guy Mueller (from PDO) who is responsible for much of the information in the chapter on Yibal geology. Thanks to the petrophysicists Patrick Hogarty and Michel Krief (from PDO) for providing shear dipole logs and help on estimating the anisotropy magnitude from these logs.

Nick Teanby's permission to use his codes (particularly the splitting code) and his advice on their use are much appreciated. Mark Chapman is greatly appreciated for supplying his frequency-dependent anisotropy code. Thanks to the computer man, James Wookey, for his scripts and tools, without which this project would have been very difficult. Thanks to the computer officers, Stuart Borthwick and Nick Barber, for putting up with my computing problems. I am also grateful to the GMT man, Ian Bastow, for his help on my GMT scripts. I would also like to thank Quentin Fisher and Mike Welch from Rock Deformation Research for their constructive comments on stress magnitude estimation. Thanks to my office mates James While, James Hammond, Andrew Gait, Lindsey, David Green, Kristof de Meersman, James Wookey and Andy Carter for their continuous help and making my time here in Leeds enjoyable. Thanks also to the Omani PhD students in the school (Bader Al-Busafi, Mohammed Al-Wardi, Mohammed Al-Kindi and Suleiman Al-Hinai) for their brotherhood and support.

To my mother, father, wife and 3 kids (Albljaa, Adam and Hawaa), may Allah reward you all for your moral support. Although my little kids are mischievous, their smiles upon returning home relieve my PhD stresses.

My Thanks also go to Graham Stuart and Phil Christie for acting as examiners. Thanks to PDO and ABB for permission to use the microseismic data. I am especially grateful to PDO for funding my PhD, MRes and BSc studies, and for permission to publish the results. Finally, thanks to every one who helped me directly (by constructive comments and supplying data and/or software) and indirectly (by moral support) to push my thesis to a finished product.

Abstract

Knowledge of the spatial characteristics of stress and fractures in reservoirs is important for optimising production and injection processes. Semi-permanent passive microseismic monitoring is being conducted in the Yibal field, Oman, to better understand reservoir geomechanics. The network comprises 12 4C stations in 5 monitoring wells which can be used for focal mechanism and anisotropy studies. In this study, I analyse 22 days of data, containing over 600 located events. In the first analysis, 43 reliable fault plane solutions (FPSs) are determined using polarities and amplitudes of direct P-, SV- and SH-waves based on a pure double-couple source. The principal stress directions are estimated using the method of Gephart and Forsyth (1984) from FPSs. Stress magnitudes are then estimated based on a friction model, and stresses are finally modelled based on a passive basin model. In the second analysis, nearly 400 reliable S-wave splitting measurements of time lag and fast shear-wave strike are determined. Shear-wave splitting modelling is used to interpret the results in terms of fracture orientation and fracture density. In the final analysis, 19 examples of frequency-dependent S-wave splitting are determined and the results are interpreted using the Chapman (2003) theory to estimate the fracture size.

I observe a transition in faulting regime from strike-slip (with a thrusting component) in the shale Fiqa cap rock to pure thrusting in the gas-charged Natih A chalk reservoir. Deeper in the field I observe another transition from strike-slip in the Nahr Umr shale cap rock to normal faulting in the oil-bearing Shuaiba chalk reservoir. The transition at each shale/chalk interface may be attributed to variations in the friction angles: from low in the shales (12° and 18°, respectively) to high in the chalks (39°). The Natih A results suggest a positive anomaly in Poisson's ratio (0.37), which is consistent with the ongoing compaction in this unit. The maximum compressive stress direction varies with depth: horizontal E in Fiqa, horizontal NNE in Natih-A, sub-horizontal E in Nahr Umr, and sub-vertical in Shuaiba. The splitting magnitudes are high (5–10%) in the SE footwall of the large eastern-most graben fault that runs through the field and low (1%) in the opposite hanging wall. The highest fracturing (5% average anisotropy) and largest fracture sizes (2 m) are predicted in the Natih A reservoir. In contrast, the Fiqa exhibits moderate fracture density (3%) with fine-scale fractures (<0.1 μm in size). Weaker anisotropy is found in the Natih B-G, which is attributed to moderate fracture density in the upper layers and preferred crystal orientation in the lower layers. The splitting orientation results are interpreted in terms of a single set of near-vertical fractures trending: 19°NNE in the Natih A, 90°E in the Fiqa and the lower part of Natih B-G, and 45°NE in the upper part of Natih B-G. The fractures are aligned parallel to the direction of the maximum compressive stress, as determined by the FPS-based stress analysis.

Cumulatively, these results show how microseismic data can be used to infer the faulting and stress regime, and the size, density and orientation of fractures in individual formations, with a high level of resolution. Such information is invaluable for field development strategies.

Contents

List of Figures

List of Tables

Abbreviations and symbols

Abbreviations.

ENZ	Geographic frame east, north, vertical
FMI	Fracture micro image
FPS	Fault plane solution
HTI	Transverse isotropy with a horizontal symmetry axis
VRH	Voigt-Reuss-Hill method
VTI	Transverse isotropy with a vertical symmetry axis

Latin symbols.

A	Amplitude of waves, area
a,b,c	SH-,SV-,P-wave directions
aw	Coefficient for frequency imaginary part
a_f	Fracture size
C,c_{ij}	Elastic tensor, elastic constants
F	Average misfit of a stress solution
$F_{95\%}$	95% confidence region of F
f	Frequency
f_d	Dominant frequency
f_{dig}	Digitizing frequency
f_p,f_s	Frequency of the P- and S-wave
f_0	Reference frequency
$ikmax$	Maximum number of iterations
k_f	Fluid bulk modulus
l	Longitudinal direction
M	Fault mechanism type
M_0	Scalar seismic moment
M_w	Moment magnitude
P,T,B	Pressure, tension, intermediate stress
$P(f)$	Power spectrum
p	Pore-fluid pressure
Q	Quality factor
Q_p	Quality factor of the P-wave
Q_s	Quality factor of the S-wave
r	Anisotropic scaling ratio
R,R'	Relative stress magnitude (real,modelled)
RMS	Root mean square
S,s_{ij}	Compliance tensor, compliance constants
t	Time, travel time
$uconv$	Convergence criteria
v	Velocity
v_p	P-wave velocity
v_s	S-wave velocity
v_{fast}	Fast-shear-wave velocity
v_{slow}	Slow-shear-wave velocity
x	Distance or offset
xl	Periodicity distance of the medium

Greek symbols.

δt	Time lag
ε	Crack density
η	Crack aspect ratio
λ	Wavelength, eigen value
μ	Shear modulus, friction coefficient
ν	Poisson's ratio
ν_t	Transition Poisson's ratio
ν_{fit}	Best fit Poisson's ratio
ρ	Density
$\sigma_{1,2,3}$	Maximum, intermediate and minimum stress, respectively
$\sigma_{H,h,v}$	Maximum horizontal, minimum horizontal and vertical stress, respectively
τ_m	Relaxation time scale
ϕ	Friction angle
ϕ_t	Transition friction angle
ϕ_{fit}	Best fit friction angle
ψ	Fast shear-wave strike
ω	Angular frequency

Chapter 1

Introduction

1.1 Introduction

Passive seismic monitoring in hydrocarbon fields has the potential to play an important role in field development (Jupe et al., 2000; Kristiansen et al., 2000). Microseismic activity can be induced by production, injection and regional tectonic processes. Such earthquake activity can be used to delineate faults, identify reservoir compartmentalization, and monitor the progress of injection fronts. Microseismic data can be also used to estimate fracture-induced seismic anisotropy (Teanby et al., 2004b), and fault regime and stress (Rutledge et al., 1998) in hydrocarbon settings. Microseismic-like data have also been used to estimate fracture size in hydrocarbon settings (Liu et al., 2003b).

In this thesis, I present an integrated study of subsurface fractures and stresses from microseismicity in the Yibal field in west central Oman (Figure 1.1). Focal mechanism analysis and stress inversion, shear-wave splitting, and frequency-dependent shear-wave splitting analysis are used to investigate the dynamic nature of the reservoir. I also present extensive synthetic tests prior to real data analysis to assess viability and limitations of the techniques and draw guidelines for subsequent analysis of real data. The Yibal microseismic data were recorded during an ongoing microseismic monitoring trial (Jones et al., 2004). The project is a collaborative venture between Petroleum Development Oman (PDO), ABB Offshore Systems (now VetcoGray), and Shell Exploration and Production Technology and Research (SepTAR).

1.2 Aims and motivations

The Yibal field in west central Oman (Figure 1.1) was discovered in 1962 and is now in tertiary stages of production. A semi-permanent deep seismic network was deployed to address questions regarding reservoir behaviour and future production. To date only basic processing has been applied to the data. The recorded data have been inverted for event locations and their magnitudes to gain insight in their spatial distribution. However, this provides little more than a basic understanding of the geomechanics in the reservoir. Detailed analysis such as focal mechanism determination has not been performed, nor has an evaluation of anisotropy in the field. Application of these techniques should provide a more detailed picture of spatial and temporal variations in reservoir stress, which is the overall aim of this PhD thesis.

1.2.1 Objectives

The objectives of the thesis are to :

- Compute focal mechanisms of microearthquakes and invert for the stress regime.
- Perform shear-wave splitting analysis to estimate the spatial distribution of fracture orientation and fracture density.
- Determine fracture size using frequency-dependent anisotropy.

1.3 Importance of this thesis

In 1999, the Yibal field displayed disappointing production rates. Geomechanical issues such as well damage/failure, high water cuts at production wells, subsidence of 4cm per year and compaction are some of the main problems in the Yibal field. The microseismic work was carried out in the hope that it could help optimise hydrocarbon recovery and give insights into the field geomechanics (Jones et al., 2004).

Knowledge of in-situ stress state and fracture parameters from focal mechanism and shear-wave splitting analysis, respectively, can be significantly useful. The impact of the in-situ stress acting on the rock and the fracture network in hydrocarbon flow is pronounced. The permeability of cracks is strongly dependent on the in-situ stress acting on them (Gutierrez et al., 2001; Thomas et al., 2003). Therefore, stresses are important in determining the role of faults as seals or fluid pathways in fractured reservoirs such as those investigated in this thesis.

Incorporating the spatial distribution of stress and fractures together with the Yibal geological model in a 3D geomechanical model can predict more accurately the reservoir behaviour throughout the lifetime of the field. The parameters of the static 3D geological and structural model can be extracted from seismic images and from routinely acquired petrophysical logs such as density, seismic velocity, saturation and porosity (Fanchi, 2003; Liu et al., 2004). In addition to stress, other geomechanical parameters such as rock strength can also be calculated from the logs using empirical relationships (Arifin et al., 2003). The resulting 3D geomechanical model is ultimately coupled with fluid flow to solve for in-situ stress, as well as rock and fluid flow properties in space and time (Tran et al., 2004; Walters et al., 2002; Garcia and Teufel, 2005).

A 3D geomechanical model has many advantages in drilling and field management that could be implemented in Yibal. It can predict zones prone to well failure so they can be alleviated, and new safe well trajectories can be designed (Arifin et al., 2003). It can also predict water-front movements (from the water injection wells) to minimise water cut affected wells. Khan and Teufel (2003) found the maximum fluid permeability direction aligned with the maximum principal stress direction. Thus, the geomechanical model can also be used to maximise well productivity by considering drilling perpendicular to fractures or the maximum stress direction (Al-Ruwaili and Chardac, 2003). Forecasting 3D subsidence and compaction due to gas depletion from the Natih reservoir is another potential benefit of a 3D geomechanical model.

1.4 Thesis outline

The thesis introduction outlines previous work in the study area and provides a broad picture of the seismic network, recorded data and preprocessing.

Chapter 2 provides a geological and structural description of the study area. More importantly, it also presents different fracture and in-situ stress data that have been collected from the field. The chapter ends with a summary of the fracture and stress parameters from geology that are used to forward-predict some of the main modelling parameters used in subsequent chapters. Towards the end of each subsequent chapter dealing with real data, one can refer back to this summary to assess the agreement between the results and the field geology.

Chapter 3 describes the work carried out in focal mechanism determination and stress inversion. The first part (focal mechanism) starts with a description of the focal mechanism theory, followed by synthetic tests, and finishes with the analysis of real data to determine fault plane solutions. The second part (stress inversion) presents the theory in detail, stress inversion based on the focal

mechanisms, and finally provides estimates of stress magnitudes.

Chapter 4 provides theoretical predictions of shear-wave splitting in different likely fracture scenarios in Yibal, via synthetic modelling with an emphasis on differentiating brine versus gas-filled cracks. The chapter is ultimately meant to provide guidelines for shear-wave splitting analysis of the real data performed in the following chapter (Chapter 5) and also help in the interpretation of the real data results.

Chapter 5, previously presented in Al-Anboori et al. (2005), summarises shear-wave splitting results for the real data and the interpreted fracture strike and dip, and fracture density. It concludes with the likely causes of anisotropy at Yibal.

Chapter 6 presents estimates of fracture size by means of frequency-dependent anisotropy derived from shear-wave splitting analysis. It first describes the crack model of Chapman (2003) that handles frequency-dependent anisotropy. Applications to real data from two fields, Yibal and Valhall, are then presented.

The final chapter outlines the main conclusions and significant contributions of the project. It also presents possible options for future work.

1.5 Previous studies of Yibal

There has been little previously published work concerned with the Yibal field. Neither earthquake focal mechanism nor shear-wave splitting studies are commonly done with microseismic data in general. Recently, Al-Abri (2003) studied anisotropy and frequency dependent shear-wave splitting using 4 days of Yibal microseismic data. Time lag results were between 0-26 ms, the anisotropy magnitude was between 0-3% and the fast shear-wave strike was east (E) with estimated mean direction of 96°. His frequency dependent anisotropy results indicate a fracture size on the order of 1-10 m.

Potters et al. (1999) performed an anisotropy study in a nearby field named Natih, $\approx$ 80 km north-east of Yibal. Both fields share the same geological history since they are part of the Fahud Salt Basin. Anisotropy was determined in the Fiqa shales and chalky Natih reservoir using observations of shear-wave splitting in a 9-component 3-dimensional (9C3D) experiment. Anisotropy up to over 20% was observed in the survey. The Fiqa fast shear-wave direction was oriented north (N) over the north-east part of the survey and north-east (NE) in the south-east part. The Fiqa splitting time lag was generally small (0-8 ms), but time lags as high as 30 ms

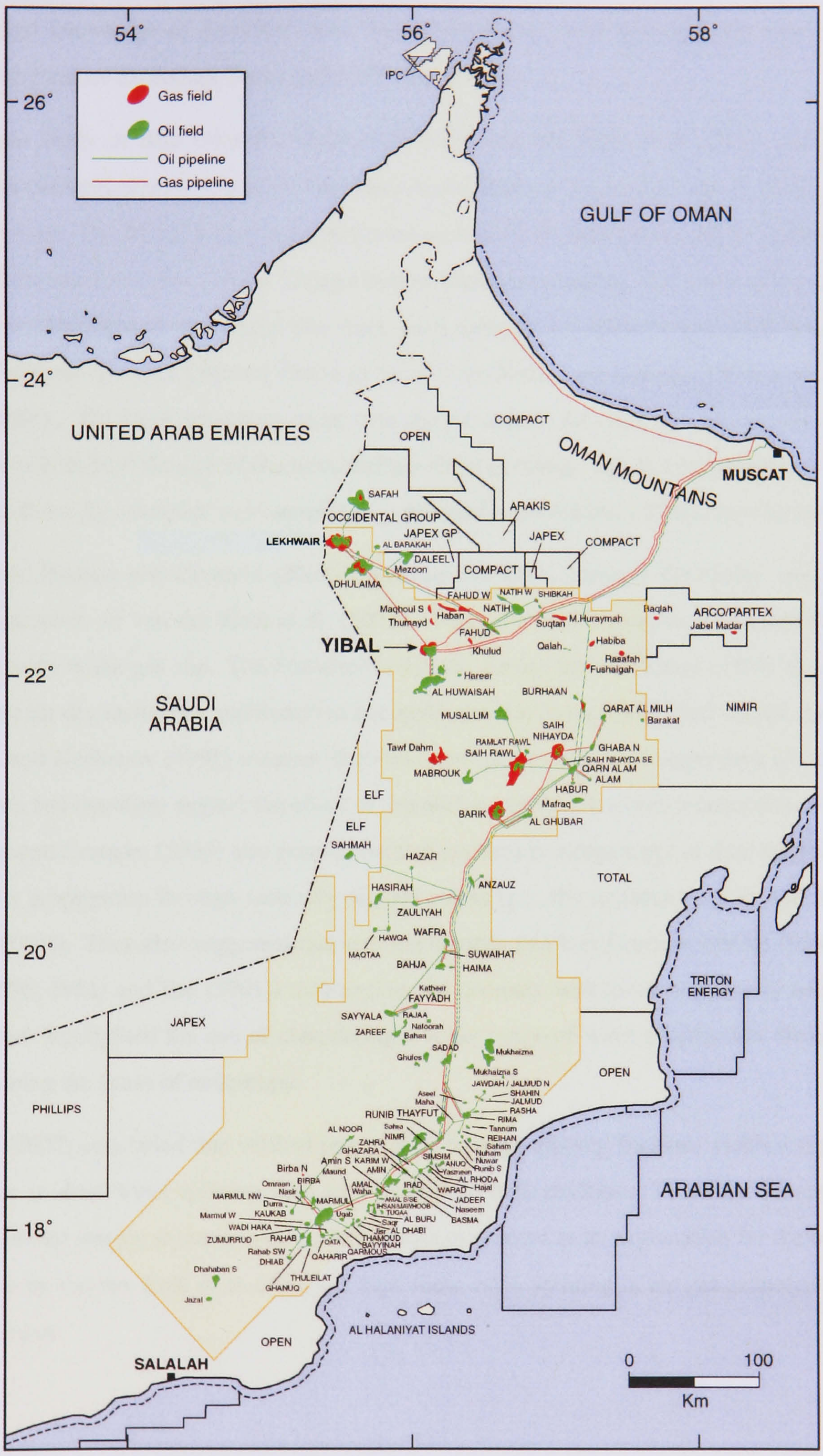

Figure 1.1 Map of Oman showing the Yibal field and nearby fields (modified from Al-Busaidi (1997)).

are encountered in some areas. The Natih fast shear wave trend was NE (in agreement with geological knowledge of dominant open fracture direction) with high splitting time lags and anisotropy values exceeding 30 ms and 15%, respectively.

In a later study of data from the same experiment, van der Kolk et al. (2001) used BOSK effective-medium theory to explain two shear-wave splitting anomalies, one in Natih and the other in Fiqa. The BOSK theory is based on research work by Budiansky and O'Connell (1977) and Sayers and Kachanov (1991). Using effective medium modelling, and considering only vertical wave propagation they found that shear-wave splitting is higher for gas-filled than liquid-filled fractures. The first anomaly shows splitting at the Natih crest is higher (50% or more) than at the flanks. The large anisotropy value over the gas cap on the crest was interpreted as being a result of both high density of fractures and gas-filled fractures. The second anomaly, observed on Fiqa above the reservoir was interpreted in terms of a gas chimney above the reservoir.

However, Hudson and Crampin (2003) suggested two main errors in the theory, and thereby the application, of van der Kolk et al. (2001). This called into question the interpretation of the anomaly in the gas cap. The first error is that the Sayers and Kachanov (1991) approximations are for dry inclusions and therefore not applicable for in-situ fluid-filled cracks. Secondly, Sayers and Kachanov (1991) assumes that fluid-flow parameters are independent of crack orientations and therefore neglect the effect of orientation, distribution and connectivity of cracks. Hudson and Crampin (2003) also pointed out that lag time is independent of fluid type for vertical wave propagation through vertically aligned cracks (i.e., the raypaths used by van der Kolk et al. (2001)). They also suggested that existing theories (such as Crampin (1978; 1984); Hudson (1980; 1981) and Tod (2001)) may explain the anomaly with lower amounts of anisotropy. They also highlighted the use of considering a wider range of wave propagation directions in determining the cause of anisotropy.

Sayers (2002) concluded that vertical propagation through dipping fractures yields a significant decrease in shear-wave splitting with increasing fluid bulk modulus. Therefore Sayers (2002) proposed that steeply-dipping, non-vertical cracks may serve as an explanation for the observed anomaly by van der Kolk et al. (2001) of high shear-wave splitting in the gas-saturated zone of the reservoir.

1.6 Passive seismic monitoring at Yibal

Micro-seismic monitoring started in October 1999 in response to a tremor felt at the surface by the Yibal team in 1997. The goal of this monitoring is improved hydrocarbon production and injection optimisation. Initially, a shallow network was deployed followed later on by a deeper borehole network deployed by ABB Offshore Systems Limited (the data and event locations have also been processed by ABB).

1.6.1 Description of network and sensors

The experiment, described by Jones et al. (2004), consists of five deep boreholes containing permanent recording geophones (down to 1400 m depth). Figure 1.2a shows the location of these wells. For best coverage over the whole field, four wells (Y053, Y279, Y385 and Y425) are situated at the peripheries of the field forming a parallelogram-like shaped network of 2km×2km dimension. The fifth well (Y080) is positioned at the centre of the network. Throughout this thesis I refer to wells Y053, Y080, Y279, Y385 and Y425 as wells 1, 2, 3, 4 and 5, respectively.

Each well installation comprises an array of 8-level, 4 component (tetrahedral) sensor packages. The 3-Cartesian components can be constructed using only 3 components, rendering the fourth component as a coherence trace that can be used as an indicator of coupling, sensitivity and calibration. The tetrahedral system also has the advantage that 3 orthogonal components can be constructed even if one sensor is dead or malfunctioning. Figure 1.2b shows the geometry of the array in each well. Station locations are listed in Appendix B.1. The stations (within the array) are evenly spaced in wells 3, 4 and 5 with station spacings of about 28.5, 65 and 80 m, respectively, while in wells 1 and 2 stations are not evenly spaced.

1.6.2 Data acquisition

The downhole geophones continuously record signals, digitized at 2kHz (i.e., sample rate of 0.5 ms). A microseismic detection scheme is used on specific continuous channels (i.e., only particular channels are allowed to trigger). When triggered, a 4 second record (including some data before and after the trigger time) of all channels is saved to disk as an event.

(a)

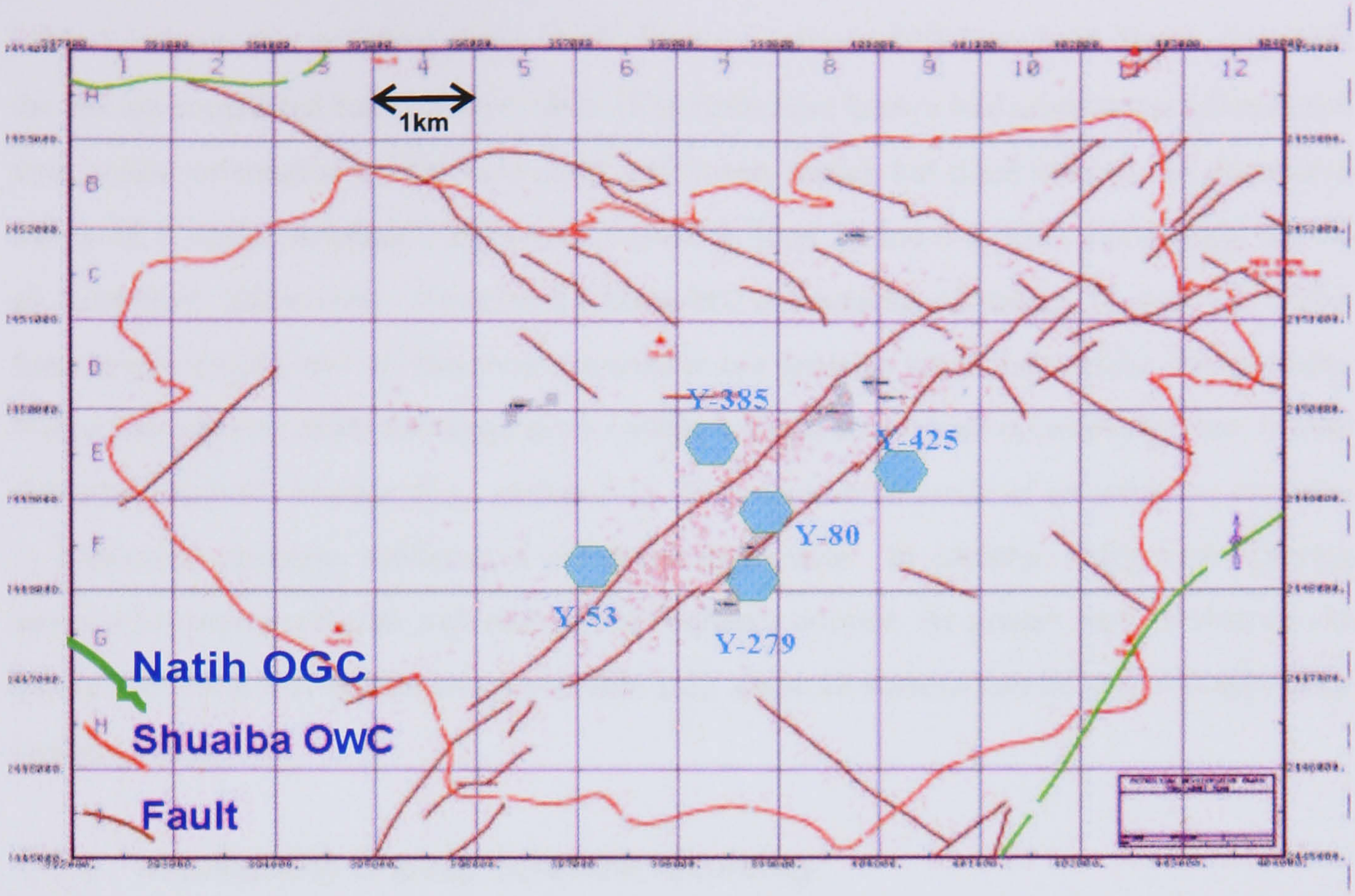

(b)

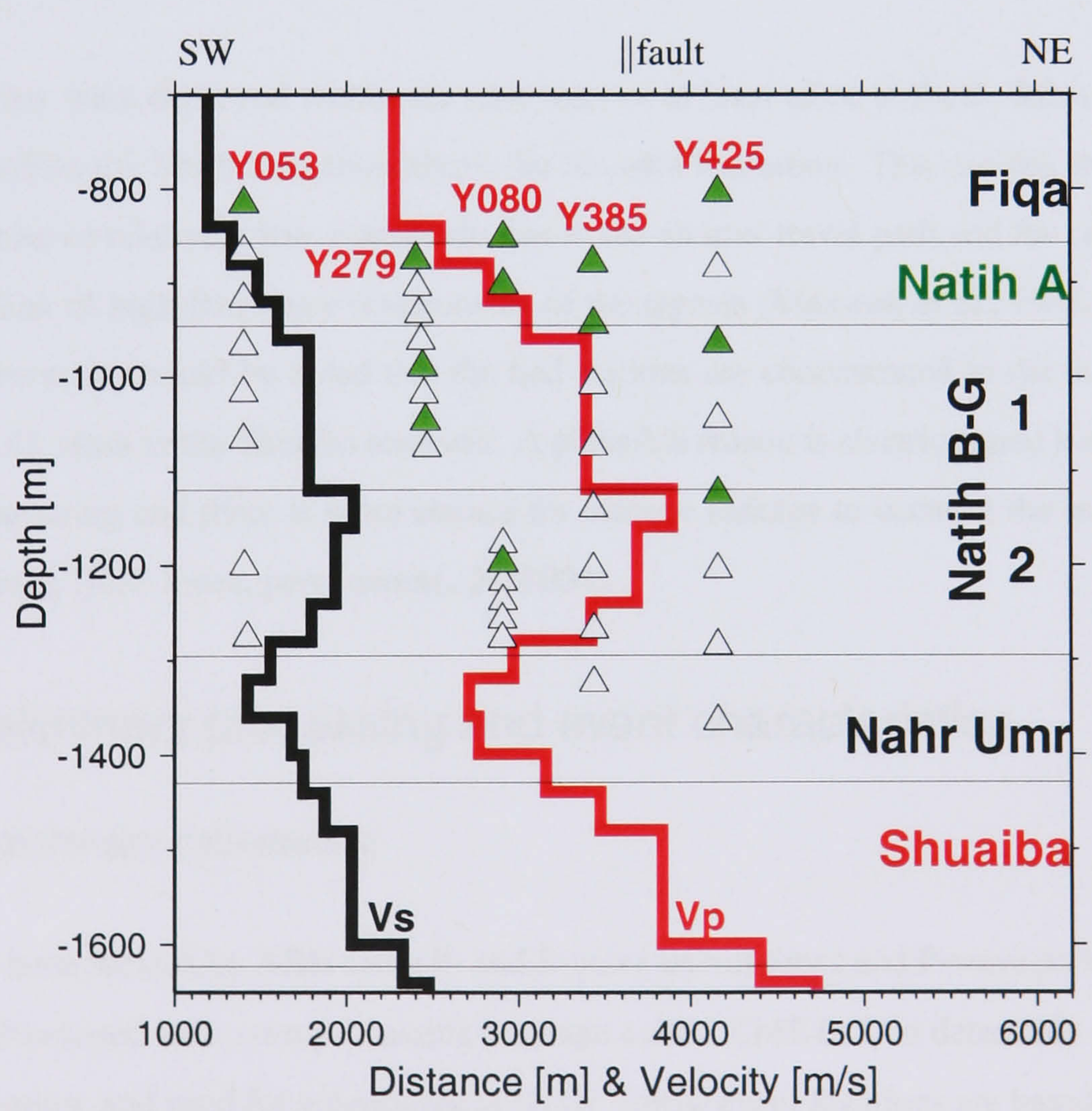

Figure 1.2 [**a**] Map of the five observation boreholes (blue hexagons) containing permanent sensors (ignore the small red dots). Horizontal and vertical axes are universal eastern and northern co-ordinates, respectively. [**b**] SW-NE cross section of the 8-level, 4C array (triangles) in the five boreholes. The datum is the mean sea level + 150 m. Stations of known tool orientation are marked by green filled triangles. Also shown are the P-wave (red) and S-wave (black) velocity models. Distances in the horizontal axis are relative.

1.6.3 Recording status of sensors

Table 1.1 shows the recording status of all channels. Around 40% have been functioning well, the rest are considered bad channels. Only 12 stations have known tool orientations (determined from sensor orientation check-shots using a vibroseis truck), but these stations are distributed across all 5 wells. Another 2 stations, 3.2 (well 3, level 2) and 3.6, have a hodogram set but no orientation information. However the horizontal components of station 3.6 generally suffer from severe ringing and are therefore not used in our analysis when they exhibit this problem. With a few stations, different components (within a single station) are occasionally seen to have different frequency content (e.g., station 3.1). This could be a result of an unknown variation in instrument response, rendering a correction impossible. In addition, shear-wave splitting analysis becomes unreliable with such varied frequency content. As a result, only 14 stations can be used for focal mechanism analysis (Table 1.2), while 12 stations can be used for anisotropy analysis (Table 1.3).

1.6.4 Implications of deep borehole recording

The geophones were deployed within the reservoirs or at least close to them. Most of the geophones lie within the Natih formation above the Shuaiba formation. This enables the recording of many events of relatively low magnitude due to the shorter travel path and the reduced seismic attenuation of high-frequency components of the signals (Maxwell et al., 1998; Jupe et al., 2000). However, it should be noted that the bad stations are concentrated in the bottom levels (see Table 1.1), close to the Shuaiba reservoir. A plausible reason is electric signal leakage across the geophone string and there is more chance for electric leakage to occur at the bottom of the geophone string (Rob Jones, pers. comm., Jan2004).

1.7 Preliminary processing and event characteristics

1.7.1 Preliminary processing

Events have been located by ABB using P- and S-wave arrival times and P-wave particle motion. ABB have developed their own processing package called XMETAL to determine event origin time and location, and used for subsequent analysis. Initial event locations are based on iterative ray tracing through a 1D velocity model (shown in Figure 1.3a), calculating a solution with a minimum root mean square (RMS) time error. The velocity model is based on well logs. From

Table 1.1 Recording status of the sensors. Numbers refer to the channel number.

Level	Tool	Well				
		Y053	Y080	Y279	Y385	Y425
1	V	**1**	**25**	**49**	**73**	**97**
	H1	**2**	**26**	×	×	**98**
	H2	**3**	**27**	**50**	**75**	**99**
	H3	×	×	**51**	**76**	**100**
2	V	5	**29**	*52*	**77**	×
	H1	6	**30**	×	×	×
	H2	×	**31**	*53*	**78**	×
	H3	×	**32**	*54*	**79**	×
3	V	×	×	55	80	**103**
	H1	10	×	56	×	**104**
	H2	×	×	×	×	**105**
	H3	×	×	×	83	**106**
4	V	×	×	57	×	×
	H1	×	**35**	×	×	×
	H2	×	**36**	×	×	×
	H3	15	**37**	59	85	×
5	V	×	38	**60**	×	**109**
	H1	×	×	**61**	86	×
	H2	18	×	**62**	87	**111**
	H3	×	×	**23**	×	**112**
6	V	19	40	*64*	×	×
	H1	×	×	*65*	88	×
	H2	×	×	×	×	×
	H3	21	×	*66*	×	×
7	V	×	44	**67**	×	×
	H1	×	×	**68**	×	×
	H2	23	×	**69**	×	×
	H3	×	×	×	×	118
8	V	×	×	×	×	×
	H1	×	×	×	×	×
	H2	24	×	×	×	×
	H3	×	×	72	×	×

25 Hodogram set- orientation available

25 Hodogram set- no orientation available

25 Good channel

× Bad channel because either: (1) Dead - No signal seen during VSP or microseismic monitoring.

(2) Very Weak - Signal much weaker (below noise level). On big events it can be seen above noise but not suitable for picking or hodogram use.

(3) X-talk - Signal seen but identified as cross talk energy from another channel. Dead or very weak channel overwritten by X-talk from another channel.

Table 1.2 14 stations used for focal mechanism determination. The numbers refer to #well.#level (i.e., 1.1 refers to well 1 and level 1).

	Well				
	1	2	3	4	5
Stations	1.1	2.1	3.1	4.1	5.1
		2.2	3.2	4.2	5.3
		2.4	3.5		5.5
			3.6		
			3.7		

Table 1.3 12 stations used for shear-wave splitting. The numbers refer to #well.#level (i.e., 1.1 refers to well 1 and level 1).

	Well				
	1	2	3	4	5
Stations	1.1	2.1	3.1	4.1	5.1
		2.2	3.5	4.2	5.3
		2.4	3.7		5.5

anticlinal-structural maps of the whole field, the maximum dip of the layers is 6° with an average dip of 2°. Therefore, the 1D velocity model is valid and yields accurate locations of events inside the monitoring network (i.e., the crestal part). XMETAL can also compute source parameters (source moment, source radius, stress drop and magnitude) from the frequency spectrum of P- and S-wave windows using the methodology of Madariaga (1976).

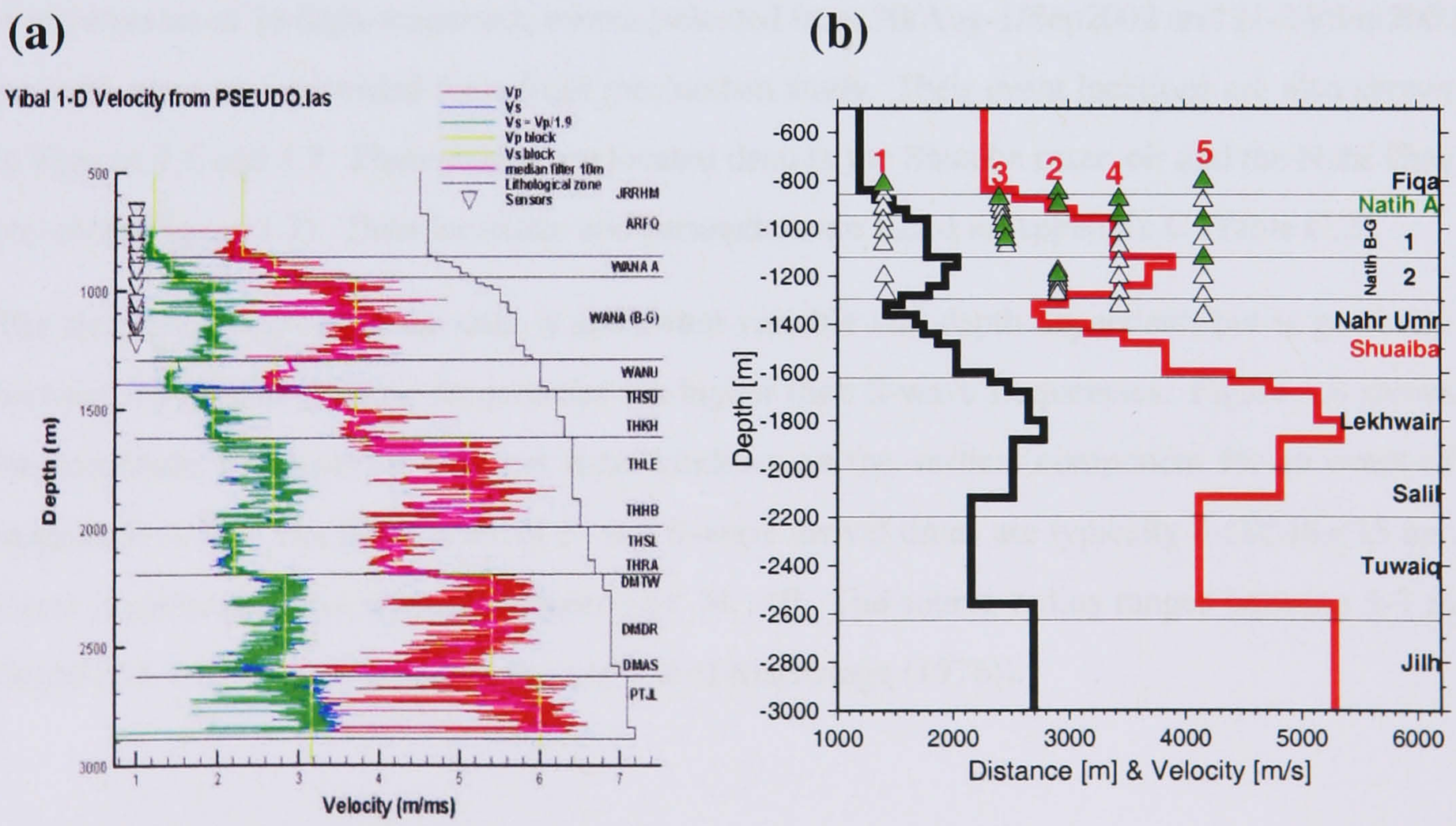

Figure 1.3 [**a**] Sonic logs of P- and S-wave velocities and the approximate 9-layer model (yellow lines), initially used by ABB for locating events. [**b**] A more precise 21-layer model for Yibal. The depth scale in (a) and (b) are identical to ease comparison.

1.7.2 Event statistics

Only two separate weeks of data (4-10/June2002 and 19-26/Oct2002) were made available for this project. The total number of located events is 641, with an average rate of 43 events per day. Initial event locations were refined with a more detailed 21-layer velocity model (shown in Figure 1.3b). The 21-layer velocity model is derived from a 3D seismic velocity volume. Event locations and parameters are listed in Appendix C (Table C.1). Event locations (June week in Figure 1.4 and October week in Figure 1.5) show spatial and temporal variations in activity. For instance, the high Natih activity around well 5 (a region called Horseshoe due to its horseshoe-like shape) in June (Figure 1.4) is less apparent in October (Figure 1.5). This may be associated with high and low gas production in the summer and the winter, respectively.

Event locations for the entire dataset analysed, both in map view and in 3D (Figures 1.6(a,b)) and in fault-parallel and fault-perpendicular cross sections (Figures 1.7(a,b)), show that the events are clustered near the two graben faults and that they are concentrated in the Natih reservoir. This suggests that the two graben faults are still active and act as weak preexisting slip planes prone to reactivation. Figure 1.7 also shows the alignment of events at the top and bottom of the Natih B-G1 layer (top=-960m, bottom=-1120m). These two lines of seismicity are an artifact of the 1D velocity model (21-layer), where there is a tendency for poorly located events to locate on interfaces (Dan Raymer, pers. comm., Nov2004).

A separate set of 26 high-magnitude events (selected from 30/Aug-1/Sep2002 and 21-24/Sep2002 periods) were also provided for a focal mechanism study. Their event locations are also shown in Figures 1.6 and 1.7. These events are located deep in the Shuaiba reservoir and the Nahr Umr cap rock (Figure 1.7). Their locations and parameters are listed in Appendix C (Table C.2).

The frequency content of the data is somewhat variable and depth dependent, but is generally between 10-400Hz. P-wave frequencies are higher than S-wave frequencies. Figure 1.8 shows the amplitude spectrum of different time windows on the vertical component for an event of magnitude -0.95. The RMS error of P- and S-wave arrival times are typically 5<RMS<15 ms. Event magnitudes have a range between $-2 < M_l < 0$. The source radius ranges between 1-7 m (XMETAL calculations based on the method of Madariaga (1976)).

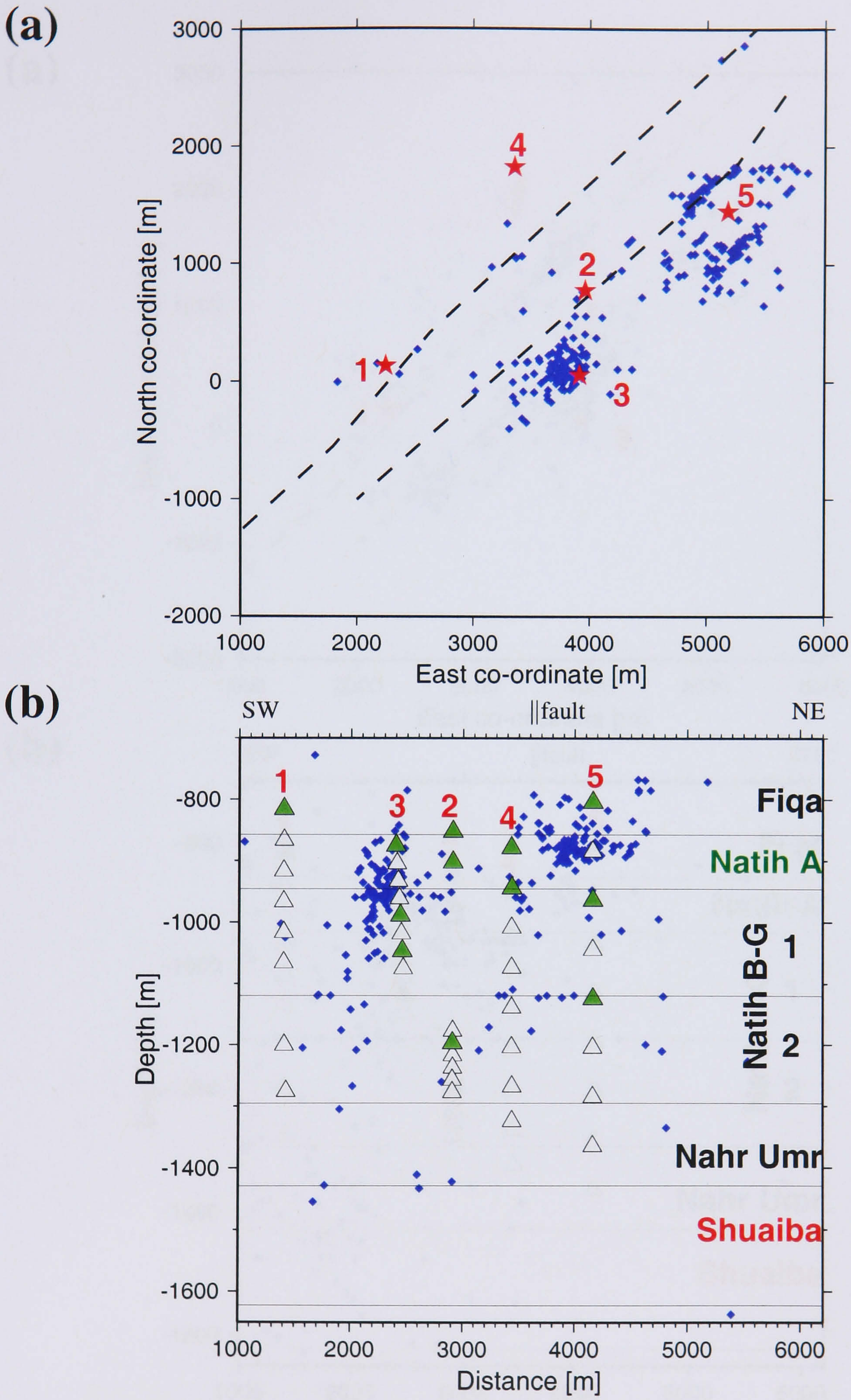

Figure 1.4 Event locations (blue) for a 7 day period 4-10/Jun02: [**a**] map view (local co-ordinates) and [**b**] fault-aligned cross section (NE-SW orientation). Sensors are shown by triangles and those used for anisotropy analysis are marked by green triangles. Well head positions are in red (stars). The surface locations of the two main graben faults (see Figure 1.2a) are superimposed as dashed lines. See Appendix B.1 for local co-ordinate definition in (a).

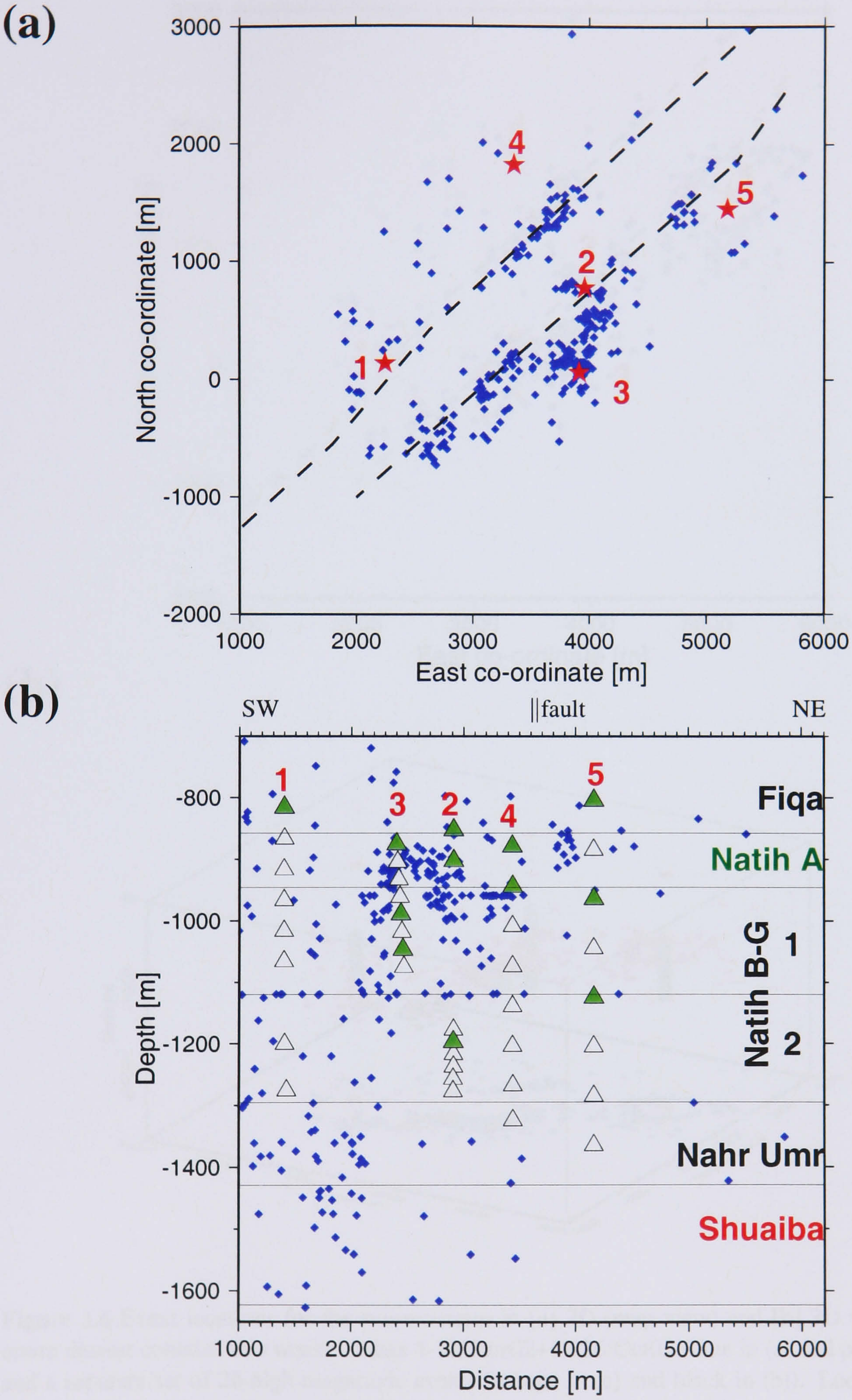

Figure 1.5 Same as Figure 1.4 but for the 19-26/Oct02 dataset.

(a)

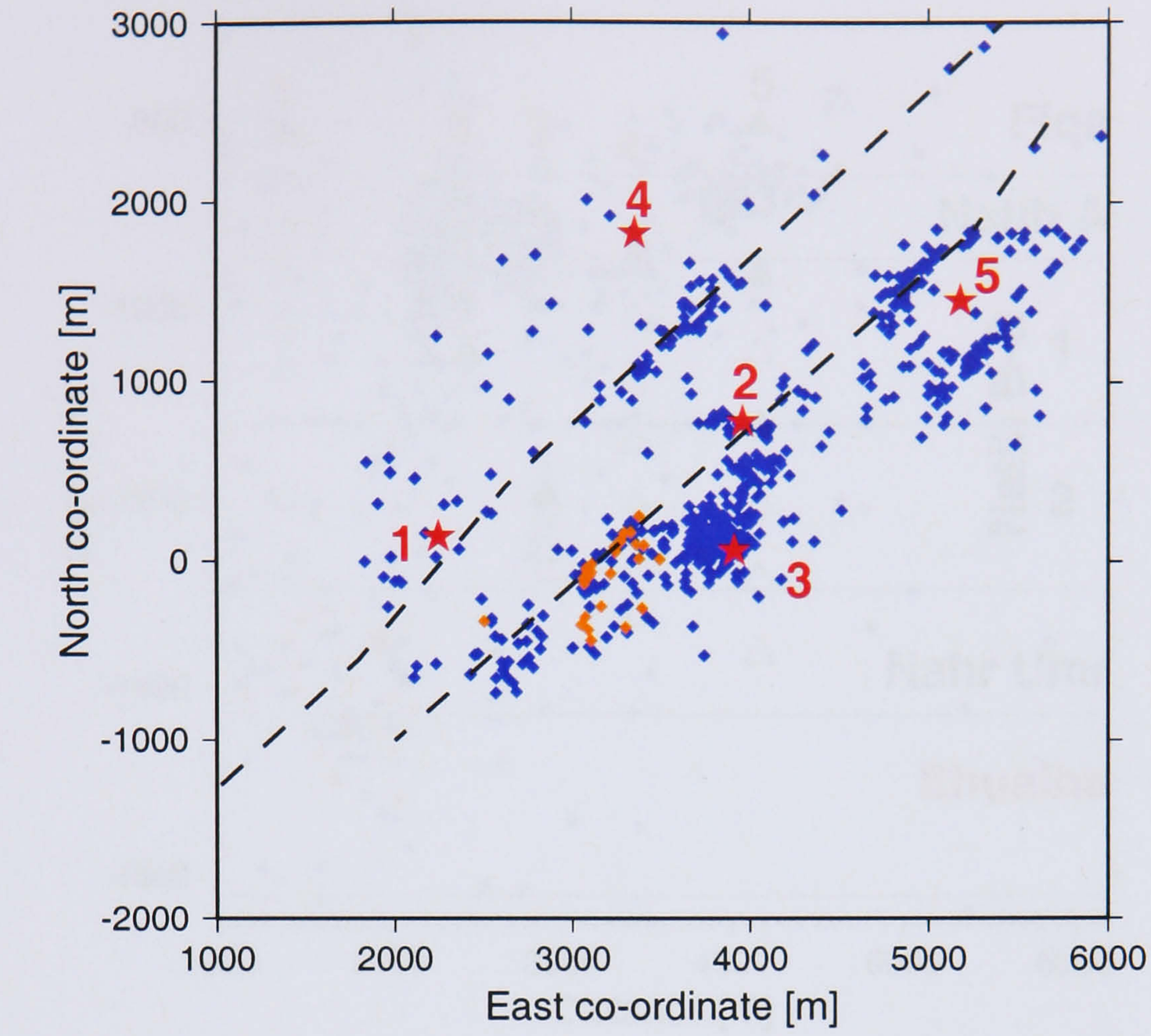

(b)

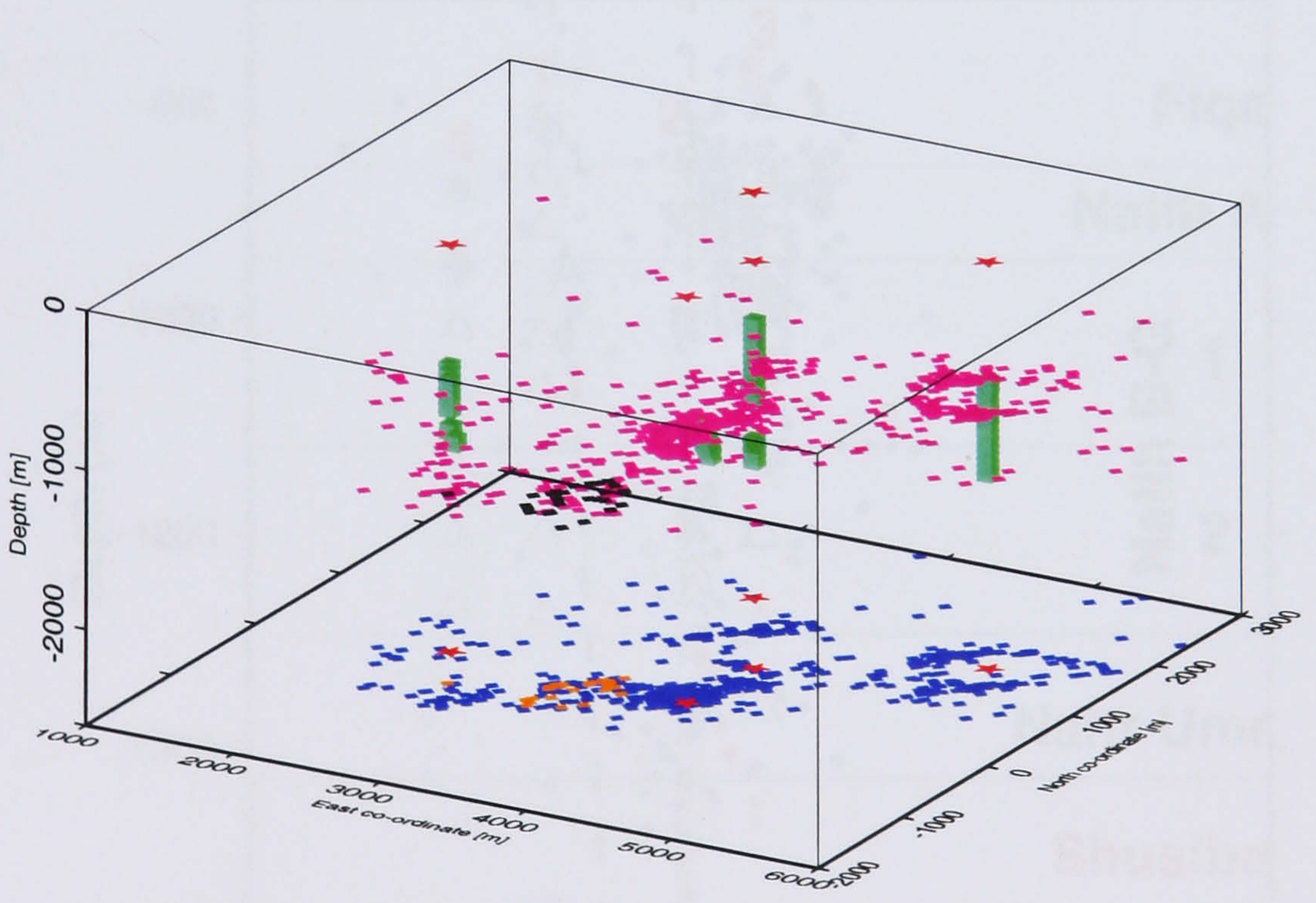

Figure 1.6 Event locations for the entire dataset in [**a**] 2D (map view) and [**b**] 3D view. The entire dataset contains two weeks of data 4-10/June02+19-26/Oct02 (blue in (a) and pink in (b)) and a separate set of 26 high magnitude events (orange in (a) and black in (b)). Locations are also projected downwards on to the base to show a map view (blue+orange). Sensors are in green and well head positions are in red (stars). Events mainly cluster around two linear features that are NE-trending graben bounded faults.

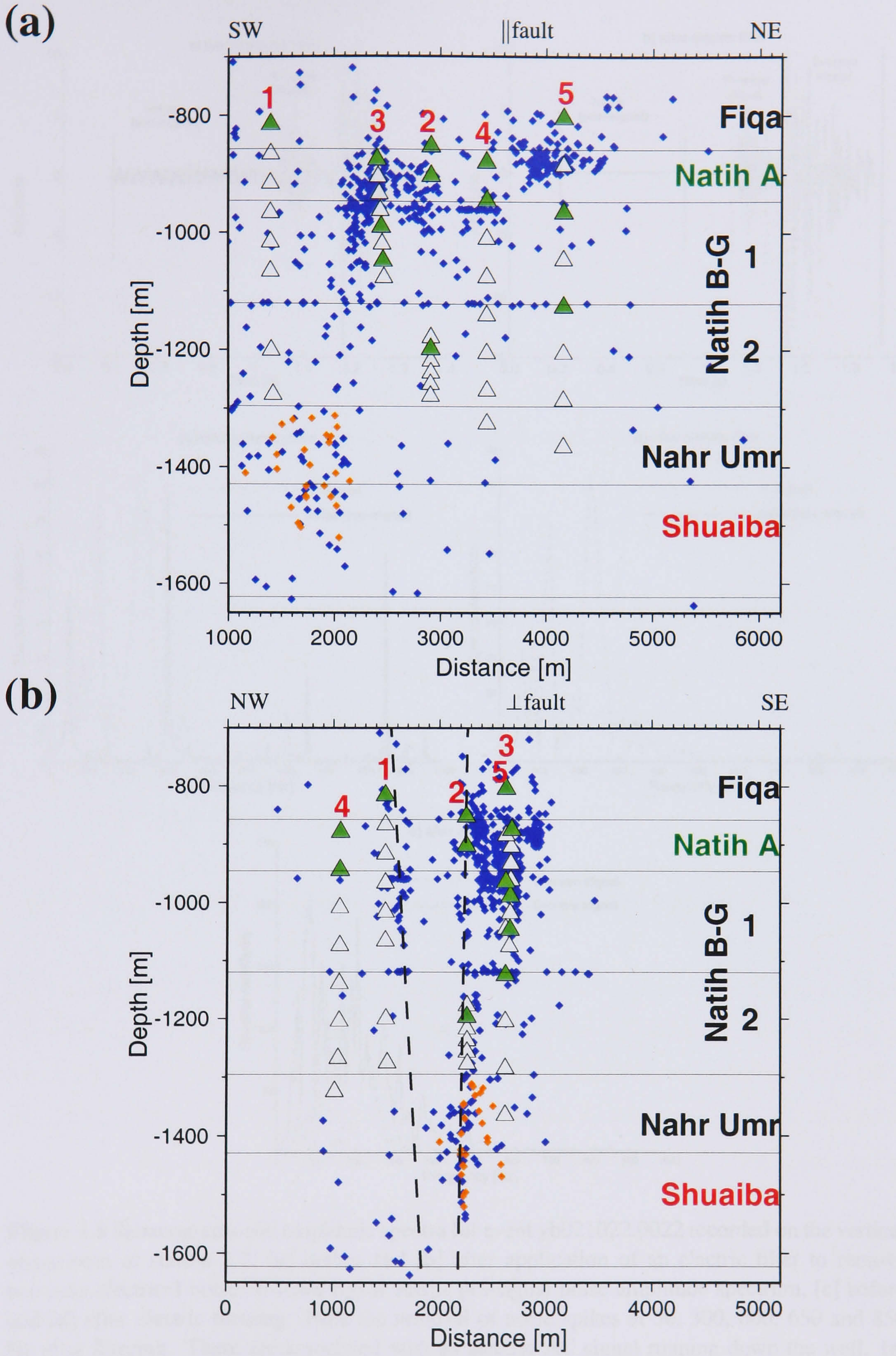

Figure 1.7 Cross sections of event locations for the entire dataset shown in Figure 1.6. [**a**] parallel to graben faults and [**b**] perpendicular. The two weeks of data 4-10/June02+19-26/Oct02 are in blue, while the separate set of 26 high magnitude events is in orange. The fault parallel and perpendicular cross sections are oriented roughly SW→NE (55° anticlockwise from E) and NW→SE (45° clockwise from E), respectively.

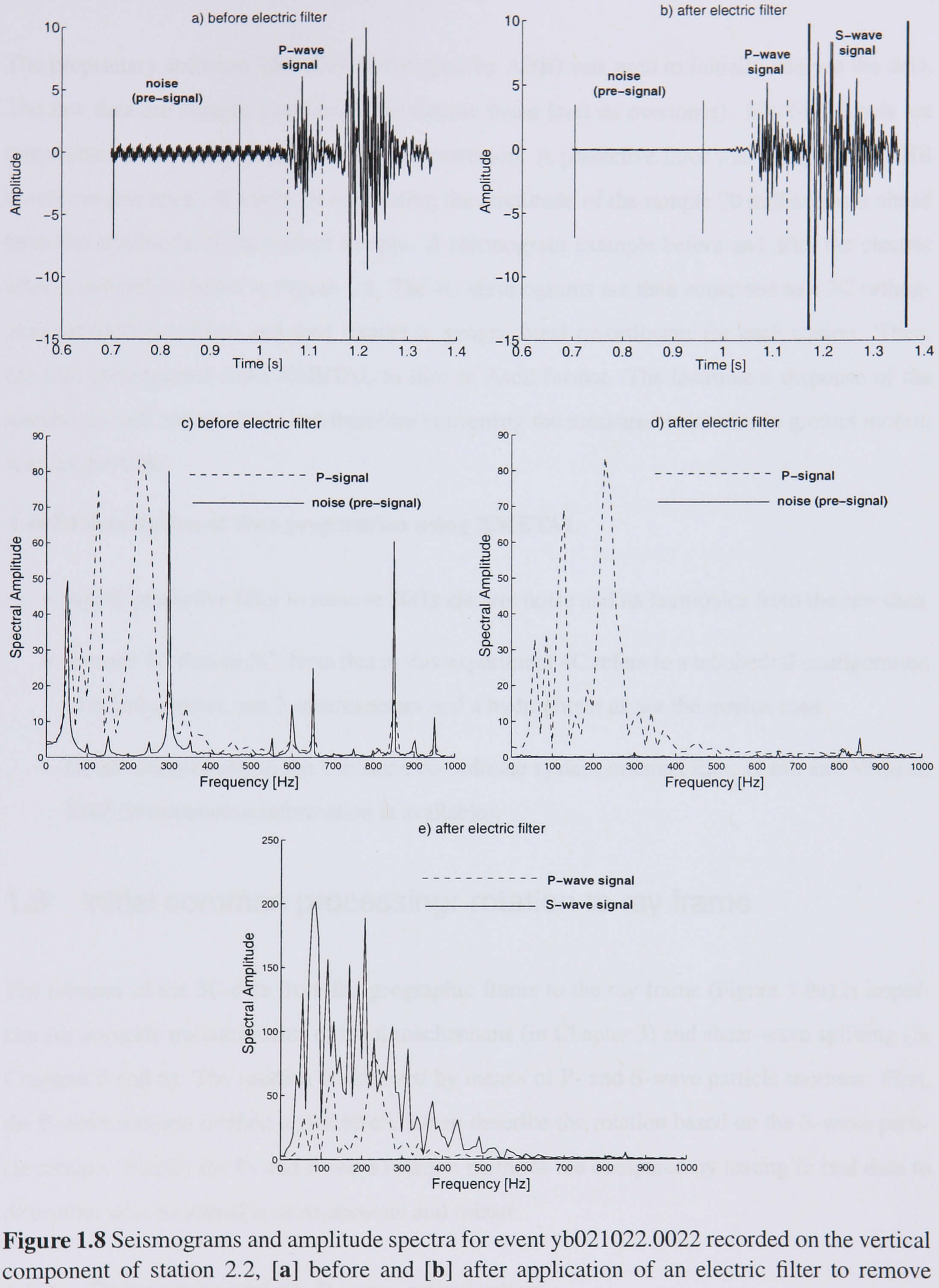

Figure 1.8 Seismograms and amplitude spectra for event yb021022.0022 recorded on the vertical component of station 2.2, [**a**] before and [**b**] after application of an electric filter to remove borehole electrical noise. P-wave signal versus pre-signal noise amplitude spectrum, [**c**] before and [**d**] after electric filtering. Note the removal of noise spikes at 50, 300, 600, 650 and 850 Hz after filtering. These are associated with an electric AC signal running down the well. [**e**] P-wave versus S-wave amplitude spectra. Pre-signal noise, P- and S-wave time windows used for amplitude spectrum calculations are shown in (a) and (b).

1.8 Data preparation prior to analysis

The proprietary software XMETAL (developed by ABB) was used to initially analyse the data. The raw data are contaminated by 50Hz electric noise (and its overtones). Electric signals are transmitted down the well pipes to prevent corrosion. A predictive filter was designed by ABB to remove this noise. It works by subtracting the amplitude of the sample 20 milliseconds ahead from the amplitude of the current sample. A seismogram example before and after the electric filter is applied is shown in Figure 1.8. The 4C seismograms are then converted to a 3C orthogonal set (hodogram set) and then rotated to geographical co-ordinates for each station. Then, the data are exported from XMETAL to files in Ascii format. The instrument response of the geophones was not available and therefore converting the measured velocities to ground motion was not possible.

A brief description of data preparation using XMETAL

- Apply predictive filter to remove 50Hz electric noise and its harmonics from the raw data.
- convert 4C data to 3C. Note that in this experiment 4C refers to a tetrahedral configuration of seismometers, not 3 seismometers and a hydrophone as per the marine case.
- Rotate components to the Cartesian co-ordinate system oriented East, North and Vertical, ENZ (if orientation information is available).

1.9 Initial common processing: rotation to ray frame

The rotation of the 3C data from the geographic frame to the ray frame (Figure 1.9a) is important for accurate measurements of focal mechanisms (in Chapter 3) and shear-wave splitting (in Chapters 5 and 6). The rotation is achieved by means of P- and S-wave particle motions. First, the P-wave rotation method is described. I then describe the rotation based on the S-wave particle motion. Finally the P- and S-wave rotation methods are compared by testing in real data to determine which method is most accurate and robust.

1.9.1 Rotation based on P-wave polarisation

In isotropic/weakly-anisotropic media, P-wave particle motion is polarised parallel/near-parallel to the ray direction. Therefore, the P-wave particle motion approximates the ray direction. First, a P-wave window is picked whose length varies from one-cycle to many cycles depending on

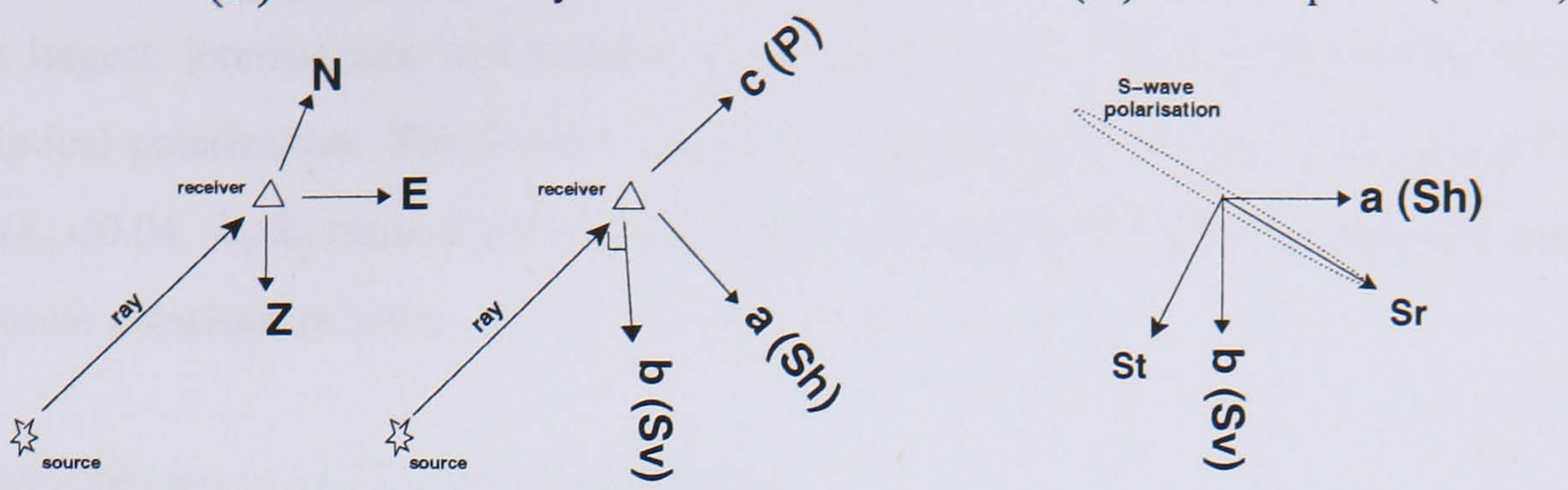

Figure 1.9 A diagram illustrating: [**a**] rotation of 3C data from the geographic frame (east, north and vertical, ENZ) to the ray frame (a:*Sh*, b:*Sv* and c:P), and [**b**] S-wave radial and transverse components (*Sr*,*St*) in the S-wave plane.

orientations of incoming later phases. Rotation angles in the horizontal and vertical planes are estimated from the selected P-wave window based on least absolute residuals (L1 norm) in the direction perpendicular to the line. Appendix D.1 describes this method and outlines the advantage of using this method over the method of L1 norm of vertical residuals in real data. Uncertainties in rotation angles are found using a bootstrap method (Press et al., 1989). Figure 1.10 depicts this rotation of unfiltered data. Rotation is preferably performed before filtering to avoid loss of information of signal orientation. Therefore, where possible filtering is avoided. Occasionally, data are contaminated by high frequency noise that obscure the image of the P-wave orientation. In these cases, filtering (without affecting the P-wave frequency band) is required to sharpen the P-wave particle motion image and results in a more accurate rotation.

1.9.2 Rotation based on S-wave polarisation

Sometimes it is necessary to rotate the 3C data into the plane of the S-wave (e.g., for S-wave splitting analysis). Since the S-wave direction may differ from the P-wave ray direction (e.g., due to variable v_p/v_s ratio), one could use the S-wave orientation in subsequent analysis. The determination of the rotation angles in the horizontal and vertical planes based on S-wave polarisation is described in Appendix D.2. Similar to P-wave orientation uncertainty calculations, a bootstrap method is used to compute uncertainties in the rotation angles of the selected S-wave window.

Figure 1.11 illustrates the rotation on a real data example. The elliptical S-wave motion is visible in the polarisation plane (Figure 1.11b). Particle motion in the tilted horizontal plane (tilted to the ray direction) is displayed in Figure 1.11c. Similarly, the particle motion in the vertical plane is displayed in Figure 1.11d. After rotation, the S-wave energy is maximised on the *a* and *b*

transverse components (Figure 1.11e). The degree of the S-wave ellipticity can be measured using the largest, intermediate and smallest eigenvalues (λ_1,λ_2 and λ_3, respectively) of the S-wave elliptical polarisation. The S-wave ellipticity measures are normally $0.2<\lambda_2/\lambda_1<0.7$ and $0.00<\lambda_3/\lambda_2<0.04$. λ_3/λ_2 ratios clearly indicate that S-wave particle motion is entirely confined to the S-wave polarisation plane.

QC criteria for usage of S-wave ray direction

The ray direction information in the S-wave window is only used if the following conditions are met:

- There is a well defined S-wave which is distinct from the P-wave.
- An elliptical S-wave particle motion. Linear S-wave particle motion poorly constrains the polarisation plane (because many possible planes of different orientations can contain that line) and thereby, the ray direction.
- The S-wave particle motion is confined to the polarisation plane perpendicular to the ray direction (e.g., as illustrated in inclined horizontal and vertical views in Figures 1.11(c,d), respectively). I use λ_3/λ_2=0.05 as a maximum limit.

1.9.3 P- versus S-wave rotation methods

18 real data examples were rotated using both P- and S-wave phase windows to investigate the effect of a particular rotation method on the determined ray orientation angles. Figures 1.12(a,b) show a comparison of the P-wave ray azimuth and inclination, respectively, with those predicted from the source-receiver geometry (assuming a straight raypath). Likewise, Figures 1.12(c,d) show the S-phase ray azimuth and inclination, respectively, versus the predicted ones. The S-wave azimuth deviations (measured-predicted) are larger (Figures 1.12(c,a)). S-wave inclination deviations (measured-predicted) are even larger than those for the P-waves (Figures 1.12(d,b)). Most measurements in Figure 1.12d plot around a 170° S-incidence angle, which is not consistent with predictions based on a straight raypath approximation. These nearly vertical S-wave incidence angles correspond to horizontal S-wave polarisations. The corresponding S-phases are more prone to contamination from other overlapping arrivals (such as P-wave reflections and local S-P conversions) for S-waves to apparently appear horizontally polarised.

The effect of P- versus S-wave rotations on the S-wave splitting measurements were also examined. The splitting lag times for rotated seismograms based on the P-wave method against those lags for rotated seismograms based on the S-wave method are plotted in Figure 1.12e for comparison. Similarly, the shear-wave fast strikes for rotated seismograms based on the P- and S-wave methods are shown in Figure 1.12f. Rotations based on the P- and S-wave methods yield almost identical splitting measurements although fast strike uncertainties inferred from the S-wave method are higher than those of the P-wave method. Comparison of the two rotation methods led to the conclusion that the S-wave method yielded similar results to the P-wave method but was less accurate, most likely due to contamination with other phases (e.g., P-wave coda) that are absent from the first P-motion. In this thesis, therefore, where possible the P-wave method is used. In cases where the P-wave signal is very weak (buried below the noise background), the S-wave energy is used. This is often due the large amplitude of the S-wave compared to that of the P-wave.

1.10 Coordinate terminology

Data are rotated from the ENZ frame to longitudinal (*l* or *P*), *Sv* and *Sh* components (c, b and a axes, respectively, see Figure 1.9a). The *l*-direction is parallel to the ray propagation direction. *Sv* and *Sh* are defined as follows. I use the term S-plane for the S-wave particle motion plane with a normal aligned with the ray. When data are rotated to the ray co-ordinates, the S plane contains *Sv*- (S component in the sagittal plane) and *Sh* (S component in the horizontal plane). The *Sr* and *St* directions (short terms for the S-radial and S-transverse, respectively, both lying within the S-plane) denote the S-wave polarisation direction and its normal, respectively (Figure 1.9b). Anisotropy introduces another two terms, fast and slow S-wave directions both approximately lying within the S-plane.

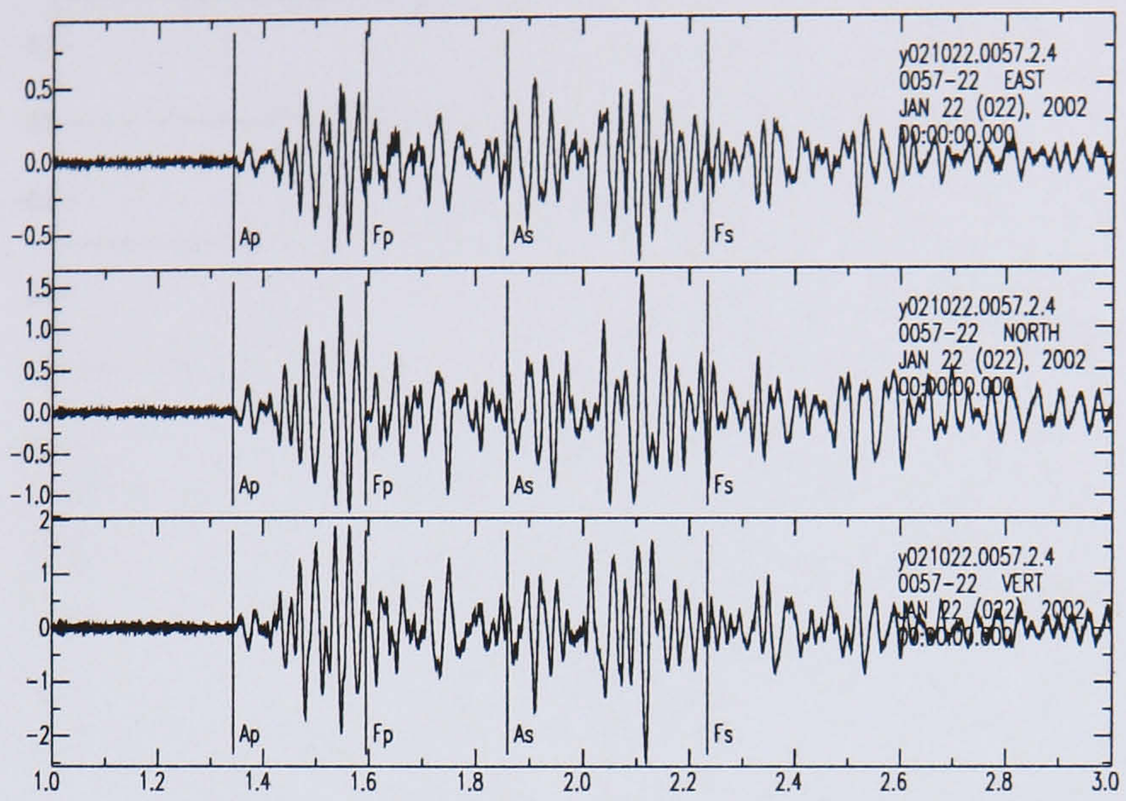

Figure 1.10 [**a**] Raw data, east, north and vertical components of event yb021022.0057 recorded in well 2 on level 4 (i.e., station 2.4). [**b,c**] P-wave particle motion on horizontal and vertical planes, respectively. [**d**] Components rotated to ray coordinates where, from top-to-bottom, a:*Sh*, b:*Sv* and c:*l*. [Ap Fp] marks beginning and end of P-wave window. Similarly [As Fs] marks beginning and end of S-wave window to be used for the anisotropy analysis. Note the linear P-wave particle motion ((b) and (c)) and minimised P-wave energy in the S-plane after rotation (d). In the top and bottom frames, the horizontal axis is arrival time in seconds and the vertical axis is amplitude.

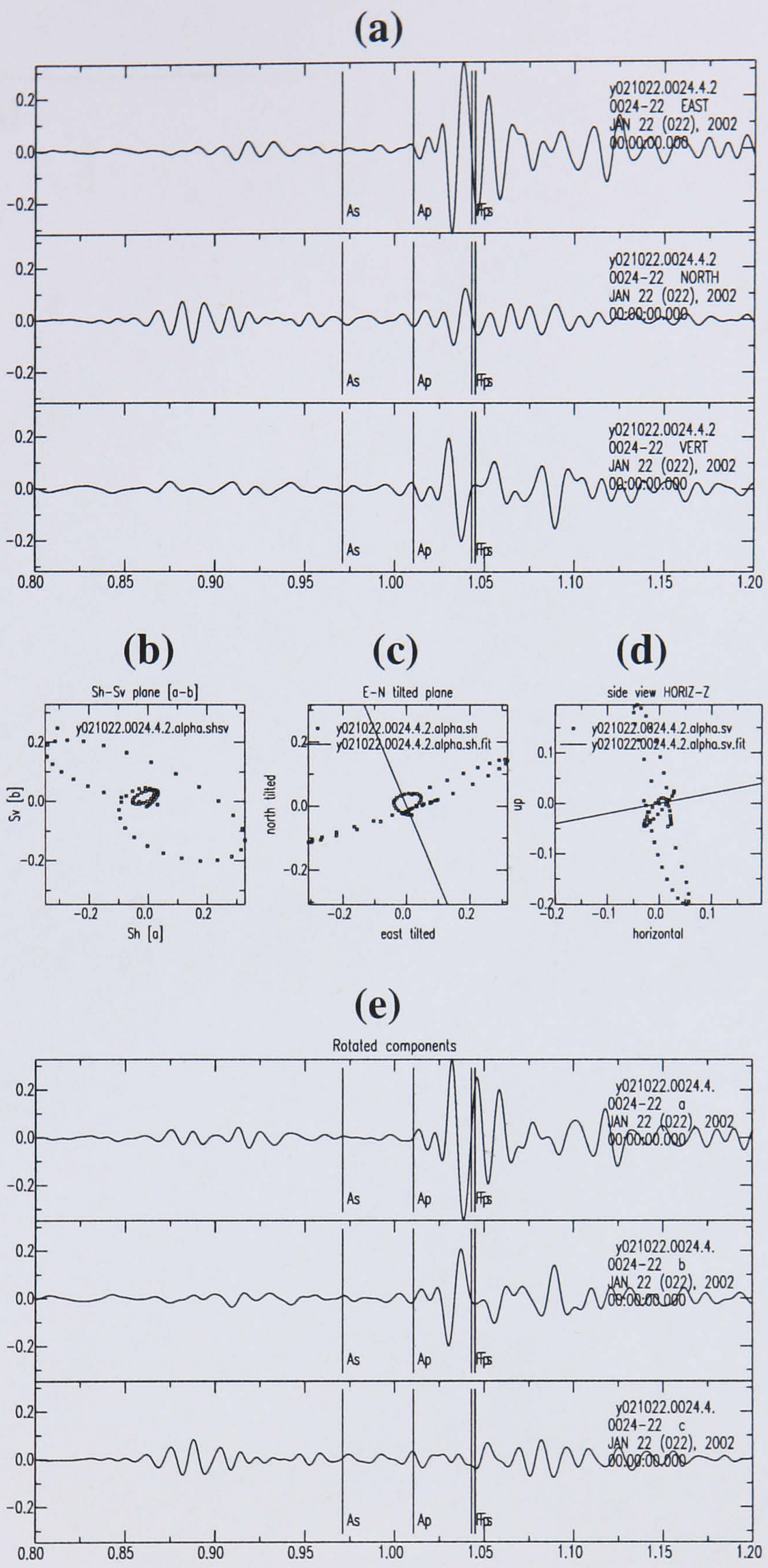

Figure 1.11 [**a**] Filtered data on east, north and vertical components of event yb021022.0024 recorded in well 4 on level 2 (i.e., station 4.2). The S-wave particle motion (dotted line) on: the S-wave polarisation plane (**b**), the tilted horizontal plane (tilted to the ray direction) illustrating ray azimuth (**c**) and the vertical plane illustrating ray dip (**d**). The calculated ray orientation is also shown (solid lines). [**e**] Components rotated into ray coordinates where top-to-bottom a:*Sh*, b:*Sv* and c:*l* or *P* components. [Ap Fp] marks the beginning and end of the window used for particle motion analysis. Similarly [As Fs] marks the beginning and end of the S-wave window to be used for the anisotropy analysis. Note the elliptic S-wave particle motion in (b). After rotation, the S-wave energy is now maximised in the transverse components, *Sh* and *Sv* (e). In the top and bottom frames, the horizontal axis is arrival time in seconds and vertical axis is amplitude.

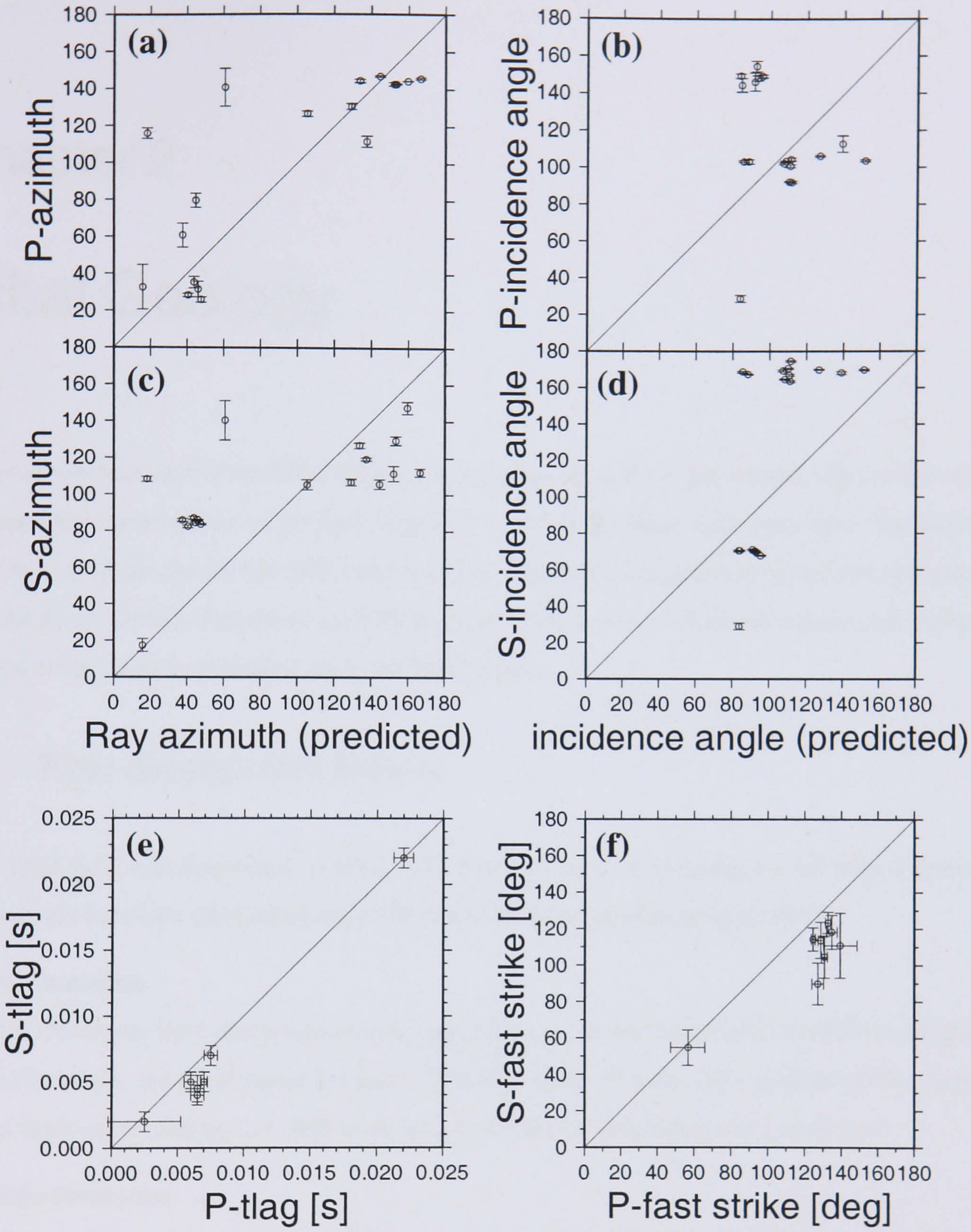

Figure 1.12 Results of different rotation methods (P- and S-wave methods) for 18 examples. [**a**] Ray azimuth and [**b**] vertical incidence angle inferred from the P-wave particle motion versus those predicted from a straight source-receiver raypath approximation. Similarly, [**c**] Ray azimuth and [**d**] incidence angle inferred from the S-wave particle motion versus those predicted with a straight raypath approximation. Cross plots of splitting measurements based on the P- and S-wave rotation methods: [**e**] lag time and [**f**] fast-shear-wave strike. In both (e) and (f), the horizontal and vertical axis are S-wave splitting results inferred from seismograms rotated using the P- and S-wave methods, respectively. In (e) and (f), only reliable splitting measurements are shown (8 out of the initial 18 examples). Note that S-wave splitting results of both rotating methods are similar but fast strike confidence regions inferred from the P-wave method are better than those of the S-wave method (f).

Chapter 2
Yibal Geology

In broad structural terms the Yibal field is a large dome created by deep-seated salt movement. A simplified cross section of the field (Figure 2.1) shows the three main reservoirs: the Natih non-associated gas and oil rim (880-1280 m depth), the prolific Shuaiba oil (1410-1510 m depth) and the Khuff Oil/Gas Reservoirs (≈3000 m depth). Much of the information presented in this section comes from unpublished, in-house PDO reports.

2.1 Field development History

The Yibal field was discovered in 1962. The two reservoirs investigated by the microseismic network are the Natih (producing since 1971) and Shuaiba (producing since 1969).

Natih Formation

In 1971, Natih gas went into production to supply lift gas for the Shuaiba oil. In 1978, Natih gas started to supply the government gas grid. Currently, about 18 wells (all clustered in the center of the field) are producing gas. However, not all of them are producing at the same time.

Shuaiba Formation

The Shuaiba reservoir started production in 1969 by natural depletion. In 1972, waterflood began with seven injection wells (Litsey et al., 1986). The initial injection pattern was expanded to a nine spot pattern and then the injection pattern continued into expansion. Water was initially injected into the oil column, but shortly thereafter this changed to deep injection. By mid-1981, 131 wells had been drilled (Litsey et al., 1986). In 1989, quarter-pattern in-fill drilling commenced on the crest of the field to increase production and improve sweep. From 1994 to 2000, high density in-fill drilling by horizontally sidetracking existing watered-out wells further developed the field. Production results for Yibal wells in 1999 proved disappointing. Consequently,

in 2001 drilling activities significantly decreased to allow time for determining an optimal field management strategy. Currently, over 480 wells are present in the entire field (not all of them reach Shuaiba).

2.2 Tectonic history and fractures

Yibal faults generally trend either southeast (SE) or northeast (NE) (Litsey et al., 1986). Seismic images of the early NE faults show that they are high-angle normal faults (Figure 2.1: cross section, and Figure 1.2: map view), this representing a tensional regime associated with salt uplift forming a NE graben system (Litsey et al., 1986). These are followed later by SE oriented faults, created by regional tectonics (Litsey et al., 1986). These tectonics are probably associated with the late Cretaceous emplacement of ophiolite thrust sheets in the Northern Oman mountains, which have a maximum stress oriented NE due to the collision of the Eurasian-Arabian plates (Al-Busaidi, 1997). The SE late Cretaceous faults show strike-slip movements. All faults were reactivated in the Tertiary (the third structure phase).

2.3 Lithology and physical properties

The stratigraphic column (Figure 2.2) shows that Cretaceous Natih and Shuaiba are disconformably overlain by the cap rocks Fiqa and Nahr Umr, respectively. Both reservoirs are chalky limestone and the two cap rocks are shale. The upper Shuaiba's thickness and unusually high porosity are highest in the central part of the field and decrease downflank. The unusually high porosity (25-45%) is attributed to pore preservation by early accumulation of oil (Litsey et al., 1986). The Shuaiba matrix permeability is very low and generally ranges between less than 1 to 50 mD (Litsey et al., 1986). In the Natih field, located $\approx$ 80 km north-east of Yibal, the Natih matrix permeability is very low 1-30 mD. Production from the matrix is almost entirely dependent upon the fracture network (Potters et al., 1999). These ideas were confirmed by a 9C3D seismic experiment (Potters et al., 1999; van der Kolk et al., 2001).

Figure 2.3 shows logs of porosity, permeability, resistivity, density and hydrocarbon saturation of various wells in the Yibal field. The porosity log ranges between 25-40%. The permeability is low (1-50 mD) in Shuaiba and Natih-A, and high (100-300 mD) in the upper Natih B-G. The resistivity background is 1 Ω.m and peaks at the Natih-A (1000 Ω.m) and Shuaiba (500 Ω.m) horizons. Density increases with depth from 2.2 g/cm^3 at 1400 m depth to 2.8 g/cm^3 at 3000 m depth. Hydrocarbon saturation is as high as 96% in the Natih-A and Shuaiba reservoirs.

The density log, P-wave velocity log and a log-scaled cross-plot of density and P-wave velocity show that the relation of Gardner et al. (1974) is close to the best fit (local Gardner) relationship (Figure 2.4). Therefore, Gardner's equation can be used to provide reliable estimates of density in areas where density logs are unavailable.

2.4 Lithological and depositional description of Natih and Shuaiba units

Natih Formation

The reservoirs of the Cretaceous (Albian-Cenomanian) Natih formation comprise two members: the Natih A and Natih B. The best reservoir is found in the Natih A sub-members A1 to A5/6. The Natih B and A7 sub-members consist of fine-grained, deep-water chalky limestone. The A6 to A3 limestones shallow upward from wackestone/mudstones into very porous bioclastic grainstone/packstones consisting mainly of rudist debris deposited in a very shallow marine environment (rudist shoals). The A2 to A1 limestones were deposited in restricted, low energy, shallow marine waters (A2 depositional phase), which became more open and slightly deeper during deposition of the A1. Rock type in this interval varies from intensely fractured/brecciated and burrowed wackestone/packstone (A2) that is highly porous and fossiliferous, to chalky, burrowed mudstone/wackestone (A1). The top of the Natih has been truncated and incised by a canyon system cutting up to 80 m off the formation. These channels merge towards the southeast, where most of the erosion has taken place.

Shuaiba Formation

The carbonate ramp reservoirs of the Lower Cretaceous (Aptian) Shuaiba Formation form the uppermost part of the Lekhwair-Kharaib-Shuaiba super-sequence. The Shuaiba reservoir consists of relatively homogeneous mudstones and wackestones deposited in an intra-shelf basin floor environment. The reservoir can be subdivided into the Upper and Lower Shuaiba separated by the Upper Shuaiba mudstone. The top of upper Shuaiba (throughout the whole field) is marked by a high water saturated zone (water-finger) observed on saturation logs, suggesting a high permeability layer probably due to leaching. Saturation logs also show water fingering occurring at diverse depths within Shuaiba reservoir for different wells. The properties and location of these water fingering units are not fully understood as they show little to no porosity or permeability variation on wireline or core compared to the matrix.

2.5 Hydrocarbon occurrence

Natih Formation

The A and B members of the Natih Formation host the largest non-associated gas reservoir in Oman, overlying a thin oil rim. The oil rim is limited to the northern, eastern and south-eastern part of the field and is thickest in the northern portion. The current Natih gas production is about 12 million m^3/d. The life expectancy for Natih gas is estimated at about 20 years.

Shuaiba Formation

The oil mainly accumulates in the upper Shuaiba. The field is currently producing approximately 13000 m^3/d. The Shuaiba oil life expectancy is estimated at about 30 years.

2.6 In-situ stress

Baker Atlas GEOScience (1999) performed an in-situ stress analysis by identifying breakouts derived from differential FMI/FMS (Formation Micro Image/Formation Micro Scanner) caliper measurements. They assumed that breakouts occur perpendicular to the maximum horizontal in-situ stress. The analysis was done in nine wells but breakouts were only detected in 6 of them (five in Nahr Umr and one in Natih). The wells are located sparsely on flanks of the field. The in-situ stress results are shown in Figure 2.5. The maximum horizontal stress results for five wells in the Nahr Umr are all consistent and indicate a NE trend. The one well breakout measurement in Natih indicates a NNE stress orientation. The NE maximum stress direction in Nahr Umr is similar to the regional stress in Oman (Filbrandt et al., in press).

2.7 Compaction

The field is experiencing compaction, and is subsiding by approximately 4 cm per year with maximum subsidence at the field crest. Both the observed subsidence and microseismic tremors are most likely induced by production activities in the Natih and Shuaiba reservoirs. The soft heterogeneous layers of the Natih A2 and A4 show the highest potential for compaction.

2.8 Fracture characteristics from well and surface data

2.8.1 Well data

Two FMI (Fracture Micro Image) logs of wells Y450 and Y451 (both located in the NW block of the field, Figure 2.9e) at the Natih level are shown in Figure 2.6a. These indicate that the fracture trend is dominantly SE in Y450, and variable in Y451. The fracture dip average is 70° for both wells. Y450 and Y451 wells encountered 41 and 13 measurable fractures, respectively. Half were conductive, and half were resistive for both wells. Conductive fracture spacing is 20 m and 50 m, respectively.

Figure 2.6b shows a rose diagram of fractures imaged by borehole imaging logs from more than 10 horizontal wells at the Shuaiba level (Al-Busaidi, 1997). Most of the fractures (open and cemented) run SE. The logs also identify highly fractured (open and cemented) zones distributed unevenly in space. Fracture densities appear to be a function of lithology, as fracture intensity was observed to vary between different Shuaiba reservoir units. The cemented fractures are filled with calcite, and are mostly subvertical (Al-Busaidi, 1997).

Figure 2.7 shows a recent FMI study, conducted in 2002, at the Shuaiba level. It shows different fracture orientations where fractures are found to align with the present maximum stress and perpendicular to it (i.e., NE and SE oriented fractures). The crest and southern flank of the field is fractured more extensively than the northern flank. Fault maps of top Natih and top Shuaiba reservoirs (Figure 2.8) also indicate similar trends.

2.8.2 Surface data

Mercadier and Mäkel (1989) collected field measurements of fracture dimensions and orientation in Natih formation outcrops located 130 km east of Yibal (the area is called the Salakh arch). These outcrops are thought to be analogous the Natih formation in the subsurface. The fractures encountered are subvertical and comprise both extensional and shear types. Fractures are thought to be fold-related due to: (1) fractures primarily run parallel and perpendicular to the fold axis, and (2) fracture dimensions and spacings vary with curvature as well as with lithology, bed thickness and to a lesser extent with fault proximity. Their fracture model in clean, thickly-bedded limestone is summarised as:

50 m (length) × 1-10 m (spacing) ×10-20 m (height) in the fold crest (gentle dipping areas).

50 m (length) × 0.1-2 m (spacing) ×10-20 m (height) in the fold flanks (steeply dipping areas).

On the other hand, the fracture dimensions in the thinly-bedded limestone are one or two orders of magnitude smaller than the clean, thickly-bedded limestone.

Nearly all fractures are found calcite cemented (same findings by Al-Busaidi (1997)). Fracture aperture varies from less than 100 microns to up to 5 cm. Due to burial the real subsurface fracture apertures are probably much less than those measured at the surface, the other fracture dimensions may well represent the subsurface fractures. A recent study (2005) of those Natih outcrops confirms that the fractures are fold-related with a NNE dominant fracture trend (after Mohammed Al-Kindi, Earth Sciences, Leeds University, pers. comm.).

2.9 Anisotropy from dipole shear velocity logs

A dipole shear sonic tool (DSI- upper and lower dipole acquisition) was run down well Y449H1, located in the NW block of the field (Figure 2.9e). It resulted in 10 dipole shear velocity logs (4 lower and 6 upper dipole). Because tool orientation may change while logging, one dipole may read the fast shear-wave in one section of the well then shift to the slow shear-wave in another section. Therefore, the velocities of the slow, v_{slow}, and the fast-wave, v_{fast}, down the well were calculated using the minimum and maximum of the 10 dipole logs, respectively. The magnitude of anisotropy is computed using $100\times(v_{fast}\text{-}v_{slow})/v_{slow}$. The minimum and maximum shear velocities, and the anisotropy results are shown in Figure 2.9a. It shows roughly less than 10% background anisotropy. Though there are unrealistically large amounts of anisotropy (over 200%) in the Fiqa and sparse thin zones in Natih B-G1. This is due to an unrealistic maximum shear velocity which is identical to the compressional wave velocity (Figure 2.9c).

The anisotropy estimates after QC are shown in Figure 2.9b. The two left dipole logs after QC were upper dipole. The measured anisotropy decreases with depth from 4% (Fiqa) to 2% (Natih A and Natih B-G1) to 1% (Natih B-G2). It also shows more highly anisotropic thin zones in the lower part of Natih B-G1. Generally, slow formations exhibit high anisotropy. The lithology is identified through gamma ray logs of the well (Figure 2.9d). It is worth noting that these anisotropy values are minimum intrinsic estimates, as DSI logging: (1) uses high frequency (sonic and ultrasonic, dynamic) waveforms that exhibit minimum anisotropy, while we, here, are interested in the low frequency (seismic, static) range (Chapman, 2003); and (2) runs over short vertical distance (less than fracture spacing), therefore, does not image fractures or thickly layered bedding effects.

Dipole shear tools have been used to estimate fast and slow shear directions, and thereby estimate

fracture orientation and maximum stress directions (Al-Ruwaili and Chardac, 2003; Chardac et al., 2005). The lack of tool orientation information while logging down well Y449H1 prevented us from estimating such useful parameters.

2.10 Summary

Minimum estimates of percent anisotropy, inferred from dipole-shear logs, decrease with depth from 4% (Fiqa) to 2% (Natih A and Natih B-G1) to 1% (Natih B-G2). The largest horizontal in-situ stress aligns along the regional maximum stress direction (NE) in Nahr Umr, while it is NNE in Natih. Two FMI studies in Shuaiba, one conducted in 1997 (Figure 2.6b) and the other in 2002 (Figure 2.7), produced contradictory results (compare the two figures). The recent study observed fractures predominantly in two directions NE and SE. Only two FMI logs of Natih A are available, but they show a variable fracture trend and indicate a 70° fracture dip, a 20-50 m fracture spacing (for the conductive fractures). The crest and southern flank of the field is fractured more extensively than the northern flank. Such lateral variation in fracture density may not exist in all the formations (e.g., the recent FMI study of Shuaiba (Figure 2.7) shows no evidence of this lateral variation). One of the objectives of this thesis is to better constrain stress and fracture patterns in the field using other seismic methods applied to microseismic data.

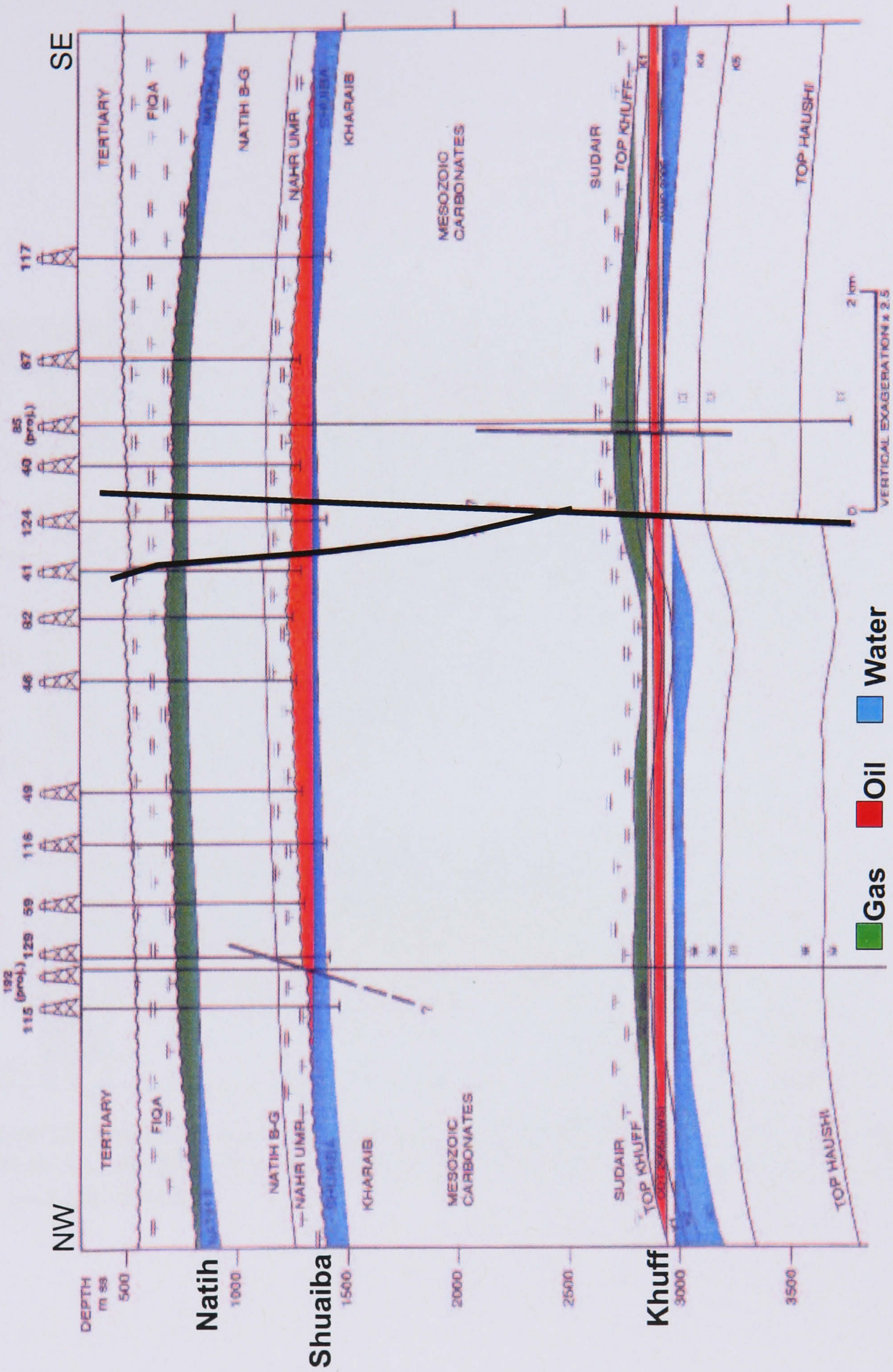

Figure 2.1 NW-SE cross section through the Yibal field showing the Natih gas reservoir, the Shuaiba oil reservoir and the Khuff oil/gas reservoir. The overburden cap shale rocks (Fiqa and Nahr Umr) are also shown. Depth is in meters. Faults are also shown by thick black lines, particularly the extensional fault system associated with the NE graben system (after Cees Van der Schans, PDO, pers. comm.).

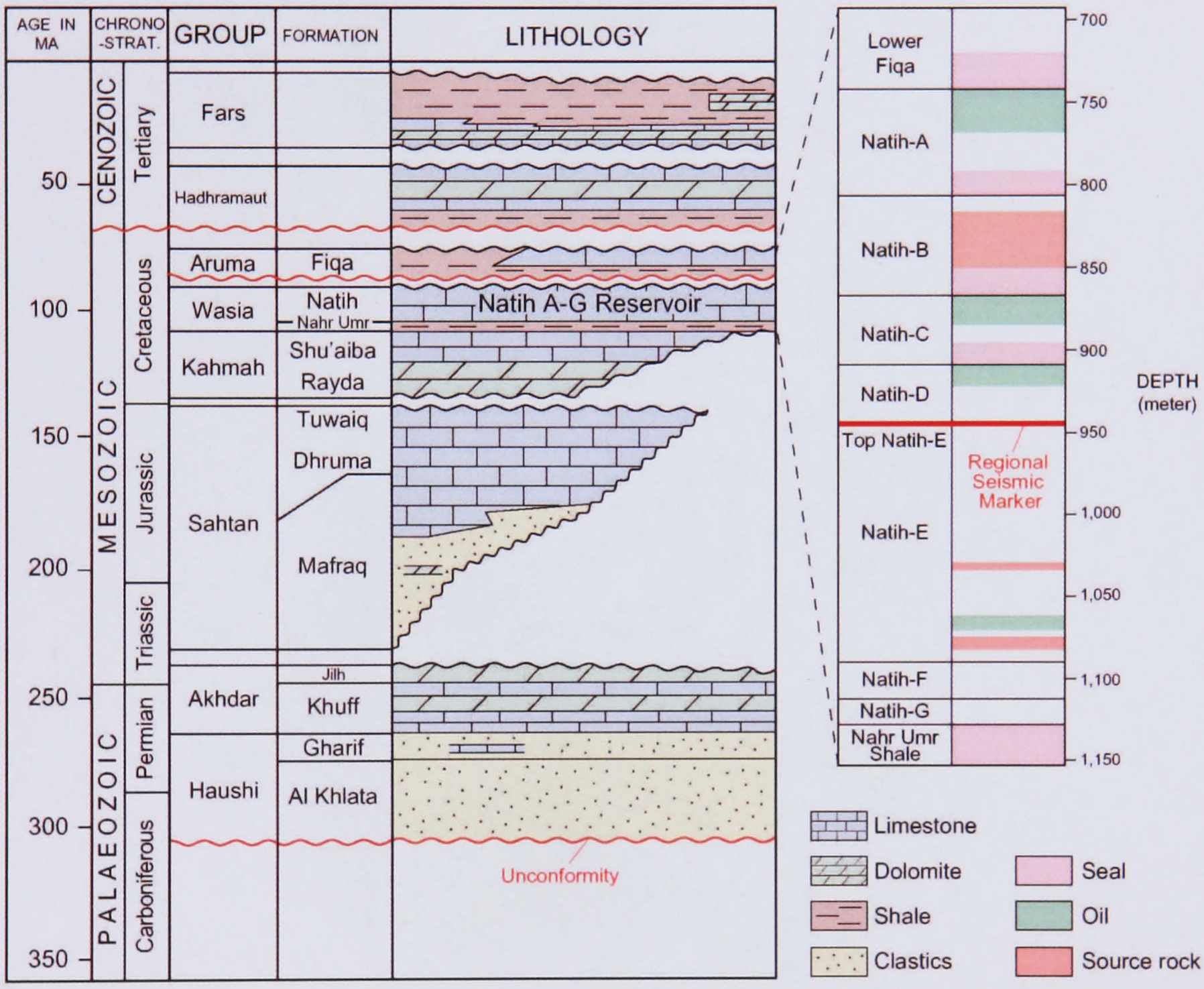

Figure 2.2 Stratigraphic column of Northern Oman (after Hitchings and Potters, 2000). Details of Natih A-G are for the Natih Field, and are similar to the Yibal field since they are both part of the same Fahud basin.

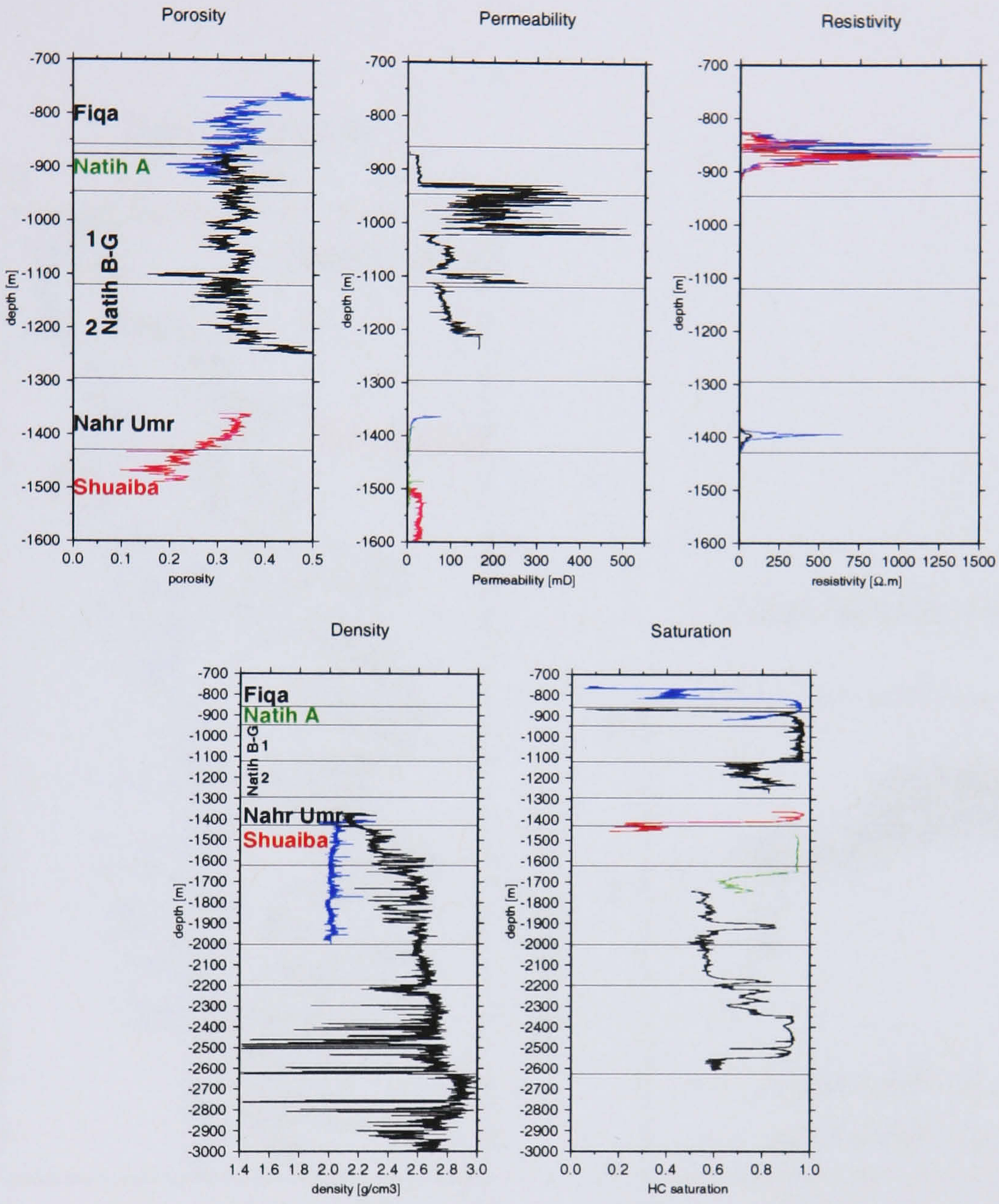

Figure 2.3 Porosity, permeability, resistivity, density and hydrocarbon saturation logs. Typical values are 0.35, 25 mD, 1 Ω.m, 2.2 g/cm^3 and 0.96, respectively. Different wells (different colour) are integrated to form each log. Note, the top and bottom panels cover different well-log lengths. The porosity log wells are y255H1(blue), y450H1(black) and y28H1(red); permeability log wells are y263H1(blue), y451H1(black), y263H2(red) and y85H1(green); resistivity log wells are y220H1(blue), y85H2(black) and y452H1(red); density log wells are y403H1(blue) and y85H2(black); and saturation log wells are y255H1(blue), y450H1(top black), y383H3(bottom black), y263H1(red) and y265H2(green). Well locations are shown in Figure 2.9.

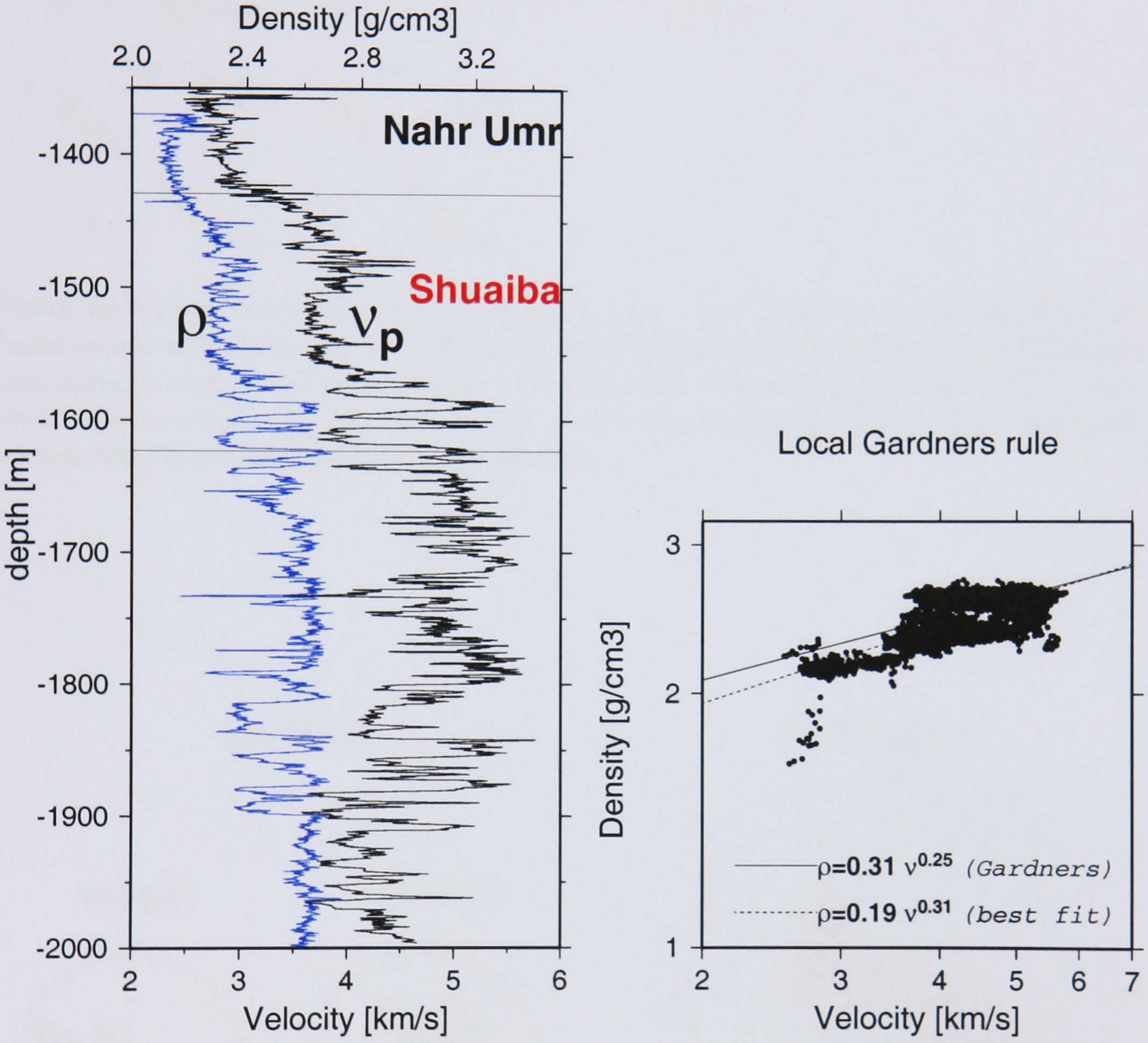

Figure 2.4 [**left**] P-wave velocity (black) and density (blue) logs for wells y2H1 and y85H2 (well location is shown in Figure 2.9), respectively. [**Right**] P-wave velocity versus density in a log-log scale. The best fit (dashed line) through the data and Gardner's rule (solid line) are shown. Their equations are also shown with ρ in g/cm^3 and v in m/s.

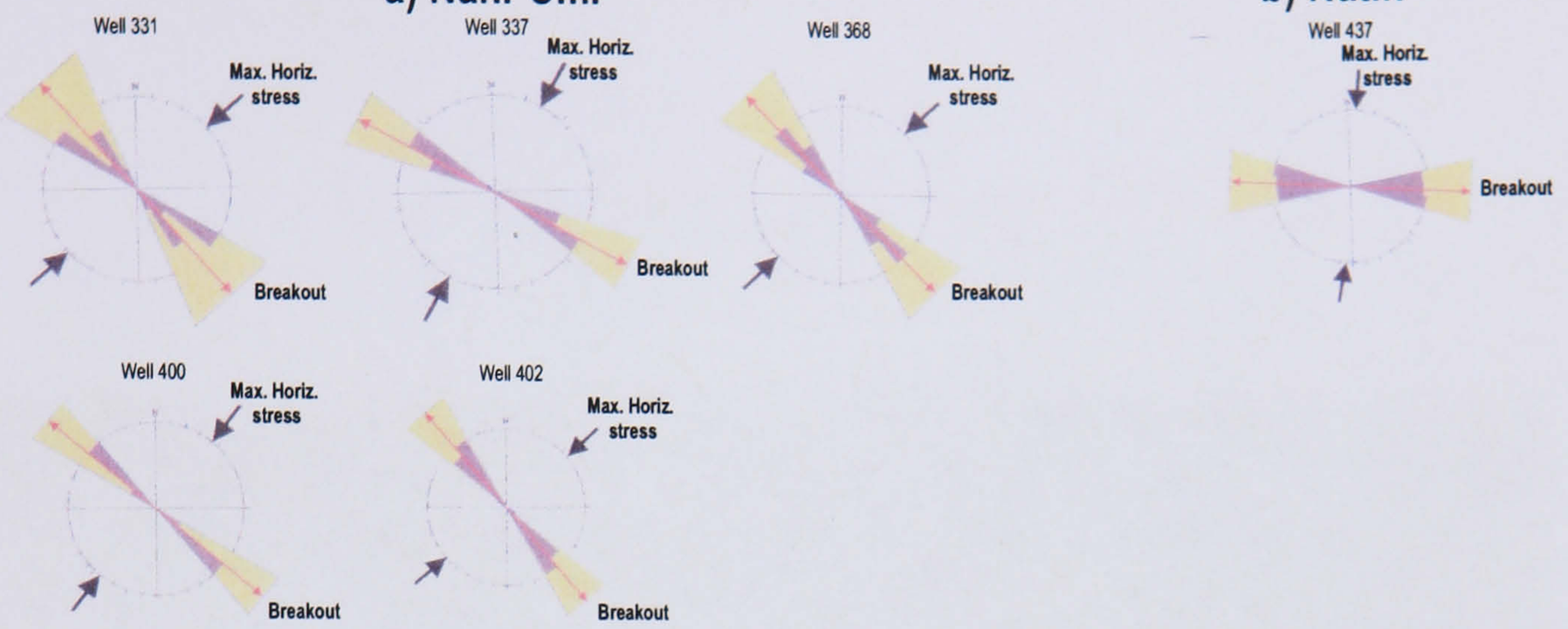

Figure 2.5 Maximum horizontal in-situ stress of [**a**] Nahr Umr (based on 5 wells) and [**b**] Natih (based on one well), inferred from wellbore breakouts derived from differential FMI/FMS caliper measurements on 6 wells located sparsely on flanks of the field (after Baker Atlas GEOScience, 1999). All five wells in the Nahr Umr indicate similar maximum stress trends of NE, while Natih exhibits NNE maximum horizontal stress direction.

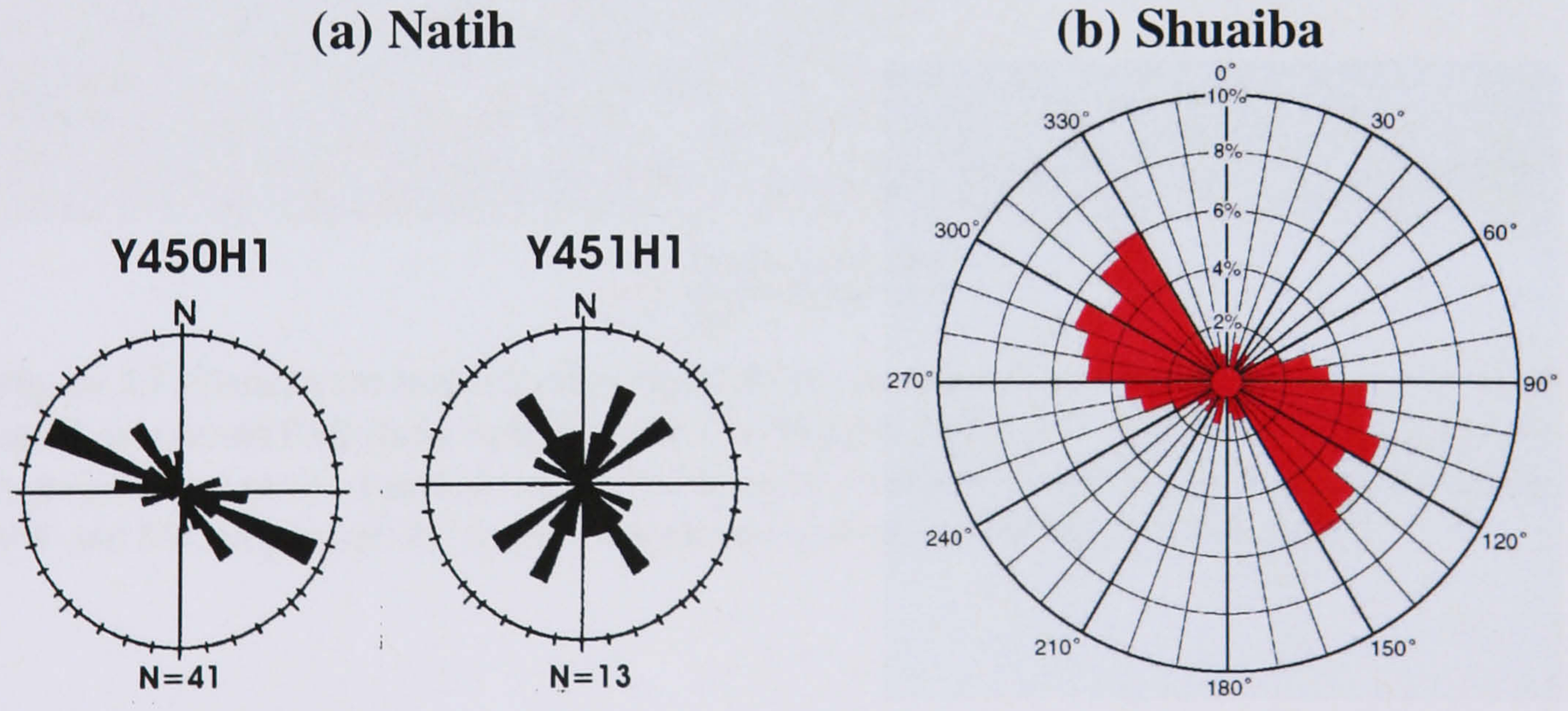

Figure 2.6 [**a**] FMI (Fracture Micro Image) logs for wells 450 and 451 of the Natih reservoir (after Baker Atlas GEOScience,). [**b**] Fracture orientation rose diagram of the Shuaiba reservoir (open fractures) obtained from borehole image logs from more than 10 horizontal wells (after Al-Busaidi, 1997). Cemented fractures exhibit similar trends to open fractures (Al-Busaidi, 1997).

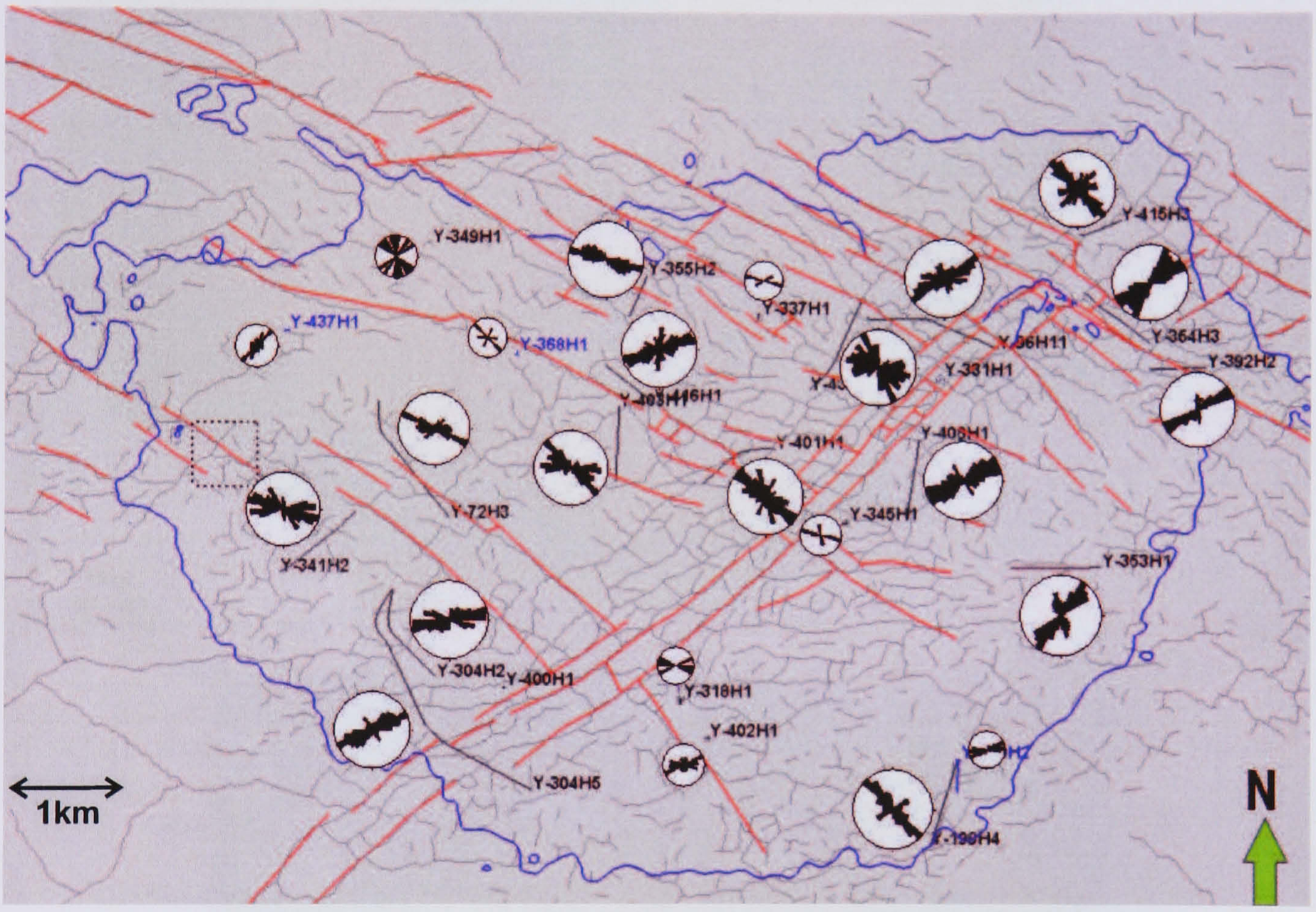

Figure 2.7 Shuaiba fracture map showing fracture orientation rose diagrams for different wells based on a recent FMI study, in 2002 (after Guy Mueller, PDO, pers. comm.). Rose diagram size is proportional to the detected number of fractures. The map shows two preferred orientations, NW and SW. In general, the fracture orientation appears to follow fault orientations.

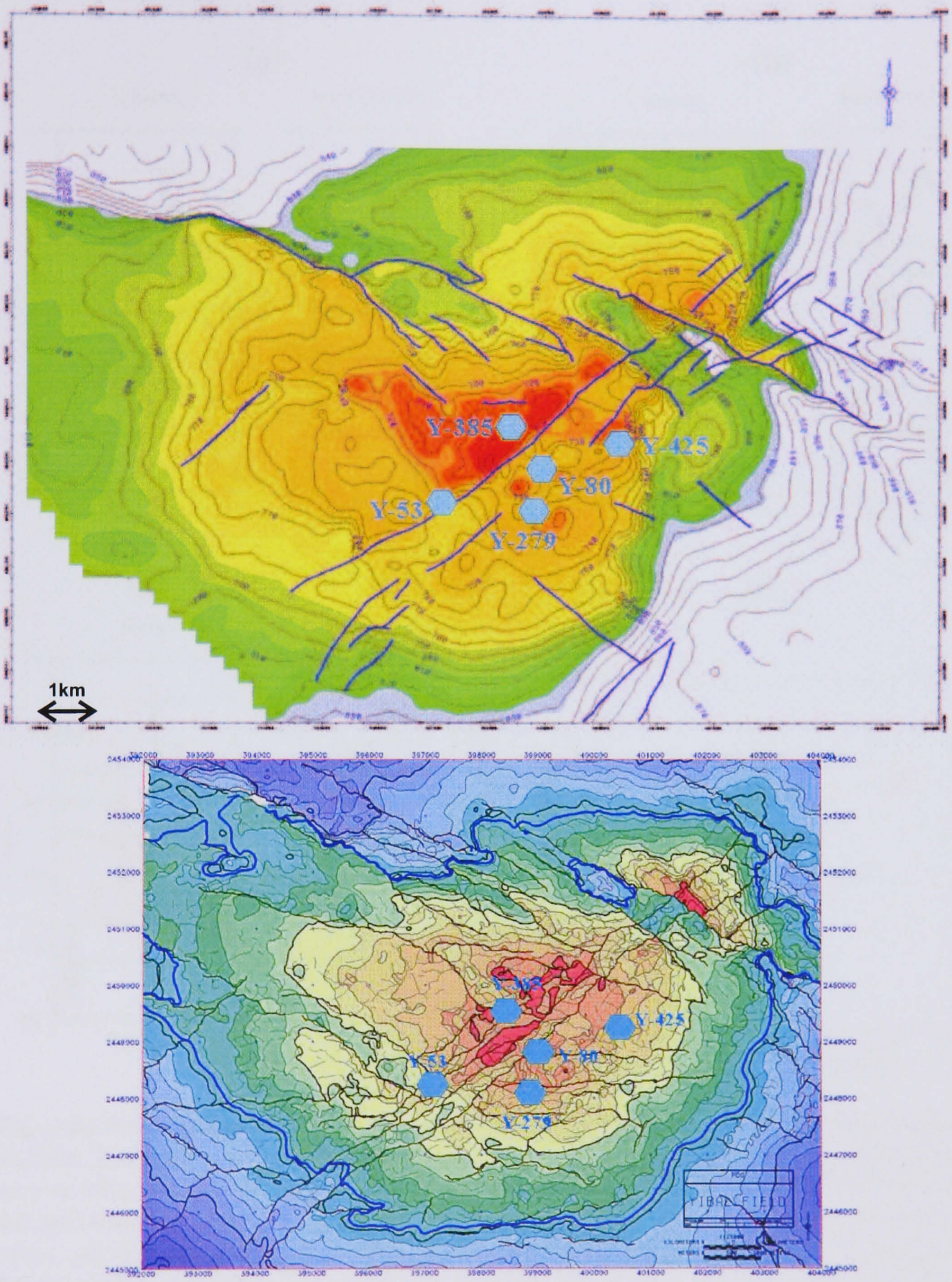

Figure 2.8 Seismically derived structure map of [**top**] top Natih and [**bottom**] top Shuaiba showing faults and observation wells (after Jones et al., 2004). Depth contours (in meters) are also shown illustrating the domal structure of both formations (red: shallowest, and blue: deepest).

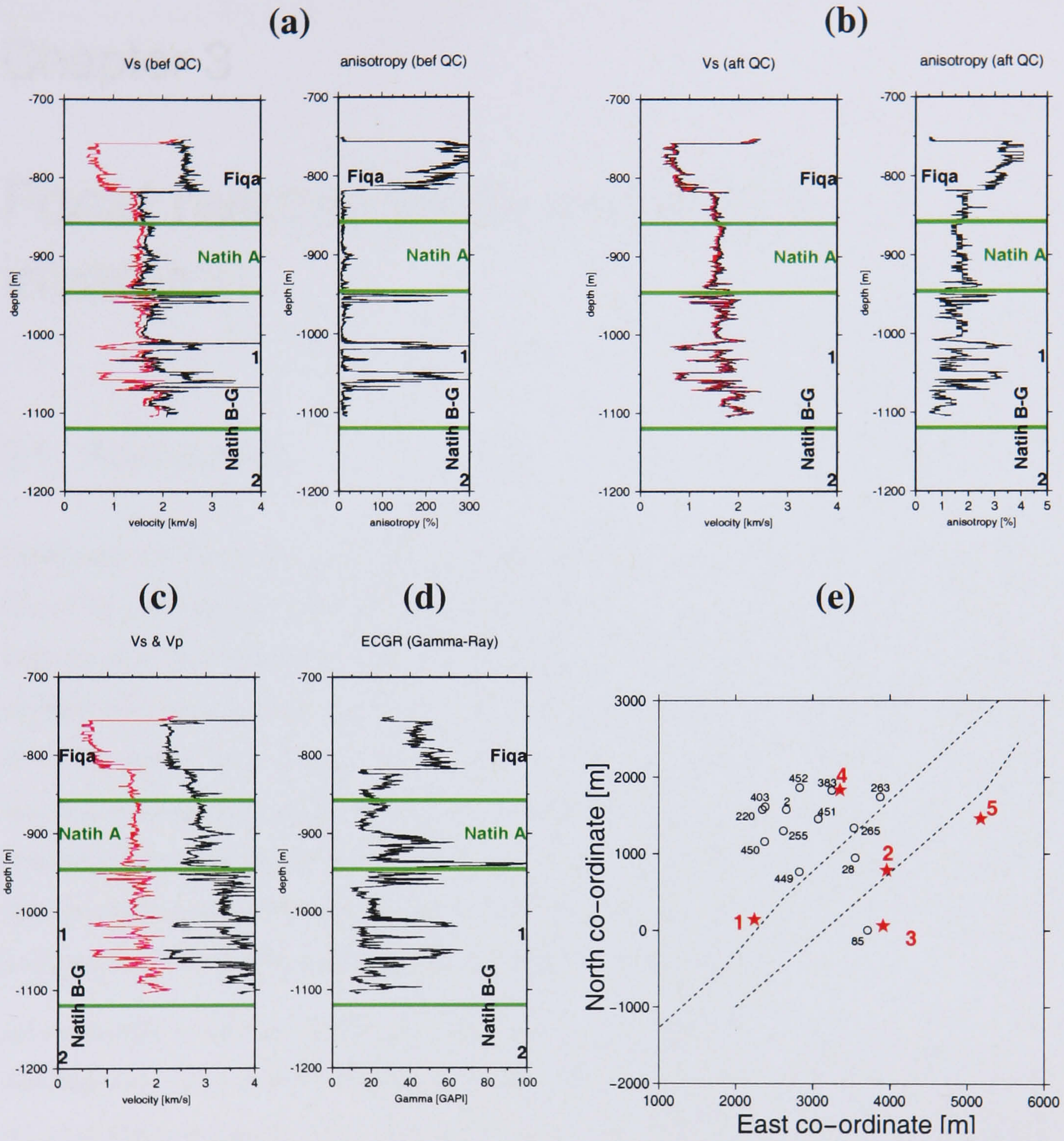

Figure 2.9 Sonic, anisotropy and Gamma-ray logs for well 449H1 (located exactly at the crest of the field). Estimates of minimum (Red) and maximum (black) shear velocity (of 10 dipole-shear velocity logs), and calculated shear anisotropy percentage [**a**] before QC and [**b**] after QC. QC was performed by removing eight dipole-shear velocity logs of abnormal dipole-shear velocity values. [**c**] Minimum dipole shear (Red) and compressional (black) velocity logs. [**d**] Gamma-Ray log used as a lithology indicator. [**e**] A map showing well 449 and other wells whose logs are depicted in Figure 2.3 and 2.4. The true Yibal model for well 449H1 is clearly 40 m above the displayed one because well 449H1 is at the apex of the field.

Chapter 3

Focal mechanisms and stress inversion

3.1 Introduction

Earthquake focal mechanism analysis is a widely used tool in seismology as it provides information on the orientations of fault planes, their slip directions and offers insight into the stress field. Only recently has this type of analysis been introduced to reservoir microseismicity studies. For example, Zoback and Zinke (2002) applied it to Valhall oil field microseismicity recorded by a downhole array of 6 receivers. Rutledge et al. (1998) determined focal mechanisms of microseismic events and estimated the stress field in the Clinton County oil field. House et al. (1996) computed focal mechanisms for microseismic events induced during hydraulic fracture operations by solid-waste injection into unconsolidated sand in the Frio formation, East Texas. Here I analyse microearthquakes at various depths in the Yibal field, Oman.

An earthquake's focal mechanism can be determined by analysing variations in signal polarity and amplitude ratios at many stations. Reliable estimates of fault plane solutions (FPSs) require (a) good station coverage of the microearthquake, (b) well known seismic velocity in the microearthquake region and (c) that the data show impulsive P-wave first arrivals (Snoke, 2003). Unfortunately, with the Yibal data, the first condition is not well satisfied due to the limited number of wells (maximum 5). The detailed Yibal 1D 21-layer velocity model is a fair representation of the real subsurface and, thus, the second condition is satisfied. The third condition requires large magnitude events. Strong events in our over 600 event pool are few and, therefore, limits our analysis to a few events (75 events).

For better constrained solutions, I use P, SV and SH polarities and their amplitude ratios since 3C records are available. P- and SH- arrivals are usually well defined. In contrast, SV polarities

and amplitudes are usually ambiguous due to the ringy P-wave coda. However, there are a few cases where strong events show sharp and well defined SV-wave arrivals. Generally, I rely on the P-wave polarity and the SH/P amplitude ratio. Given the limited focal coverage, I invert for the double-couple solutions as extra degrees of freedom cannot be resolved (i.e., non double-couple components).

Stress tensor inversion from FPSs can be utilised to estimate regional stress directions (Gephart and Forsyth, 1984). After focal mechanisms are determined for the Yibal events, they are used in an inversion scheme to infer the local stress field.

In this chapter, I start with a description of the method used for estimating focal mechanism, followed by tests on synthetic data. Results are then shown for the Yibal field data. Finally, I invert for the stress field using the resulting FPSs.

3.2 Method

At each station the data have been recorded on 3 components oriented in E, N and vertical (Z) directions. The ENZ data are rotated to the ray frame using the P-wave particle motion and the source location. Source locations are used to resolve the 180° ambiguity in the ray direction inferred from the P-wave particle motion (i.e., to point away from the source). I adopt the convention of Snoke (2003) where positive longitudinal (P) is defined as away from the source, positive transverse (SH) to the right with respect to an observer at the source facing the station and positive transverse (SV) pointing down (see Figure 1.9a). Note that longitudinal, transverse SV and transverse SH form a left-handed coordinate frame. Polarities and amplitudes are measured in windows comprising one cycle of the P- and S-waves. A SAC macro has been written to do the rotation, polarity and amplitude picking. I use peak-to-peak amplitudes to mitigate any DC offset problems. The data are not filtered to preserve amplitude ratios. In rare cases, filtering is done to suppress noise. It is only used to remove noise when its dominant frequency lies outside the range of dominant signal frequencies. This is checked by comparing pre-signal noise and signal frequencies.

The program FOCMEC, developed by Snoke et al. (1984), is used to determine FPSs. In addition to the input of phase polarities and/or amplitude ratios, the FOCMEC program also requires azimuth and takeoff angles (from the downward vertical direction) of the corresponding rays at the source. They are extracted from XMETAL as they are calculated when ray tracing is performed to help determine event locations. A Q correction for amplitude ratios is also allowed.

This is achieved by using an exponentially decaying solution for plane propagating waves in an attenuative medium. That is

$$A(x) = A_0 exp[-\frac{\omega x}{2vQ}], \tag{3.1}$$

where A, x, ω and v are amplitude, raypath distance, angular frequency and phase velocity of the propagating wave (Aki and Richards, 1980). This can be reformulated in terms of the usual input parameters t (travel time) and f (frequency):

$$A(x) = A_0 exp[-\frac{\pi t f}{Q}]. \tag{3.2}$$

Using simple algebra, the Q corrected amplitude ratios are

$$\log_{10}(\frac{A_0^S(x)}{A_0^P(x)}) = \log_{10}(\frac{A^S(x)}{A^P(x)}) + \log_{10}(exp[\frac{\pi t_S f_S}{Q_S} - \frac{\pi t_P f_P}{Q_P}]). \tag{3.3}$$

3.3 FOCMEC program description

FOCMEC performs a grid search over all possible orientations of double-couple fault planes in a systematic way. It searches over the model space of strike (0-360°), dip (0-90°) and rake (-90-90°) of fault planes in a uniform angle grid. The solutions follow the geometrical convention of Aki and Richards (1980) as displayed in Figure 3.1. For each possible solution in the model space, FOCMEC calculates the theoretical polarities (P,SV,SH) and amplitude ratios (SV/P, SH/P,SV/SH) at the focal sphere points corresponding to the input measured data, assuming a double-couple source and a far-field measurement. See Aki and Richards (1980) for the theoretical radiation-pattern equations for a double-couple source.

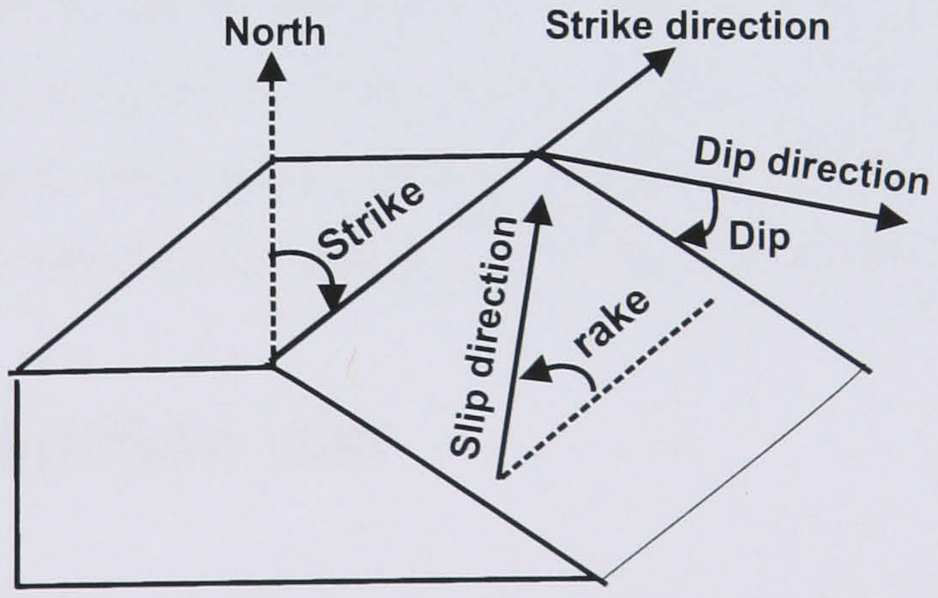

Figure 3.1 Geometry of FPS parameters (strike, dip and rake) following the convention of Aki and Richards (1980). The strike is measured clockwise from North, with the fault dipping down to the right of the strike direction. The dip is measured down from horizontal. The rake angle is defined by the slip direction anticlockwise from the strike direction in the fault plane.

For each possible solution, FOCMEC computes polarity errors and amplitude ratio errors. Polar-

ity errors are the number of input polarities inconsistent with the calculated FPS. The amplitude ratio error is the difference between the measured and predicted (calculated for each single measured amplitude ratio). FOCMEC then reports all solutions compatible with the input polarities and amplitude ratios based on a selection criteria for the number of allowed polarity errors, number of allowed amplitude ratio errors, and maximum amplitude ratio error. Amplitude ratio with errors in excess of the maximum amplitude ratio error are flagged as errors. The selection criteria also allows weightings for rays leaving the source near nodal planes.

In this study the grid search is done with 5° increments. Given the limited focal coverage and 1-D velocity model limitations, a finer grid search (<5°) is not needed. The v_p/v_s ratio at the source is 1.9 which is fairly constant with depth in the Yibal model. The v_p/v_s ratio is required to calculate the theoretical amplitude ratios, SV/P and SH/P. The maximum allowed amplitude ratio error is set to 0.6. I chose not to apply weightings on rays leaving the source along the nodal plane. The choice of these parameters has been guided by synthetic tests (see Section 3.4).

The FOCMEC program plots the possible FPSs in a hemisphere projection. It also has the option of plotting the input P and S polarities (including emergent ones) and amplitude ratios on the FPS plot. Although emergent P-wave arrivals are not used in FOCMEC computations, plotting them together with the other picks in a FPS has the advantage of providing a QC on the robustness of the solution. Low-amplitude emergent P-wave arrivals should fall very near nodal planes (fault plane and auxiliary plane).

FOCMEC assumes (a) a pure double-couple model (i.e., pure shear slip) and (b) far-field measurements. The first assumption cannot be verified since the maximum additional pressure caused by fluid injection (to the natural hydrostatic fluid pressure) relative to the 3 principal stresses is unknown (assuming injection induced seismicity). The second assumption is satisfied by almost all measurements since raypath distances (300m-3km) are generally much longer than typical wavelengths (10-100 m for an average velocity of 3 km/s and frequencies 30-300 Hz).

3.4 Tests with synthetic data

There are many questions regarding the suitability of the Yibal data for focal mechanism analysis and FOCMEC sensitivity to input parameters. Are source radiated amplitude ratios preserved along the entire raypath, despite transmission losses across interfaces? Also the effect of Q on the ratios and results has received little previous attention. In short, what is the minimum input information needed to obtain a reliable solution for Yibal events and to what degree can

amplitude ratios be trusted? To answer these questions focal mechanism analysis on synthetic seismograms was conducted to check the applicability of the technique (FOCMEC), accuracy of the solution, and influence of input parameters on the final result.

3.4.1 Reflectivity synthetic seismograms

To simulate data-like synthetic seismograms, I use reflectivity modeling since it has the advantage of computing the full wavefield for a layered 1D model (i.e., it includes all P-, S-, P-S conversions, S-P conversions, head waves, multiples, etc.). The reflectivity function is generally computed in the frequency-wavenumber domain by a layer-matrix method that automatically includes contributions from all possible generalized rays within the reflecting zone. The computed data are then transformed into the time-distance domain using a Fourier-Hankel transformation (Mallick and Frazer, 1987).

Choice of Reflectivity code

I tested 3 available reflectivity codes: *axitra*[1], *skb*[2] and *sureflpsvsh*[3]. The *axitra* program has the advantage of incorporating intrinsic attenuation (Q) and dispersion, and has the ability to handle explosive sources, fault-slip and/or combined sources and it can accommodate buried receivers and sources. In addition, careful tests of *axitra* amplitudes using a homogeneous half-space model showed that the *axitra* program computes correct amplitudes (i.e., proportional to $1/distance$) whereas this was not clear with *skb* and *sureflpsvsh*. *axitra* was therefore used to create synthetic traces. It was modified to calculate the moment magnitude (M_w) from fault properties (fault area and displacement). The M_w scale developed by Kanamori (1977) is defined as

$$M_w = \frac{2}{3}\log_{10} M_0 - 10.7, \tag{3.4}$$

where M_0 is the scalar seismic moment measured in dyne-cm (10^5 dyne=1 N; thus 10^7 dyne-cm=1 N-m) (Shearer, 1999). M_0 is given by

$$M_0 = \mu DA, \tag{3.5}$$

where μ is the shear modulus, D is the fault displacement and A is the area of the fault. The shear modulus μ is calculated using the shear-wave velocity, v_s, and the density ρ of the medium

[1]Written by Olivier Coutant based on Kennett and Kerry (1979) and Bouchon (1981).
[2]Written by Michel Dietrich, (Dietrich, 1988).
[3]Part of Seismic Unix (SU) package.

around the fault by $\mu = v_s^2 \rho$.

Tests on input parameters of axitra program

Various tests were carried out with *axitra* input parameters such as f_{dig} (digitizing frequency), *aw* (coefficient for frequency imaginary part), *xl* (periodicity of the medium), *ikmax* (maximum number of iterations) and *uconv* (convergence criteria). Synthetic seismograms with minimal ringing, numerical noise and end-point signals were attained by setting *aw* $\leq$2, *ikmax* $\geq$400 and $10^{-5} <$ *uconv* $\leq 10^{-2}$. Theoretically, the digitizing frequency should be at least twice the desired signal frequency to avoid aliasing. *xl* should be at least five times the source-station distance for a record length of 2s.

Reflectivity modelling

A minimum phase wavelet with corner frequency 40Hz is used as a source pulse. This is accomplished by low-pass filtering the impulse response traces with a Butterworth filter of corner frequency 40Hz, 2 poles and one pass. The digitizing frequency is 250 Hz. The reflectivity computation time for one station is $\approx$2 minutes, using an 800 MHz SUN processor and the SUN f77 compiler.

Density values, ρ, for Yibal are unavailable and are therefore approximated using Gardner's rule (Gardner et al., 1974). Q values are also unavailable. Since Q_p ranges 20-200 for sedimentary rock and Q_s is normally 1/3 to 1/2 of Q_p (Sheriff and Geldart, 1994), I approximate Q_p as 100 and Q_s=0.5Q_p. Figure 3.2 shows the location of two events considered for synthetic tests: y021022.0042 (at the south of the network) and y021022.0057 (at the NE corner of the network in the Horseshoe area). This allows us to examine the applicability of focal mechanism analysis for events with different focal sphere coverage. Additionally 3 pure-shear fault mechanisms (*M*) (Table 3.1 and Figure 3.9a) are considered. The tests start with a homogeneous half-space model (simplest case) and end with the complicated 21-layer Yibal attenuation model (realistic case) to investigate the effects of layering and attenuation.

Table 3.1 Fault mechanisms considered in synthetic modeling.

M	Fault type	dip	strike	rake
1	Reverse	45°	0°	90°
2	Reverse	20°	0°	90°
3	Strike slip	90°	0°	0°

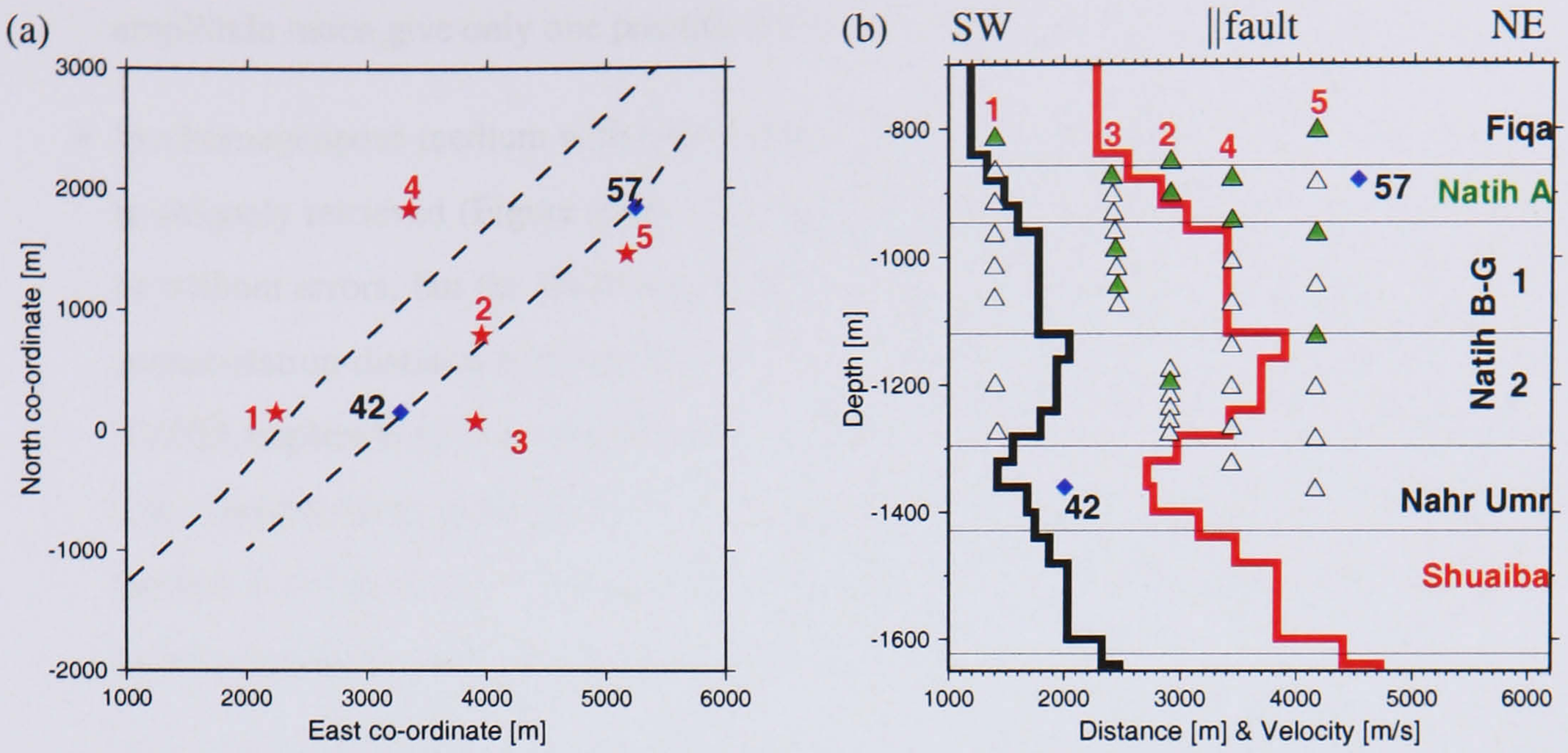

Figure 3.2 The location of the two events y021022.0042 and y021022.0057, marked by diamonds, used in the synthetic tests: [**a**] map view and [**b**] cross section.

3.4.2 Half-space velocity model

For event y021022.0042 and mechanism M=1, 3C seismograms were created for the shallowest station in each of the 5 observation wells in a simple half-space velocity model (v_s=1.9 km/s, ρ=2200 kg/m^3), both with and without attenuation. The synthetic data for the simple half-space attenuation model is shown in Figure 3.3. The direct P- and S-arrivals are impulsive and well defined in the synthetic seismograms (Figure 3.3). The synthetic seismograms also include other arrivals which are P- and S-wave reflections from the free surface. The synthetic data are then processed in the same way as the real data to determine the FPS (Section 3.2). Table 3.2 summarises the resulting polarity errors, and amplitude ratio errors obtained when using all possible well information, and the minimum information required for a unique solution. The subcolumns "P polarity" and "amp. ratio" of the column "min. wells" in Table 3.2 show the minimum wells needed for a unique solution listed in well number. For example, for both Q_p=10^6 and Q_p=100, amplitude ratios of 3 wells (well 1, well 2 and well 3) are enough for a unique FPS without needing P polarities from any well (empty subcolumn "P polarity" in Table 3.2). The "Max. amp. ratio error" column reports the largest amplitude ratio error (of any of SV/P, SH/P and SV/SH) encountered when all the wells are used.

The results can be summarised as follows:

- In a homogeneous medium without attenuation (Q_p=10^6 and Q_s=0.5×10^6), the input FPS can be uniquely retrieved (Figure 3.4b). The (P,SV,SH) polarities and (SV/P, SH/P,SV/SH)

amplitude ratios give only one possible solution with no polarity or amplitude ratio errors.

- In a homogeneous medium with attenuation (Q_p=100 and Q_s=50), similarly, the input FPS is uniquely retrieved (Figure 3.4c). The (P,SV,SH) polarities and SV/SH amplitude ratios fit without errors, but the SV/P and SH/P amplitude ratio errors increase with increasing source-station distance and reach -0.41 for the furthest station (well 5 in this case). The SV/SH amplitude ratio is unaffected because both SV and SH suffered identical attenuation. The amplitude ratio errors become significantly smaller after a Q correction has been applied to the amplitude ratios prior to FOCMEC analysis. For the Q correction, I used P- and S-wave frequencies f_p=f_s=20 Hz and Equation 3.3.

- Remarkably the input focal mechanism can be uniquely recovered with knowledge of amplitude ratios in only 3 wells: well 1, well 2 and well 3 (Table 3.2). This is true for models without and with attenuation (Figures 3.4(d,e), respectively), and means that polarities of P-, SV-, SH- waves are not required for unique determination of FPSs in the simple half-space models. In these cases (Figures 3.4(d,e)), to get constrained solutions one has to lower the maximum allowable amplitude ratio error in the selection criteria of the FOCMEC program.

- Similar results are expected for the other synthetic mechanisms (M=2 and 3) as there are no interfaces in the models. Thus the radiated amplitude ratios are purely affected by attenuation.

Table 3.2 Polarity and amplitude ratio errors in recovering theoretical focal mechanisms from 3C synthetic seismograms, using a homogeneous half-space model of v_p=3.7 km/s, v_s=1.9 km/s, ρ=2200 kg/m^3 ($Q_s = 0.5Q_p$ in all cases). Fault mechanism type (M) of 1 refers to a reverse fault (Table 3.1). Synthetic seismograms are for event y021022.0042 recorded at the top-most station in each well. The "polarity" and "maximum amplitude ratio error" columns show the errors when using all possible well information. The final column (*) shows the minimum wells needed to recover uniquely the focal mechanism. Note that we can recover the fault mechanism M=1 uniquely using only amplitude ratios from 3 wells (well 1, 2 and 3). Note also the perfectly recorded polarities at the stations, resulting in zero polarity errors.

Q_p	M	P,SV,SH polarity		Max. amp. ratio error			Min. wells*	
		wells	error	wells	Q corr		P polarity	amp. ratio
					bef	aft		
10^6	1	1,2,3,4,5	0	1,2,3,4,5	0.08	0.08		1,2,3
100	1	1,2,3,4,5	0	1,2,3,4,5	-0.41	0.08		1,2,3

3.4.3 21-layer Yibal velocity model

3C seismograms were also created for the two events y021022.0042 and y021022.0057 in the 21-layer Yibal velocity model, both with and without attenuation. The three synthetic fault mechanisms (Table 3.1) were again tested. Synthetic seismograms for event y021022.0042 using fault mechanism M=1, and including attenuation, are displayed in Figure 3.5. For comparison, the real data from this event are shown in Figure 3.6. Similarly, synthetic and real seismograms for event y021022.0057 are displayed in Figures 3.7 and 3.8, respectively. For accurate identification of the direct P- and S-wave windows, I use ray tracing (Guest and Kendall, 1993) to determine their arrival times. The differences between real and synthetic data suggest that the Yibal subsurface is more complex than the 1D 21-layer velocity model.

The synthetic data were run through the focal mechanism processing flow and the input FPSs were successfully and uniquely retrieved for the two events and three mechanisms. Table 3.3 summarises the polarity errors, amplitude ratio errors and minimum information required for a unique FPS. The three recovered focal mechanisms for event y021022.0042 and y021022.0057 in the Yibal attenuation model are shown in Figures 3.9(b,c), respectively. Event 42 is better constrained than event 57 due to better focal sphere coverage and closer well proximity. Figure 3.9 also shows that the proximity of focal picks to nodal planes is a significant factor in constraining the FPS. For example, focal coverage of both nodal planes, as for event 42 (for M=1 and 2 in 3.9b), better constrains the FPS than when only a single nodal plane is sampled as in event 57 (for M=1 and 2 in 3.9c). This is partly because the points on the focal sphere in event 42 spread across the whole sphere providing more control on both nodal plane locations. With event 57, the focal points are all positioned within a single quadrant rendering a poorly constrained location of the furthest nodal plane.

Amplitude ratios at the source can be modified along the raypath from both attenuation and transmission effects. Models without attenuation generally show less amplitude ratio error than those with attenuation. Amplitude ratios in the Yibal 21-layer model display significantly more error than those of the half-space model (compare Tables 3.3 with 3.2). This is due to the layering which causes differential transmission losses of P, SV and SH at each interface. They also depend on the radiation pattern, as Q and transmission effects affect the amplitude ratios for SV/P, SH/P and SV/SH waves differently for different fault mechanisms. Even SV/SH amplitude ratios (considered reliable in the half-space model because SV and SH waves are equally attenuated) can be as high as 0.5 in the Yibal attenuation model. Figure 3.10 shows the amplitude ratio error

as a function of source-receiver distance (for four neighbouring wells) for two events and for focal mechanism M=2. Generally the error increases with increasing distance.

Note, unlike the results for the half-space model, not all wells can be used to estimate FPSs. This is because of attenuation and transmission effects. Since both effects increase with increasing ray-path distance, information from the most distant wells is the most affected. It is also contaminated by other arrivals, such as head waves (see Section 3.4.4).

Table 3.3 Polarity and amplitude ratio errors in recovering theoretical focal mechanisms from 3C synthetic seismograms using the 21-layer Yibal model ($Q_s = 0.5Q_p$ in all cases). Mechanisms (M) 1, 2 and 3 are defined in Table 3.1. Synthetic seismograms are for events y021022.0042 (recorded at the top-most station in each well) and y021022.0057 (recorded by stations 1.1, 2.4, 3.6, 4.2 and 5.5). The "polarity" and "maximum amplitude ratio error" columns show the maximum number of wells that can be used to estimate FPSs and the associated errors. The final column (*) show the minimum wells needed to uniquely recover the focal mechanism. $\star$ $\frac{SV}{SH}$ ratio only. † plus SV and SH polarity from stations in well 5.

Event	Q_p	M	P,SV,SH polarity		Max. amp. ratio error			Min. wells*	
			wells	error	wells	Q corr		P polarity	amp. ratio
						bef	aft		
y021022.0042	10^6	1	1,2,3,4	0	1,2,3,4	-.30	-.30		1,2,3
		2	1,2,3,4	0	1,2,3,4	.50	.50	1	1,2,3,4
		3	1,2,3,4	0	1,2,3,4	.40	.40		1,2,3
	100	1	1,2,3,4	0	1,2,3,4	-.54	-.2		1,2,3
		2	1,2,3,4	0	1,2,3,4	-.65	.40		1,2,3
		3	1,2,3,4	0	1,2,3	-.50	-.32		1,2,3
y021022.0057	10^6	1	2,3,4,5	0	2,5	.12	.12	4,5	4*,5†
		2	2,3,4,5	0	2,4,5	-.32	-.32	5	4,5†
		3	2,3,4,5	0	5	-.08	-.08	4,5	4*,5†
	100	1	2,3,4,5	0	2,5	-.51	-.16	2,4,5	2,4*,5†
		2	2,3,4,5	0	2,5	-.55	-.21	5	4,5†
		3	2,3,4,5	0	2,5	-.24	.27	4	2,5†

3.4.4 Overview of far station polarity and amplitude ratio usage

The synthetic seismograms for events 42 and 57 (Figures 3.5 and 3.7, respectively) show that direct P and S arrivals at the furthest station (well 5 for event 42 and well 1 for event 57) are clearly preceded by head waves and are difficult to pick. Even if picked accurately their amplitude ratio errors are high (e.g., absolute value of 0.7 for the y021022.0042 event and fault mechanism M=1). Therefore, picks from the furthest well should not be used.

For the y021022.0042 event, all polarity and amplitude ratio picks for the three nearest wells (well 1,2 and 3) are reliable (Figure 3.10). At station 4.1 the direct P- and S-waves are followed

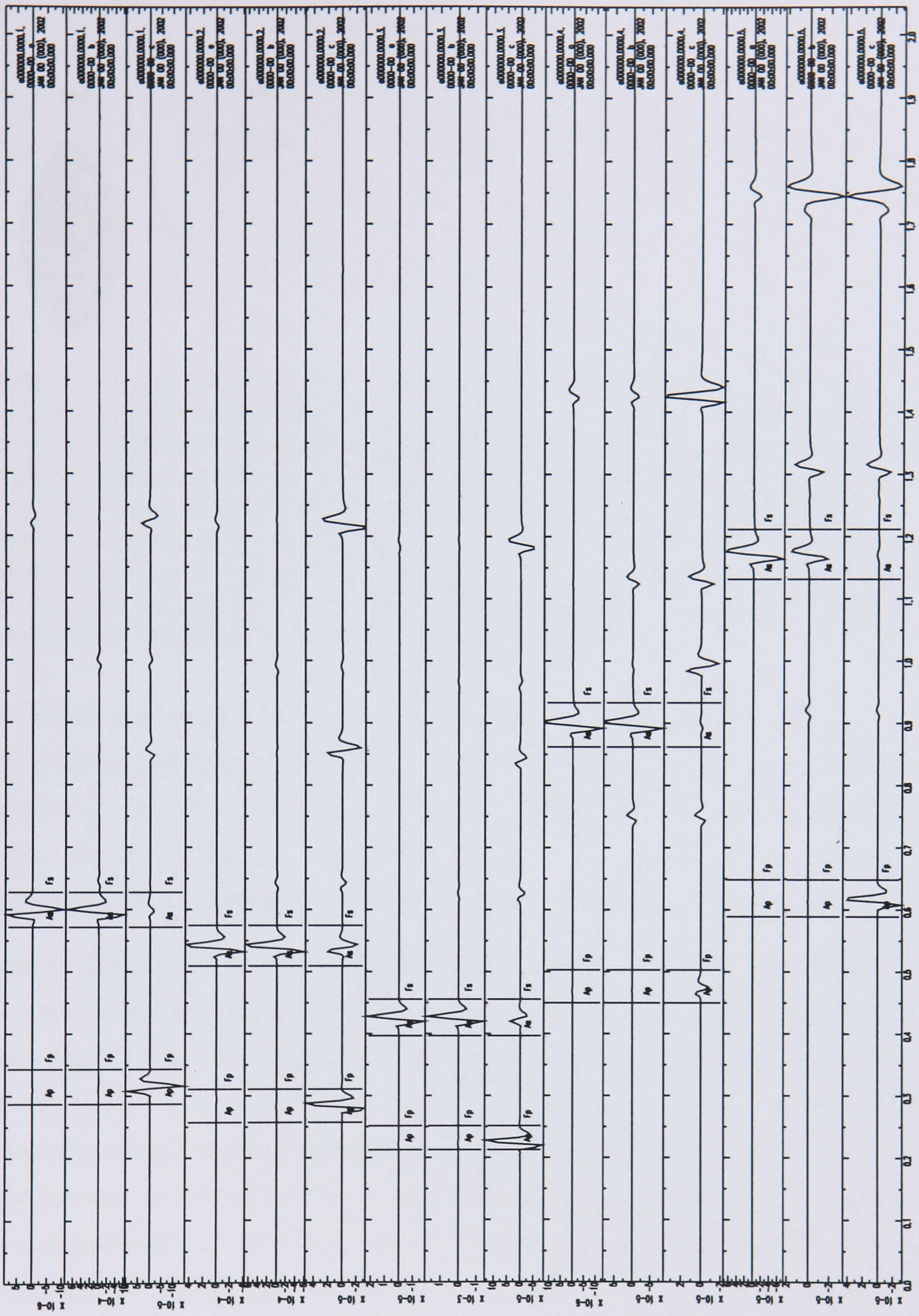

Figure 3.3 Synthetic seismograms for the simple half-space model with attenuation. Seismograms are calculated for the top-most stations in each of the observations wells using fault mechanism M=1 (Table 3.1) for event y021022.0042. Well number increases top to bottom from 1 to 5 (i.e., stations 1.1, 2.1, 3.1, 4.1 and 5.1, respectively). Traces are rotated to ray co-ordinates. Horizontal and vertical axis are time [0–2.048s] and velocity amplitude, respectively. Components are a,b,c (SH,SV,P) from top to bottom for each station. [Ap Fp] and [As Fs] mark the P- and S-wave windows over which polarities and amplitudes are determined. Later spurious arrivals are associated with P- and S-wave reflections from the free surface of the model.

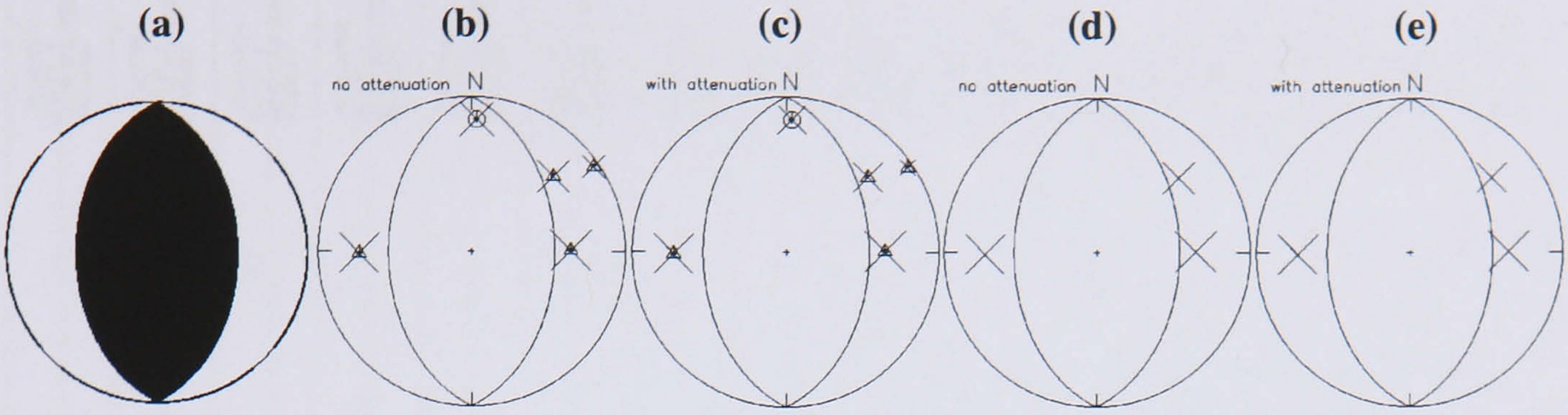

Figure 3.4 Tests of FPS recovery using synthetic data calculated from the half-space velocity model for event y021022.0042 and synthetic mechanism M=1. [**a**] Input focal mechanism M=1, [**b**] recovered FPS from the half-space model without attenuation and [**c**] including attenuation. [**d**] and [**e**] same tests as (b) and (c), respectively, using only the minimum information required to retrieve a unique FPS. Note that unique FPS can be recovered from amplitude ratios at only 3 stations (no Q correction was applied). The selection criteria for the maximum allowable amplitude ratio error is lowered to 0.1 and 0.3 for (d) and (e), respectively (it is 0.6 in (b) and (c)). Projection is upper hemisphere. Circles are compressions (Black quadrant), triangles are dilatations (white quadrant) and crosses are amplitude ratios.

by relatively large amplitude P- and S- head waves, respectively (Figure 3.5). Therefore, S-wave attributes should not be used because it will be easy to select the head-wave instead of the smaller direct S-wave. Even though neither S-polarities nor amplitude ratios should be used, P-polarities can be easily picked and used without being misled by the larger second head-wave arrival. Finally, with distant stations (e.g., 4.1,5.1) the amplitude ratios have generally high errors.

The y021022.0057 event is located at the NE corner of the network, near the so-called Horseshoe. As a result polarities and amplitude ratios at only one well (well 5) are reliable. Figure 3.10 shows that wells 2 and 4 are further away and their information should be used with care. At stations 3.6 and 4.2 the S-wave direct arrivals are contaminated by small overlapping arrivals (reflections) and the resultant amplitude ratios exhibit high error. Therefore only the P-wave polarity is used. At stations 3.6 and 4.2 the SV/SH amplitude ratios show very small errors for two mechanisms M=1,2, but a large error for the fault mechanism M=3. In order to constrain the solution, SV and SH polarities at station 5.5 are used. Events in the Horseshoe area (like y021022.0057) have poor focal coverage because all well information plots in the same quadrant of the focal sphere (Figure 3.9c). Fortunately, stations from well 5 (5.1, 5.3) can be included to increase the focal coverage (see source-receiver configuration in Figure 3.2b).

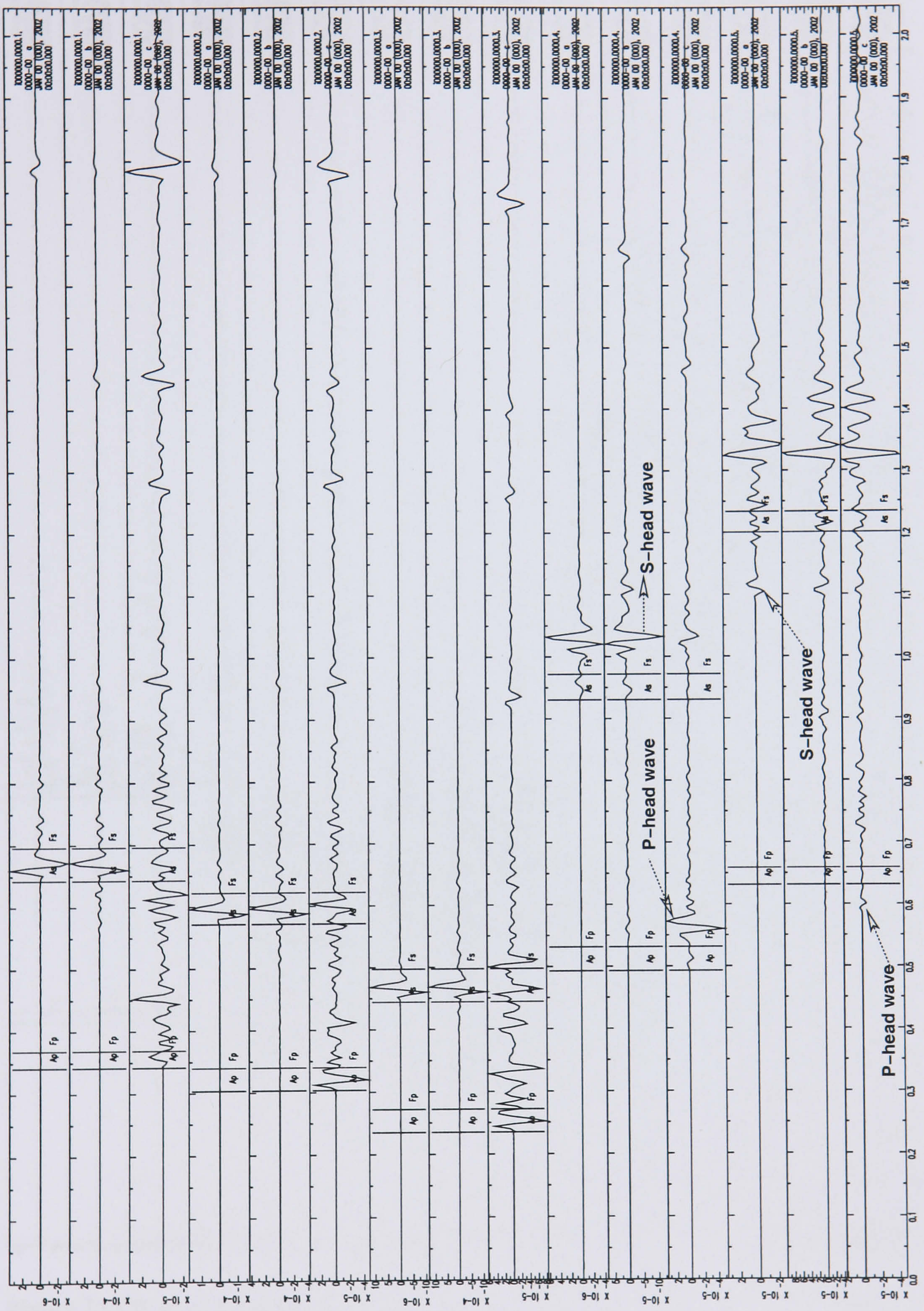

Figure 3.5 Same as Figure 3.3 for the 21-layer Yibal model with attenuation.

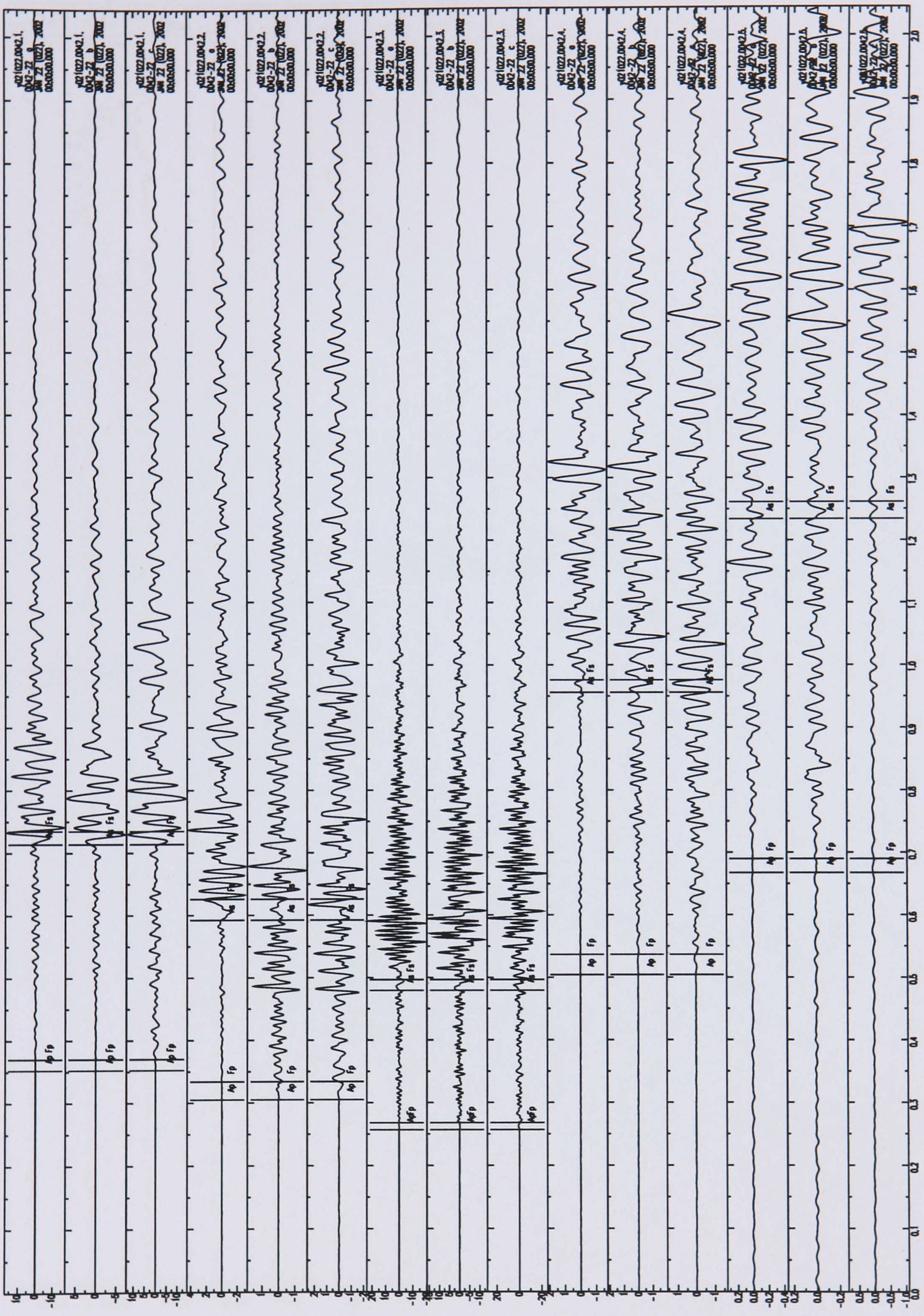

Figure 3.6 Observed seismograms for the Yibal event y021022.0042, which is modelled in Figure 3.5 (compare the two). Seismograms are filtered differently to suppress noise without affecting the signal. Filtering is performed for display purposes only and is not done in the analysis. See Figure 3.3 caption for further figure details.

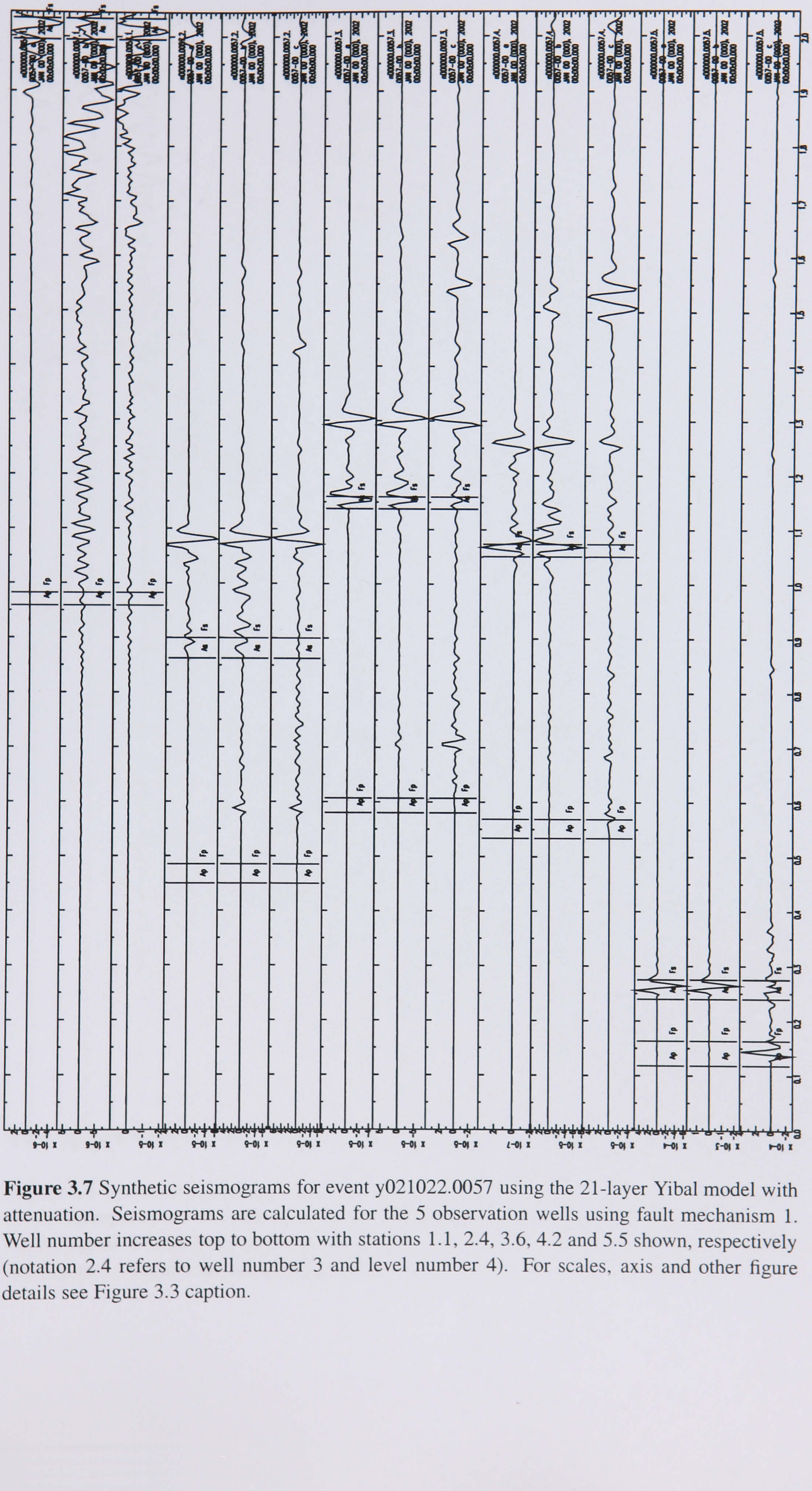

Figure 3.7 Synthetic seismograms for event y021022.0057 using the 21-layer Yibal model with attenuation. Seismograms are calculated for the 5 observation wells using fault mechanism 1. Well number increases top to bottom with stations 1.1, 2.4, 3.6, 4.2 and 5.5 shown, respectively (notation 2.4 refers to well number 3 and level number 4). For scales, axis and other figure details see Figure 3.3 caption.

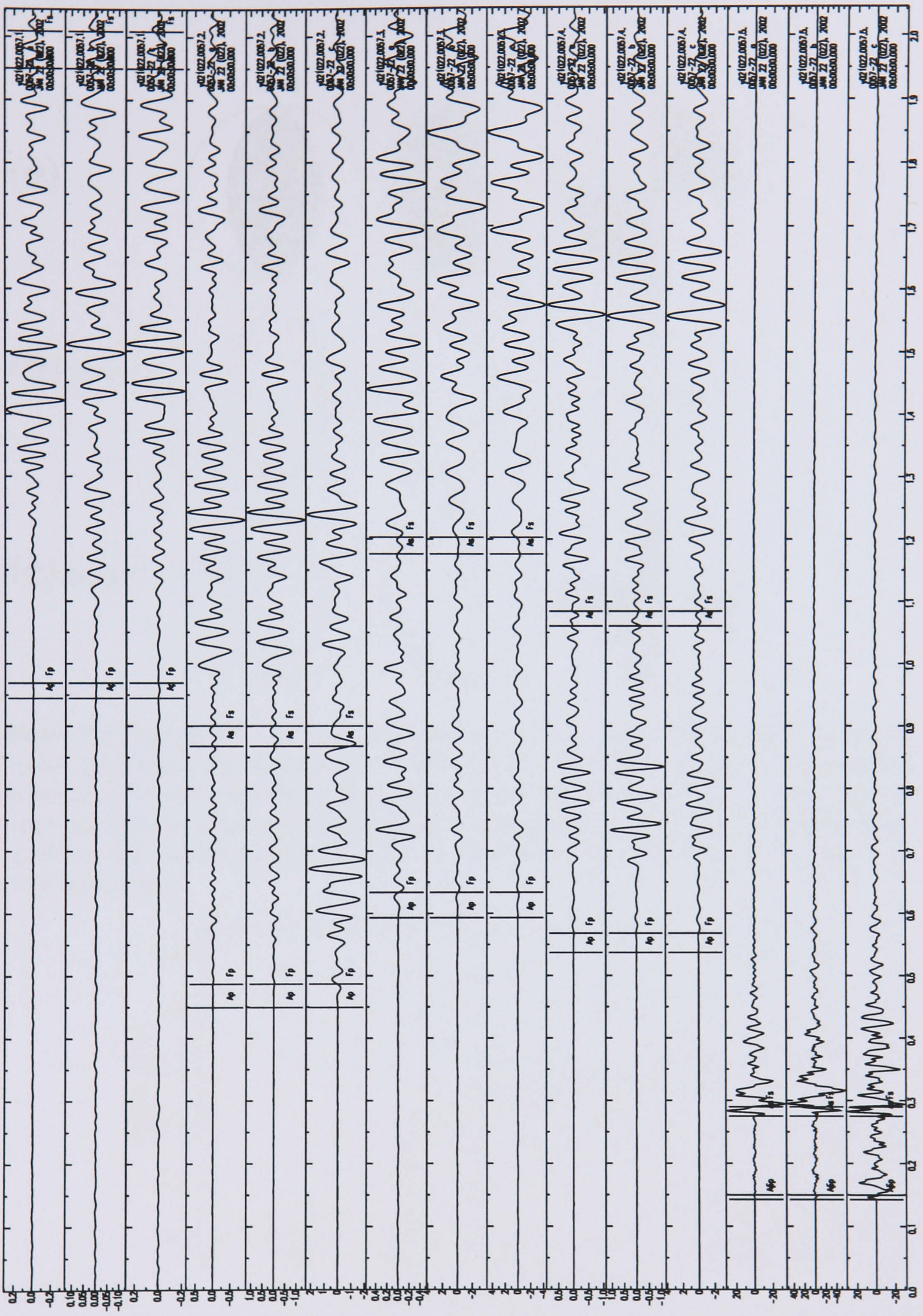

Figure 3.8 Observed seismograms for the Yibal event y021022.0057, which is modelled in Figure 3.7 (compare the two). Seismograms are filtered differently to suppress noise without affecting the signal. Filtering is performed for display purposes only and is not done in the analysis. See Figure 3.3 caption for further figure details.

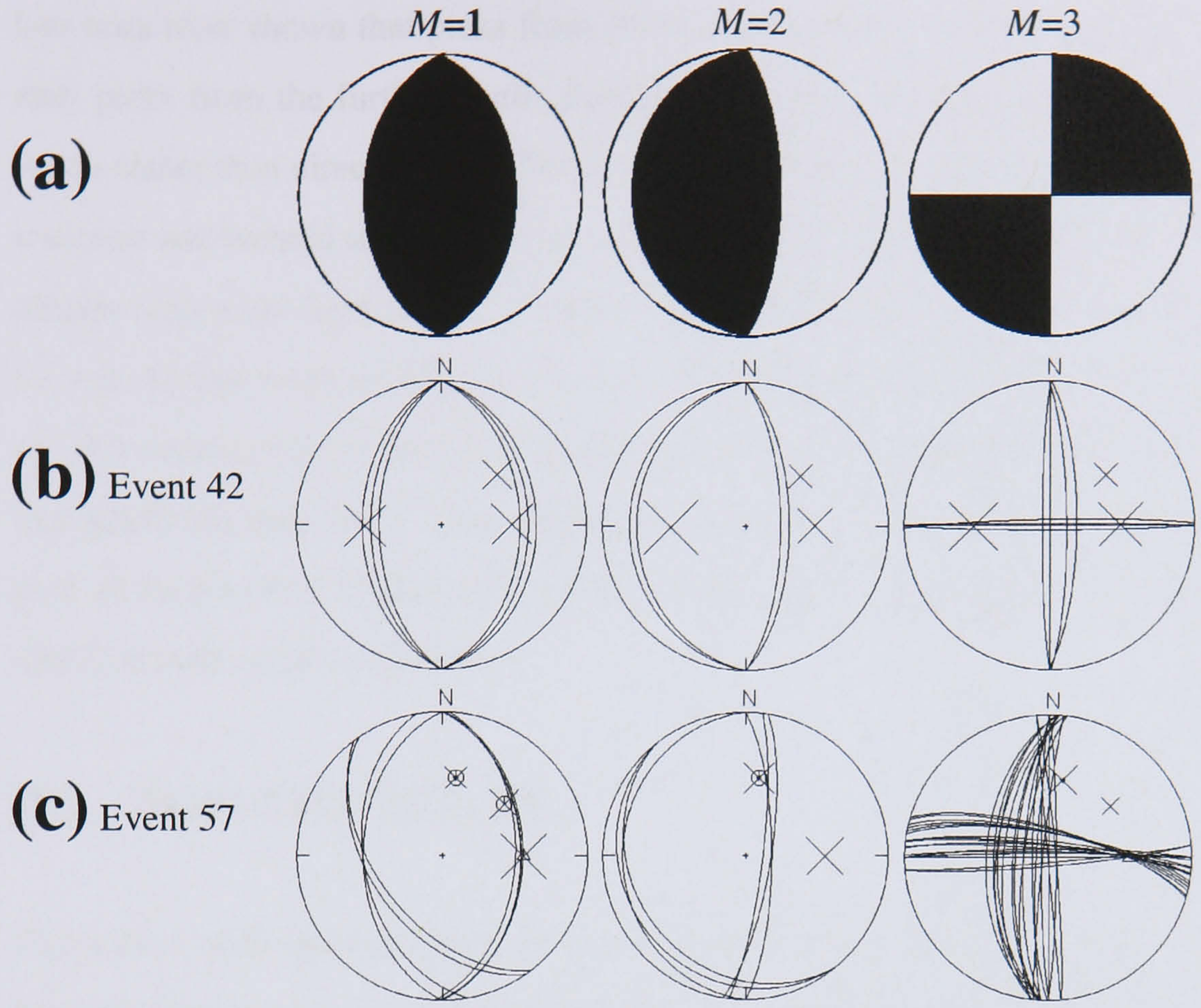

Figure 3.9 Tests of FPS recovery using synthetic data calculated from the Yibal attenuation model. [**a**] Input focal mechanisms, [**b**] recovered FPSs for event y021022.0042 using minimum information without a Q correction and [**c**] same test for event y021022.0057. Projection is upper hemisphere. Circles are compressions (Black quadrant), triangles are dilatations (white quadrant) and crosses are amplitude ratios. See the final column in Table 3.3 for all information used in (b) and (c).

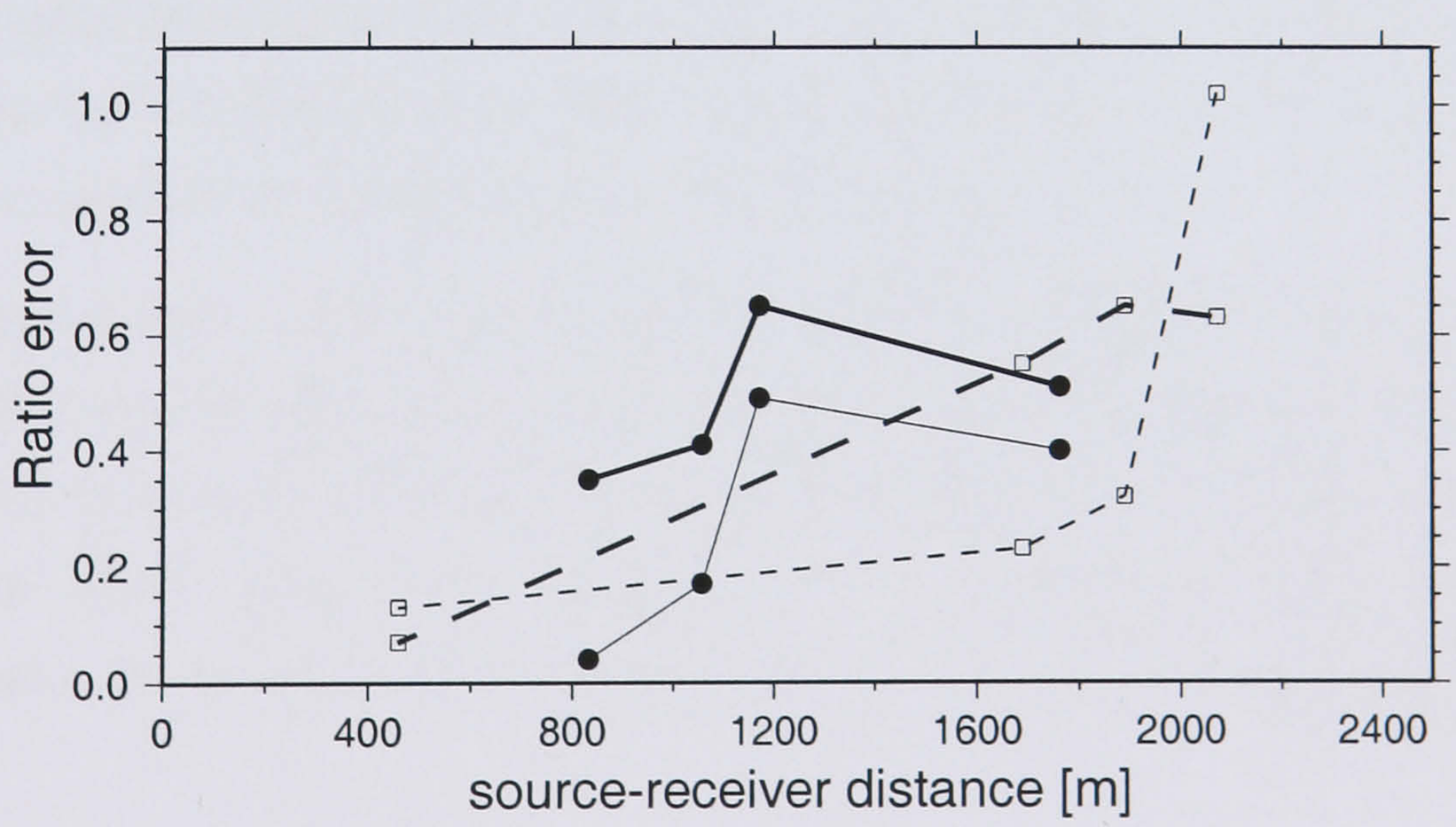

Figure 3.10 Amplitude ratio error (without Q correction) for event y021022.0042 (solid line) and y021022.0057 (dashed line) for the four neighbouring wells as a function of source-receiver distance. Calculations are based on the Yibal model with (thick line) and without (thin line) attenuation and using focal mechanism M=2 (Table 3.1). Individual results for the four tested wells are indicated by circles for event y021022.0042 and squares for y021022.0057.

3.4.5 Picking guidelines from synthetics

Our tests have shown that picks from the nearest stations can be used with confidence. In general, picks from the furthest wells should not be used because they are very likely to be head waves rather than direct arrivals. For events near the y021022.0042 event (deep near the Shuaiba reservoir and located south of the network), (a) (P,SV,SH) polarity and (SV/P, SH/P,SV/SH) amplitude ratio picks from wells 1, 2 and 3 can be used reliably, (b) Only the P-polarity pick from the next further well (well 4) can be used, and (c) the furthest well (well 5) should not be used at all. For events close to the y021022.0057 event (in the shallow Horseshoe area), (a) all polarity and amplitude ratio picks from stations in well 5 can be used reliably, (b) only the P-polarity pick of the two next further wells (well 2 and 4) can be used, and (c) the furthest wells (well 3 and 1) should not be used at all.

3.5 Real data analysis

Experience with synthetic data showed that amplitudes should be picked within the first cycle because later cycles may represent waves other than the direct arrival (e.g., head-waves and mode conversions). Synthetic seismograms are used as a guide for carefully picking polarities and amplitudes. Our picks are divided in two categories: confident and unconfident. A pick is marked confident when the arrival is sharp and shows a well defined first motion. Poorly-defined first arrivals are deemed unconfident. Unconfident measurements are however used later as complementary information, and for further quality control. Figure 3.11 shows how P, SV and SH polarities, and amplitude ratios are picked on real data. Figures 3.11(a,b,c) show examples of impulsive, emergent and unconfident P-wave polarities, respectively.

Over 600 located events in the 22 days (30/Aug-1/Sep2002, 21-24/Sep2002, 4-10/June2002 and 19-26/Oct2002) are considered in our analysis. However, many events have poor well coverage. Consequently, focal mechanism analysis is applied to events recorded by at least two stations (which image diverse points on the focal sphere) containing impulsive P-waves and reliable amplitude ratios. As a result, our analysis is applied to 75 events with magnitudes ranging from -2.0 to 1.0.

3.5.1 Selection criteria of picks

A P-wave polarity is chosen if it meets the following criteria:

(a)

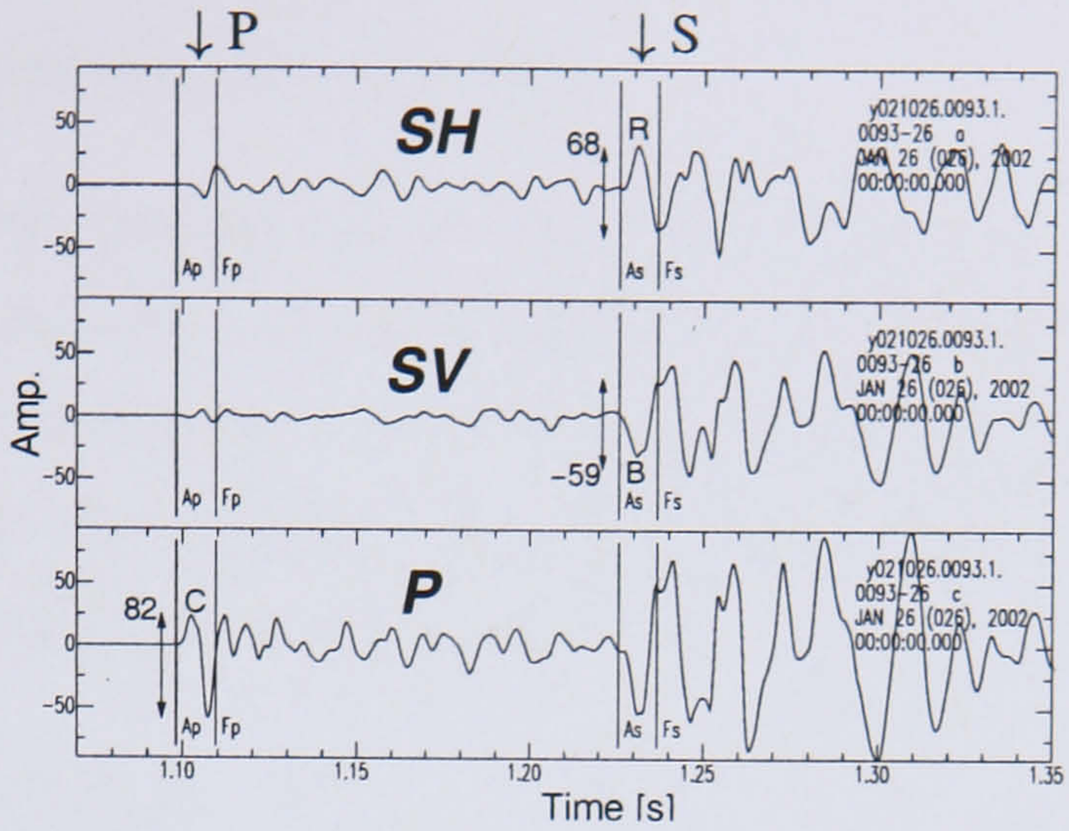

(b)

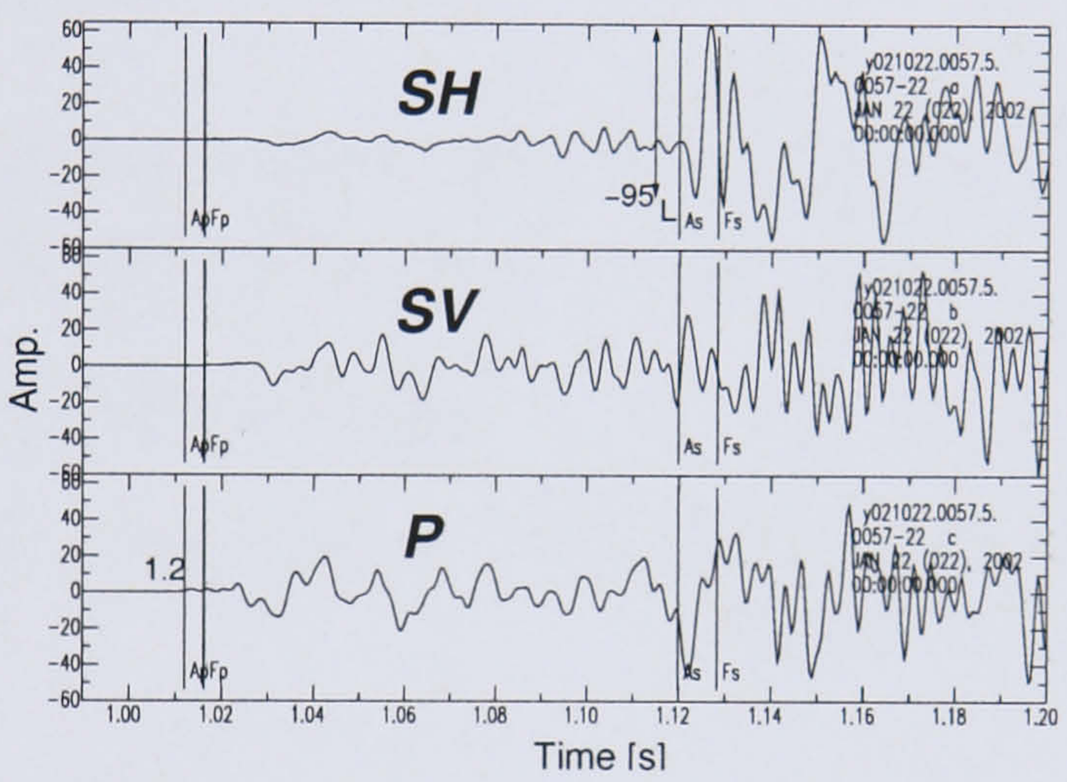

(c)

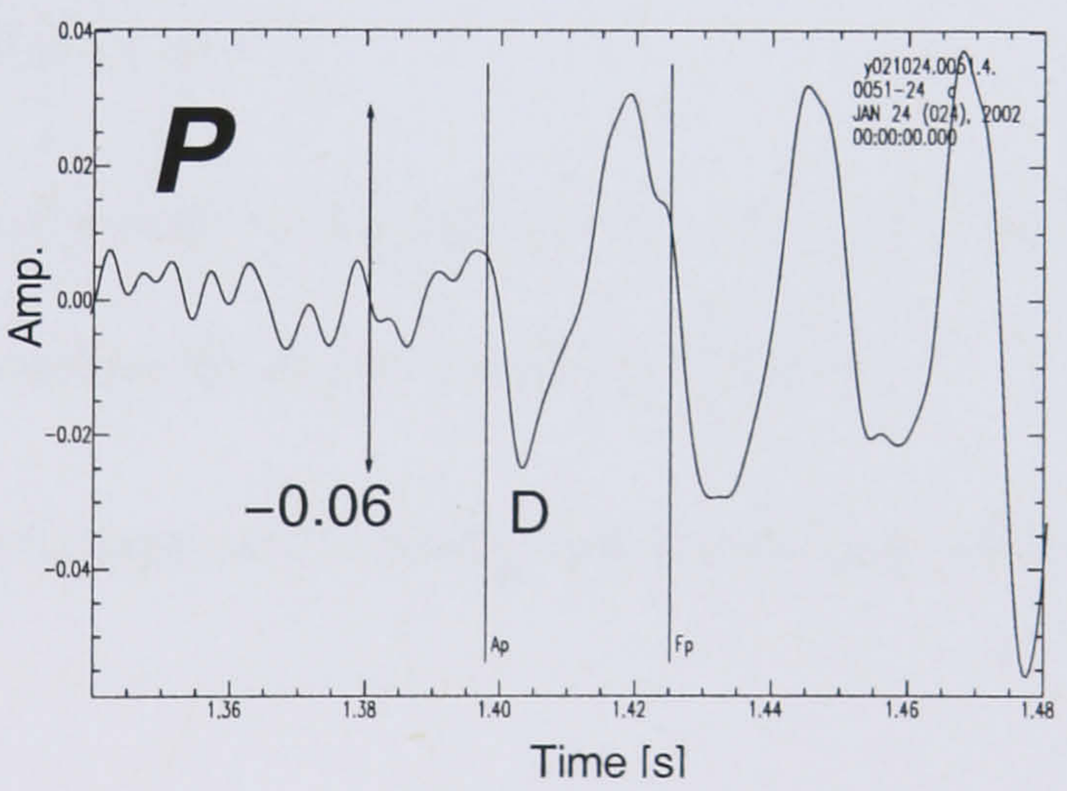

Figure 3.11 Examples of polarity and amplitude-ratio picks. [**a**] Impulsive P- and S- wave arrival on event y021026.0093.1.1, [**b**] emergent P-wave arrival on event y021022.0057.5.3 and [**c**] unconfident polarity pick on event y021024.0051.4.1, due to pre-signal noise. P-wave polarities are either marked C (compression) or D (dilatation); SH-wave polarities are either marked R (right) or L (left); and SV-wave polarities are either marked F (forward) or B (backward). Also shown are peak-to-peak amplitude values used to calculate ratios. Ap, Fp and As, Fs mark beginning and end of P-wave and S-wave analysis windows, respectively.

- The station must be sufficiently close such that head-waves arrive later than direct arrivals.
- The P-wave arrival must be impulsive.
- The P-wave particle motion must be linear.
- The ray orientation (azimuth and inclination) from the P- or S-wave particle motion is consistent with predicted ray azimuth and inclination angle based on a straight source-receiver raypath assumption. As a general rule, the inferred azimuth from the particle motion should be within 20° of the ray azimuth. The deviation in inclination angle can be much higher than 20° due to ray bending effects.

An S-wave polarity is chosen if:

- The station is near enough for a confident direct-wave pick. At distant stations direct S-waves can be obscured by large refractions or reflections.
- An impulsive S-wave arrival is visible.
- The inferred azimuth from the particle motion should be within 20° of the expected ray azimuth.

P- and S-wave amplitudes are used if:

- The station is close enough to confidently pick a direct-wave arrival.
- The wave arrives within 20° of the expected ray direction.

Amplitudes have the advantage over polarities in that emergent signals with elliptical particle motion be used.

3.5.2 FPS classification

The following classification system is used to rank the reliability of the focal mechanism estimates.

- A. Only one possible mechanism.
- B. Two possible mechanisms but additional complementary information (unconfident measurements) are used to favour one solution.

- C. Two possible mechanisms.
- D. Many possible solutions, but additional complementary information (unconfident measurements) are used to favour one solution.
- E. Many possible solutions.

3.5.3 Results

Analysis of 75 events resulted in 38 FPSs of class A (Figure 3.12), 5 of class B (Figure 3.13), 9 of class C (Figure 3.14) and 23 of classes D and E (Figure 3.15). Tables 3.4 and 3.5 list the FPS parameters (azimuth, dip and rake), P (pressure) axis and T (tension) axis parameters for class A and B results, respectively. Both P and T axes are 45° from the two nodal planes and 90° apart. However, the P-axis lies in the white dilatational quadrant, whereas the T-axis lies in the black compressive quadrant of a FPS. The tables also list the number of P, SH and SV polarities and amplitude ratios used in the analysis. Picks repeated at the same point in the focal sphere are not counted because they do not further influence the solution. This is often the case with nearby stations (e.g., stations in one well). On average, 4 P-, 2 SH- and 0.7 SV-polarities, and 3.1 $\frac{SH}{P}$, 1.3 $\frac{SV}{P}$ and 1.2 $\frac{SV}{SH}$ amplitude ratios are picked per class A event (overall, 6.7 polarities and 5.6 amplitude ratios are picked per class A event). There are generally more SH than SV polarities and amplitude ratios used.

The FPSs in map view and cross section for class A are displayed in Figures 3.16(a,b), respectively. The FPSs are well separated in depth, and there is little suggestion of lateral variations. Around 90% of the FPSs are located in 3 lateral patches. Therefore, I divide the data into three clusters, G, H and W4 (Figure 3.16a). Both the G and H clusters are along the eastern-most fault. The G cluster is in the southern part of the network, while the H cluster is in the north-east corner of the network around well 5. The W4 subset is along the western-most fault, near well 4.

The H and G cluster solutions are shown in detail in Figures 3.17 and 3.18, respectively. Figure 3.17 shows a transition from oblique thrust faulting with a strike-slip component in the Fiqa cap rock to pure thrust faulting in the gas-charged Natih-A reservoir. Figure 3.18 shows a transition from strike-slip faulting in the Nahr Umr cap rock to normal faulting in the oil-bearing Shuaiba reservoir. Figure 3.19a shows the results of the entire FPSs in ternary diagrams of the dip of the P (pressure), T (tension) and B axes (intermediate stress direction, which is defined by the intersection of the fault and auxiliary planes). Azimuths of the P, T and B axes are neglected in

the plots. Ternary diagrams are useful for visualising the 3 faulting components and illustrating the dominant fault type. The scatter in Figure 3.19 suggests that a wide range of faulting regimes exist in the field. A Ternary diagram showing subsets from the four depths (Fiqa, Natih-A, Nahr-Umr and Shuaiba) is shown in Figure 3.19b. It is evident that the fault regimes for the four formations cluster in discrete regions.

3.5.4 Discussion

In general, SH picks are more reliable than SV picks of both polarity and amplitude. This is due to interference from P-SV and SV-P conversions; SV-first motions are generally poorly defined and the associated amplitude ratios are greatly affected by the interference. SH-waves do not suffer such problems as they are not coupled to P-waves. Similar to the synthetic data, the real data (Figure 3.12) show that focal points close to nodal planes significantly limit the number of possible FPSs. Therefore, the accuracy of FPS estimates depends greatly on the focal coverage and relative position to the true fault plane.

The estimated FPSs show that the fault mechanisms vary with depth and can be separated into 4 distinctive zones: a transition from oblique thrust faulting with a strike-slip component in the Fiqa cap rock to pure thrust faulting in the gas-charged Natih-A reservoir, and a transition from strike-slip faulting in the Nahr Umr cap rock to more normal faulting in the oil-bearing Shuaiba reservoir. The P (pressure) axis is predominantly horizontal in Fiqa and Natih A, subhorizontal in Nahr Umr and subvertical in Shuaiba (via visual inspection in Figures 3.18b and 3.17b – the P axis is roughly in the center of the FPS white quadrant). The key observations are summarised in a diagram in Figure 3.20.

The W4 cluster, along the western-most fault, shows mainly thrust faulting. One focal mechanism, located further south along the western-most fault near well 1 and in the Natih B-G2 (Figure 3.16), also suggests thrusting regime. This may indicate that the entire western-most fault is undergoing thrust faulting.

3.5.5 Interpretation

It appears that the style of faulting correlates with both lithology and proximity to the major graben faults in the field. Shear movements near the eastern-most graben fault show depth-dependent faulting mechanisms. Given the present normal graben faults and the extensional

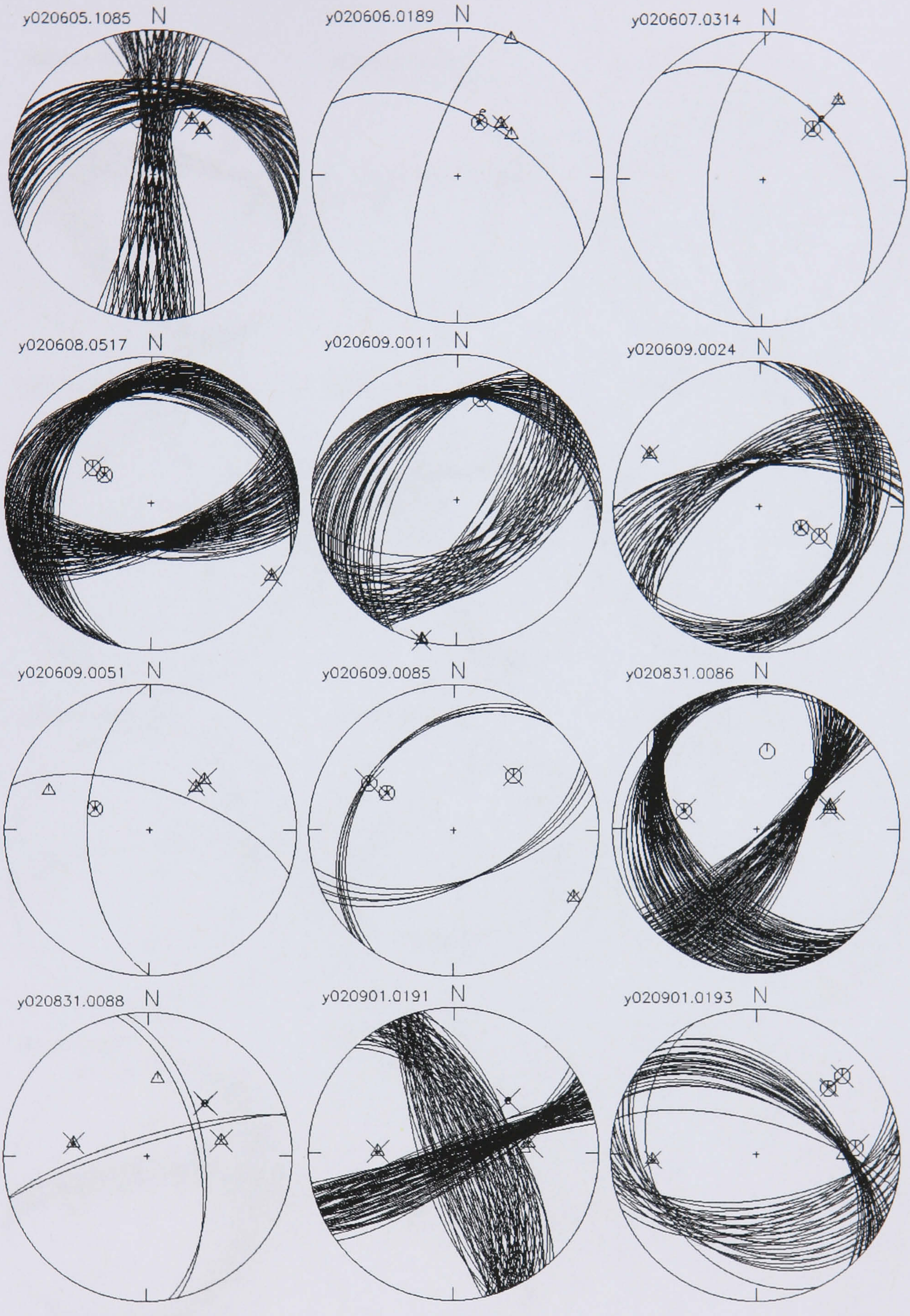

Figure 3.12 Class A focal mechanisms [upper projection]. Circles mark compressions, triangles dilatations, symbol e marks emergent P-arrivals and arrows mark SH polarities. Size of cross symbols is proportional to amplitude ratio. Also shown above each sphere is the event number.

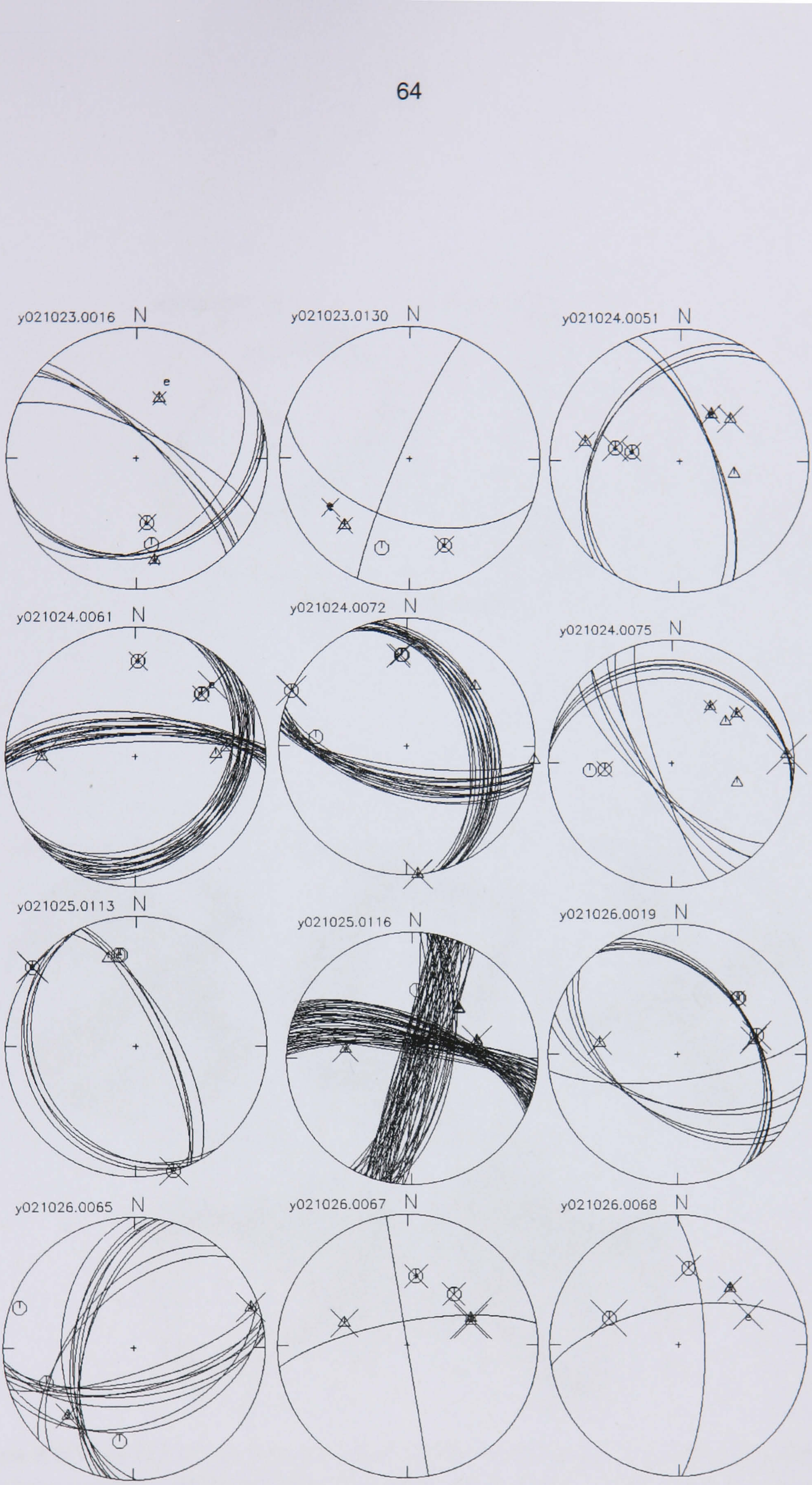

Figure 3.12 Continued.

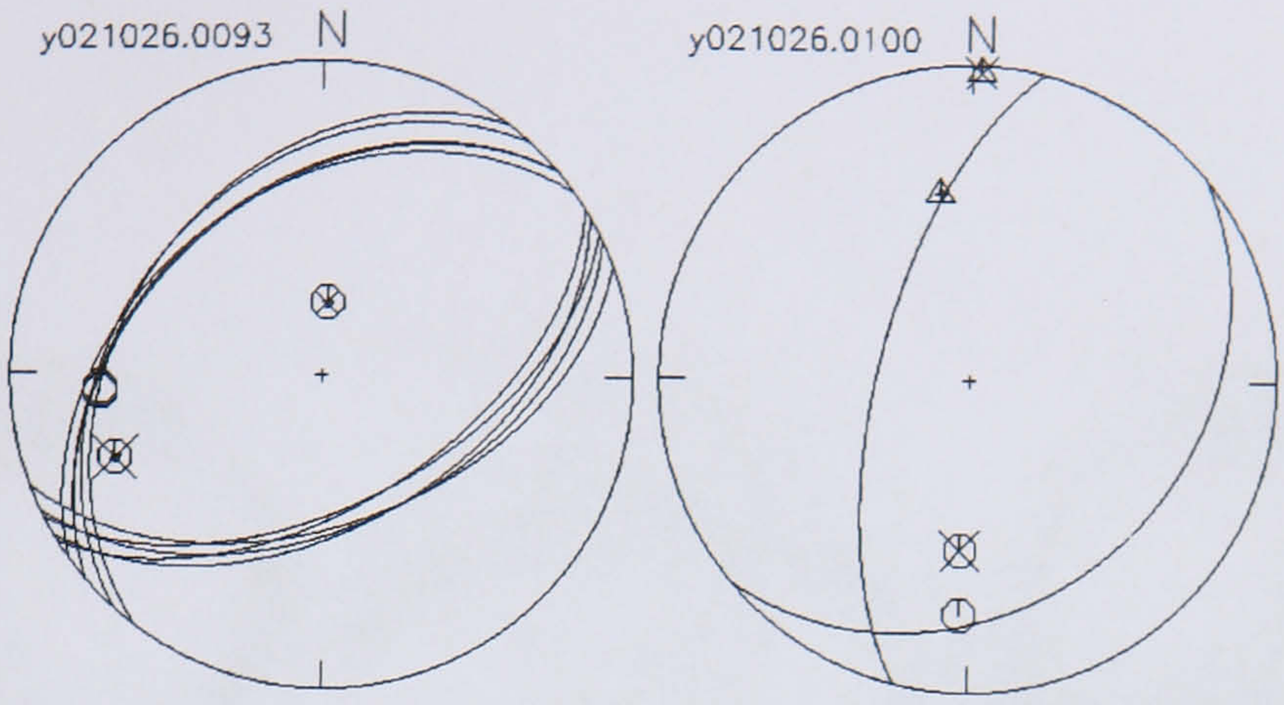

Figure 3.12 Continued.

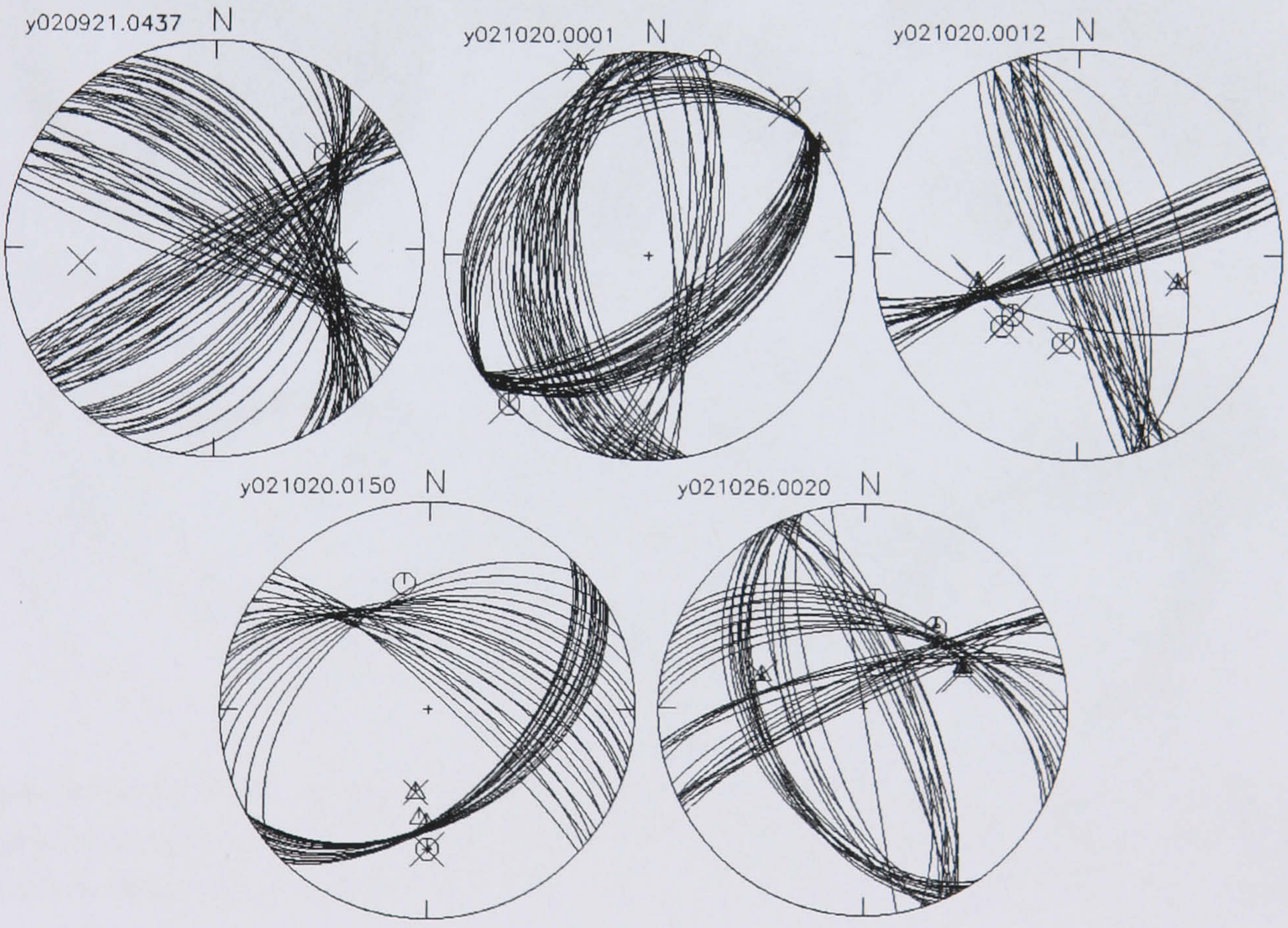

Figure 3.13 Class B focal mechanisms [upper projection]. Circles mark compressions, triangles dilatations, symbol e marks emergent P-arrivals and arrows mark SH polarities. Size of cross symbols is proportional to amplitude ratio. Also shown above each sphere is the event number.

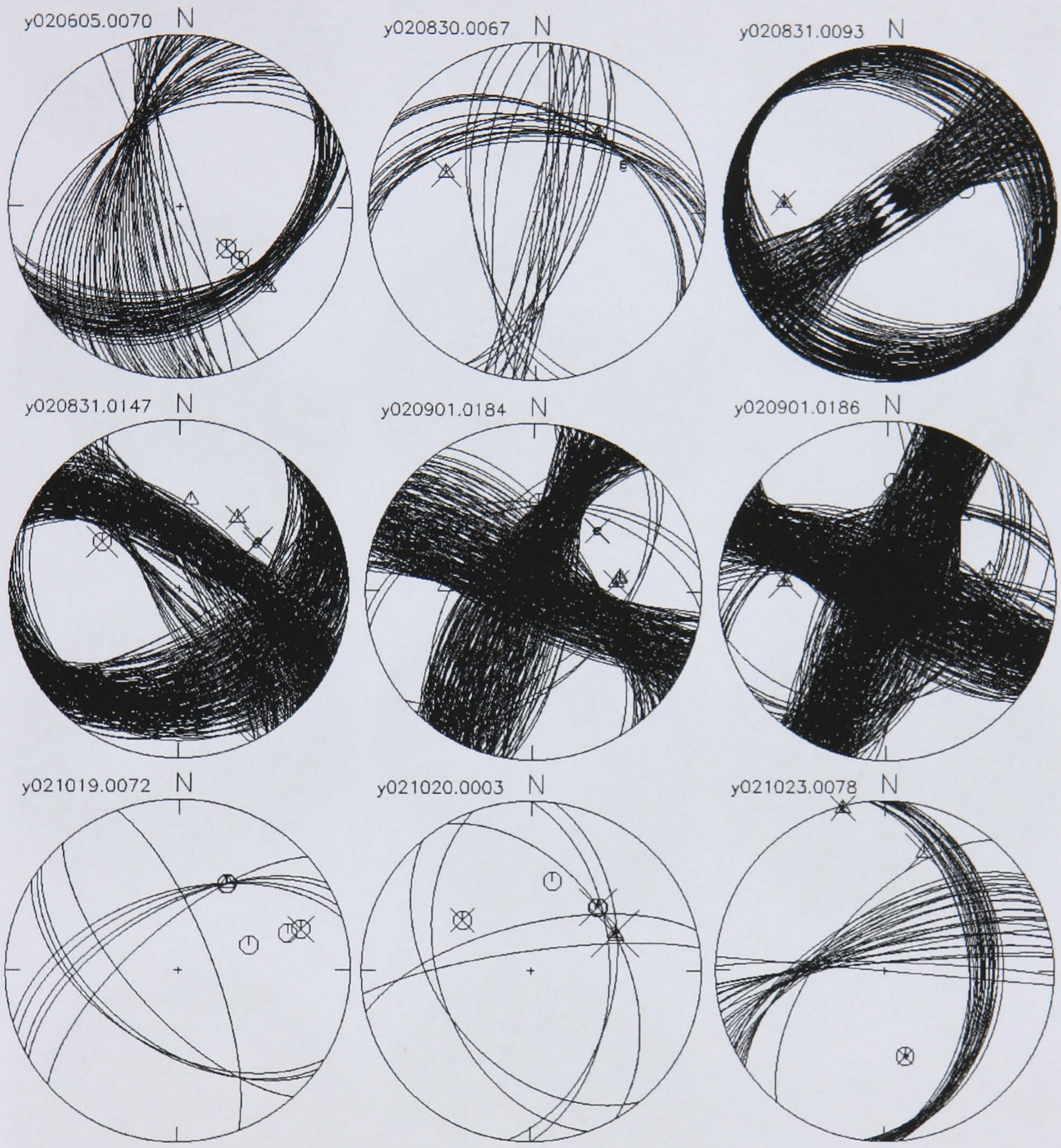

Figure 3.14 Class C focal mechanisms [upper projection]. Circles mark compressions, triangles dilatations, symbol e marks emergent P-arrivals and arrows mark SH polarities. Size of cross symbols is proportional to amplitude ratio. Also shown above each sphere is the event number.

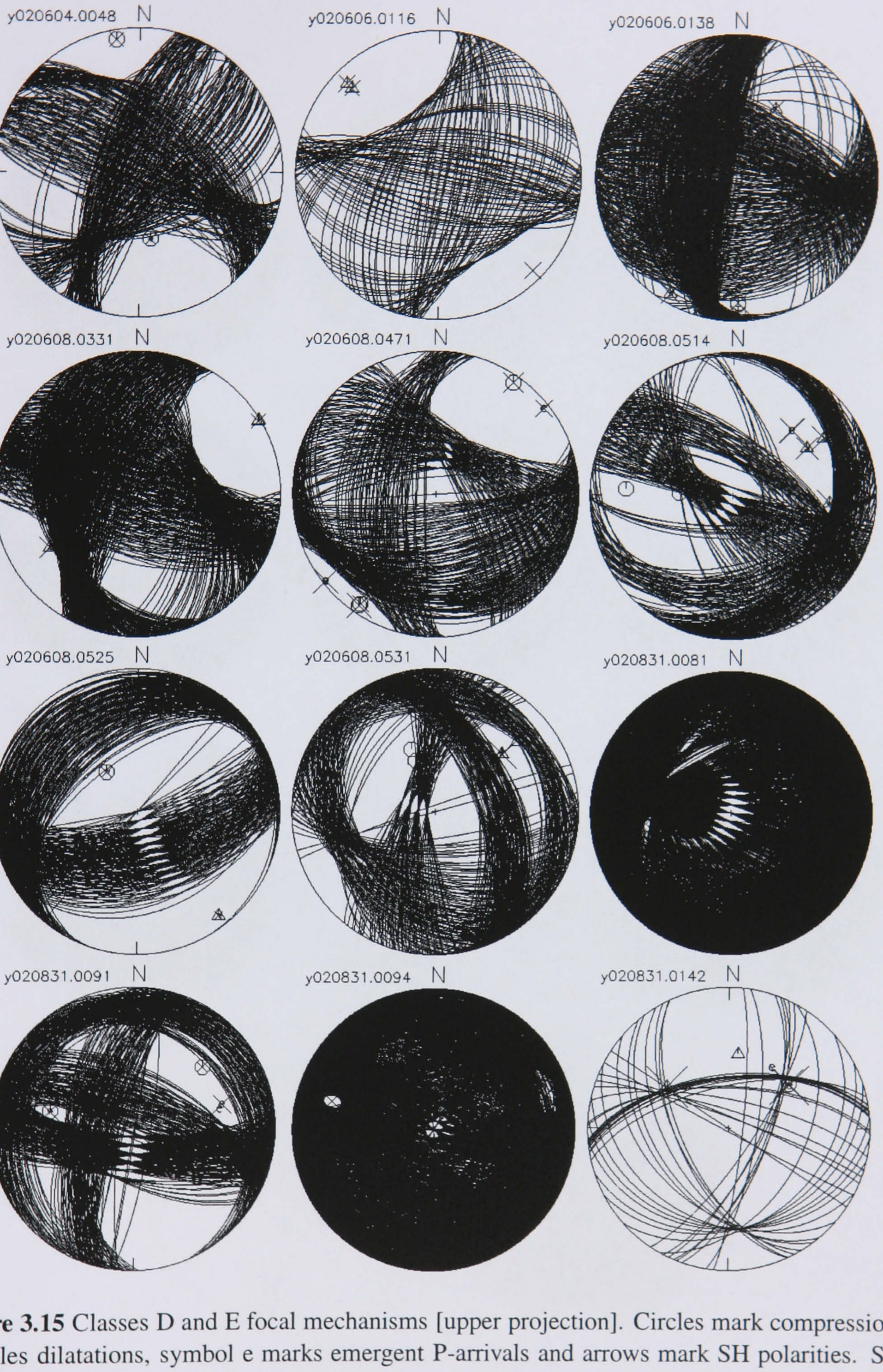

Figure 3.15 Classes D and E focal mechanisms [upper projection]. Circles mark compressions, triangles dilatations, symbol e marks emergent P-arrivals and arrows mark SH polarities. Size of cross symbols is proportional to amplitude ratio. Also shown above each sphere is the event number.

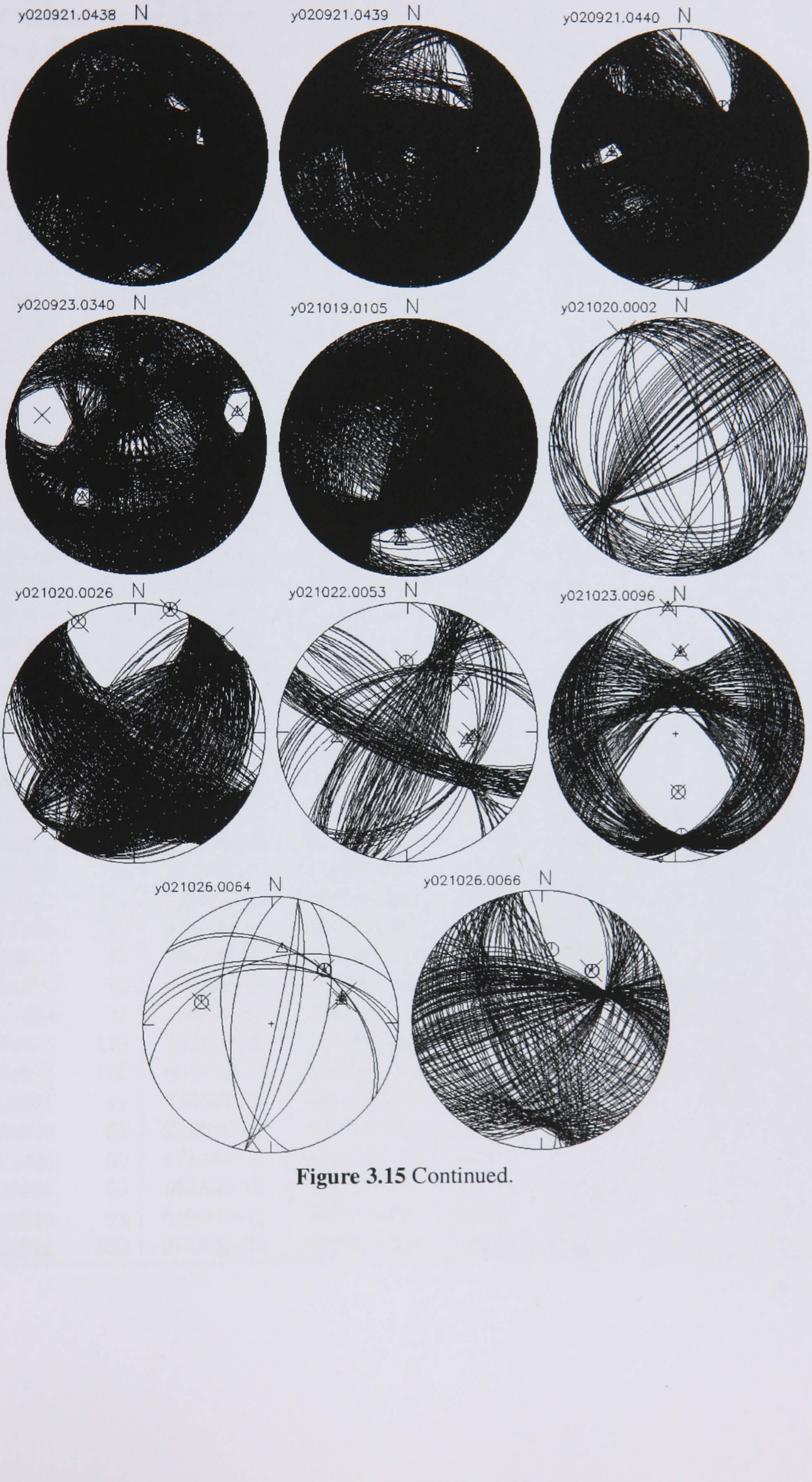

Figure 3.15 Continued.

Table 3.4 Parameters of class-A FPSs and number of polarity and amplitude-ratio picks used to determine the solution. Polarities and amplitude ratios of different stations belonging to the same well (plotted exactly in the same spot in the focal sphere) are counted as one pick. Emergent P-wave picks are not counted. Both confident and unconfident picks are listed.

Date	Ev.	1^{st} plane Az/Dip/Rake [°]	2^{nd} plane Az/Dip/Rake [°]	P Az/Dip [°]	T Az/Dip [°]	Polarity P	SH	SV	Ratio $\frac{SH}{P}$	$\frac{SV}{P}$	$\frac{SV}{SH}$
020605	1085	354/86/-55	090/35/-173	295/39	055/32	3	2	1	2	1	1
020606	189	119/56/+23	016/71/+144	071/10	333/38	4	2	0	2	0	0
020607	314	135/42/+51	003/59/+120	072/09	324/63	2	2	2	3	0	0
020608	517	040/22/+63	250/70/+101	331/25	176/63	3	2	2	3	3	3
020609	11	222/55/+84	052/35/+099	316/10	109/79	3	2	1	2	1	0
020609	24	201/25/+52	062/71/+106	140/24	356/61	3	2	1	3	3	3
020609	51	108/66/+39	359/55/+150	231/07	328/44	4	3	0	3	0	0
020609	85	032/33/+62	245/61/+107	323/14	191/69	4	2	1	3	2	1
020831	86	321/40/+26	210/74/+127	273/20	159/48	4	1	1	2	2	2
020831	88	167/61/+09	073/83/+151	123/14	026/26	3	1	1	4	2	2
020901	191	152/56/-07	246/84/-145	115/28	014/19	2	3	1	4	1	1
020901	193	127/53/-65	269/44/-120	097/69	199/05	5	2	0	4	0	0
020921	23	326/45/-45	091/60/-125	310/59	205/09	3	1	2	3	2	2
020922	36	193/76/+27	096/64/+164	323/07	057/29	3	2	0	2	2	2
020923	352	114/29/+29	358/76/+116	068/27	298/52	3	0	0	3	1	1
021021	4	172/61/+73	024/33/+118	274/14	046/69	5	2	0	2	0	0
021021	14	078/52/+12	340/80/+141	035/19	292/34	4	3	0	5	1	1
021021	44	198/46/+76	038/46/+104	118/00	028/80	3	1	3	3	3	3
021021	72	193/40/+26	082/74/+127	145/20	031/48	5	3	0	4	1	1
021021	113	259/52/-71	050/42/-113	228/74	336/05	5	2	0	5	0	0
021022	22	145/42/-51	277/59/-120	136/63	028/09	5	2	1	2	1	1
021022	37	086/73/-58	202/36/-149	032/52	152/21	4	2	1	4	3	3
021022	42	176/41/-12	275/82/-130	149/39	036/26	4	0	0	3	2	2
021022	57	285/54/+59	151/46/+126	037/05	136/65	6	2	2	3	2	2
021023	16	255/25/+35	132/76/+111	206/28	068/54	4	2	1	3	2	2
021023	130	288/51/-08	024/84/-140	254/32	150/22	3	2	1	3	1	1
021024	51	155/67/+63	028/35/+138	265/18	027/58	6	3	1	5	1	1
021024	61	090/76/-69	213/25/-145	025/54	164/28	5	3	0	4	0	0
021024	72	280/64/+56	157/41/+139	034/13	144/57	6	3	0	3	2	2
021024	75	320/75/-80	104/18/-124	244/59	041/30	7	4	0	4	0	0
021025	113	335/15/-90	155/75/-090	065/60	245/30	4	1	1	2	1	1
021025	116	097/76/-27	194/64/-164	053/29	147/07	4	2	0	2	1	1
021026	19	148/40/-58	288/57/-114	149/68	035/09	4	2	0	4	0	0
021026	65	259/69/-41	006/52/-153	216/43	316/11	5	2	0	2	1	1
021026	67	171/90/+15	081/75/+180	305/11	037/11	4	2	0	4	2	2
021026	68	081/66/-18	179/73/-155	042/30	309/05	3	2	1	4	2	2
021026	93	049/41/+75	249/51/+103	330/05	214/79	3	3	1	3	1	1
021026	100	014/66/+74	230/29/+122	116/19	255/65	4	0	2	1	2	1

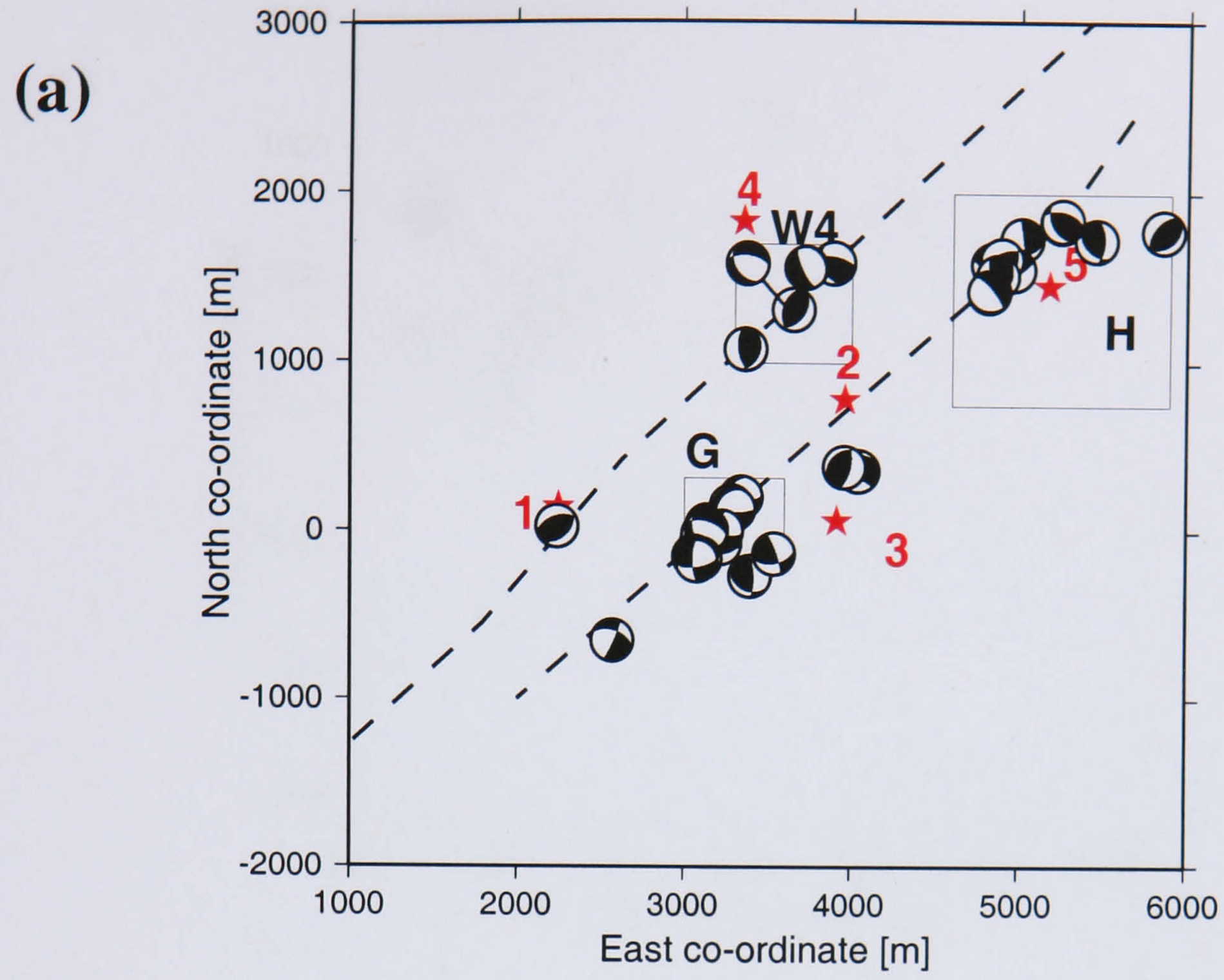

Figure 3.16 Class A focal mechanisms [lower hemisphere projection] in [**a**] map view and [**b**] fault-perpendicular cross section (solutions are also shown in Figure 3.12).

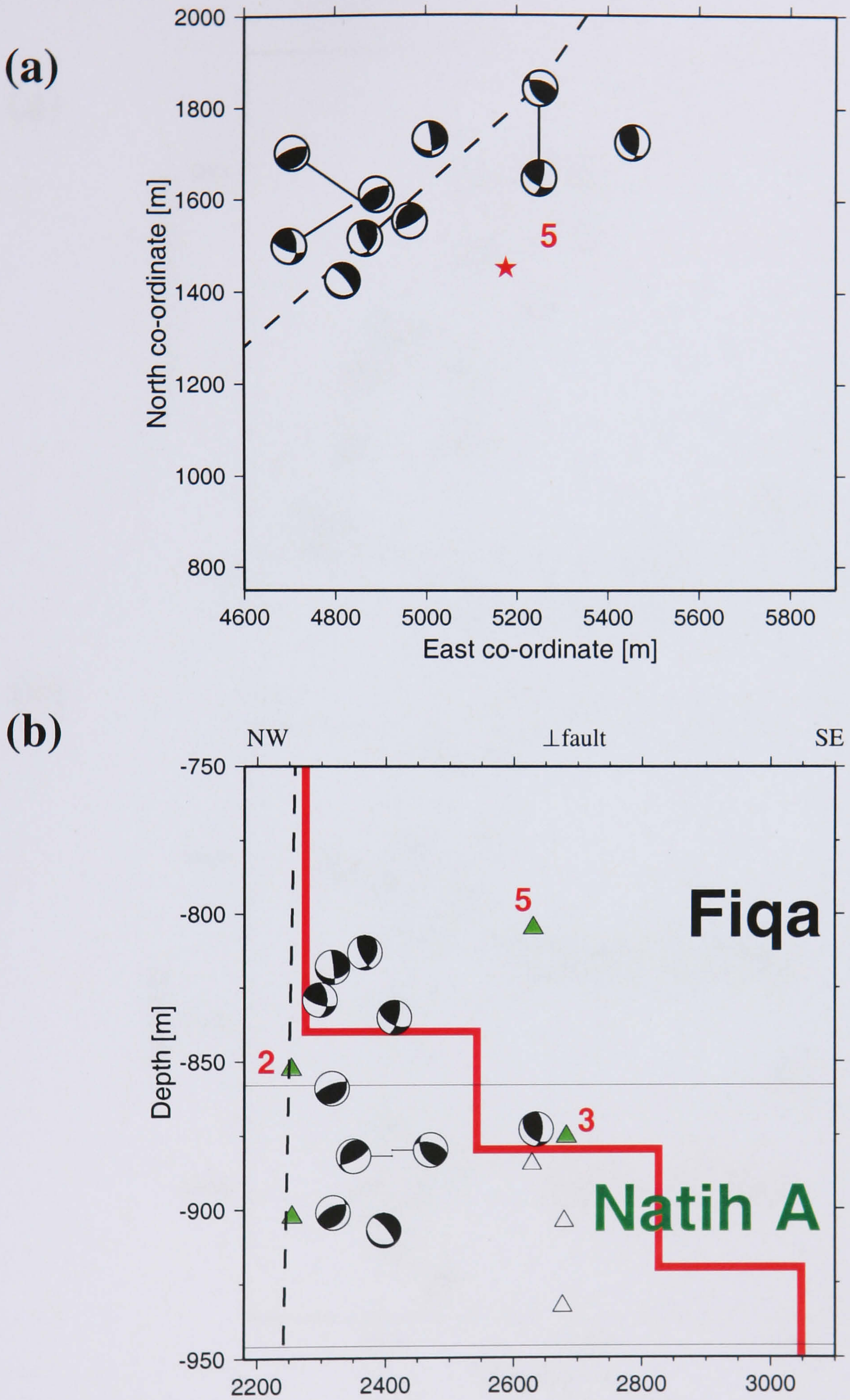

Figure 3.17 FPSs for the H cluster in [**a**] map view and [**b**] fault-perpendicular cross section. Note the transition between more strike-slip faulting in the Fiqa to more pure thrust faulting in the Natih A formation.

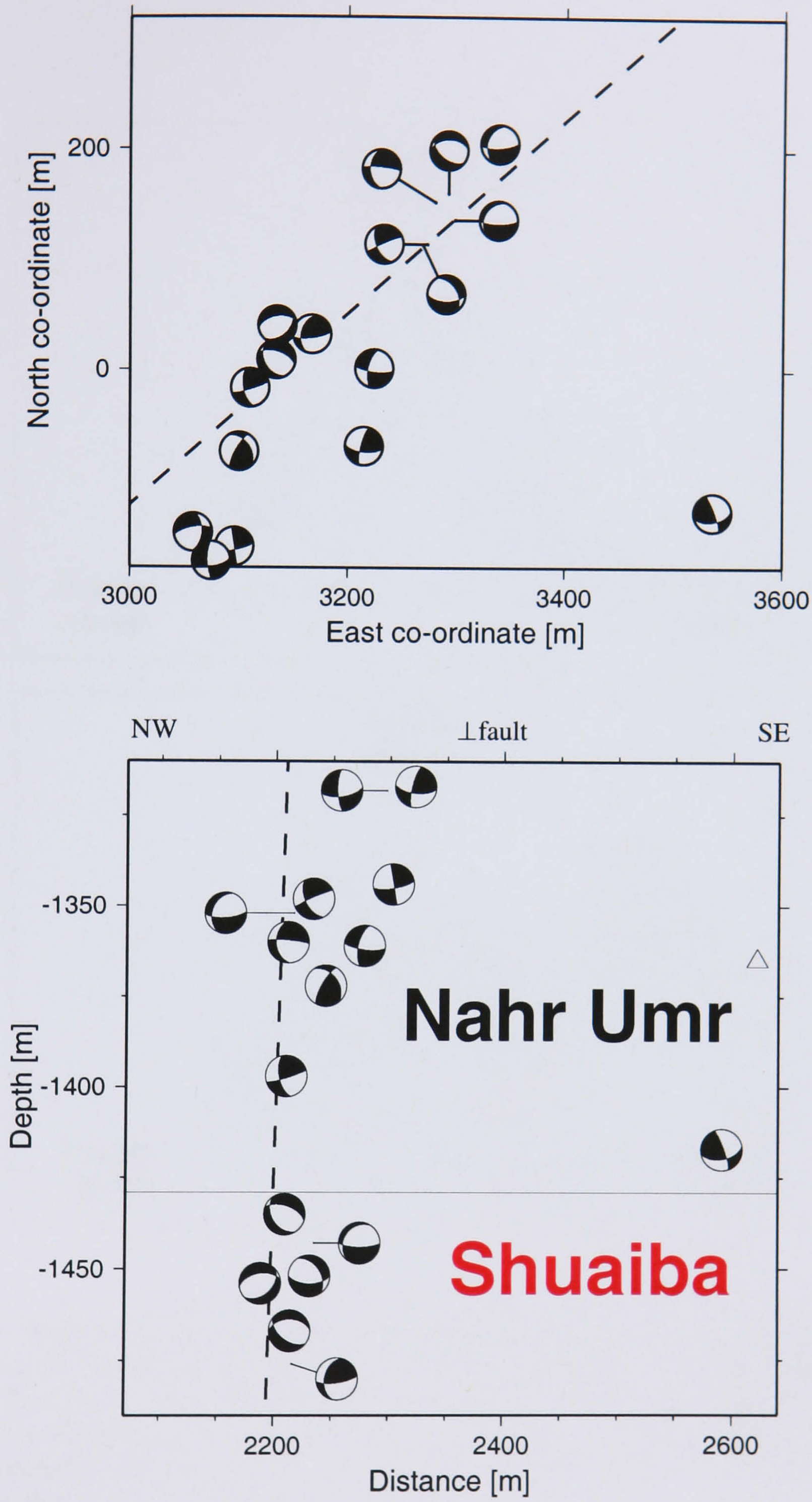

Figure 3.18 FPSs for G cluster in [**a**] a map view and [**b**] fault-perpendicular cross section. Note the transition between more strike-slip faulting in the Nahr Umr to more normal faulting in the Shuaiba formation.

(a)

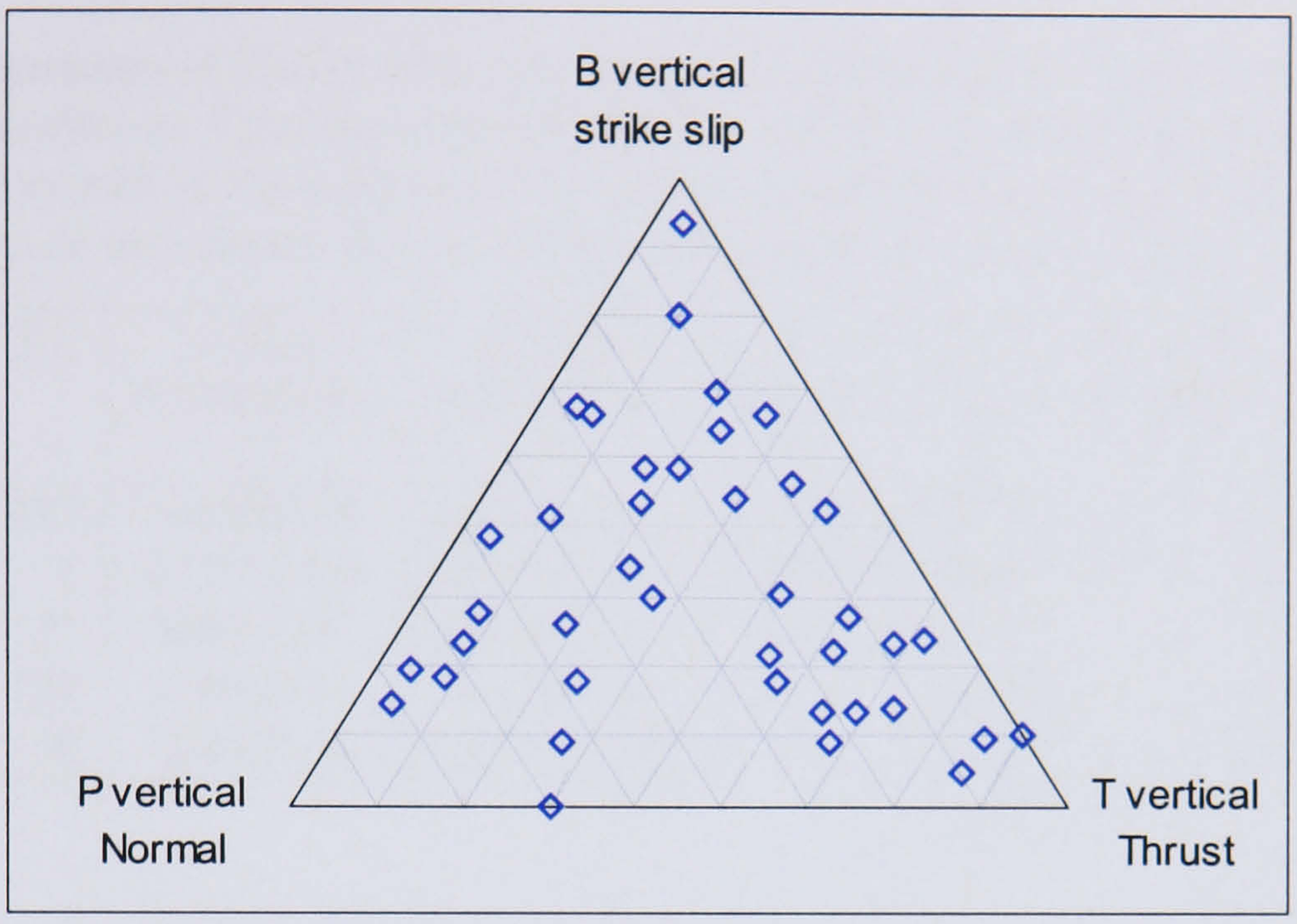

(b)

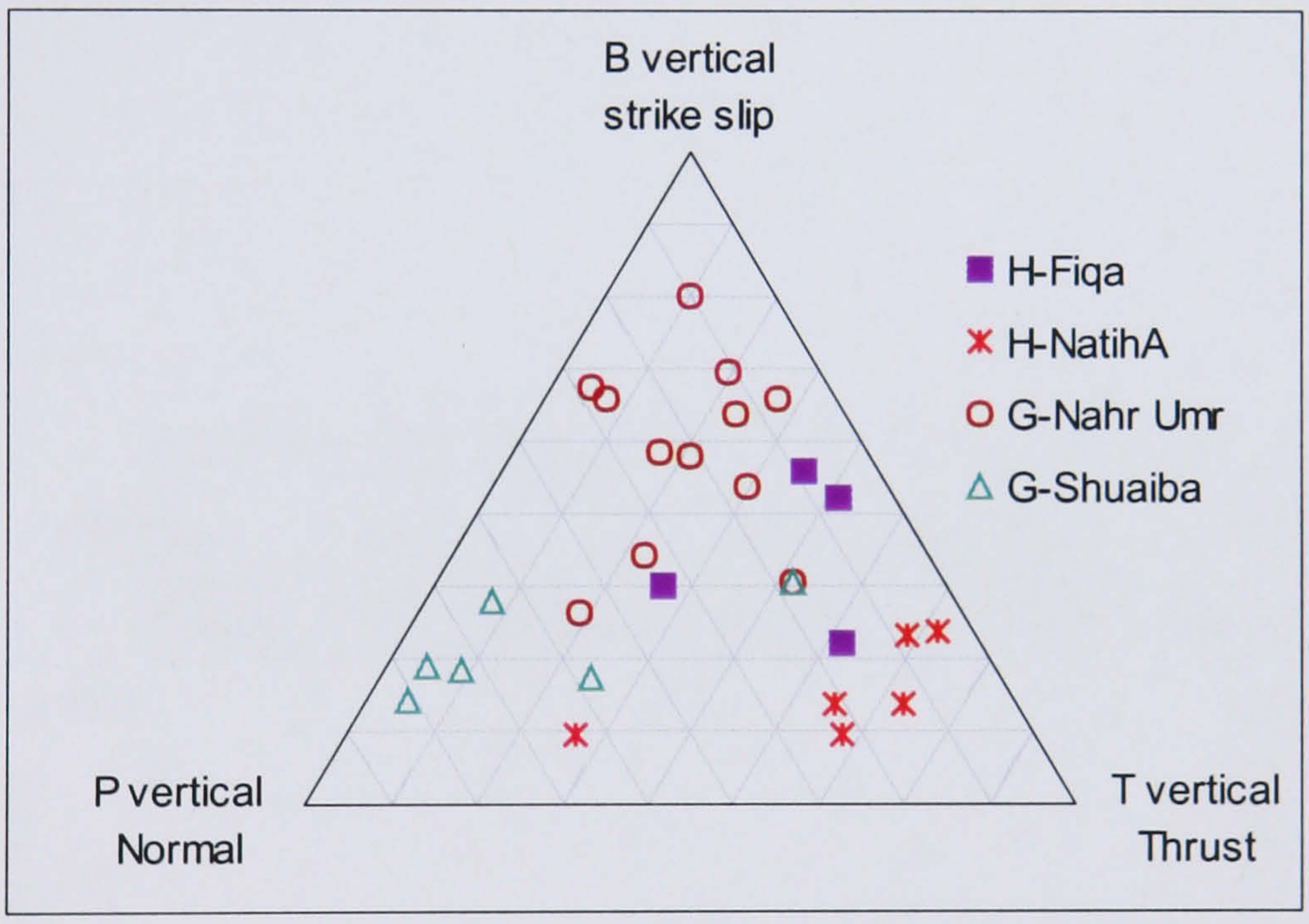

Figure 3.19 Ternary diagram of P, B and T dip angles for [**a**] all 43 results (38 class A and 5 class B) and [**b**] results of four subsets confined to Fiqa, Natih-A, Nahr Umr and Shuaiba formations. The three corners represent the pure-end members of each fault type. The dip scale is 0°–90°. Note the separate fault regimes in the four horizons: oblique thrust faulting with a strike slip component in the Fiqa cap rock, pure thrust faulting in the Natih A reservoir, strike slip in Nahr Umr cap rock and normal faulting in the Shuaiba reservoir.

Table 3.5 Parameters of class-B FPSs and number of polarity and amplitude-ratio picks used to determine the solution. Polarities and amplitude ratios of different stations belonging to the same well (plotted exactly in the same spot in the focal sphere) are counted as one pick. Emergent P-wave picks are not counted. Both confident and unconfident picks are listed.

Date	Ev.	1^{st} plane Az/Dip/Rake [°]	2^{nd} plane Az/Dip/Rake [°]	P Az/Dip [°]	T Az/Dip [°]	Polarity P	SH	SV	Ratio $\frac{SH}{P}$	$\frac{SV}{P}$	$\frac{SV}{SH}$
020921	437	147/55/+00	057/90/+145	108/24	006/24	2	1	1	3	1	1
021020	1	175/76/+69	052/25/+145	281/28	059/54	4	1	2	4	2	2
021020	12	340/85/+01	250/89/+175	295/03	205/04	5	3	1	5	1	1
021020	150	110/61/-42	224/54/-143	074/50	169/04	4	1	2	2	2	2
021026	20	154/66/+07	062/84/+156	110/12	016/21	4	2	1	2	1	1

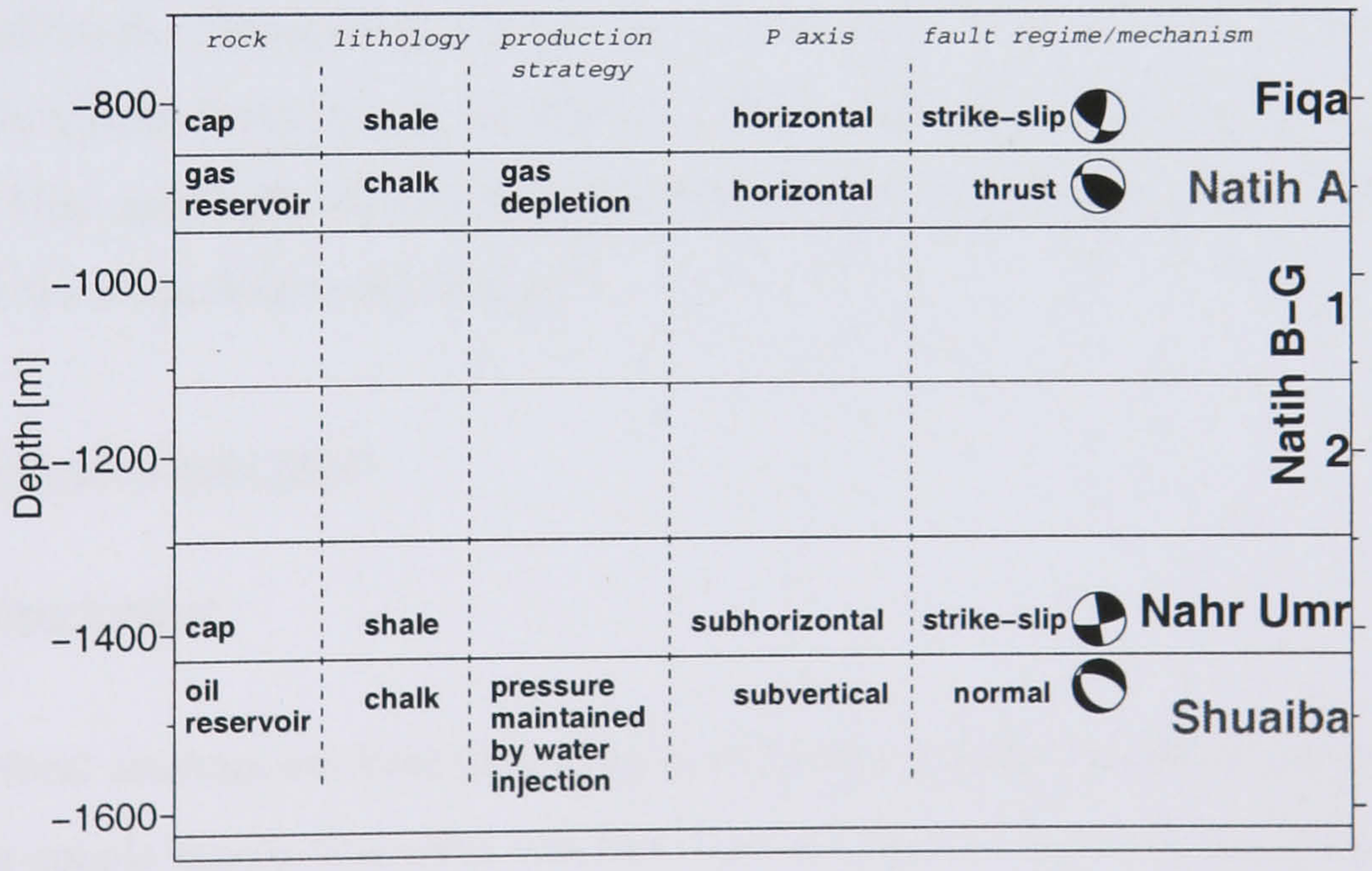

Figure 3.20 A diagram showing the key observations from FPSs.

regime the Yibal field is experiencing (Litsey et al., 1986), the normal faulting regime in the Shuaiba reservoir is anticipated. Since thrusting is expected above compacting zones (Segall, 1989), the observed thrusting in both the Fiqa cap rock (with a significant strike slip component) and Natih A reservoir are believed to be subsidence and deformation-related. The highest potential for compaction due to gas production is the chalky Natih zone where soft and heterogeneous units are present. Additionally, the faulting regime may also be lithology-related since both shale cap rocks (Fiqa and Nahr Umr) show significant strike slip components; this will be investigated in the next section. On the other hand, the FPSs from the most westerly fault suggest thrust faulting from the Fiqa down to Natih B-G2. This is not however conclusive due to limited FPS coverage along the fault. The observed thrusting regime is also perhaps an expected result for Fiqa and Natih A due to compaction.

We can also forward predict the stress field in the four horizons assuming that the maximum, intermediate and minimum stress orientations are parallel to P, B and T axes, respectively. The maximum stress direction is therefore predicted to be subhorizontal in the Fiqa, Natih A and Nahr Umr, and subvertical in the Shuaiba. However, the subhorizontal P-axis in Fiqa, Natih A and Nahr Umr varies greatly in azimuth, rendering estimation of maximum stress azimuth difficult. In Natih A, Nahr Umr and Shuaiba, the subvertical stress is more constrained and predicted to represent the minimum, intermediate and maximum stress, respectively (Figure 3.19b). It may imply that the vertical stress increases with depth as would be expected if the pore pressure remains hydrostatic. This may also suggest that the vertical stress is below the maximum and minimum horizontal stress (σ_H, σ_h) in Fiqa and Natih A, increases above σ_h but remains below σ_H in Nahr Umr, and finally exceeds both horizontal stresses σ_H, σ_h in Shuaiba. The next section investigates the stress field in more detail.

3.6 Stress inversion

3.6.1 Introduction

Individual focal mechanisms have been used to estimate the local directional stress field. For a pure double-couple source, it is often assumed that the P, B, and T axes are oriented towards the maximum, intermediate, and minimum compressive stress directions, respectively. However, the P, B, and T axes can deviate significantly from the principal stress directions when the computed FPS comes from reactivated cohesionless faults (McKenzie, 1969). A preexisting fault may have formed in a previous stress field that is not necessarily oriented with the present field. Different

preexisting fault orientations can therefore generate a range of different FPSs all consistent with the same stress field.

For the simplest models, the P and T axes are oriented 45° to the auxiliary and fault planes. In reality the separation angle is not 45° but on the order of 30° depending on the coefficient of internal friction and amount of normal stress (Hinzen, 2003). However, this is the case when the fault is created purely by the applied stress field. The Yibal field experienced at least 3 former and varied stress phases (see Section 2.2), so preexisting faults of diverse orientations are present in the region. This could well explain the diversity in fault plane orientations (in the observed FPSs) in the individual formations.

I use the method of Gephart and Forsyth (1984) to estimate principal stress directions from fault plane solutions. It has been used by different authors in different settings: microearthquakes induced during injection experiments in Germany (Bohnhoff et al., 2004), in volcanic regions (Wyss et al., 1992; Sanchez et al., 2004), at the Alps-Dinarides junction (Kravanja and Panza, 2005), in the Ryukyu-Kyushu Wadati-Benioff zone (Christova, 2004), in the lithosphere beneath Sicily (Caccamo et al., 1996; Neri et al., 2005), in the central European rift (Hinzen, 2003), and in the Alaska subduction zone (Lu et al., 1997).

3.6.2 Method

The focal mechanism stress inversion (FMSI) package developed by Gephart and Forsyth (1984) is used. FMSI performs a grid search over all possible stress field models. It seeks a stress model solution with the minimum discrepancy between the observed FPSs and those predicted by the stress model. Four key parameters are determined: three principal stress directions (azimuth and dip of greatest σ_1, intermediate σ_2 and least σ_3) and the relative stress magnitude (R) defined by:

$$R = \frac{\sigma_1 - \sigma_2}{\sigma_1 - \sigma_3}, \tag{3.6}$$

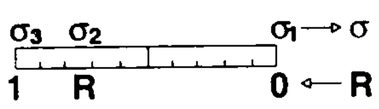

where $0 \leq R \leq 1$. The FMSI package allows two approaches: a fast "approximate" and a slow "exact" method. The approximate method searches roughly through the parameter space, and has the advantage of short computation time. The time consuming exact method searches through the parameter space for the best fitting model by computing the exact minimum average misfit F.

For each stress model (σ_1,σ_2,σ_3,R) in the parameter space, FMSI calculates a minimum misfit angle for each nodal plane for each FPS. The minimum misfit angle is the smallest angle between the observed nodal plane geometry and any acceptable nodal plane geometry allowed by the stress model. The nodal plane geometry includes both the nodal plane and the slip vector. This does not only allow errors or variation in the slip vector but allows errors and variation in the nodal plane orientation to obtain a better estimate of misfit. See Gephart and Forsyth (1984) for the misfit equation, its derivation and a more thorough description of the technique. The two nodal planes are examined by FMSI because both are possible fault planes. From among the two nodal planes, the nodal plane with the smallest misfit is selected to represent the fault plane in each FPS. The smallest misfit is automatically chosen to represent the individual FPS misfit. The average misfit F is simply the average of the absolute individual misfits.

Initially, the approximate method is used to search over a wide grid (10°) in stress directions through the whole parameter space. It searches over 90° cones (hemisphere) around the primary and secondary principal stresses in 10° spacing. For all inversions, I use σ_1 for the primary and σ_3 for the secondary stress components. Consequently, the search is over 145 σ_1 directions in total. The rough best fitting stress model is fed into the exact method as a starting model. A narrower grid search (5°) over 30° and 90° cones around the primary and secondary principal stresses, respectively, is performed. This leads to a search over 85 σ_1 directions in total. R is finely sampled over the full range (0 to 1) in 0.05 increments for all trial solutions. The FMSI package also allows FPS weightings. In all our inversions I used no weighting (i.e., I assigned equal weights of 1.0 to all FPSs).

Gephart and Forsyth (1984) quantify the 95% confidence limit of the solution misfit, in a statistical approach following Parker and McNutt (1980), as

$$F_{95\%} = \frac{1.96(\pi/2-1)^{1/2}n^{1/2}+n}{n-k}F, \tag{3.7}$$

where n and k are the number of FPSs and the unknown parameters to be solved for (4 in this case), respectively. The $F_{95\%}$ expression is evaluated once the inversion is complete. In a polar diagram, the uncertainty region of the inverted stress solution can be determined by contouring $F_{95\%}$ around the average misfit F of the inverted stress solution.

3.6.3 Assumptions, accuracy and average misfit F

The FMSI method of Gephart and Forsyth (1984) assumes: (1) uniform stress in space and time, (2) pure shear-slip earthquakes that occur on preexisting faults, and (3) a slip direction along

the direction of the maximum shear stress on the fault plane. The average misfit F value is, in principle, zero if the FMSI assumptions are not violated and the FPSs are perfect. The F value increases with increasing stress heterogeneity and uncertainties in observed FPSs. In the case of error-free FPSs, the average misfit F is purely due to inhomogeneities in the stress field. Based on synthetic tests, realistic errors of 10-15° in a single FPS can result in F values up to 6.0° (Wyss et al., 1992; Lu et al., 1997; Gillard et al., 1996). Therefore, it is generally accepted that datasets producing $F < 6.0°$ are suggestive of homogeneous stress and those yielding $F >$ 6.0° indicate heterogeneities in the stress tensor. Datasets resulting in F larger than 6.0° can be subdivided into sub-volumes or sub-time periods, or a combination of both, where the stress field is uniform.

Using synthetic focal mechanisms the accuracy of the inversion scheme of Gephart and Forsyth (1984) was examined by Hardebeck and Hauksson (2001). They showed that the inversion leads to accurate results, particularly with high quality data, but in general produces overly large confidence limits. Consequently, I conclude that the computed $F_{95\%}$ values in this chapter are an upper bound and the solutions are in fact more accurate.

3.6.4 Results

Principal stress directions

I use the class B and class A results to form a database of 43 FPSs for our stress inversion. The FMSI results of the entire reliable FPS dataset and various subsets are summarised in Table 3.6. The second solutions for H-NatihA and G-Nahr Umr listed in Table 3.6 show alternate potential solutions that also fit the data (i.e., a second local misfit minimum). The average misfit F of these secondary solutions are higher by just 0.7° than the global minimum and still within $F_{95\%}$ for both subsets. In all the subsequent plots I only show these secondary solutions for the H-Natih A and G-Nahr Umr subsets as they are more consistent with in-situ stress field and fault regime. Table 3.6 shows that the average misfit F is significantly higher than 6° for the entire dataset and for the different combinations of subsets (H and G; H and G-Nahr Umr; H and G-Shuaiba). It is also just larger than 6° for subsets based on lithology (shale: H-Fiqa and G-Nahr Umr and carbonate: H-Natih A and G-Shuaiba). On the other hand, subsets based on lithology and cluster group show F values generally below 6° (Table 3.6).

The inverted principal stress directions, together with P, B and T axes of the FPSs, are plotted in Figure 3.21 in polar diagrams for the entire dataset and various subclusters. These show

Table 3.6 Stress inversion results. N is the number of FPSs used in the inversion, R relative magnitude, F average misfit and $F_{95\%}$ 95% confidence limit. † Secondary local minimum misfit. See Figure 3.16 for the spatial distribution of clusters.

Data set	N	R	F [°]	$F_{95\%}$ [°]	σ_1 Az/Dip [°]	σ_2 Az/Dip [°]	σ_3 Az/Dip [°]
All	43	0.05	12.2	16.5	081/00	351/69	171/21
Lateral subsets							
H	10	0.60	4.5	11.0	070/01	160/17	338/73
G	20	0.55	5.9	9.8	245/53	101/31	360/17
W4	5	0.05	1.9	15.8	083/29	190/28	316/48
Vertical subsets							
H-Fiqa	4	0.70	0.4	∞	267/06	172/35	005/54
H-NatihA	6	0.30	2.3	11.1	272/09	178/24	021/64
H-NatihA†	6	0.70	3.1	14.9	184/05	094/03	336/84
G-Nahr Umr	12	0.70	4.6	9.8	092/28	350/21	229/54
G-Nahr Umr†	12	0.90	5.3	11.3	096/27	229/53	354/23
G-Shuaiba	6	0.80	2.8	13.5	150/63	282/19	019/19
Lithology subsets							
H-Fiqa + G-Nahr Umr	16	0.65	6.6	12.0	240/45	107/34	358/25
H-NatihA + G-Shuaiba	12	0.15	8.5	18.1	297/35	101/54	201/07
Various combination of subsets							
H + G	30	0.85	10.3	15.1	247/45	104/39	357/19
H + G-Nahr Umr	22	0.30	10.0	16.1	091/12	358/13	221/72
H + G-Shuaiba	16	0.05	8.7	15.9	275/30	163/33	036/42

substantial deviations in the P, T, and B axes from the inverted principal stresses, and a relatively high average misfit (except perhaps the H cluster). Conversely, polar diagrams for the solutions with low average misfit subsets (H-Fiqa, H-Natih A, G-Nahr Umr, G-Shuaiba and W4; Figure 3.22) show less deviation. The maximum compressive stress direction (σ_1) varies with depth: horizontal E in Fiqa, horizontal NNE in Natih-A, subhorizontal E in Nahr Umr, and subvertical in Shuaiba (Figure 3.22). More precisely, σ_1 is 30° and 60° off horizontal in the Nahr Umr and Shuaiba, respectively. Figure 3.22 also shows that the subvertical stress is approximately the minimum stress direction in the Fiqa and Natih A, the intermediate stress direction in the Nahr Umr and the maximum stress direction in the Shuaiba.

To assess the uniqueness of the inverted stress directions, the grid search results of the average misfit F for σ_1 and σ_3 are shown in Figure 3.23 and 3.24, respectively, for the four studied formations. The figures display the existence of local minima beside the global minimum for all formations and either σ_1 or σ_3. Although the azimuths of σ_1 and σ_3 appear somewhat unconstrained, their dips demonstrate unique and constrained solutions.

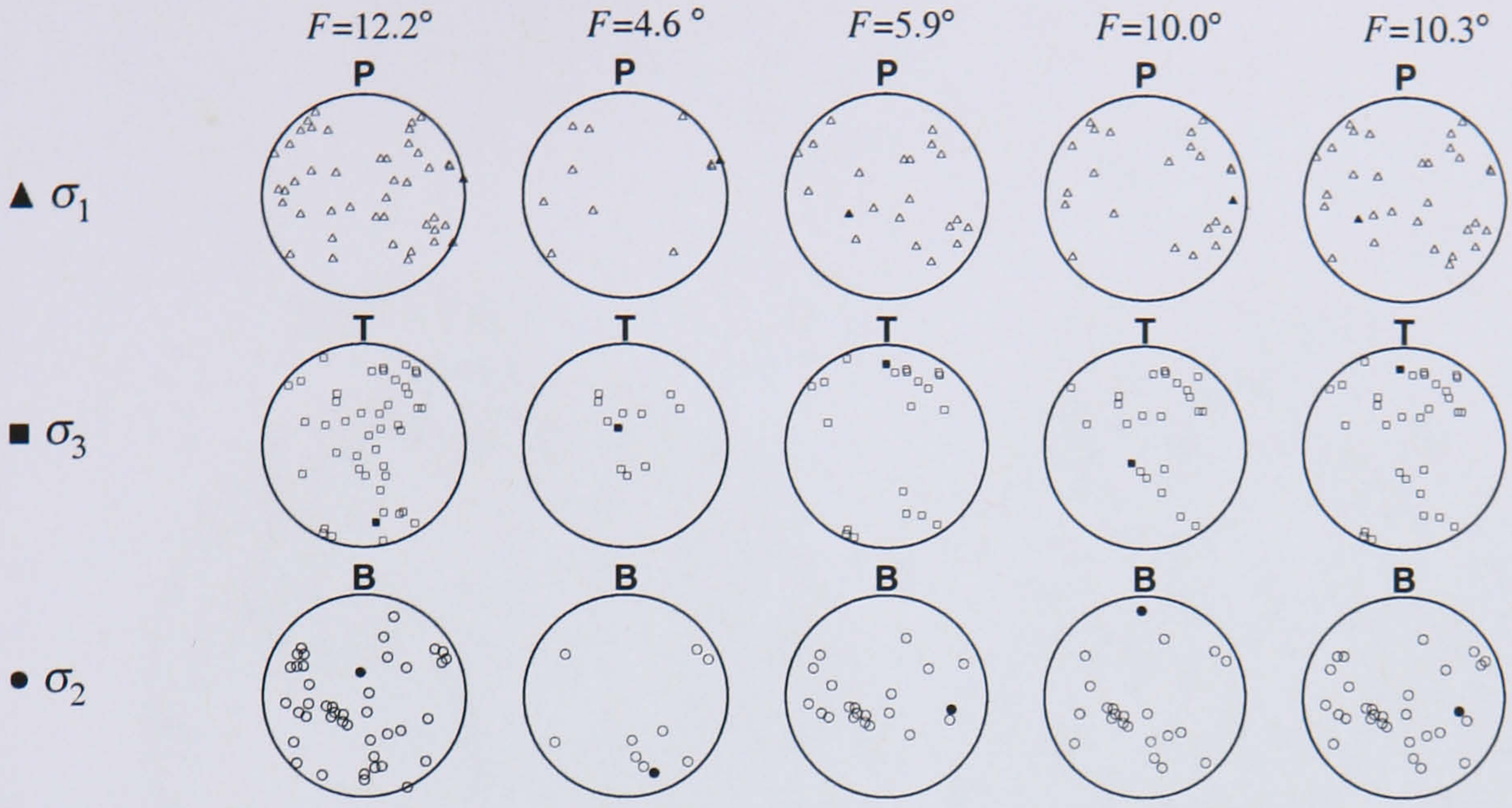

Figure 3.21 Polar diagrams of P, T and B axis for [**a**] entire data (43 mechanisms), [**b**] H cluster (10 mechanisms), [**c**] G cluster (20 solutions), [**d**] combined H and G-Nahr Umr subsets (22 mechanisms) and [**e**] combined H and G clusters (30 mechanisms). The inverted principal stress orientations $\sigma_{1,2,3}$ are shown by black-filled symbols. See Figure 3.16 for the spatial distribution of clusters. Note the great variations of P, T and B axis around the inverted principal stresses for these datasets and the high average misfit F.

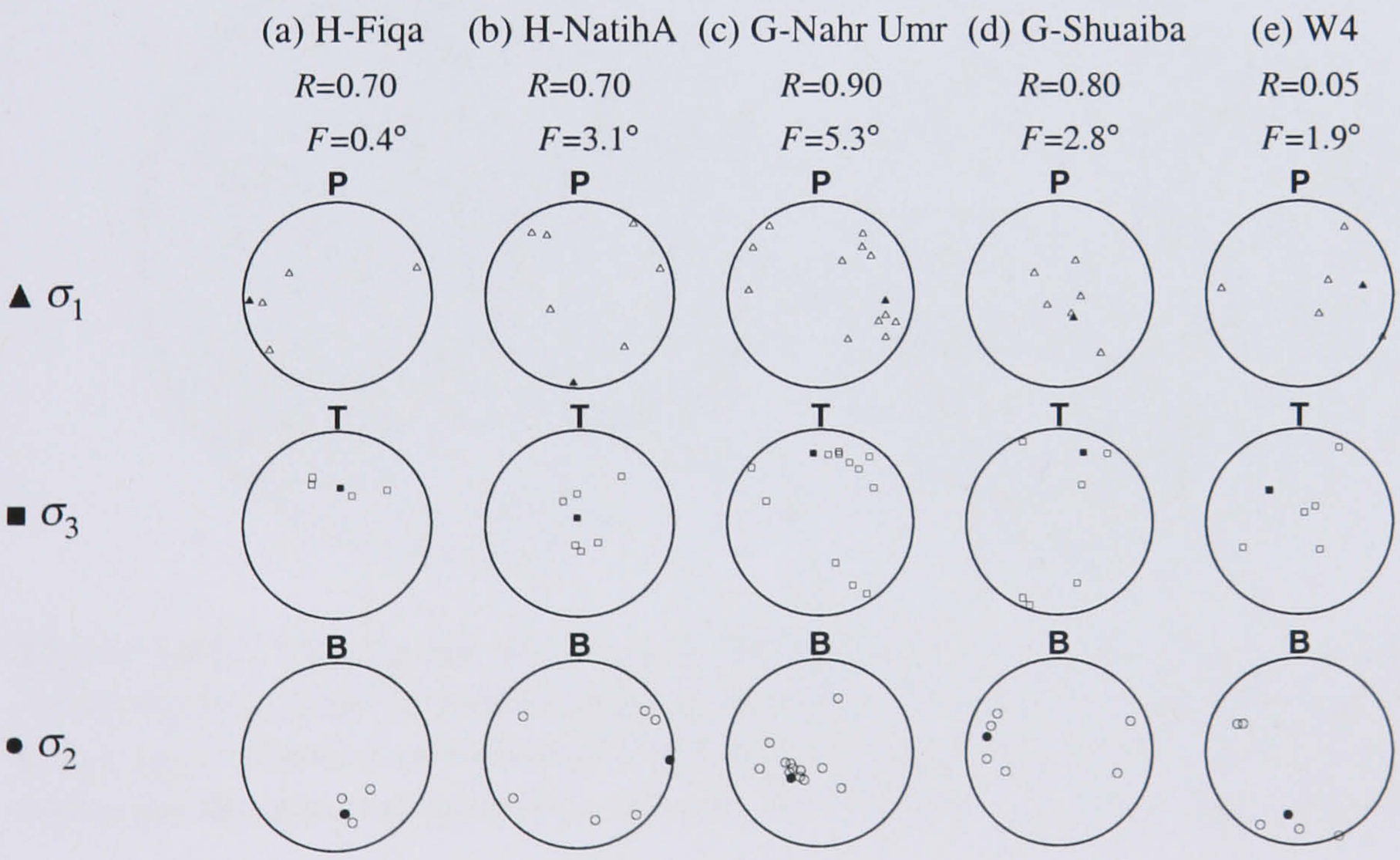

Figure 3.22 Polar diagrams of P, T and B axis for [**a**] H cluster confined within the Fiqa shale (4 solutions), [**b**] H cluster confined within the Naith-A carbonate (6 solutions), [**c**] G cluster confined within the Nahr Umr shale (12 solutions), [**d**] G cluster confined within the Shuaiba carbonate (6 solutions) and [**e**] W4 cluster (5 solutions). The inverted principal stress orientations $\sigma_{1,2,3}$ are shown by black-filled symbols. See Figure 3.16 for the spatial distribution of clusters. The deviations of P, T and B axis from the inverted principal stresses are small for these clusters and the average misfit F is small.

Figure 3.23 Contour polar diagrams of the average misfit F of σ_1 for [**a**] H cluster confined within the Fiqa shale (4 solutions), [**b**] H cluster confined within the Naith-A carbonate (6 solutions), [**c**] G cluster confined within the Nahr Umr shale (12 solutions), [**d**] G cluster confined within the Shuaiba carbonate (6 solutions). The inverted σ_1 is shown by a grey triangle.

(a) H-Fiqa

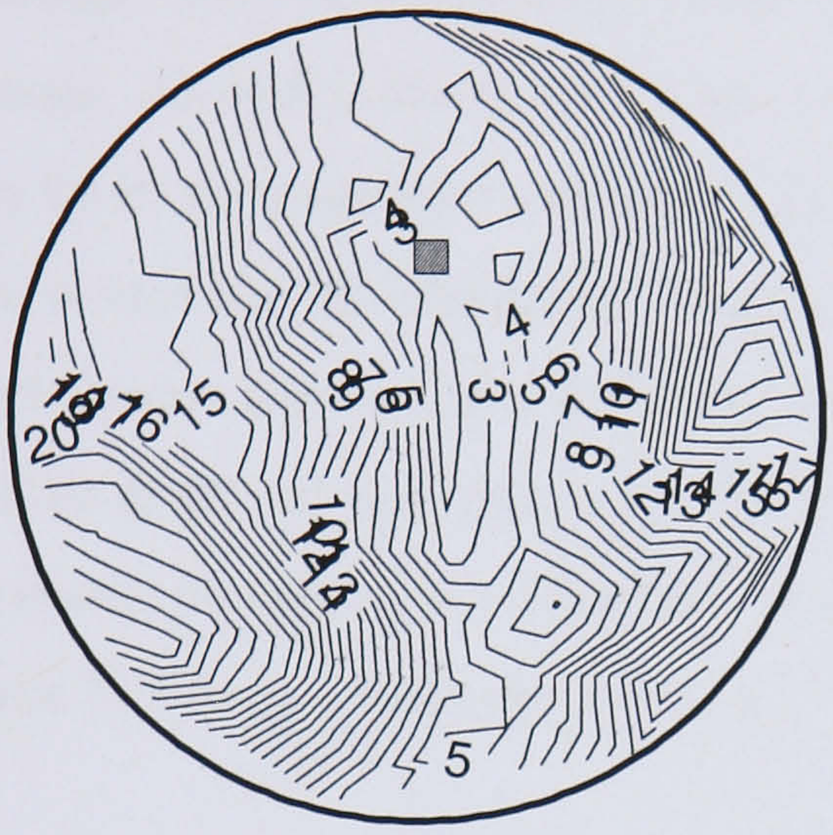

(b) H-NatihA

(c) G-Nahr Umr

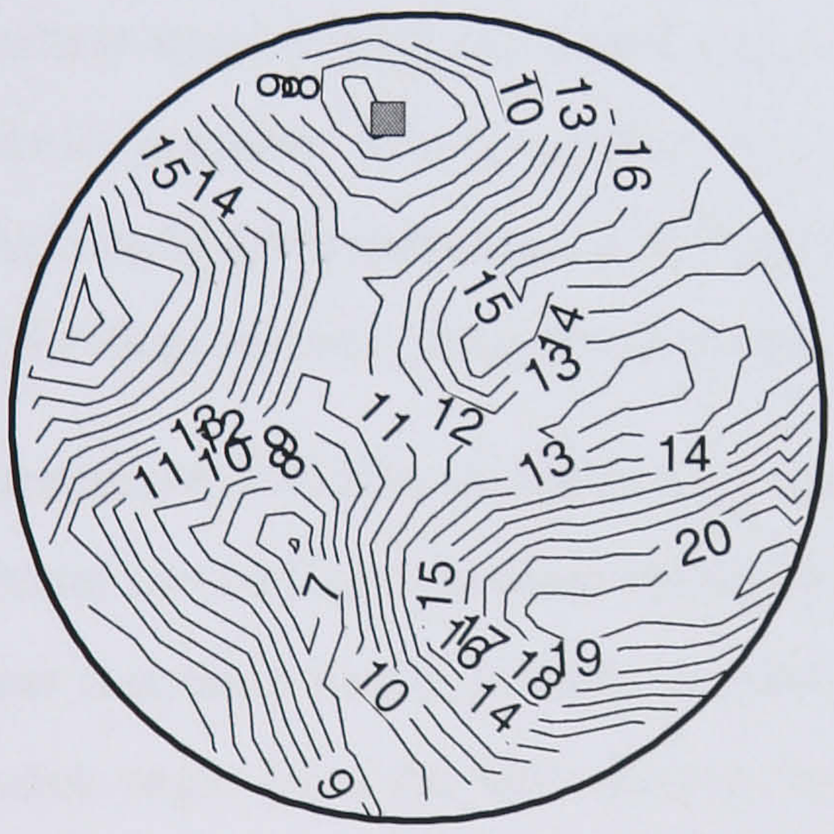

(d) G-Shuaiba

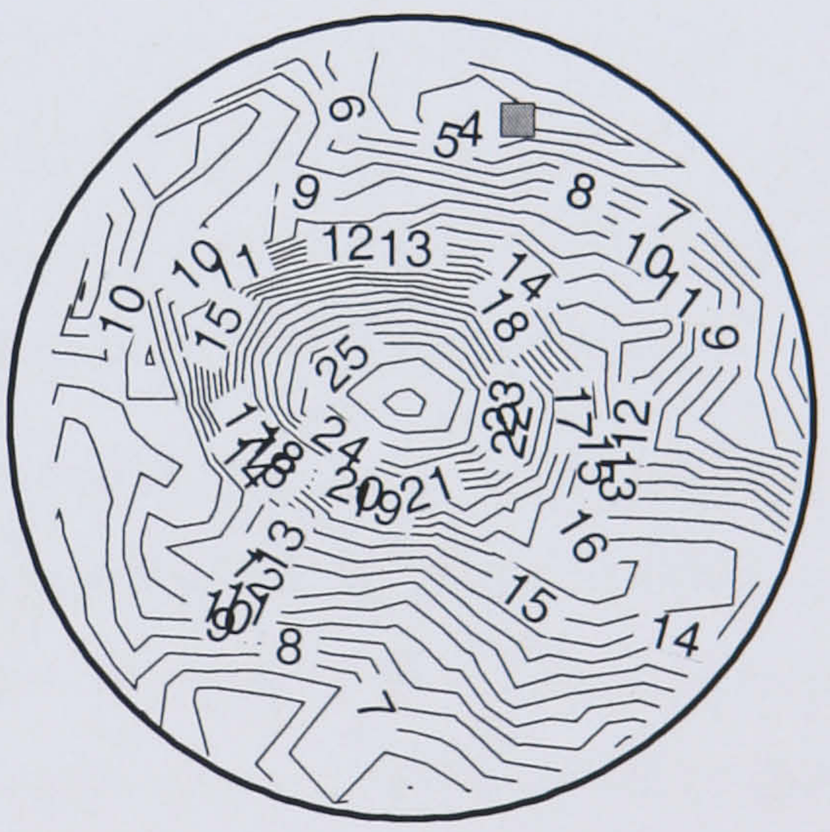

Figure 3.24 Same as Figure 3.23 for the average misfit F of σ_3. The inverted σ_3 is shown by a grey square.

Stress variation with event magnitude

In a study of induced seismicity in the KTB borehole, Bohnhoff et al. (2004) observed that the strongest events tend to represent the regional stress tensor better than weak events. Therefore, the strongest events may be more representative of the local stress field (Hinzen, 2003), while weak events may represent local stress perturbations. To examine this relationship, I first show magnitude scaled FPSs in cross section for clusters H and G (Figures 3.25a and 3.25b, respectively). They show that FPSs do not appear to vary with magnitude in the individual four formations. Secondly, due to the limited coverage, the small FPS dataset does not allow us to reliably invert for magnitude subsets of FPSs. Therefore, I use P, T and B as proxies of stress directions to examine the relationship between event magnitude and stress field. Magnitude scaled P, B and T polar diagrams for the H-Fiqa, H-NatihA, G-Nahr Umr, G-Shuaiba subsets and entire dataset are displayed in Figure 3.26. There is no obvious clustering of P and T directions for strong events, compared to weak events around the inverted stresses. A magnitude histogram of the entire FPS dataset is shown in Figure 3.27.

3.6.5 Estimates of stress magnitudes from real data

The vertical stress can be calculated assuming it is approximately equivalent to the overburden (lithostatic) pressure. The horizontal stress magnitudes, however, are difficult to estimate from only the principal stress directions owing to their sensitivity to regional tectonic stresses. A lower bound for these tectonic stresses can be determined for a given failure criterion.

Since the recovered FPSs are believed to originate from reactivated faults, estimates of the stress magnitudes can be based on shear failure along preexisting faults. The shear failure occurs when the shear resistance along the fault is overcome. This is governed by the friction coefficient μ (or friction angle ϕ) of the fault surface. It is worth noting at this stage that the friction angles ϕ of preexisting fractures are less than those of an intact rock. The sliding friction angles are in the range of 31°-40° for new faults (Byerlee, 1978) and 5°-39° for preexisting faults (Wu et al., 1998). Consequently, the differential stress (i.e., the difference between maximum and minimum stresses) required to reactivate faults (to overcome the shear resistance) is less than that required to form new faults in undeformed rocks.

I assume the following: (1) one of the principal stresses is near vertical and the other two are near horizontal, (2) the lithostatic load equals the vertical principal stress σ_v, (3) the pore pressure p is equivalent to the hydrostatic pressure. This is not true in Natih A where pore pressure data

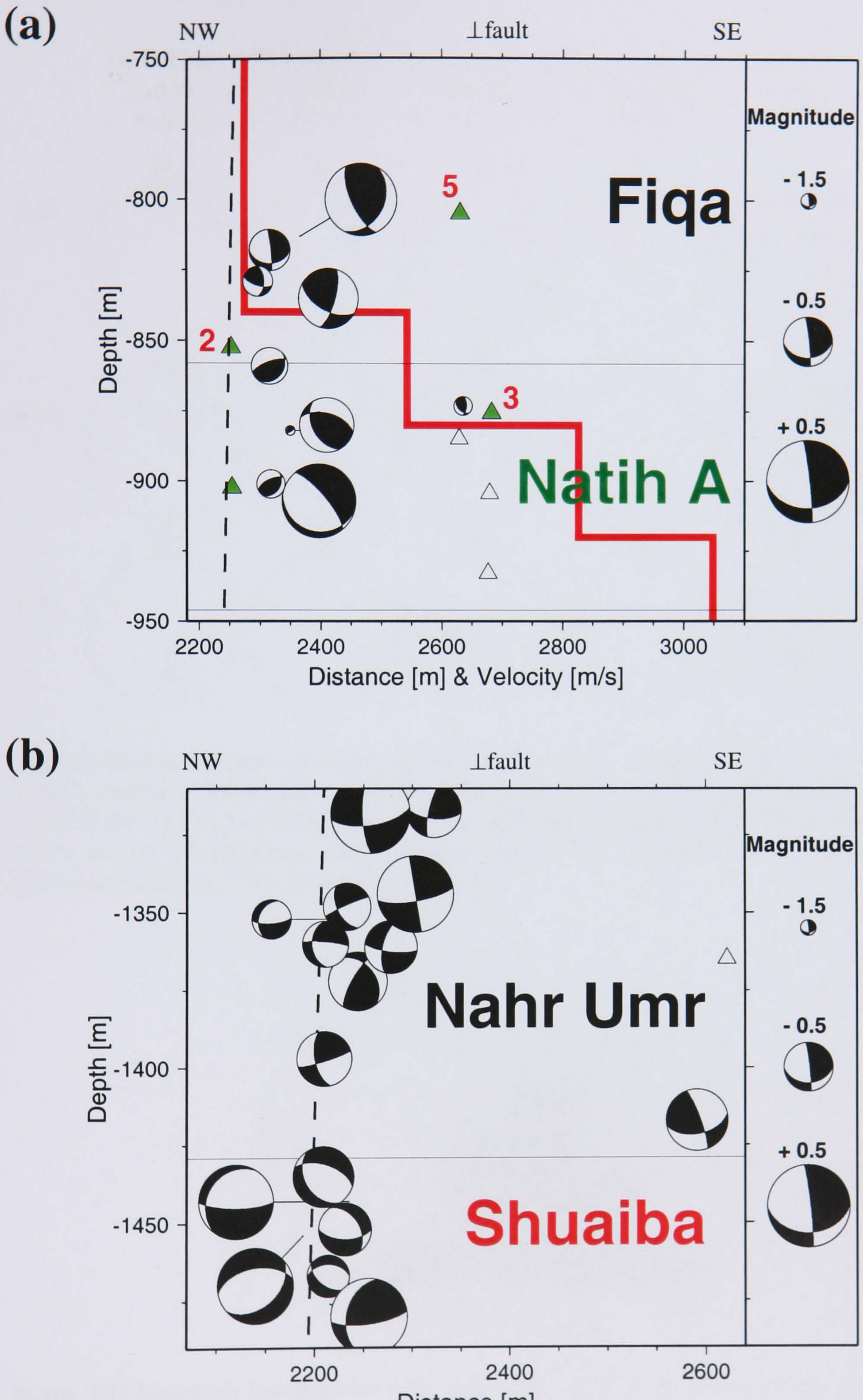

Figure 3.25 Magnitude scaled FPSs in fault-perpendicular cross section for [**a**] the H cluster and [**b**] the G cluster. The magnitude scale for (a) and (b) is identical to facilitate comparison.

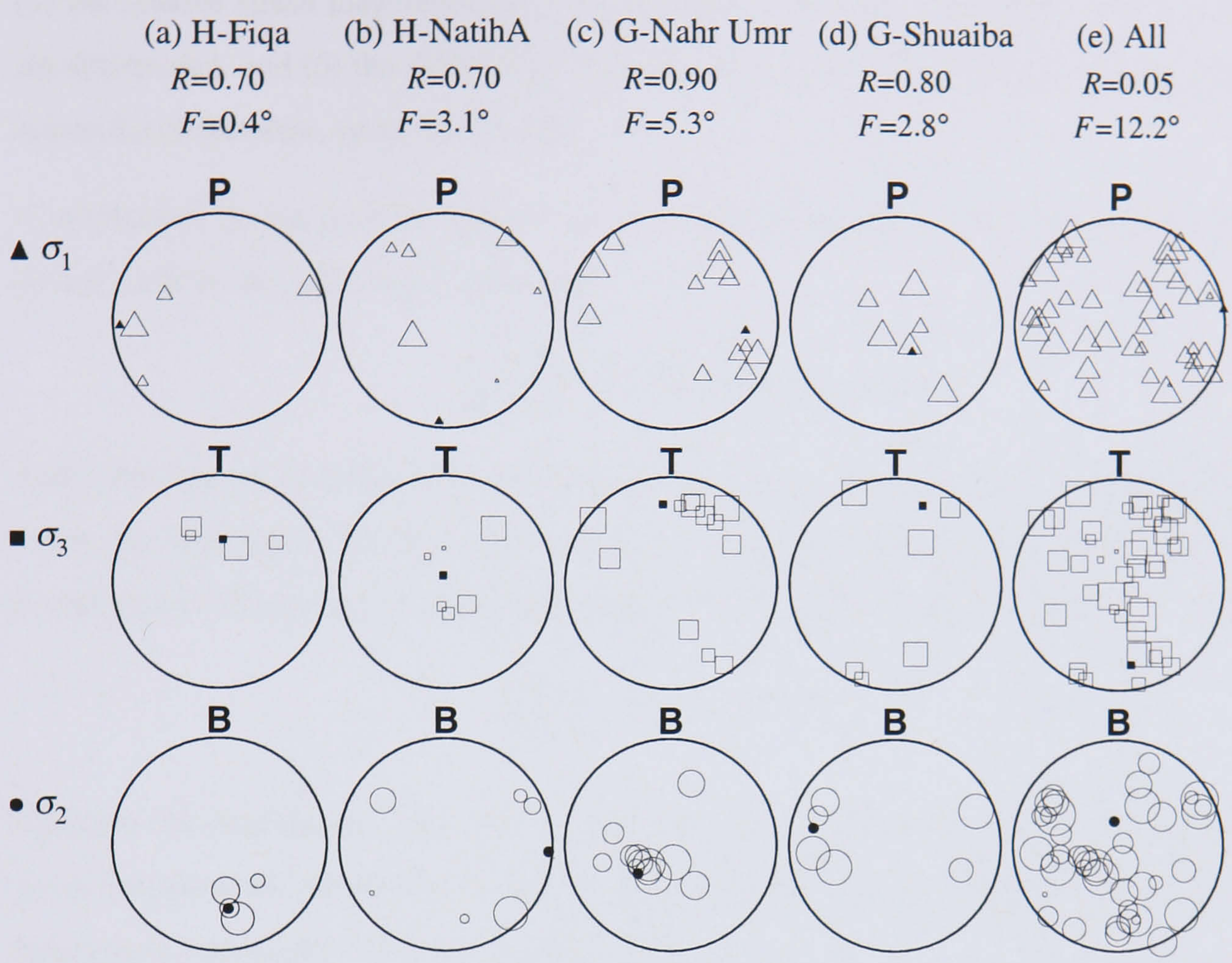

Figure 3.26 Polar diagrams of magnitude scaled P, T and B axis of [**a**] H cluster confined within Fiqa (4 solutions), [**b**] H cluster confined within Naith-A (6 solutions), [**c**] G cluster confined within Nahr Umr (12 solutions), [**d**] G cluster confined within Shuaiba (6 solutions) and [**e**] entire data set (43 solutions). The inverted principal stress orientations $\sigma_{1,2,3}$ are shown by black-filled symbols. Class B results are included.

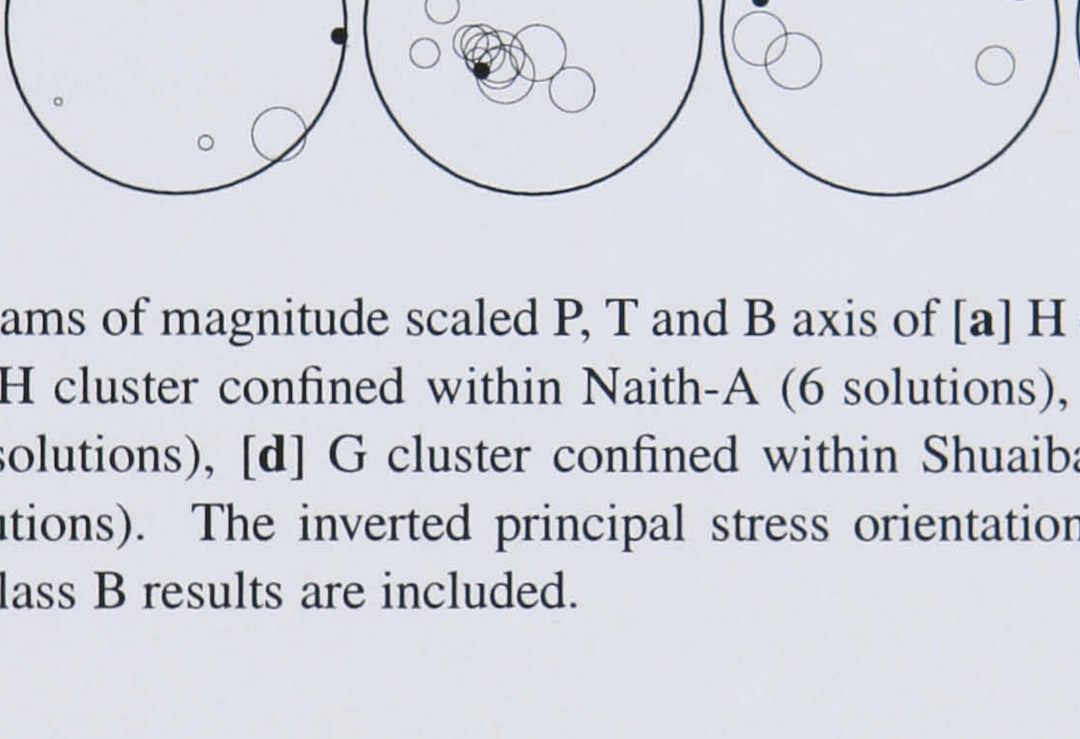

Figure 3.27 Magnitude histogram for the entire 43 FPSs used in the stress inversion (38 class A and 5 class B).

show significant depletion due to gas production. In this case I use the measured pore pressure. (4) the relative stress magnitude, R, constrains the third stress magnitude once the other two are determined, and (5) the differential stress is sufficient to cause slip failure along optimally-oriented, cohesionless, preexisting faults.

Consideration of the fault geometry with the minimum required differential stress to initiate sliding leads to the following relationship

$$\frac{\sigma_1 - p}{\sigma_3 - p} = (\sqrt{1+\mu^2} + \mu)^2 = U, \tag{3.8}$$

where the friction coefficient $\mu = \tan(\phi)$ and hence U is only a function of ϕ (Sibson, 1974; 1985). By rearranging 3.6 as an expression of σ_1 and substituting into 3.8, the sliding condition in expression 3.8 can also be expressed in terms of σ_2 and σ_3 for a given R as

$$\frac{\sigma_2 - p}{\sigma_3 - p} = R + (1-R)U. \tag{3.9}$$

Equation 3.8 (and thereby Equation 3.9) are applicable to all the three fault regimes. Hence, given the above assumptions and stress inversion results (stress orientations and R), the stress magnitudes can roughly be estimated if ϕ is known.

The hydrostatic pressure is estimated using fresh water column density of 1000 kg/m^3 and 9.81 m/s^2 gravity acceleration. The pore pressure is sketched in Figure 3.28a and it steadily rises with depth. The imposed abrupt decline in pore pressure in the Natih A reservoir due to gas depletion (Figure 3.28a) is from reservoir pressure data in 2002. The Shuaiba reservoir does not display significant pore pressure depletion as the reservoir pressure is maintained by water injection.

The lithostatic pressure is also sketched in Figure 3.28a and calculated using the depth-dependent density values of the Yibal 21-layer model. It increases almost linearly with depth starting at about 15 MPa at top Fiqa and ending at about 35 MPa at bottom Shuaiba. The friction angle ϕ varies with lithology, where it is typically lowest (4°-20°) in shale depending on the clay content and cementation (Wu et al., 1998; Blyth and de Freitas, 1984; Osipov et al., 2004) and larger (20°-40°) in chalk (Wu et al., 1998; Blyth and de Freitas, 1984; Jaeger and Cook, 1989). Therefore I account for ϕ variation by assigning ϕ of 12° and 18° to mechanics in the shale cap rocks Fiqa and Nahr Umr, respectively, and ϕ of 39° to those in the chalk reservoirs (Natih A and Shuaiba). These ϕ values are actually the resulting ones from the numerical modelling in the next section.

According to the stress inversion results, the subvertical stress σ_v is associated with σ_3 in Natih

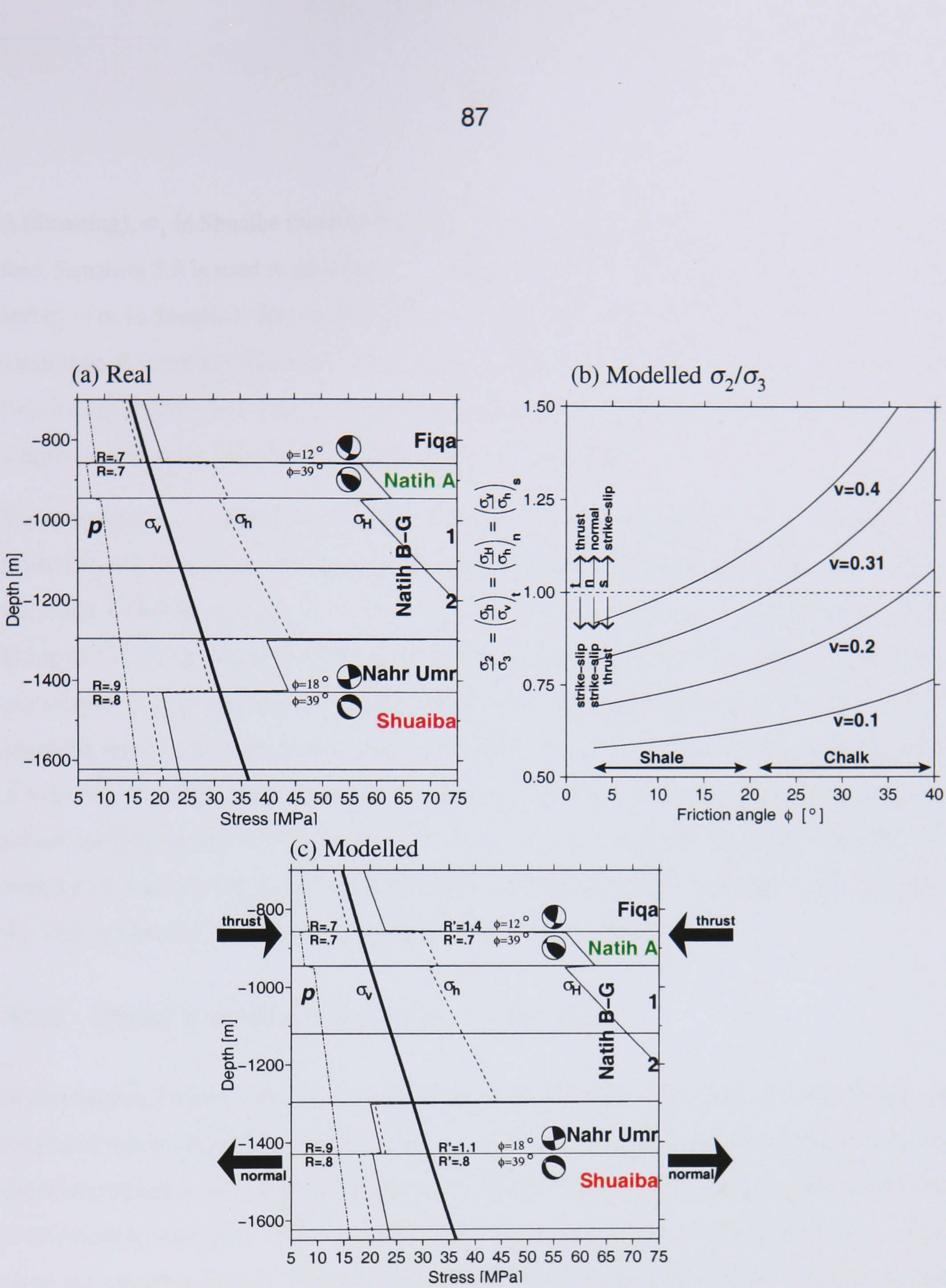

Figure 3.28 [**a**] Vertical (σ_v), maximum horizontal (σ_H) and minimum horizontal (σ_h) stress and pore pressure (p) variations with depth. The measurements are based on the inverted stress directions and R, and failure along favourably oriented preexisting faults with typical lithology dependent friction angles, ϕ (shown). [**b**] σ_2/σ_3 modelled ratio as a function of friction angle for various Poisson's ratio values (ν) based on pure slip original condition (p/σ_v=0.47 is used). Symbols t:thrust, n:normal and s:strike-slip faulting regimes. The typical ranges of ϕ of shale and chalk are also shown. Note the remarkable transition in each system for lower ν and ϕ (e.g., for ν=0.31 the transition friction angle (ϕ_t) is at 22°). [**c**] Modelled stresses when applying thrusting system in both Fiqa and Natih A, and normal faulting system in both Nahr Umr and Shuaiba using shale cap rock ϕ with the best fit friction angles. A representative focal mechanism is also plotted for each layer.

A (thrusting), σ_1 in Shuaiba (normal faulting), and σ_2 in Fiqa and Nahr Umr (strike-slip). Therefore, Equation 3.8 is used to estimate σ_1 in Natih A and σ_3 in Shuaiba (using $\sigma_3 = \sigma_v$ in Natih and $\sigma_1 = \sigma_v$ in Shuaiba). The σ_2 magnitude in both formations is then constrained by the relative magnitude R (from the inversion results). For formations favouring strike-slip (shale cap rocks Fiqa and Nahr Umr) where σ_2 is only known, Equation 3.9 is used to determine σ_3. Again, R is used to constrain the magnitude of the final stress component.

The estimated σ_1, σ_2 and σ_3 are renamed in terms of maximum horizontal, σ_H, minimum horizontal, σ_h and vertical, σ_v, stress, depending on the observed faulting regime (e.g., in the thrusting Natih A formation $\sigma_H=\sigma_1 > \sigma_h=\sigma_2 > \sigma_v=\sigma_3$). The magnitudes of σ_H, σ_h and σ_v are plotted in Figure 3.28a. The results in Natih B-G are extrapolated from Natih A assuming identical ϕ, R and a faulting regime similar to that of Natih A. The stress magnitudes σ_H and σ_h (Figure 3.28a) generally increase with depth as p and σ_v increase, but show flips/intersections at the Fiqa/Natih A and Nahr Umr/Shuaiba interfaces. These σ flips are consistent with differences in the observed faulting regime between each layer. It also shows that differential stress (the difference between σ_1 and σ_3) is higher in the chalk reservoirs (higher ϕ) than in the shale cap rocks (lower ϕ). This is expected because I forced higher and lower ϕ, respectively.

3.6.6 Stress modelling on pure dip or strike-slips

In this section I explore the reason behind the observed faulting regime transition at each cap rock/reservoir interface based on a friction model and subsequently determine estimates of mechanical properties such as fault friction angles in the Yibal field. The starting point for the work in this section comes from Wu et al. (1998). In the previous section the differential stress is evaluated for a given ϕ, and σ_2 is then constrained by R from the real data (stress inversion results). In this section, the evaluation of the differential stress is the same, but here I compare the real R (used to constrain σ_2) with what would be expected from a passive basin model. The modelled R and the real R can be further examined by calculating the best fit ϕ that brings the modelled R into agreement with the real R. The procedure is illustrated in a flow chart in Figure 3.29.

To determine a possible cause for the observed faulting regime transition in the upper and lower reservoirs, I examine the stress behaviour of several fault block models based on the condition of sliding on optimally-oriented, cohesionless, preexisting faults (Equation 3.8) and a $\sigma_1 - \sigma_3$ plane strain condition. The latter condition means that only biaxial strain is allowed, and that σ_2 is strong enough for zero strain along the σ_2 direction. In other words, this condition considers only pure dip-slip in thrust and normal faults and pure strike-slip in strike-slip regimes. It follows

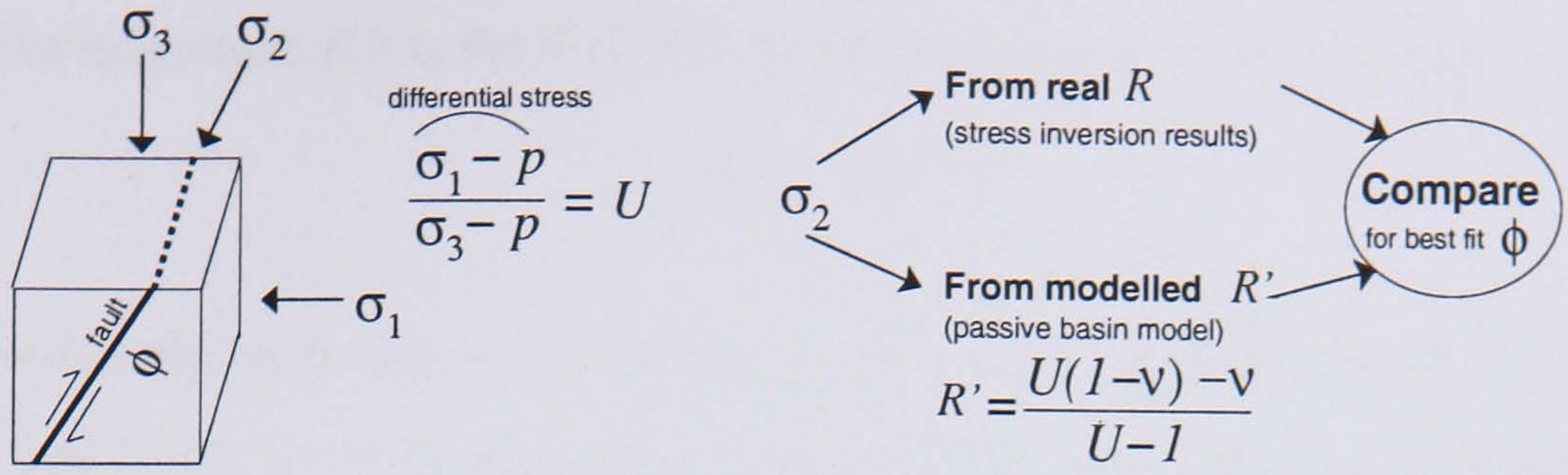

Figure 3.29 A flow chart illustrating the numerical stress modelling objective. p is the pore pressure, U a function of ϕ, and R' (relative stress magnitude) a function of ϕ and ν where the latter two are the fault friction angle and Poisson's ratio. The example is for a thrust fault but applicable to all three end member fault regimes.

from this condition that the three principal stresses are related by Poisson's ratio ν as

$$\sigma_2 - p = \nu(\sigma_1 - p + \sigma_3 - p). \tag{3.10}$$

This relation simply results from basic 3D stress-strain relationships by setting the strain along σ_2 direction to 0 (Jaeger and Cook, 1989). Rearranging Equation 3.10 as an expression of σ_1 and substituting into Equation 3.8, the sliding condition in Equation 3.8 can also be expressed in terms of σ_2 and σ_3 as

$$\frac{\sigma_2 - p}{\sigma_3 - p} = \nu(1 + U). \tag{3.11}$$

Again, 3.8 and 3.11 are applicable to all three end-member fault systems. In Figure 3.28b the σ_2/σ_3 ratio (Equation 3.11) is plotted as a function of friction angle, ϕ, for Poisson's ratios ν of 0.1, 0.2, 0.31 and 0.4 for the three faulting regimes. Surprisingly, the σ_2/σ_3 ratio can be less than 1 (i.e., $\sigma_2 < \sigma_3$) for lower ϕ and ν. Physically, this means that σ_2 and σ_3 can swap orientation. As a result, two faulting mechanisms can exist on each preexisting fault system (Wu et al., 1998). A system originally dominated by thrusting can switch to strike slip, normal system to strike-slip, and strike-slip to thrusting regime (Figure 3.28b).

It can be shown from Equation 3.11 that the Poisson's ratio (ν_t) and friction angle (ϕ_t) values where such transitions occur can be written as,

$$\nu_t = \frac{1}{2}(1 - sin\phi), \tag{3.12}$$

$$\phi_t = sin^{-1}(1 - 2\nu). \tag{3.13}$$

Rearranging Equations 3.8 and 3.11 as expressions for σ_1 and σ_2, respectively, and substituting

in the relative magnitude R 3.6, the R of this synthetic model (R') can be written as

$$R' = \frac{U(1-\nu)-\nu}{U-1}, \tag{3.14}$$

which depends only on ϕ and ν, and principally can be in the range $0 \leq R' \leq \infty$ (considering $0 \leq \nu \leq 0.5$ and $1 \leq U \leq \infty$ that corresponds to $0 \leq \phi \leq 90$). Again the surprising transition from the original faulting system to another regime is also indicated by $R'>1$ breaking the theoretical limit of R=1 and inducing $\sigma_2 < \sigma_3$ (or physically swapping orientations of σ_2 and σ_3). The real R is described by R' when $R'<1$ and $1/R'$ when $R'>1$. The nearly constant v_p/v_s ratio (=1.9) with depth in Yibal implies depth-invariant ν of 0.31. Therefore, I use ν=0.31 for all depths. Hence, the transition friction angle ϕ_t is 22° for all depths and all three faulting systems (Equation 3.13 and Figure 3.28b). The 22° friction angle separates the corresponding typical values of the shale and chalk rocks (Figure 3.28b). Therefore, the only plausible stress system that would cause the observed faulting regime in Yibal is a regional thrust system in the top reservoir and normal faulting system in the bottom reservoir. I use the same assumptions to calculate the real stress magnitudes except that the second constraint on real R (from the inversion results) is now modified by the synthetic R' (that depends on ϕ and ν).

Moreover, the real and synthetic R can be compared. Using Equation 3.14, the best fit Poisson's ratio values (ν_{fit}) and the best fit friction angle values (ϕ_{fit}) that both generate R' consistent with real R values (say from the stress inversion results) can be calculated as

$$\nu_{fit} = \frac{1}{2}\Big(1 - sin\phi(2R' - 1)\Big), \tag{3.15}$$

$$\phi_{fit} = sin^{-1}\left(\frac{1-2\nu}{2R'-1}\right). \tag{3.16}$$

It turns out from Equation 3.16 that ϕ_{fit} is a physical (real positive) value as long as the condition $R' > 1\text{-}\nu$ is satisfied. Therefore, in our case where ν=0.31, ϕ_{fit} can only be obtained for observed $R' > 0.69$. This value is just below the lowest observed R in the four studied zones (R=0.7). Thus inversion for ϕ_{fit} of all the four zones is feasible. I therefore evaluated ϕ_{fit} for each reservoir and cap rock (from Equation 3.16) that would result in the observed faulting regime under regional thrust system imposed in Fiqa and Natih A, and normal system applied in Nahr Umr and Shuaiba. In ϕ_{fit} computation, it is worth pointing out that $R'=R$ in both reservoirs and $R'=1/R$ in both cap rocks due to fault regime transition. The resulting ϕ_{fit} are 12° and 18° in the shale cap rocks Fiqa and Nahr Umr, respectively, and 39° in the Shuaiba. The Poisson's ratio of 0.31 in the Natih A reservoir (where R=0.7) resulted in unrealistic ϕ_{fit} of 70°. For a realistic ϕ_{fit} value of 39 °

(like ϕ_{fit} of the Shuaiba), an increase in Poisson's ratio, to 0.37 (Equation 3.15) is required in the Natih A. Therefore, ν=0.37 is used in the Natih-A formation.

Figure 3.28c displays the modelled stresses for the calculated best fit friction angles. The modelled stress fits well the real stress data (Figure 3.28a) and yields the observed faulting regimes. The only difference occurs in the Nahr Umr zone where the strike-slip faulting is not clear in the modelled values (i.e., the intermediate stress is not vertical). However the model prediction of the transition from the originally normal faulting system to the new one reorients σ_h parallel to the strike of the fault (Wu et al., 1998) (while maintaining σ_v=σ_1 rendering transition to the strike-slip regime). In the context of the real stresses (Figure 3.28a), the magnitude of σ_H is larger than σ_v above the Shuaiba and can be up to 20 MPa in the Fiqa, 63 MPa in the Natih A, 43 MPa in the Nahr Umr. In contrast, in the Shuaiba it is lower than σ_v and as low as 24 MPa. However, σ_h can be up to 17 MPa in Fiqa, 28 MPa in Natih A, 30 MPa in Nahr Umr and as low as 20 MPa in Shuaiba.

I also attempted to force a regional strike-slip regime in all the layers. Although the modelled results can explain the real data if abnormal ϕ are used ($\phi > \phi_t$ for shale $\phi < \phi_t$ for carbonate) but they can't explain the observed normal faulting in Shuaiba as only strike-slip/thrust transition is permitted (Figure 3.28b). Similar demand to abnormal values of ϕ and inconsistent results were attained with imposing regional normal and thrusting systems in all layers (Figure 3.28b). I also examined exerting strike-slip system in both Fiqa and Nahr Umr, thrusting system in Natih A, and normal system in Shuaiba. However, it required abnormal ϕ values for the cap rocks to bring the resulting regime compatible with the observed one. Therefore, the observed faulting regimes can be explained by only one plausible scenario: a regional thrust system in top reservoir and cap rock and a regional normal system in the bottom reservoir and cap rock.

3.6.7 Discussion and Interpretation

I have applied the stress inversion algorithm to as few as four fault plane solutions. In practice, 10 focal mechanisms or more are generally required for stress inversion (Wyss et al., 1992; Caccamo et al., 1996; Neri et al., 2005). The least reported number of FPSs inverted for is 11 by Bohnhoff et al. (2004) and Neri et al. (2005). However, in principle, at least four different orientations of fault planes are necessary for a unique estimate of R and principal stress directions (Gephart and Forsyth, 1984). This is due to the four unknown variables (3 principal stress directions and R) that require a minimum of four data points for a unique solution.

I favor the secondary misfit solutions for H-NatihA and G-Nahr Umr subsets as they agree more with the P, B and T axes (Figures 3.22(b,c), respectively) while still being within the $F_{95\%}$ of the primary (global) minimum. The average misfit F is significantly higher than 6° for the entire dataset (Figure 3.21a) which is suggestive of inhomogeneities in the stress field. The subdivided sets in depth horizons show much lower F values that are generally below 6° (Figure 3.22). In other words, division into depth zones successfully resulted in nearly uniform stress regimes within each horizon. Inversion results show variations in the maximum compressive stress direction with depth: horizontal E in Fiqa, horizontal NNE in Natih-A, subhorizontal E in Nahr Umr, and subvertical in Shuaiba (Figure 3.22). Strictly, σ_1 is 30° and 60° off horizontal in Nahr Umr and Shuaiba, respectively.

The subvertical principal stress (σ_v) results of the four zones (Figure 3.22) match those of the ternary diagram of P, T and B axes of FPSs (Figure 3.19). As predicted from FPSs, the inversion results indicate that σ_v is represented approximately by σ_2 in shale cap rocks Fiqa and Nahr Umr, σ_3 in thrusting Natih A and σ_1 in Shuaiba. The inverted $\sigma_{1,2,3}$ directions agree well with the observed faulting regimes inferred from FPSs. They imply fault regime transition associated with the two reservoirs: thrust with strike-slip component to pure thrust at the Fiqa/Natih A interface, and strike-slip to pure normal faulting at the Nahr Umr/Shuaiba interface. The two cap rock fault regimes (shale Fiqa and shale Nahr Umr) are consistent with each other both indicating strike-slip regime. The thrust faulting component in Fiqa is expected considering that it lies above a compacting reservoir (Segall, 1989). The highest potential of compaction due to gas depletion is the chalky Natih zone where soft and heterogeneous units are present.

The horizontal NNE σ_1 direction in Natih-A reservoir is in good agreement with the in-situ σ_1 direction inferred from wellbore breakouts derived from differential FMI/FMS caliper measurements (Baker Atlas GEOScience, 1999) (Figure 2.5). However, the E σ_1 trend in Nahr Umr does not agree with NE in-situ σ_1 azimuth (Baker Atlas GEOScience, 1999) (Figure 2.5). The in-situ measurements of Baker Atlas GEOScience (1999) are collected in the flanks of the field while ours are from the crest. Thus, the deviation in Nahr Umr can be due to lateral stress variation. The measured NE maximum stress direction in Nahr Umr is similar to the regional stress in Oman (Filbrandt et al., in press). Stress inversion results of the entire dataset cannot be used to infer for the regional stress field due to heterogeneities in the entire dataset.

Uniform stress can be assumed in individual H, G and W4 clusters as they yielded average misfit F values less than 6° (see Table 3.6). A useful procedure for identifying where the homogeneous stress assumption exactly breaks down is to start with one stress-uniform subset, then add other

uniform-stress subsets one at a time, and doing a stress inversion at each step. I employed this approach, attempting different combination of subsets, as shown in Table 3.6. I believe, from the F values in Table 3.6, that stress non-uniformity rises from the combined subsets H-NatihA and G-Shuaiba (F=8.5° > 6°) as expected due to their completely opposite fault regimes (reverse and normal, respectively).

In the four studied depth zones, the encountered relative stress magnitude R values are in the range 0.70-0.90. Such close values to 1 means σ_2 is much closer to σ_3 than to σ_1 and, therefore, suggests flattening rather than constricting. The largest observed R is 0.90 in the Nahr Umr cap rock. Conversely, R in the W4 cluster is lowest (0.05) and, therefore, indicates constricting rather than flattening. Furthermore, the inverted stress for W4 cluster favours a reverse faulting regime.

It is assumed that strong events are more representative of the local stress than weak events (Bohnhoff et al., 2004). Event magnitude scaled FPSs (Figure 3.25) suggest unchanging faulting regime with respect to event magnitude in each formation. Magnitude scaled P, T and B axes (Figure 3.26) similarly indicate no distinct relationship between magnitude and local stress. Therefore, I believe that all FPSs along the eastern-most graben fault, weak and strong, are representative of the local in-situ stress field in each layer and not to local stress perturbations which would be expected to occur away from the eastern-most graben fault. This suggests that the microseismic events are actually located exactly at the fault and the observed fluctuation of event locations around this fault may have developed from the imperfect velocity model and errors in time and hodogram picks. I also feel that all the observed microseismic events are considerably very weak (magnitude range -2 to 1), and thereby, strong events did not occur.

From stress modelling based on a pure sliding condition, regional thrusting and normal regimes in the upper and lower reservoirs, respectively, appears the only realistic scenario. Hence, the sharp transition at the cap rock/reservoir interface is suggestive of lower friction angle in the shale cap rocks compared to the carbonate reservoirs. Our calculated best fit friction angles of shale and chalk are within the typical shale and chalk ranges reported in the literature. As a result, the modelled relative magnitude R' are consistent with observed R values (0.7-0.9) from the stress inversion. A positive anomaly in the Poisson's ratio (0.37) in Natih A is needed to explain the relative magnitude R from the stress inversion results. However, this is not far from expected as compaction in Natih A could cause such a change in the Poisson's ratio. The observed sense of change in Poisson's ratio due to compaction is consistent with laboratory deformation measurements elsewhere (Goodman, 1989), pressure data (Schön, 1996) and laboratory data for limestones (Avseth et al., 2005) (i.e., Poisson's ratio increases with increasing compaction).

Based on the best fit friction angles, the real and modelled principal stresses (Figures 3.28(a,c), respectively) match each other and produce the observed faulting regime in each formation. The calculated differential stress (Figures 3.28(a,c)) is a lower bound while the true value could be larger. The maximum principal stress is encountered in Natih A lying horizontally at about 63 MPa. The lack of stress magnitude measurements from the field renders testing the accuracy of our results very difficult. The predicted transition from thrust to strike-slip faulting based on the model was also found to fit in-situ stress measurements in Western Canadian foothills (Woodland and Bell, 1989; Woodland, 1990; Wu et al., 1998). The model prediction of stress magnitudes in the transition zone from pure normal faulting was also found to be consistent with in-situ stress observations in different lithologies (shale/mudstone and sandstone) in the US DOE's multiwell experiment site, Colorado (Warpinski et al., 1985; Wu et al., 1998).

Additionally, one can argue that the regional stress in Yibal is controlled by strike-slip regime and the resulting perturbation in Natih A (thrust) and Shuaiba (normal) is due to hydrocarbon extraction. Although our modelling does not support this scenario as it leads to abnormal friction angles, lower in chalk and higher in shale (contradicting the documented typical properties) and also predicts thrust regime in Shuaiba which contradicts the observed normal regime, other models that handle gas and oil production may fit the observations.

Our assumption of one principal stress being subvertical and other two subhorizontal is only valid in flat geology (Addis, 1997). Therefore, the significantly rotated inverted principal stress orientations from horizontal (e.g., σ_1 is dipping roughly 30 and 60 in Nahr Umr and Shuaiba, respectively) are not surprising due to the Yibal domal structure.

3.7 Conclusions

In this study, I analyse 22 days of data, containing over 600 located events recorded by a maximum of 5 monitoring wells (10 downhole 3-component stations in total). The application of focal mechanism proved effective in synthetic Yibal-like data. In the real data, the application was successful and useful in detecting variations of focal mechanism that are controlled by lithology and deformation. Forty-three reliable fault plane solutions (FPSs) were determined. The solutions are calculated using polarities and amplitudes of direct P-, SV- and SH-waves. The results clearly show that the shale cap rocks are failing differently from the chalk reservoirs along the eastern-most graben fault. A strike-slip regime is observed in the shale cap rocks Fiqa (with thrusting component) and Nahr Umr; thrusting in the Natih A gas carbonate reservoir;

and normal faulting in oil-bearing carbonate Shuaiba reservoir. The thrusting above the Natih A reservoir is consistent with the fact that Natih A is undergoing compaction.

The stress tensor inversion from the forty three FPSs is also found to be useful. The deduced stress field in the Natih reservoir is consistent with the in-situ stress inferred from wellbore breakouts (Baker Atlas GEOScience, 1999). The observed relative stress magnitude in Natih A suggests a positive anomaly in Poisson's ratio (increasing by about 0.06) which is consistent with the ongoing compaction in this unit. The inversion results are also in agreement with FPSs and indicate the same fault regime in each of the cap rocks and reservoirs. The maximum compressive stress direction varies with depth: horizontal E in Fiqa, horizontal NNE in Natih-A, sub-horizontal E in Nahr Umr, and sub-vertical in Shuaiba. More importantly, the subvertical (lithostatic pressure) acts as σ_3 in Natih A (thrusting), σ_1 in Shuaiba (normal faulting), and σ_2 in Fiqa and Nahr Umr (strike-slip).

Considering pure slip condition in optimally-oriented preexisting cohesionless faults, the modelling shows only one acceptable scenario. That is an exerted regional thrusting system in the top reservoir and its cap rock and normal system in the bottom reservoir and its cap rock. The transition at each shale cap rock/carbonate reservoir could be formed by variation in fault friction angles across the interface. I developed a method to estimate friction angles from observed focal mechanisms (from microseismic data). The resulting best fit friction angles in shale (12° in Fiqa and 18° in Nahr Umr) and chalk (39° in Natih A and Shuaiba) closely agree with the reported values in the literature. The three principal stress magnitudes (lower bound of differential stress) were calculated at each depth in the four zones with the maximum stress occurring in Natih A at about 63 MPa. Furthermore, investigating the fidelity of these calculated stress magnitudes requires field measurements, which are unavailable.

It is interesting to consider any temporal variation in the stress field. Our results do not show any significant variation but the dataset is too limited to make a firm conclusion. Additionally, no variations in faulting regime/stress with event magnitude were observed in each layer along the eastern-most graben fault. I interpret this as that the local stress field acting on the fault is steady with no local perturbations.

Finally, the exciting results of focal mechanism analysis and stress inversion in this chapter contribute to the geomechanical understanding of the Yibal field. Failing to integrate the observed spatial variations in stress in the geomechanical model may lead to failure in predicting the true reservoir behaviour during the field life.

Chapter 4

Modelling shear-wave splitting in fractured anisotropic media

4.1 Introduction

In the previous chapter focal mechanisms were used to understand the nature of faulting in Yibal and estimate the stress field. Shear-wave splitting measurements will add further constraints to our knowledge of stress and fracture patterns in Yibal. When a shear-wave encounters an anisotropic medium it splits into nearly perpendicular fast and slow shear-waves which separate with time. Such shear-wave splitting can be described by the separation time between the shear-waves, δt, and the orientation of the fast shear-wave polarisation, ψ(strike,dip). The anisotropy can arise from preferentially aligned fractures and/or the preferred orientation of minerals (intrinsic anisotropy) (Bokelmann and Harjes, 2000; Winterstein, 1990). However, due to this variety of possible causes of anisotropy, inverting for the true model from shear-wave splitting measurements is not easy and can be non-unique.

In this chapter I investigate the effects of fracturing and intrinsic anisotropy on shear-wave splitting through numerical modelling. This work will help interpret observations of shear-wave splitting in real data. Estimating shear-wave splitting with downhole-recorded microseismic data is a bit more complicated than more conventional earthquake shear-wave splitting analysis (e.g. Silver and Chan, 1991).

In this chapter synthetic modelling is used to predict shear-wave splitting in possible fracture models in Yibal and help guide the real data analysis in the next chapter. The main objectives of this chapter are: 1) understand the limitations in shear-wave splitting analysis in using the Yibal microseismic network geometry to determine fracture strike, dip and density, 2) draw guidelines to assist interpreting the real data, 3) examine the capability of the data to differentiate between

fractures and intrinsic anisotropy and 4) test the feasibility of using shear-wave splitting analysis to contrast between gas and liquid filled cracks. The fact that there is a gas reservoir and a liquid reservoir in Yibal, makes the last objective plausible.

First the method used to carry out the synthetic study is described. Then the effect of ray orientation (azimuth, inclination) on splitting observations is investigated for: (1) a single set of vertical cracks (horizontal transverse isotropy, HTI), (2) two sets of vertical cracks, (3) vertical transverse isotropy (VTI) caused by the preferred orientation of anisotropic minerals or fine-scale layering, and 4) a combination of (3) and (1). In each case differences between brine versus gas filled cracks are highlighted. Finally, I examine the effects of fluid exchange between cracks and pore spaces (i.e., cracks interconnected with pores).

4.2 Theory

4.2.1 Fracture elasticity

Elastic constants for the various anisotropic models are calculated using the program CIJSTAN[1] (developed by Hall and Kendall (2000)). Hall and Kendall (2000) describe the compliance of fractures based on an extension of the effective medium theory of Schoenberg and Sayers (1995), appealing to the theory of Hudson (1981) to parameterise fractured media with no equant porosity (impermeable matrix) and the theory of Hudson et al. (1996) to parameterise fractured media with equant porosity (permeable matrix) that hydraulically connects fractures and pore spaces. The method assumes elastic behaviour, Hudson-style penny-shaped cracks and a crack spacing much less than a seismic wavelength.

4.2.2 VTI shale elasticity using crystal alignment data

In the fractured chalky reservoirs (Natih A and Shuaiba) I assume an isotropic background. However, the shale cap rocks (Fiqa and Nahr Umr) are unlikely to be isotropic. Numerous studies have shown that shales have an intrinsic anisotropic background due to the preferential alignments of mica minerals (e.g. Valcke et al., in press; Hornby et al., 1994). I therefore assume an anisotropic background in the Yibal cap rocks based on realistic shale rocks. In this section I describe how I calculate the shale rock elasticity from the measured elastic constants of constituent minerals.

[1]Restricted to isotropic backgrounds. Updated now by A. Al-Anboori to allow anisotropic backgrounds such as a VTI model (discussed later). This was done using the additive property of compliances (i.e., simply replacing the isotropic background compliances by anisotropic medium compliances).

Anisotropy due to the alignment of mica minerals of muscovite and chlorite has been measured in two samples of shales from a borehole in the North Sea Valhall field (Casey, 2004). The analysis is based on X-ray texture goniometry (XRTG) using a method described by Valcke et al. (in press). The elastic constants for the Valhall shale samples are shown in Appendix F. They are all similar and all exhibit VTI symmetry with similar levels of shear-wave anisotropy (maximum shear-wave splitting of 10%). An average has been computed to represent the anisotropy due to aligned mica in this shale (matrix shown in Appendix F). The Voigt-Reuss-Hill (VRH) method is used to calculate the elastic constants of the entire shale rock, based on the elasticity of the constituent minerals (Anderson, 1965) (see Appendix E for VRH expressions). The shale is approximately composed of 30% mica minerals and 70% isotropic minerals (Casey, 2004), therefore the anisotropy of the shale aggregate rock is approximately a third of the anisotropy due solely to mica mineral alignment (i.e., 3% anisotropy). Although the Valhall shale may not be identical to the Yibal shale, it is appropriate for illustrating the effects of a background intrinsic anisotropy in our modelling exercise.

The anisotropy due to the micas in the shale is blended with the background isotropic component. This mixing scheme should not change the aggregate P- and S-wave velocities of the rock, v_p and v_s, respectively. The isotropic tensor, $\mathbf{C_I}$, of the background rock is

$$\mathbf{C_I} = \begin{pmatrix} c_{11} & c_{11}-2c_{44} & c_{11}-2c_{44} & 0 & 0 & 0 \\ & c_{11} & c_{11}-2c_{44} & 0 & 0 & 0 \\ & & c_{11} & 0 & 0 & 0 \\ & & & c_{44} & 0 & 0 \\ & & & & c_{44} & 0 \\ & & & & & c_{44} \end{pmatrix}, \tag{4.1}$$

where $c_{11} = v_p^2\rho$, $c_{44} = v_s^2\rho$, ρ is density and v_p and v_s are obtained from a VRH average. $\mathbf{C_I}$ is symmetric and has two independent constants (i.e., isotropy). The elasticity tensor of a rock comprised entirely of mica crystals is denoted $\mathbf{C_M}$. Voigt (1928) averaging approximates the elasticity tensor of a polycrystalline aggregate using the arithmetic mean of the single crystal elastic constants. The Voigt method (which assumes constant strain) is used to compute the elastic tensor of the rock, $\mathbf{C_{R_V}}$ via a scaling of the elastic constants,

$$\mathbf{C_{R_V}} = r\mathbf{C_M} + (1-r)\mathbf{C_{I_V}}, \tag{4.2}$$

where r is the anisotropic scaling ratio and $\mathbf{C_{I_V}}$ is $\mathbf{C_I}$ determined using the Voigt method. The method of Reuss (1929) (which assumes constant stress) is used to obtain the compliance matrix

of the rock, $\mathbf{S}_{\mathbf{R}_\mathbf{R}}$, via a scaling of compliance matrices,

$$\mathbf{S}_{\mathbf{R}_\mathbf{R}} = r\mathbf{C}_\mathbf{M}^{-1} + (1-r)\mathbf{C}_{\mathbf{I}_\mathbf{R}}^{-1}, \tag{4.3}$$

where $\mathbf{C}_{\mathbf{I}_\mathbf{R}}^{-1}$ is $\mathbf{C}_\mathbf{I}^{-1}$ determined using Reuss method. The Hill average for the elastic tensor of the entire shale rock, $\mathbf{C}_\mathbf{R}$, is

$$\mathbf{C}_\mathbf{R} = \frac{1}{2}(\mathbf{C}_{\mathbf{R}_\mathbf{V}} + \mathbf{S}_{\mathbf{R}_\mathbf{R}}^{-1}). \tag{4.4}$$

The program "ani_scale_VR" executes such scaling and, as a QC, checks the Hill aggregate isotropic velocities based on $\mathbf{C}_\mathbf{M}$ and $\mathbf{C}_\mathbf{R}$ are equal. Using ρ=2200 kg/m^3, the Hill based velocity estimates are shown in Table 4.1 and using r=0.3; the estimated elastic constants for the shale are listed in Appendix F. It is worth noting that these values are for a shale rock at standard pressure and temperature (surface conditions). The estimated Hill velocities (Table 4.1) can be considered representative of shale rocks in Yibal as they match those of the shale Fiqa rock (compare with the Yibal velocity model in Figure 1.4).

4.3 Method

4.3.1 Splitting analysis

The anisotropic ray-tracer ATRAK (Guest and Kendall, 1993) is used to generate synthetic seismograms for various elastic models. The methodology of Silver and Chan (1991) is then used to estimate shear-wave splitting. The synthetic data are processed in the same way as real data to determine the splitting parameters. The 3C seismograms are rotated from the geographic ENZ frame to ray coordinates using the P-wave particle motion (described in Section 1.9.1).

If δt is comparable to the pulse-width the S-wave particle motion will be elliptical. A rotation by the ψ and time shift by δt will remove the effects of the anisotropy and linearise the particle motion. Shear-wave splitting analysis is done using the methodology of Silver and Chan (1991) to determine δt and ψ. A grid search over $0 < \delta t \leq 40$ ms and $-90° \leq \psi \leq 90°$ is used to find the δt and ψ which best linearise the S-wave particle motion; the process minimises the second eigenvalue of the covariance matrix. Error estimates come from the 95% confidence interval determined using the F-test (Silver and Chan, 1991).

The estimated ψ in the ray frame is then mapped into the geographic ENZ frame to yield two parameters, strike and dip, that describe the orientation of the fast shear-wave polarisation (Figure 4.1a). I use the strike of the fast-shear vector (Figure 4.1b) and the dip of the fast polarisation

plane (Figure 4.1c). The fast-shear polarisation plane is defined by both the ray vector and the ψ vector. The fast vector was chosen over the fast plane to define the strike due its advantage of accurate recovery of the crack strike (presented in Section 4.9). In a similar manner, error estimates are also mapped into the geographic ENZ frame.

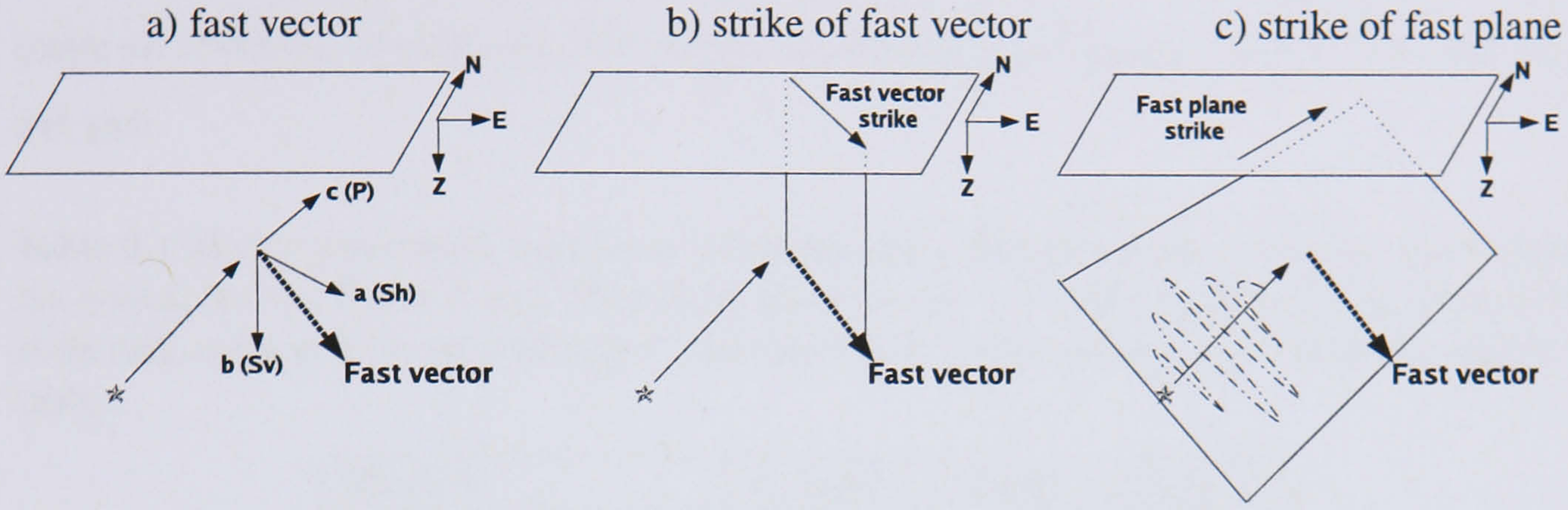

Figure 4.1 Diagrams illustrating the difference between strikes of the fast-shear plane and fast-shear vector. [**a**] Fast-shear vector in the ray frame, [**b**] strike of the fast-shear vector and [**c**] strike of the fast-shear plane. The fast-shear plane is described by the ray vector and the fast vector. The fast-shear vector is confined to the a-b plane.

4.3.2 2D velocity and 3D anisotropy plots

In order to facilitate interpretation, 2D group-velocity plots and 3D anisotropy plots are generated for the various models. The 2D group-velocity plots show cross sections of the group velocities of the fast and slow shear waves as a function of ray azimuth with a user defined dip (cone geometry) or as a function of dip for a constant azimuth (e.g., Figure 4.2) . The 3D plots display the phase velocities of P-waves, and the magnitude of the S-wave splitting and the associated fast-shear-wave polarisations for all directions and plotted on an upper hemisphere projection (e.g., Figure 4.3). The amount of anisotropy is calculated from $100\times(v_{fast}\text{-}v_{slow})/v_{slow}$ where v_{fast} and v_{slow} are velocities of fast and slow shear-waves, respectively.

4.4 Fracture and background models

The modelling is used to investigate the sensitivity of shear-wave splitting measurements to ray direction, fractures and fluid type. In order to simplify things: (1) only vertical cracks are considered (a reasonable assumption in Yibal as indicated from geology), (2) a constant crack aspect ratio, η, and crack density, ε, of 0.001 and 0.05, respectively, are assumed, and (3) the ray distance is always 1300m (an average source-receiver distance for the Yibal data) and the ray azimuth is always 90° unless stated otherwise. The P-wave velocity, v_p, S-wave velocity, v_s,

and density, ρ, for the cracks are listed in Table 4.2.

I first consider cases where I neglect the effect of connectivity between cracks and pores (i.e., equant porosity equals zero). The cases considered are: isotropic chalk with a single set of cracks (unicrack), isotropic chalk with two sets of cracks (bicrack), a VTI shale and a VTI shale with a single set of cracks. In each case, two models are simulated with respect to crack fluid-fill (brine and gas).

Table 4.1 Matrix parameters used for a carbonate and a shale medium. Carbonate input values are typical for the Natih A and Shuaiba chalk reservoirs. † Hill's aggregate velocities of the shale rock using ρ value of 2200 kg/m^3 (see Section 4.2.2 for estimating the elastic constants of shale).

Medium	v_p [m/s]	v_s [m/s]	ρ [kgm^{-3}]
Carbonate (Isotropic)	3500	1800	2400
Shale (VTI)	2220†	1240†	2200

Table 4.2 Crack fluid parameters (surface conditions) used in modelling wave propagation.

Crack fluid type	v_p [m/s]	v_s [m/s]	ρ [kgm^{-3}]
gas	340	0	1
brine	1530	0	1000

4.5 Results

4.5.1 Fractured isotropic medium (carbonate) with a single set of cracks

The first model investigated is a fractured isotropic medium (carbonate) with a single set of cracks. I first consider the simple case of gas filled cracks. Figures 4.2(a,b,c,d) show the splitting measurements (δt, the strike and dip of the fast shear-wave) as a function of crack strike. The ray azimuth is held constant at 90°E. In each figure the ray inclination (from vertical) is 0°, 30°, 60°, 90°, respectively, where 90° is horizontal and 0° is vertical. The 2D group-velocity plots of a medium with a crack strike of 90° are also shown. The amount of anisotropy (time lag), as expected, correlates with the group velocity separation between the fast and slow shear waves (Figure 4.2). The maximum amount of anisotropy is encountered when the ray travels parallel to the crack strike (Figures 4.2(a,b,c,d)).

For a vertical ray, the fast strike is identical to crack strike (dash line in Figure 4.2) showing the crack strike can be accurately recovered. As the direction of ray propagation varies from vertical to horizontal in increments of 30° inclination (Figures 4.2(a,b,c,d)), the fast strike ac-

curately recovers the crack strike except for horizontal ray propagation. Conversely, the crack dip (90° for vertical cracks) is retrieved accurately for horizontal rays (Figure 4.2d). Similarly, as the direction of ray propagation varies from horizontal to vertical, the fast dip becomes a less accurate representation of the crack dip (Figures 4.2(d,c,b,a)). It becomes meaningless for vertical rays (Figure 4.2a) since the fast dip is entirely dependent on the ray inclination (i.e., fast dip is always 90° for a vertical ray). All of above observations can be inferred from the 3D anisotropy plot in Figure 4.3a. The highest amount of anisotropy occurs along the crack strike direction and it gradually dwindles radially from the crack strike to zero anisotropy. Figure 4.3a also shows fast-shear waves polarised E-W (direction of crack strike) for subvertical rays and vertically polarised (i.e., indicating vertical cracks) for horizontal rays in all azimuths.

In Figures 4.3b and 4.4 the cracks are filled with brine, rather than gas. The results are exactly identical for vertical propagation (compare Figures 4.4a and 4.2a). However, for non-vertical propagation, the brine results are more complicated as there is a cross over on the shear-wave sheets (see the group velocity plots in Figure 4.4). The time lag is zero at these singularities and the time lag shows a 3θ variation with azimuth (Figures 4.4(c,d), 4.3b). It affects the fast strike and dip in a way that the true crack strike and dip, respectively, can be retrieved only when the ray propagates within about ±30° of the true crack strike (Figures 4.4(c,d)) because the fast-shear-wave alters its polarisation from vertical to horizontal across the cross-over point (Figure 4.3b).

The gas-filled fracture case does not exhibit the shear-wave sheet cross-over, seen in the brine case. Therefore, such effects may be a useful fluid indicator. In both tested fluid types, the crack strike and dip can be recovered reliably from subvertical and subhorizontal rays, respectively. However, in the brine case the crack dip must be inferred from the region of maximum anisotropy (shear-wave splitting).

4.5.2 Fracture isotropic medium (carbonate) with two sets of cracks

In this case, two sets of cracks (with crack strikes of 50° and 130°) are embedded in the isotropic carbonate medium. The 3D anisotropy plots for this model with gas and brine filled cracks are displayed in Figures 4.3(c,d), respectively. Figures 4.5(a,b), respectively, show the splitting measurements as a function of ray azimuth for horizontal ray propagation. Due to horizontal ray propagation, the fast strike plots are meaningless. Similar to the results for a single set of cracks, the bicrack model results are simpler for gas than brine due to the absence of shear-wave sheet cross overs.

In the simpler gas case, the fast dip is always indicative of crack dip (Figure 4.5a). Figure 4.5a also shows two peaks in the magnitude of shear-wave splitting (time lag) that correspond to each crack-set strike. Therefore the true crack strikes can be retrieved from ray azimuths where two anisotropy peaks occur. These two peaks are reasonably well separated (Figures 4.3c and 4.5a) but it is not clear that this separation will be discernible in real data. It will be difficult to detect the existence of two crack sets when their strikes are close together.

In the more complicated brine case, the percent anisotropy (time lag) shows a 4θ variation with ray azimuth for horizontal ray propagation, again due to S-wave sheet cross overs (Figure 4.5b). Similar to the gas case, Figure 4.3d shows that two anisotropy bulges are aligned with the true crack-set strikes but in this case there are also other anisotropy maxima (see Figure 4.5b). However at a 60° ray inclination, the percent anisotropy shows a 2θ variation with azimuth, where the peaks correspond to the individual crack strikes (Figure 4.3d). Therefore, subhorizontal propagation is required to infer the strike of multiple cracks. Similar to the brine-filled unicrack model, Figure 4.5b shows fast dip as an indicator of crack dip as long as the recording azimuth is near the individual crack strikes (i.e., between the S-wave cross overs that bound each crack set). Outside these regions, the horizontally polarised shear-waves are faster than vertically polarised shear-waves.

For vertical ray propagation in both the gas and brine-filled bicrack models, the fast strike is identical and show a strike that is an average of the two crack strikes, weighted by their crack aspect ratios and densities (Figure 4.3d). For instance, for 50° and 130° strikes, the average is 90° (Figure 4.3d). Cumulatively, these results suggest that detecting multiple fracture sets will require high quality data with a good ray direction coverage.

4.5.3 VTI medium (shale)

Elastic constants for the shale model are computed in Section 4.2.2. Figure 4.6 shows the splitting measurements in this VTI medium as a function of ray inclination and Figure 4.7a shows the 3D anisotropy plot. The Figures show that horizontally polarised shear-waves are always faster than vertically polarised shear-waves in this VTI model with percent anisotropy gradually increasing from zero at vertical incidence to maximum anisotropy at horizontal incidence. In general, horizontally polarised fast-shear-waves propagating horizontally can be used as an indicator for VTI media.

4.5.4 VTI medium (shale) plus single set of cracks

A single set of vertical fractures is added to the VTI model to form an orthorhombic medium whose HTI(vertical cracks)/VTI S-wave anisotropy ratio is about 5/3 (for both gas and brine). The splitting measurements as a function of crack strike for this model with gas-filled cracks are shown in Figures 4.8(a,b) for ray inclinations of 90° and 60°, respectively. Similarly, Figures 4.8(c,d) show the case for gas-filled cracks. Figures 4.7(b,c) show the 3D anisotropy plots for gas and brine filled cracks, respectively.

Figure 4.8 show that the gas case is simpler than the brine one, but both exhibit similar cross over features for horizontal wave propagation. For vertical wave propagation the fast strike indicates the crack strike in both models (Figures 4.7(b,c)). In weakly HTI regions and horizontal wave propagation, the VTI symmetry can dominate producing larger δt values than those predicted by the crack models (compare Figures 4.7(b,c) with HTI Figures 4.3(a,b) and VTI Figure 4.7a).

4.6 Key observations

In the case of an isotropic medium, fractured with a single set of cracks:

- Vertical wave propagation is only useful for estimating crack strike, horizontal propagating rays should not be used to estimate crack strike (Figures 4.2a and 4.4a).

- Horizontal wave propagation is only useful for estimating crack dip, vertical propagating rays should not be used to estimate crack dip (Figure 4.2d). In brine-filled cracks, only ray azimuths in the region of maximum anisotropy can be used to retrieve the crack dip correctly (Figure 4.4d).

- Horizontal wave propagation can be useful for estimating crack fluid type (brine versus gas) by considering the number of anisotropy minima points (corresponding to S-wave cross-over points). 1θ and 3θ variations in the anisotropy response with azimuth indicate gas and brine-filled cracks, respectively (Figures 4.2d, 4.4d and 4.3(a,b)).

In the case of the Valhall shale VTI medium:

- In the Valhall model the fast-wave is always horizontally polarised for horizontal wave propagation. In other shales the horizontally polarised shear-wave is fastest, but shear-wave surface cross overs can occur with more vertically propagating rays (Caddick et

al., 1998). In the Valhall samples the percent anisotropy increases from zero at vertical incidence to maximum at horizontal incidence. As with any VTI medium there is no azimuthal variation in splitting parameters (see Figure 4.7a).

In the case of VTI plus a single set of cracks:

- There is a trade-off between HTI and VTI properties depending on the relative strength of each component. Pure HTI and pure VTI media have maximum anisotropy in vertical and horizontal planes, respectively. Thus when blended, HTI and VTI properties can be retrieved by studying vertical and horizontal rays, respectively (compare Figure 4.7 with 4.3(a,b)).

- Generally (when both have similar weights), vertical wave propagation is a useful indicator of crack strike (Figures 4.7(b,c)).

- Generally (when both have similar weights), horizontal wave propagation is a useful indicator of VTI symmetry from horizontally polarised fast-waves (Figures 4.7(b,c)).

In the case of an isotropic medium fractured with 2 sets of cracks (of equal ε and η):

- Horizontal propagation may be used as fluid-type indicator (using cross-over points) and for individual crack strike estimates as follow. For nearly all ray inclinations, percent anisotropy variation of 1θ and 2θ with ray azimuth demonstrate gas and brine-filled cracks, respectively (Figures 4.3(c,d)). Ray azimuths having the two maximum anisotropy bulges are indicative of individual crack set strikes (Figures 4.3(c,d)).

- For vertically propagating rays, the fast strike retrieves the average value of the two crack strikes (Figures 4.3(c,d)). Therefore, this can be utilised as a QC on the retrieved two crack strikes from subhorizontal rays.

4.7 Burial effects

The previous modelling was based on crack properties at surface conditions. In reality, reservoirs are buried. Burial effects on liquid-filled cracks are negligible because liquids are incompressible. However, changes of anisotropy behaviour can occur when gas-filled cracks are buried in a reservoir, due to the high compressibility of gas. Therefore, the burial effect of gas-charged rocks is examined in this section.

Table 4.3 shows the incompressibility (k_f), viscosity, P-wave velocity (v_p) and density (ρ) of fluids at Natih and Shuaiba reservoir levels. The calculation is based on Gassmann theory (Avseth et al., 2005), using average measured 2002 Natih and Shuaiba reservoir pressures of 7000 KPa and 13000 KPa, respectively (Guy Mueller and Cees Van der Schans, PDO, pers. comm., Feb2004). The burial effect on gas density is more obvious than those for the brine case (compare burial and surface parameters in Tables 4.3 and 4.2). The shear-wave splitting modelling was repeated for the gas-filled unicrack and bicrack models both with an isotropic and VTI background. The parameters in Table 4.4 are used to test the burial effect of gas-saturated rocks. The predicted splitting measurements for horizontal rays are shown in Figures 4.9(a,b,c).

The effects of burial are also shown in 3D anisotropy plots in the 2nd column of the summary Figure 4.10. The Figures 4.9(a,b,c) show changes due to burial effect but they are not very pronounced (compare with Figures 4.2d, 4.5b and 4.8c). Similar small changes are apparent in the corresponding 3D anisotropy plots (Figure 4.10). In particular, the cylindrical region of maximum δt in the unicrack model is slightly shorter (Figures 4.9b and 4.10b). In a bicrack model, the two δt peaks are more pronounced (Figure 4.10, compare Figure 4.9b with 4.5b). In a unicrack VTI model, it behaves nearly as if the cracks are filled with brine (compare gas and brine-filled unicrack VTI media in Figures 4.10(m,n)). It is somewhat that the observed burial effects are not substantial. I conclude that the key observations for models under surface conditions can be applied to buried rocks.

Table 4.3 Pore fluid parameters at Natih and Shuaiba levels based on Gassmann theory (Avseth et al., 2005). Reservoir pressure values are as measured in 2002. Gas undersaturated oil is assumed for oil parameter estimates. Compare with surface pressure conditions (Table 4.2).

Fluid	Reservoir	Pressure [MPa]	k_f [GPa]	Viscosity [Pa.s]	v_p [m/s]	ρ [kgm^{-3}]
gas	Natih	7.0	0.006	1.36×10^{-5}	341	57
brine	Natih	7.0	2.30	4.36×10^{-4}	1527	985
brine	Shuaiba	13.0	2.37	4.54×10^{-4}	1551	988
oil	Shuaiba	13.0	1.90	6.85×10^{-4}	1431	965

Table 4.4 Crack fluid parameters under burial.

Crack fluid type	v_p [m/s]	v_s [m/s]	ρ [kgm^{-3}]
gas	341	0	57
brine	1527	0	985

4.8 Porosity effect

The previous modelling has neglected the effect of fluid flow between cracks and equant porosity. It is well known that this effect alters the response of cracks to an applied stress depending on crack dimensions, frequency of the waves sampling the cracked medium, and viscosity (Thomsen, 1995; Hudson et al., 1996). In this study, the pore-crack fluid connectivity effect on buried rocks has also been examined by considering a porosity of 0.35 and permeability of 25 mD (typical values for the chalk reservoirs in Yibal, see Chapter 2) in the isotropic chalk matrix. The shale cap rocks (VTI media) are impermeable and therefore remain unaffected. I consider a typical S-wave frequency in Yibal microseismic dataset of 40 Hz. I also use a crack aperture of 2×10^{-3} m. This corresponds to η of 0.001 with the 2 m crack size in the Natih A reservoir as determined from frequency-dependent anisotropy analysis in Chapter 6). I use viscosities of gas and brine as shown in Table 4.3. The parameters used to test the effect of fluid interconnectivity between pore spaces and cracks are summarised in Table 4.5.

The resulting 3D anisotropy plots are shown in the 3rd column of the summary Figure 4.10. It shows that buried porous cracked media with both brine and gas-filled cracks are identical and behave as the nonporous gas-filled models at surface conditions (i.e., the S-wave sheet cross overs no longer exist in the brine case). Furthermore, the v_p anisotropy plots for both the unicrack and bicrack models are identical (identical to gas case plots in Figure 4.3). In this case the similarity between the gas and brine results makes pore-fluid identification difficult. The gas-filled cracked VTI case is similar to the brine case, also rendering pore-fluid identification difficult. However, the corresponding v_p anisotropies (not shown here) are not similar and could perhaps be used as a pore-fluid indicator. Cumulatively, the modelling results show that interpretations of S-wave splitting can be guided by predictions for gas-filled cracks if the matrix is porous (and permeable) and the cracks are communicating with each other. In the case of isolated cracks in a non-porous matrix, the results for gas and brine are different suggesting that S-wave splitting can be used as a fluid indicator.

Table 4.5 Parameters used when including equant porosity in the shear-wave splitting modelling. Values are typical for the Yibal field and the microseismic dataset. Viscosities are as shown in Table 4.3.

Freq. of seismic wave [Hz]	Porosity	Permeability [D]	Crack aperture [m]
40	0.35	0.025	2×10^{-3}

Crack fluid type	Viscosity [Pa.s]
gas	1.36×10^{-5}
brine	4.4×10^{-4}

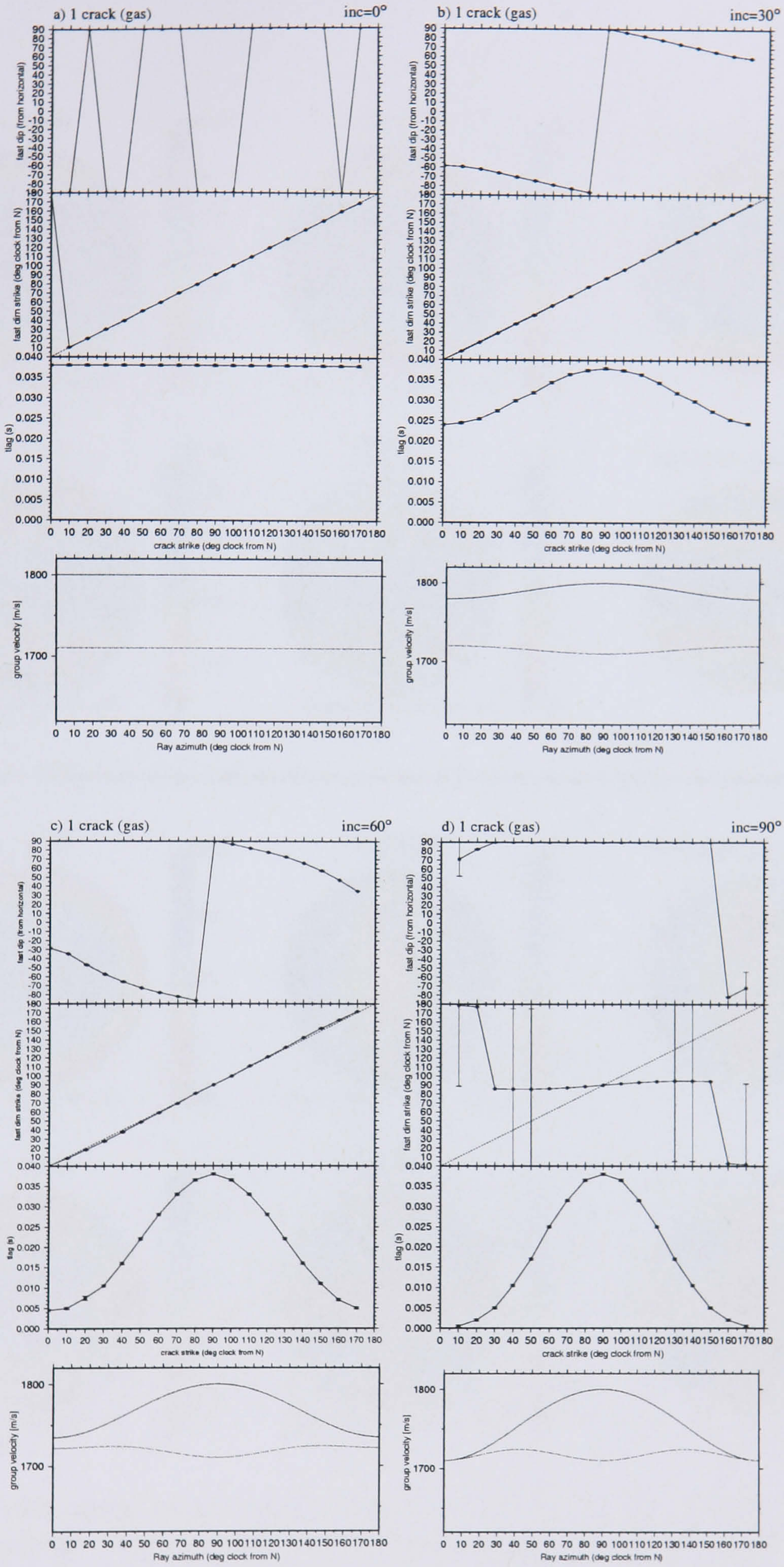

Figure 4.2 [**Top** to **bottom**] Fast shear-wave dip and strike, and lag time as a function of crack strike, and group-velocities for an isotropic chalk medium fractured with a single set of vertical gas-filled cracks. The results are shown for ray inclinations of [**a**] 0°, [**b**] 30°, [**c**] 60° and [**d**] 90°. Crack strike is 90°(from N) in the group-velocity plots. The dashed line shows where fast strike is identical to crack strike. The fast dip and strike plots are meaningless in (a) and (d), respectively. Note the perfect recovery of both crack strike for vertical rays in (a) and crack dip for horizontal rays in (d).

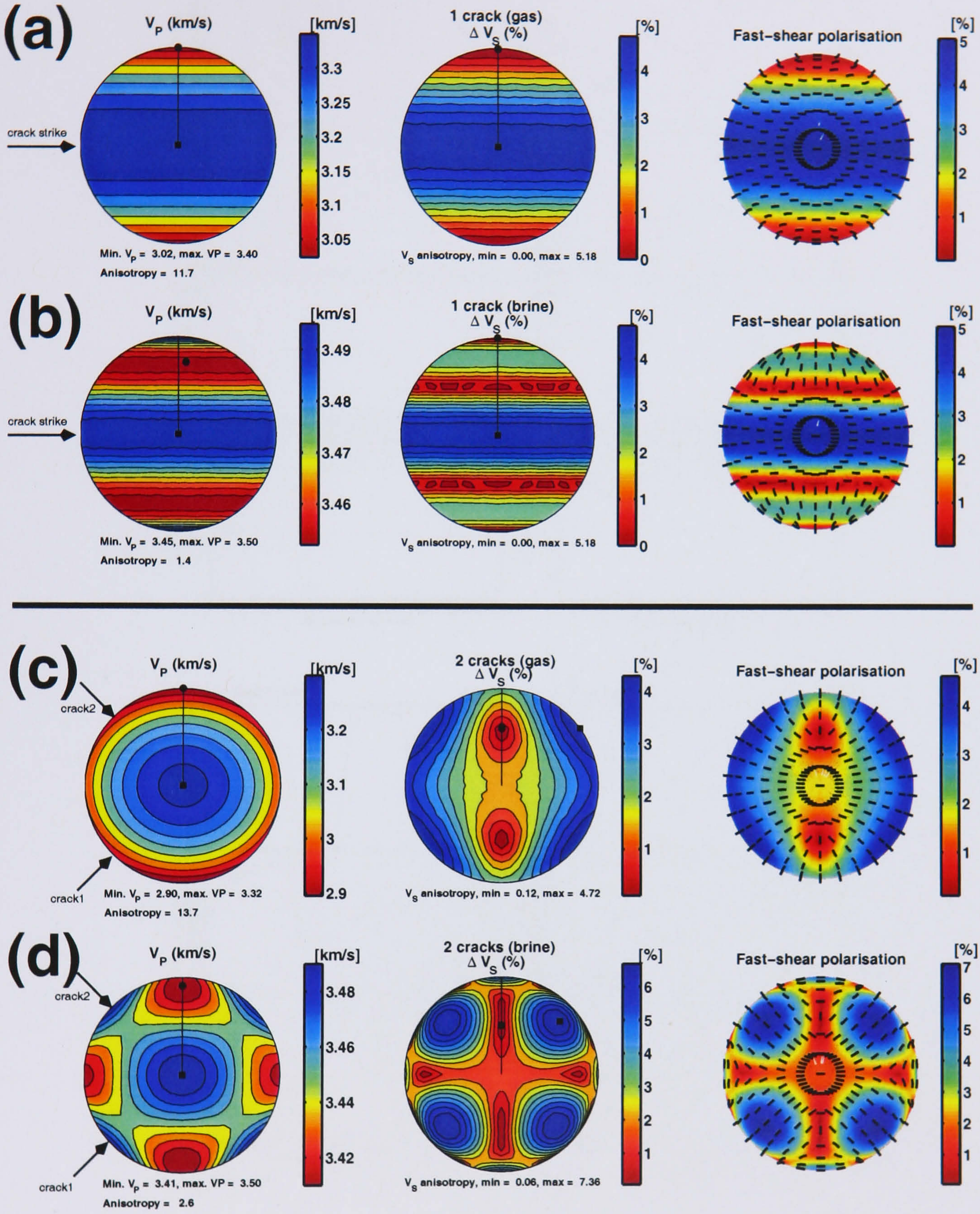

Figure 4.3 3D plots (upper hemisphere projection) of anisotropy for a fractured isotropic chalk with [**a,b**] a single set of vertical cracks with 90° strike and [**c,d**] two sets of vertical cracks with strikes of 50° and 130°. [**a,c**] Show the cases for gas-filled cracks whilst [**b,d**] show the cases for brine-filled cracks. Left column: P-wave velocity contour plot, middle column: S-wave splitting contour plot and right column: same as middle column but with fast-shear polarisation vectors shown.

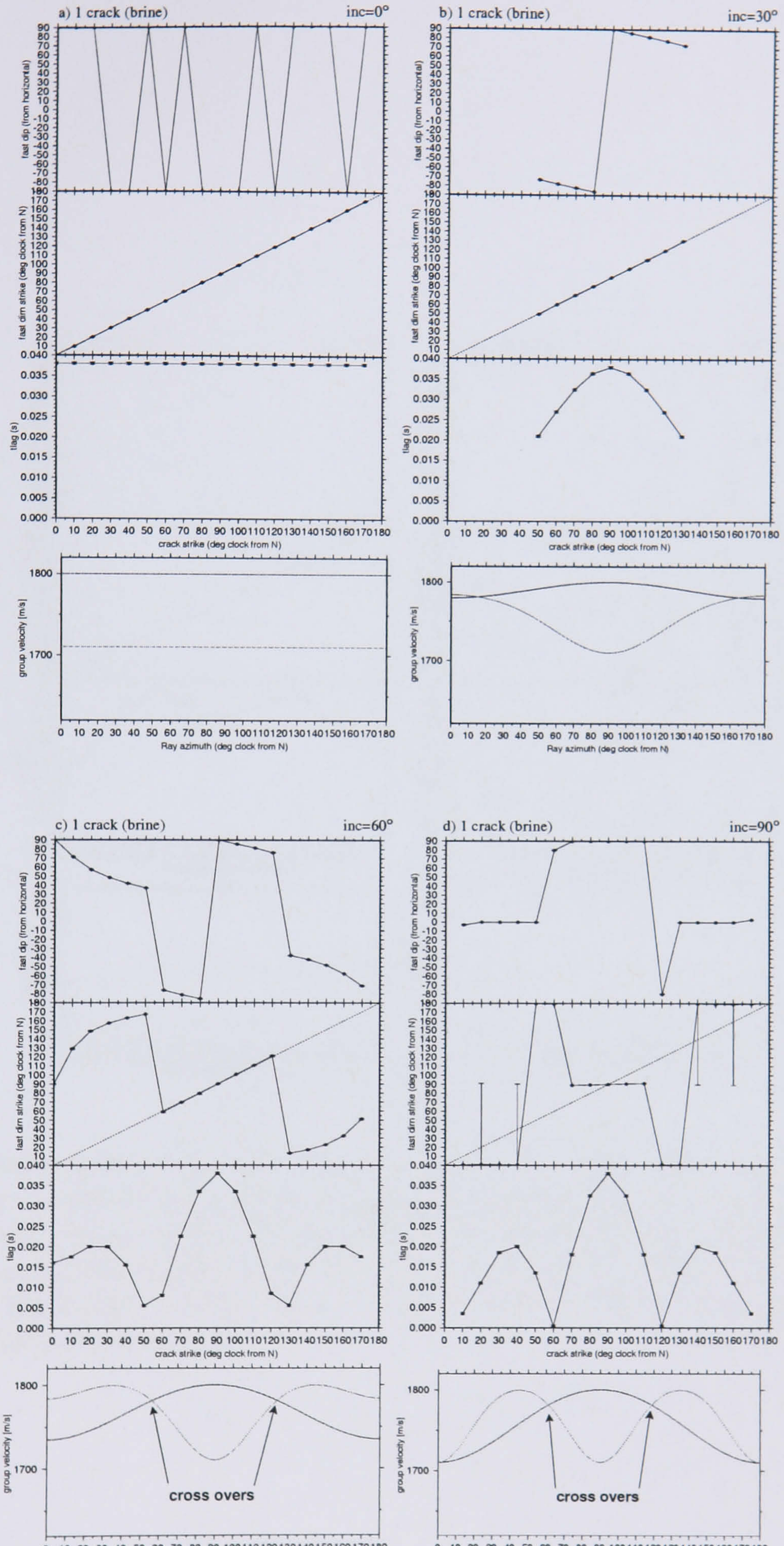

Figure 4.4 Same as Figure 4.2 for single set of brine-filled cracks. Note the fast dip and strike plots are meaningless in (a) and (d), respectively.

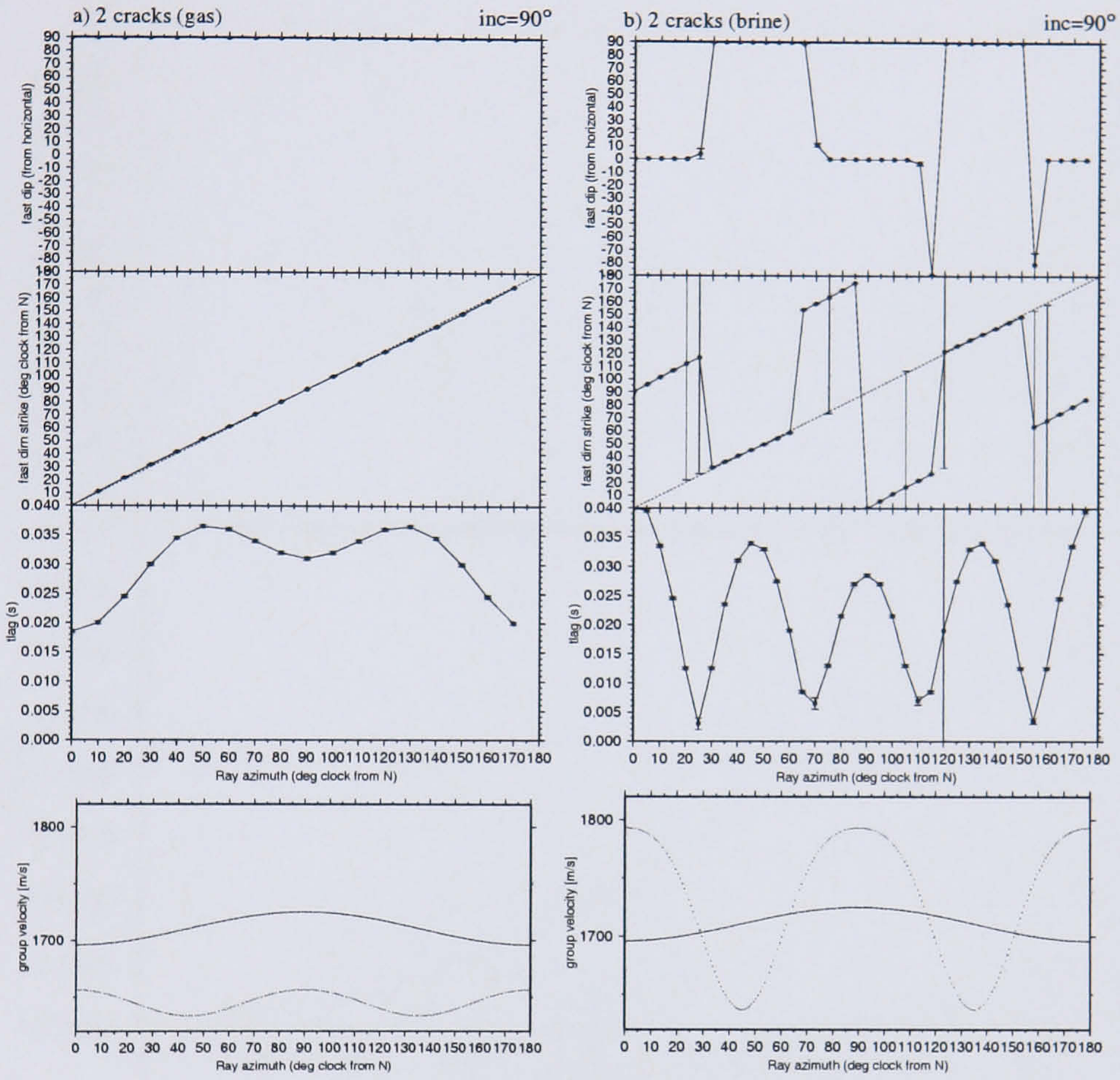

Figure 4.5 [**Top** to **bottom**] Fast shear-wave dip and strike, lag time and group-velocities as a function of ray azimuth for an isotropic chalk medium fractured with two sets of vertical cracks with 50° and 130° strikes. [**a**] Shows the gas-filled case and [**b**] shows the brine-filled case. The results are for a ray traveling horizontally (i.e., 90° ray inclination). Note the fast-strike plots are meaningless. The fast dip in (a) is constant at +90° so they are placed at the border line of the plot making them difficult to view.

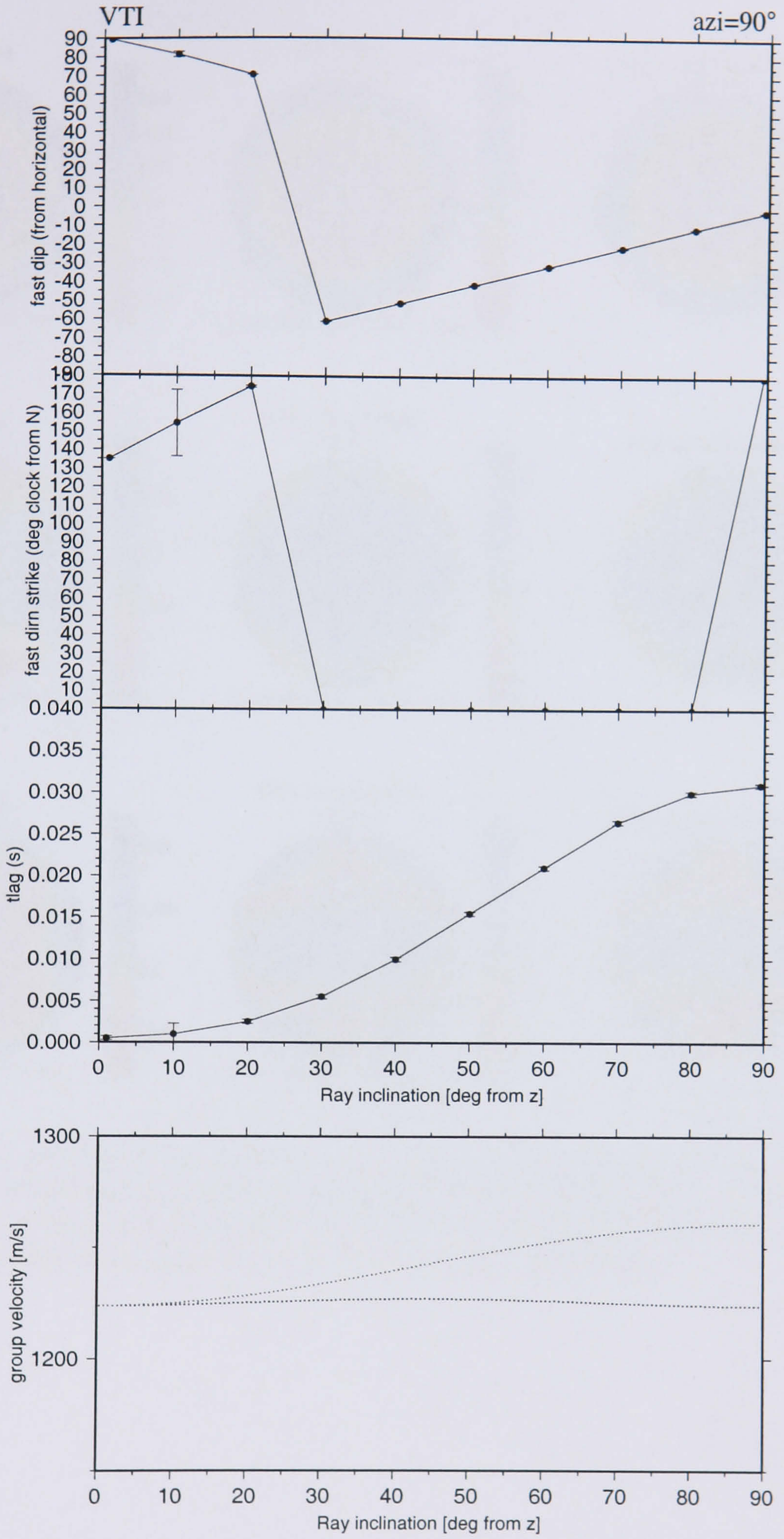

Figure 4.6 [**Top** to **bottom**] Fast shear-wave dip and strike, lag time and group velocities as a function of ray inclination for a VTI shale model. 0° inclination refers to vertical wave propagation and 90° refers to horizontal.

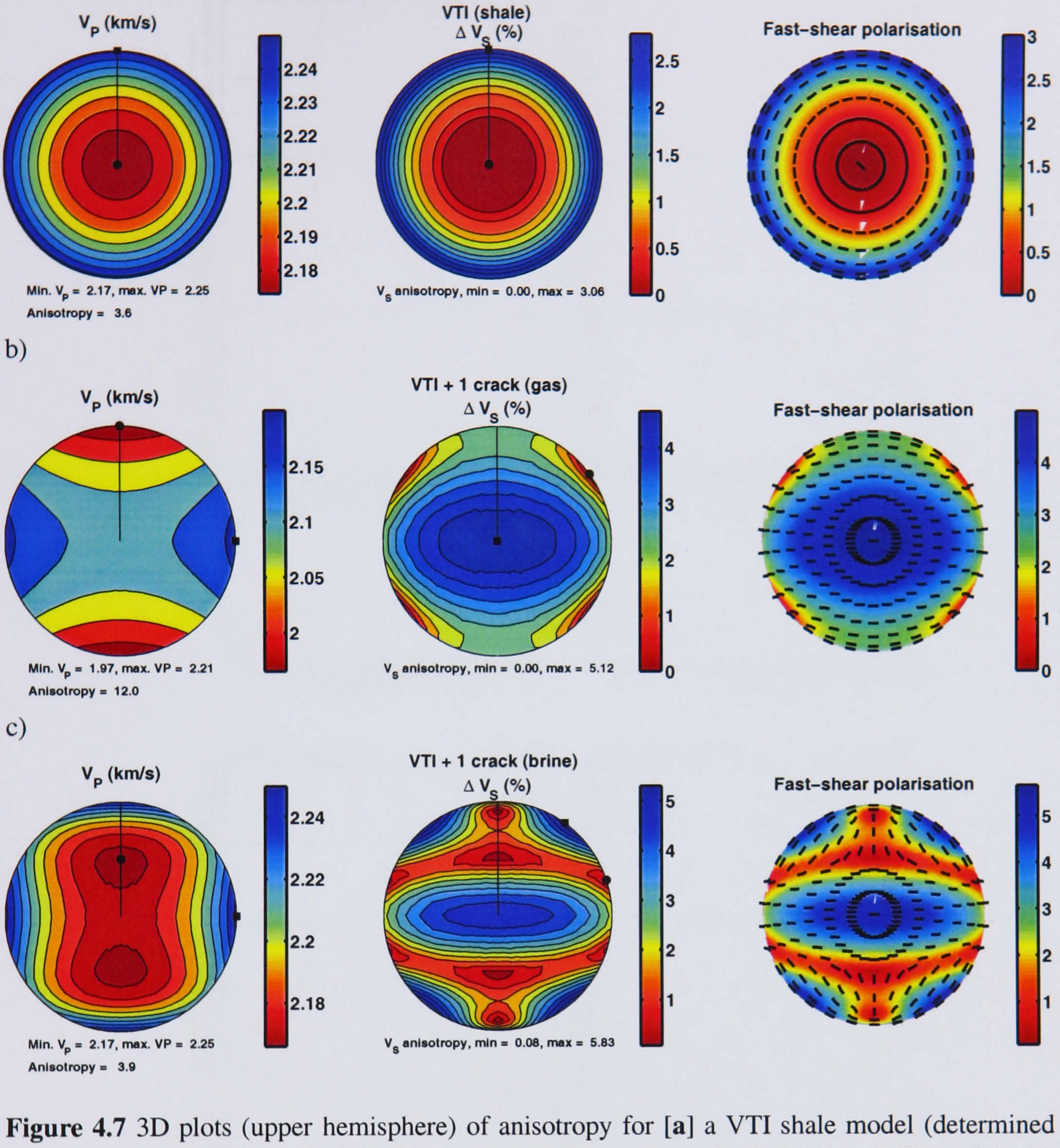

Figure 4.7 3D plots (upper hemisphere) of anisotropy for [**a**] a VTI shale model (determined from XRTG measurements on shale chippings from the Valhall field), [**b,c**] the VTI model with a single set of vertical cracks of η and ε of 0.001 and 0.05, respectively, filled with [**b**] gas and [**c**] brine. The crack strike is 90°. Refer to Figure 4.3 for plot description.

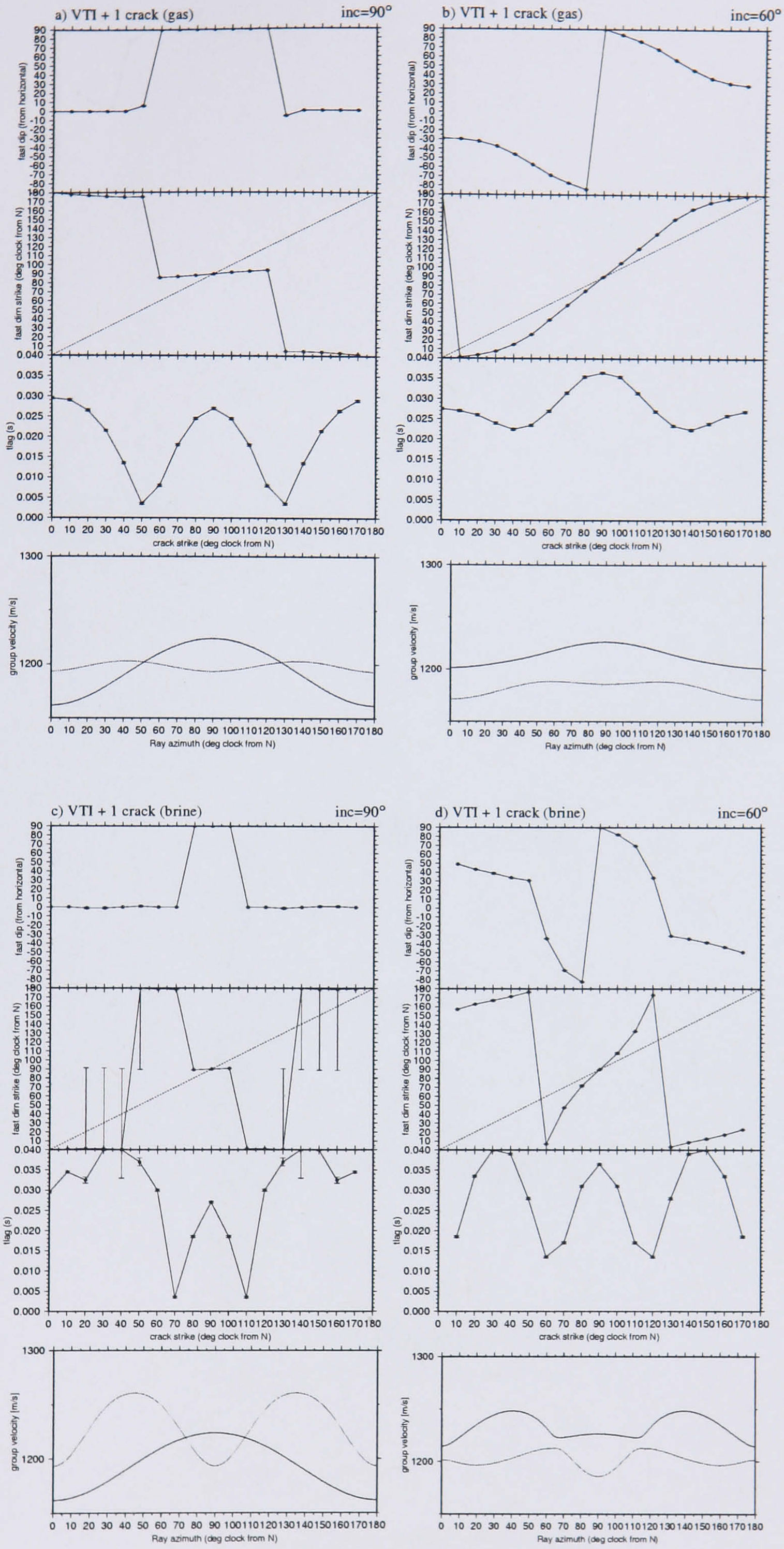

Figure 4.8 [**Top** to **bottom**] Fast shear-wave dip and strike, and lag time as a function of crack strike and group-velocities for the VTI shale model with a single set of vertical cracks. [**a,b**] Show results for gas-filled fractures, whilst [**c,d**] show brine-filled results. [**a,c**] Show results for ray inclinations of 90° (horizontal) and [**b,d**] show results for 60° ray inclinations. Crack strike is 90° in the group-velocity plots. Note the fast-strike plot is meaningless in (a) and (c).

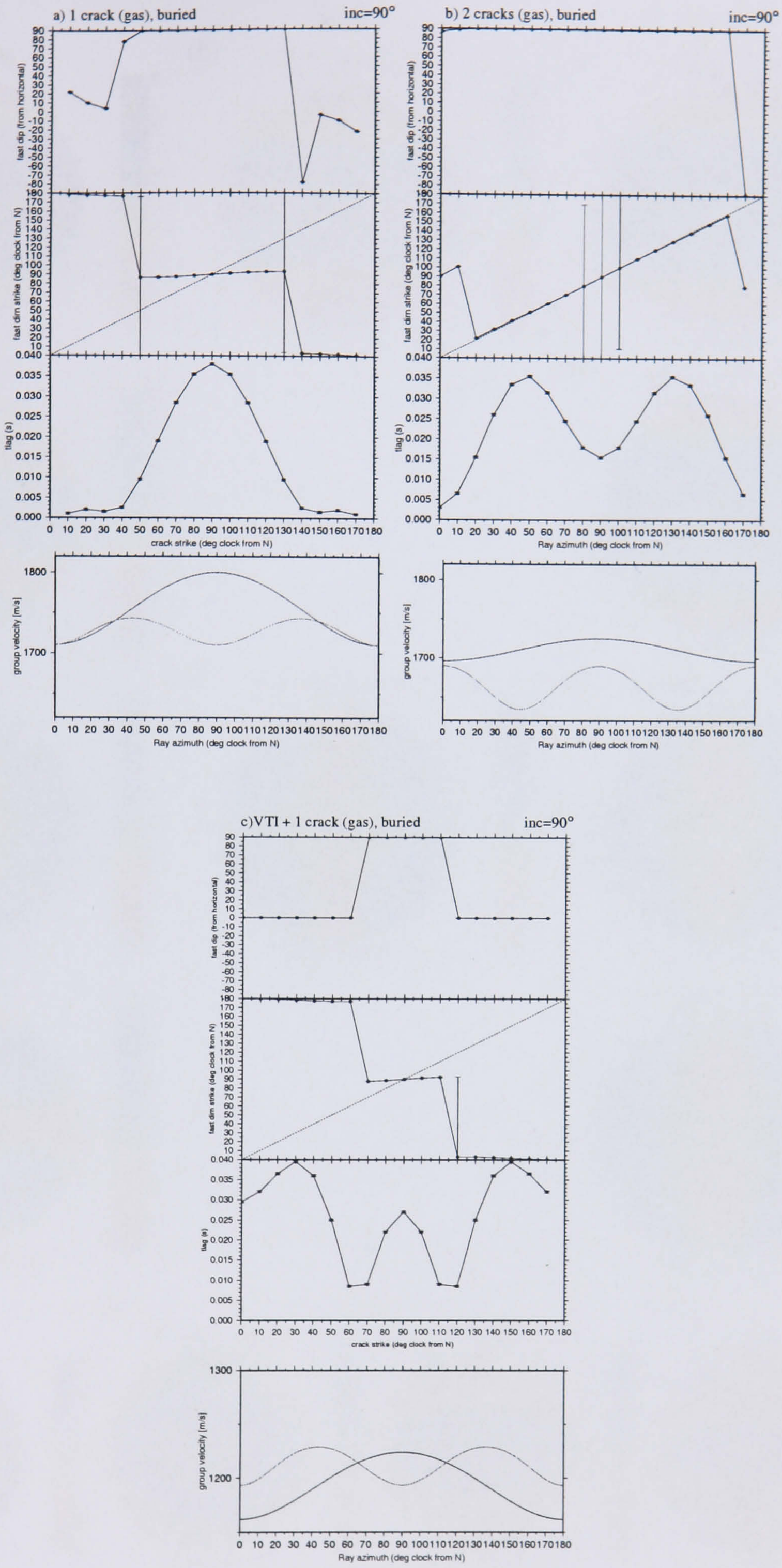

Figure 4.9 The effect of burial. [**Top** to **bottom**] Fast shear-wave dip and strike, lag time and group-velocities for a horizontal ray propagating through [**a**] the unicrack isotropic-chalk model, [**b**] the bicrack isotropic-chalk model and [**c**] the unicrack VTI-shale-matrix model. In all cases the cracks are gas-filled and under buried conditions. The bicrack model has 2 sets of vertical cracks with strikes of 50° and 130°. Note the fast-strike plots are meaningless. Compare (a) with Figure 4.2d, (b) and with Figure 4.5b, and (c) with Figure 4.8c.

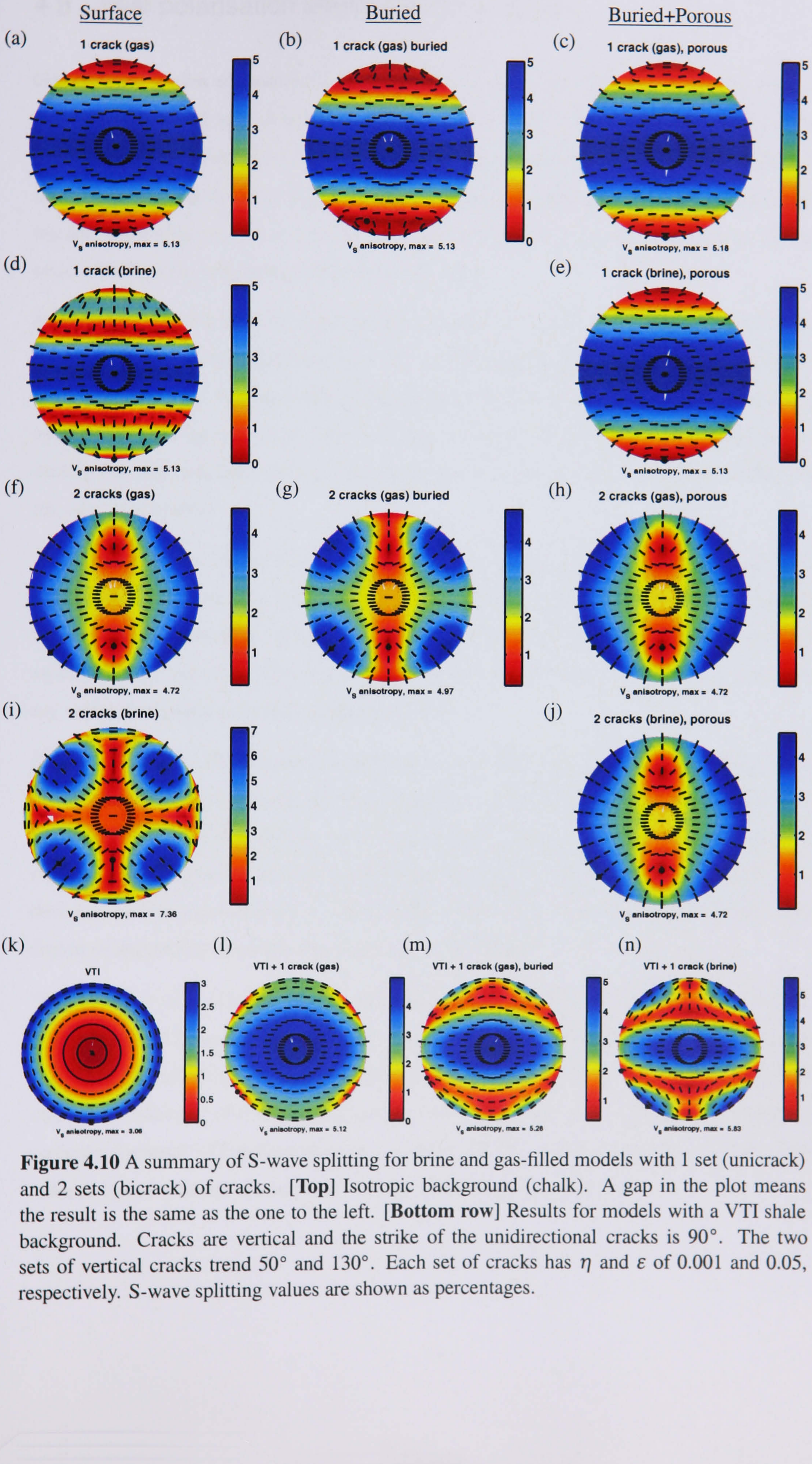

Figure 4.10 A summary of S-wave splitting for brine and gas-filled models with 1 set (unicrack) and 2 sets (bicrack) of cracks. [**Top**] Isotropic background (chalk). A gap in the plot means the result is the same as the one to the left. [**Bottom row**] Results for models with a VTI shale background. Cracks are vertical and the strike of the unidirectional cracks is 90°. The two sets of vertical cracks trend 50° and 130°. Each set of cracks has η and ε of 0.001 and 0.05, respectively. S-wave splitting values are shown as percentages.

4.9 Fast polarisation strike: plane vs vector

Conventional studies of shear-wave splitting deal with near vertical wave propagation and assume a simple set of vertical fractures. In such case it is easy to relate the polarisation of the fast-shear wave to the dominant crack strike (e.g. Bokelmann and Harjes, 2000). This is routinely done by considering the strike of the fast-shear polarisation plane defined by the ray vector and the fast vector (Figure 4.1c). In cases of arbitrary ray direction and crack orientation it is not as easy to interpret the geographical orientation of cracks.

In order to better interpret the geographical orientation of cracks I consider the strike of the polarisation vector (rather than the strike of the polarisation plane used in conventional interpretation, see Figure 4.1 for a geometrical illustration of the two terms). So far in our modelling I used the strike of the fast vector. Now I test the robustness of our strike parameter (of the fast vector) over the traditional strike (of the fast plane) in assessing the fracture strike in HTI and fractured VTI models.

Figure 4.11A shows the fast plane and vector strikes for various ray inclinations in a buried porous unicrack model. The fast vector strike accurately recovers the crack strike for nearly all ray orientations (except horizontal ray propagation). In contrast the fast plane strike estimates steadily deteriorates from vertical to horizontal propagation (Figure 4.11A). This is due to the ray vector component in the fast polarisation plane.

Similarly, Figure 4.11B shows the fast plane and vector strikes for various ray inclinations in the buried porous fractured VTI model with a single set of gas-filled cracks. The recovery of crack strike by the strike of both the fast vector and the fast polarisation plane degrades at about 60° ray inclination (Figure 4.11B). The degradation increases with increasing ray inclination. The deviation of fast vector strike from crack strike is due to the VTI component. Therefore, the degree of degradation increases with increasing VTI strength.

The fast vector strike provides a better estimate of crack strike than the polarisation plane does. In fact in pure HTI media, it refers exactly to the crack strike for nearly all ray orientations (up to 85° ray inclinations). For crack models with a VTI background the reliability of fast vector strike as an indicator of crack strike decreases with increasing VTI strength. For example, in vertically fractured VTI media with similar weights of HTI and VTI components, the fast vector strike is a good estimate of crack strike for ray inclinations only up to 60°.

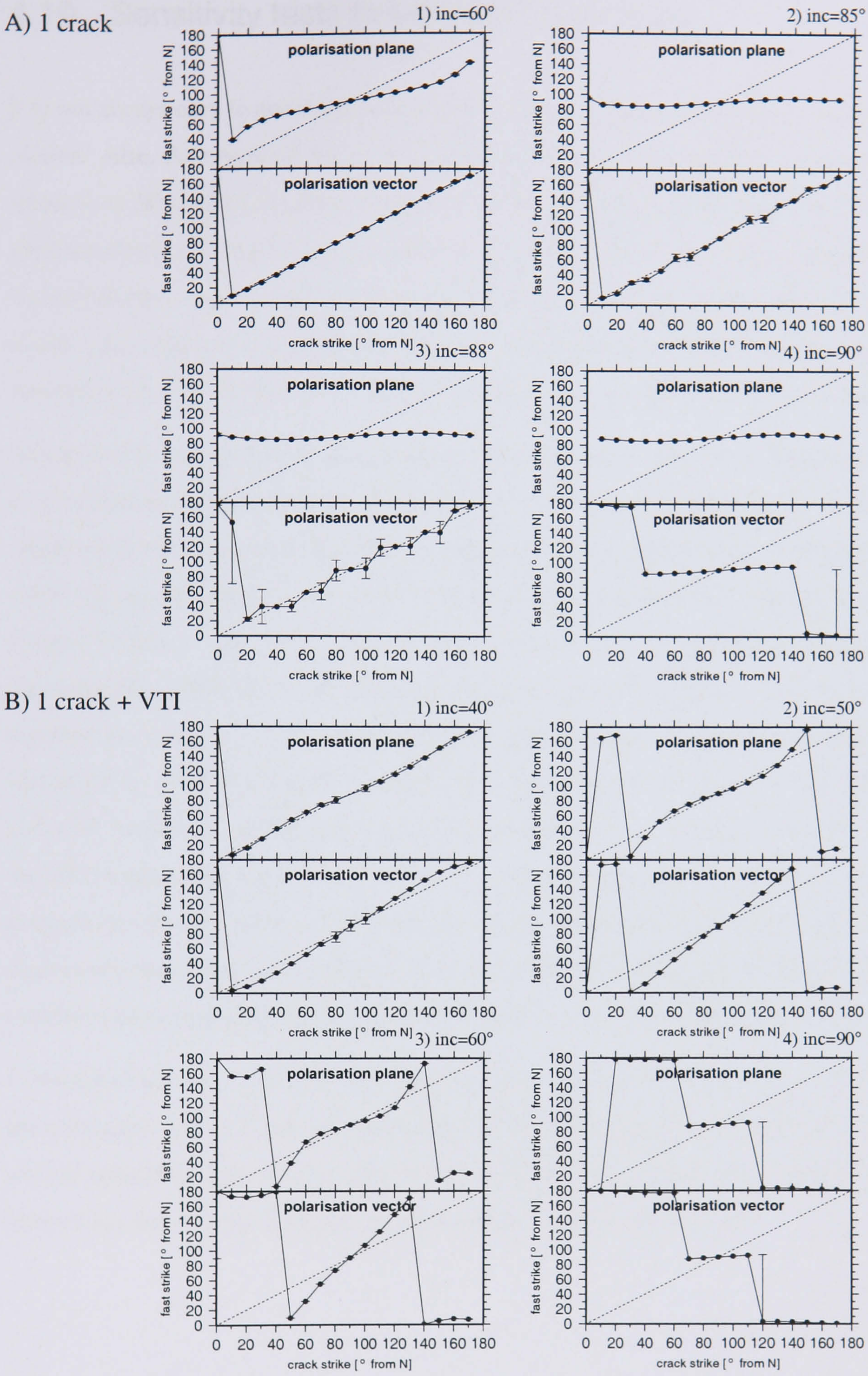

Figure 4.11 Comparison of using the polarisation vector versus the polarisation plane of the fast-shear wave for recovering the true crack strike. Fast shear-wave strike plots of [**top**] fast polarisation plane and [**bottom**] fast polarisation vector for various ray inclinations in [**A**] the unicrack isotropic model and [**B**] the unicrack VTI model. The results are for gas-filled cracks in porous media but can also be applied to brine as both behave similarly in porous media. In (A), note the advantage of using the strike of the fast polarisation vector over polarisation plane in accurately retrieving the true crack strike for pure HTI media.

4.10 Sensitivity tests to errors in ray direction

It is not always easy to accurately determine the ray orientation from the P- or S-wave particle motion. Also, the raypath between the source and receiver may deviate from a straight line in response to 3D velocity structure. Therefore sensitivity tests are conducted to determine to what accuracy the ray orientation angles need to be specified to obtain accurate measurements of time lag (δt) and fast vector strike (ψ). Tests were carried out using the buried porous fractured chalk model with a single set of vertical cracks. The upper limit of ray inclinations that are useful for estimating the crack strike (60°) is tested. Therefore, the calculated errors are an upper bound.

Figures 4.12(a to f) display the estimated fast vector strike due to ±20° perturbations (solid line) in ray orientation angles (errors in azimuth (a,b) or inclination (c,d) or both (e,f)). Incorrect ray angles yield errors in fast strike that (1) vary with the true crack-strike/ray-azimuth separation angle, (2) appear symmetric in ray azimuth (under and overestimated produce the same error, Figures 4.12(a,b), respectively), and (3) appear asymmetric in ray inclination (under and overestimated produce different errors, Figures 4.12(c,d), respectively). Errors in ray azimuth of ±20° can produce errors up to 15° in fast strike (Figures 4.12(a,b)). Under and overestimation of ray inclination by ±20° can lead to fast strike errors up to 7° and 27°, respectively. Errors of -20° and +20° in both ray azimuth and inclination generate even larger fast strike errors of up to 18° and 38°, respectively. Figure 4.12g shows δt in the extreme case of incorrect ray angles of 85°. It shows that δt is insensitive to errors in ray angles. Although the fast or slow shear energy becomes extremely weak in a nearly 90° incorrectly rotated seismogram, the signal always stands out above noise background and, therefore, leads to a successful splitting measurement.

I conclude from these tests that underestimated ray angles lead to less errors in fast strike than overestimated. In the worst case (depending on the relative angle between the true crack strike and ray azimuth), errors in ray angles of +20° leads to errors in fast strike estimates of about 40°. Conversely, the time lag is insensitive even to large errors in ray angles.

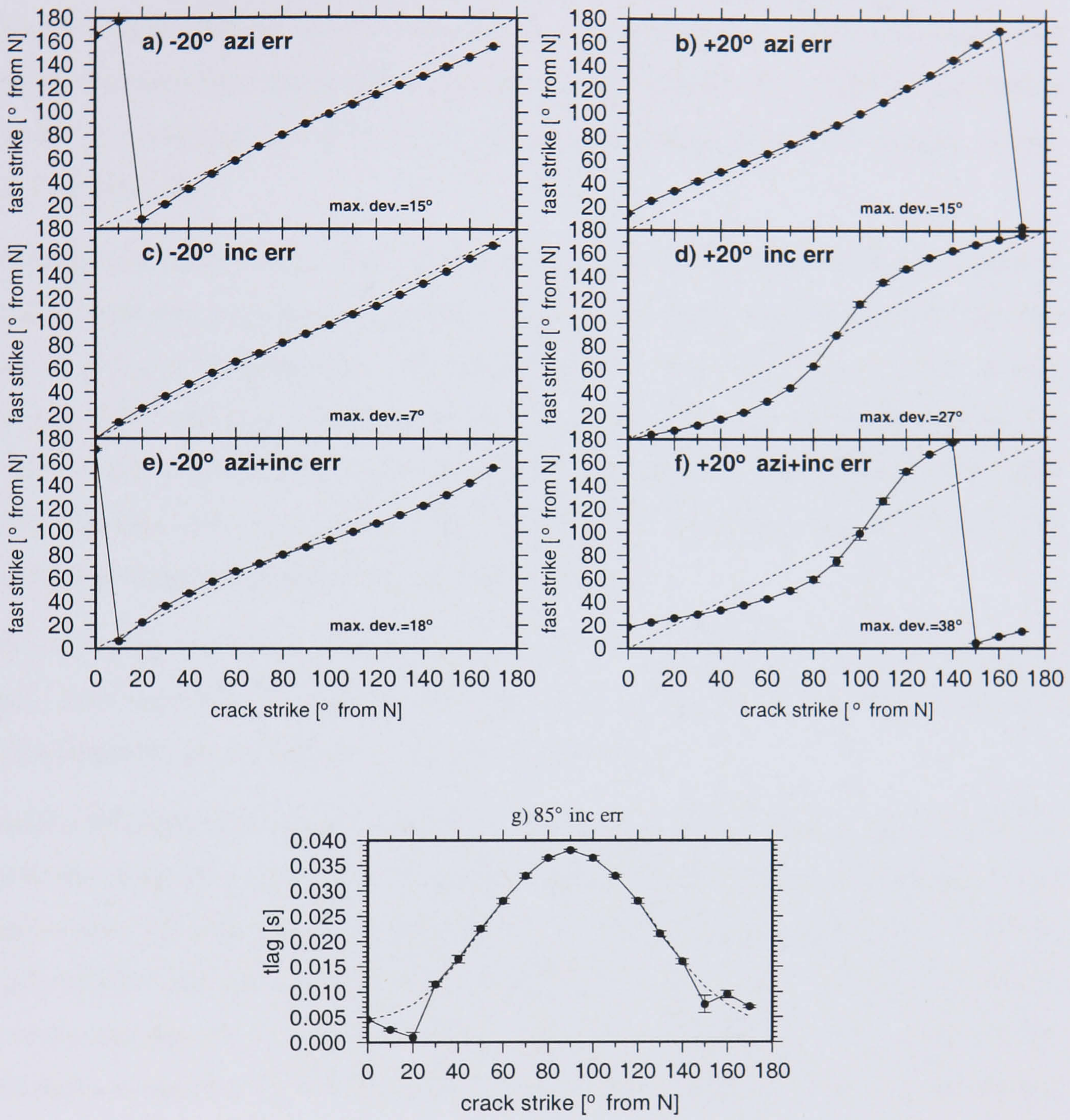

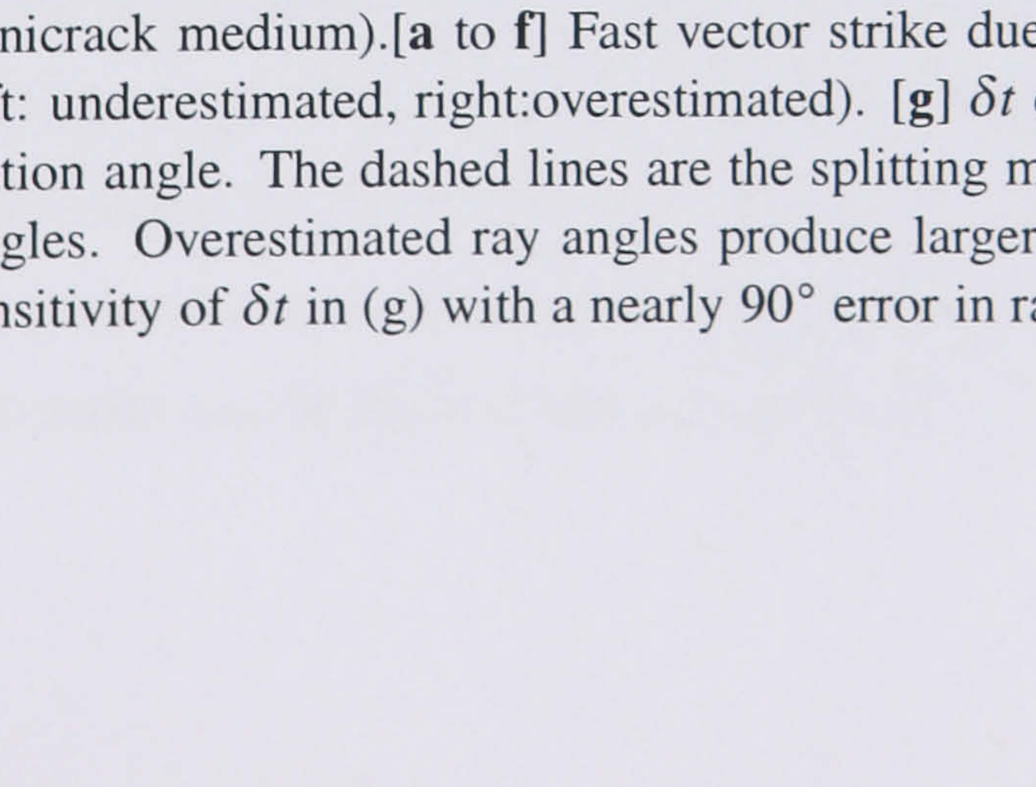

Figure 4.12 Sensitivity tests on the splitting measurements due to misspecified ray orientation angles. Example is for on a ray with a 60° inclination sampling the same HTI model as in Figure 4.11A (a buried porous unicrack medium).[**a** to **f**] Fast vector strike due to ±20° misspecified ray orientation angles (left: underestimated, right:overestimated). [**g**] δt due to an extreme case of 85° error in ray inclination angle. The dashed lines are the splitting measurements using the correct ray orientation angles. Overestimated ray angles produce larger fast strike errors than underestimated. The insensitivity of δt in (g) with a nearly 90° error in ray angles.

4.11 Conclusions

The modelling in this chapter provides guidelines that can be used in interpreting real data. Good azimuthal and inclination ray coverage is important to identify the nature of anisotropic media. HTI and VTI symmetries in reservoir and cap rocks, respectively, can be easily discriminated by vertically and horizontally polarised fast-shear-waves, respectively, for horizontal rays (Figures 4.10(c,k)). Horizontal and vertical rays are useful for estimating crack dip and strike, respectively, in HTI media.

A simple parameter, fast vector strike, was developed that accurately indicates the crack strike in pure HTI media for nearly all ray orientations. It provides a better estimate of crack strike than the strike of fast polarisation plane. The recovery of crack strike becomes more difficult with increasing VTI background contamination. For about 40% VTI background contamination, the fast vector strike can be reliably used to infer crack strike for ray inclinations up to 60° (Figure 4.11B). Therefore, rays within ±60° off the vertical are useful for estimating the crack strike in orthorhombic media comprised of HTI and VTI symmetries.

Tests have shown that splitting magnitude (δt) is not very sensitive to errors in ray orientation angles. However, up to 40° error in fast strike can result from 20° error in ray angles in a fractured medium (for subvertical rays, within ±60° off vertical).

Burial has little effect on crack-fill material. However, matrix permeability (allowing hydraulic fluid exchange between pore spaces and cracks) significantly alters the anisotropy response of brine-saturated fractured rocks. They behave like gas-saturated rocks, and hence, it is hard to identify the fluid type based on shear-wave splitting measurements. This reveals how important it is to consider pore-crack connectivity in interpretation. Therefore, the buried porous models (most likely to represent the real subsurface) in this chapter should be used to interpret the real data.

For horizontally propagating waves in HTI media, anisotropy shows 1θ variation with ray azimuth (Figure 4.2d). Hence, the crack strike can also be picked from the ray azimuth that results in the maximum percent anisotropy. Similarly, horizontal propagation is also useful in detecting multiple crack sets. For example, for two crack sets, the percent anisotropy has 2θ variation with azimuth and the two crack strikes can be peaks in percent anisotropy.

Chapter 5

Anisotropy from shear wave splitting

5.1 Introduction

In the previous chapter, shear-wave splitting analysis was applied to synthetic data generated from possible Yibal-like fracture models. In this chapter, I apply such analysis to the real dataset and interpret the results using the results from Chapter 4 as a guide. The Yibal microseismic dataset studied here comprises two weeks of data (4-10/June/02 and 19-26/Oct/02).

In Chapter 4, it has been shown that anisotropy can result from the horizontal alignment of crystals (causing HTI) as well as the vertical alignment of cracks. The Natih and Shuaiba reservoirs are highly fractured, and the rocks are carbonates. Calcite alignment does not generally produce high amounts of anisotropy in sedimentary rocks (Maddock et al., 2004). Therefore, we expect fracture-induced anisotropy to be dominant in these rocks. Consequently, the splitting measurements δt (time separation between the fast and slow shear-waves) and ψ (fast-shear-wave strike) reflect fracture density/intensity and fracture strike, respectively, in these highly fractured zones.

The aim of this chapter is to determine the fracture network geometry (i.e., the spatial distribution of fracture orientation and density) in the Yibal field. This is achieved by first using shear-wave splitting analysis to determine δt and ψ for all recorded shear-waves in the investigated period. I then study spatial variations in anisotropy by subdividing the results into formations and clusters. Finally, interpretation is guided by the anisotropy predictions in Chapter 4.

5.2 Method

5.2.1 Rotation, filtering and splitting correction

The real data are subject to the processing flow described in Section 4.3.1 (rotation and splitting correction). Prior to the splitting analysis the rotated real data are uniformly low-pass filtered with a corner frequency of 100 Hz to reduce the effect of frequency-dependent anisotropy and minimize high-frequency noise. A Butterworth filter with 6 poles and 2 passes is used.

Figure 5.1 illustrates the splitting correction method applied to an example of the real data. After the splitting correction, S-wave energy is minimised on the transverse (*St*) component (Figure 5.1b) and the S-wave particle motion becomes linear (Figure 5.1c). Moreover, the fast and slow shear waves show similar waveforms. Only one unique solution is observed in the contour plot (Figure 5.1d). Appendix G shows examples of some more unusual splitting results.

The lag time, δt, and its error are used to estimate percent anisotropy and its error. The percent anisotropy is computed assuming that the splitting is averaged uniformly over the raypath using the average S-wave velocity of the ray, based on the 21-layer model, and assuming straight source-receiver paths (using $100 \times v_s \times \delta t$ / raypath distance). Therefore, these values are average estimates of anisotropy, and the anisotropy may be more concentrated in certain regions.

5.2.2 Terminology

In Chapter 4 the strike of the fast-shear-wave polarisation vector was found to represent crack strike better than the strike of the fast-shear-wave polarisation plane (see synthetic study in Section 4.9). Therefore, throughout this chapter, I use the fast polarisation vector strike unless fast plane strike is stated. The dip still refers to the fast polarisation plane.

The ray azimuth and inclination can be calculated based on a straight source-receiver raypath approximation or estimated from P- or S-wave particle motion. However, the assumption of straight source-receiver raypath is not valid for the 1D Yibal velocity model when calculating ray inclinations. Errors in event locations and an imperfect velocity model may also degrade the quality of the calculated ray orientation angles. Therefore, throughout this chapter, I use estimated ray orientation angles based on P- or S-wave particle motion to define ray azimuth and inclination, unless stated otherwise.

Unless stated otherwise, subvertical rays, in this chapter, refer to rays propagating within 60° of the vertical. Their fast-shear-wave strikes can be used to infer crack strike (a guideline drawn

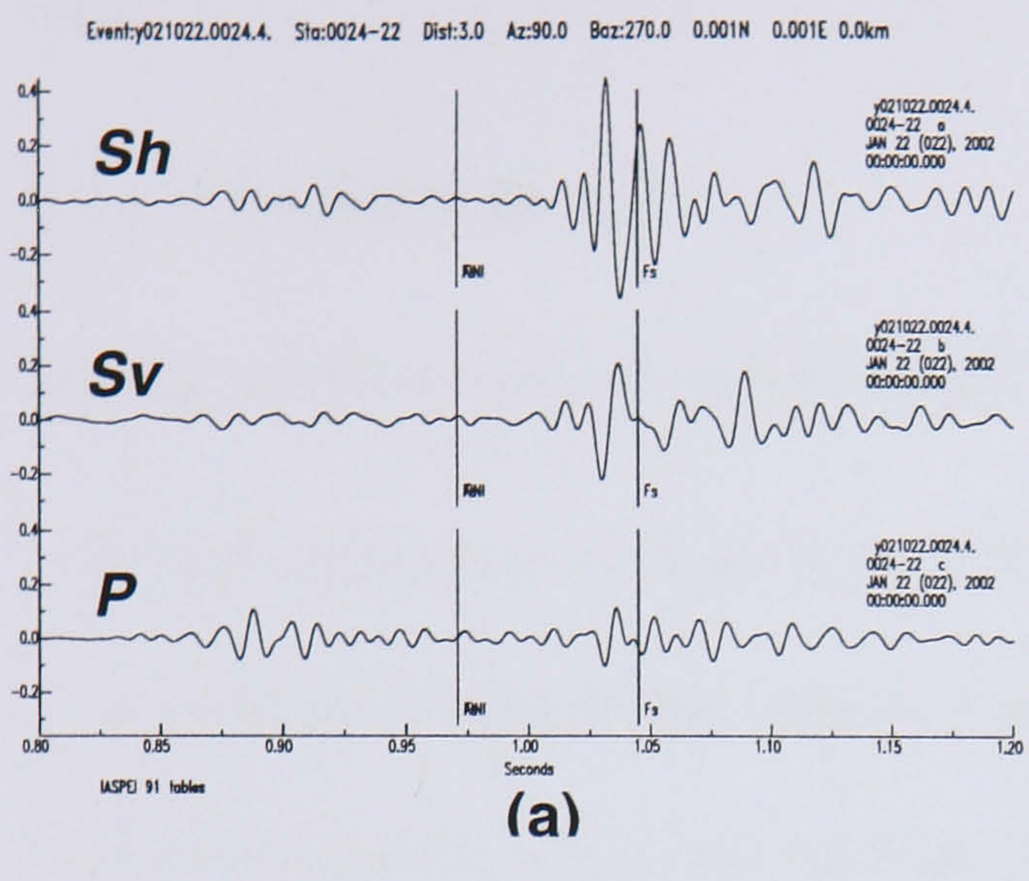

Figure 5.1 Shear wave splitting analysis on a real data example: event yb021022.0024 recorded on station 4.2. [**a**] Ray-coordinate components *P*, *Sh* and *Sv*, low pass filtered below 100Hz. [**b**] *Sr*, *St* (radial and transverse shear-wave components with respect to the initial polarisation of the S-wave before entering the anisotropic region (i.e., source polarisation)) before and after splitting correction. [**c**] [**top panel**] Fast and slow shear waves before and after correction and [**bottom panel**] S-wave particle motion before and after correction. [**d**] Contour plot of $E_t(\psi, \delta t)$, the energy on the corrected transverse component as a function of ψ and δt using a statistical F-test. Contour 1 is 95% confidence interval (double line, used to compute errorbars), contour 2 is 90% and so on. It also shows the 95% confidence solution of δt=3.00±0.25 ms and ψ=18.0±2.5° in the ray frame (after projection to ENZ frame, ψ=155.3±0.4°).

from the synthetic modelling in Chapter 4). Subhorizontal rays refer to rays propagating ±15° from horizontal. Their fast-shear-wave dips are indicators of crack dip (another guideline derived from the tests on synthetics). Unless stated otherwise, a bin size is 30° (i.e., ±15° about mid value).

5.2.3 Selection criteria

Splitting results are only accepted if they satisfy the following requirements:

- Well defined S-wave, distinct from P-wave.
- Good match between fast and slow shear waveforms.
- Linear particle motion after splitting correction.
- Energy minimised on the corrected transverse component.
- Unique 95% confidence solution in the error contour plot (i.e., no cycle skipping).

I classify a measurement as A if it meets all of the above constraints. Measurements are classified B when they fail to satisfy only one constraint. Failing to satisfy two or more constraints classifies an observation as C.

5.3 Results

15 days of data (4-10/June/02 and 19-26/Oct/02) containing 641 located events recorded by a maximum of 10 stations of known tool orientation are analysed. The data provide 2481 source-receiver combinations suitable for shear-wave splitting analysis. Out of 2481 source-receiver pairs, there are 398 good results (class A), 349 of class B and 1734 of class C. In percentages, that is 16%, 14% and 70% in classes A, B and C, respectively. The splitting results of class A and B are listed in Appendix A.2. Ultimately, 577 events were analysed, the other events are either recorded by a receiver of unknown tool orientation or have a bad signal-to-noise ratio.

The 398 reliable results are further sorted by imposing error constraints of ±10° on angles and ±2 ms on δt. This leaves 385 δt and 345 ψ results in the ray frame. Rotating ψ in 3D yields 295 fast-shear-wave vector strikes and 375 fast plane dip results. The associated ψ errors are also rotated in 3D resulting in differences between ψ(strike) and ψ(dip) when imposing the ±10° error constraint. In contrast, the δt error is not affected by the rotation in 3D.

Figure 5.2 displays histogram plots of δt and percent anisotropy. δt ranges mostly between 0-20 ms and percent anisotropy generally ranges between 0-10% but values up to 15% are encountered. A rose diagram of the fast-shear-wave strike is shown in Figure 5.3. Similar rose diagrams of fast vector strike versus fast plane strike for rays propagating subvertically ($< 60°$ inclination) are shown in Figure 5.4. The results for fast vector strike are more clustered than the ones for fast plane strike. This agrees with our findings for vertically fractured media in Chapter 4. Therefore, throughout this chapter, I use the strike of the fast vector rather than that of the fast plane. Figure 5.4a shows two predominant fast strikes with 15°NNE(±7°) and 84°E(±7°) trends.

The ray coverage has also been computed (Figure 5.5) showing good azimuthal coverage in the horizontal plane and moderately good coverage in the vertical plane, within which the majority of rays travel horizontally. Thus, the fast dip direction is much better constrained than the strike direction. The accuracy of the estimated ray orientation angles is important for the subsequent analyses. A quality control on the estimated ray azimuth and inclination was achieved by comparison with those based on straight-ray source-receiver path calculation (Figure 5.6). It shows a good correlation in ray azimuth and to a lesser extent in inclination reflecting the robustness of ray angles and event locations. The increased scatter in the calculated ray inclination plot is expected due to the ray bending effect being neglected.

Figure 5.7 displays the strike of the fast polarisation vector and polarisation plane estimates versus ray azimuth for rays propagating ±30° from horizontal. Fast strike, as theoretically expected (Figure 4.11A4), is biased by the ray azimuth and, therefore, should not be used for crack strike determination. As predicted by theoretical modelling (Figure 4.11A4), the strike of the fast vector is perpendicular to the ray azimuth direction while the strike of the fast plane aligns with the ray azimuth. Similar plots for subvertical rays (Figure 5.8) do not show azimuth-dependent fast strike as theoretically predicted (Figure 4.11A1) and, therefore, can be used to estimate crack strike (as done in Figure 5.4). Therefore, throughout this chapter, I use subvertical rays (within ±60° off vertical) to indicate crack strike and subhorizontal rays (within ±15° off horizontal) to estimate crack dip.

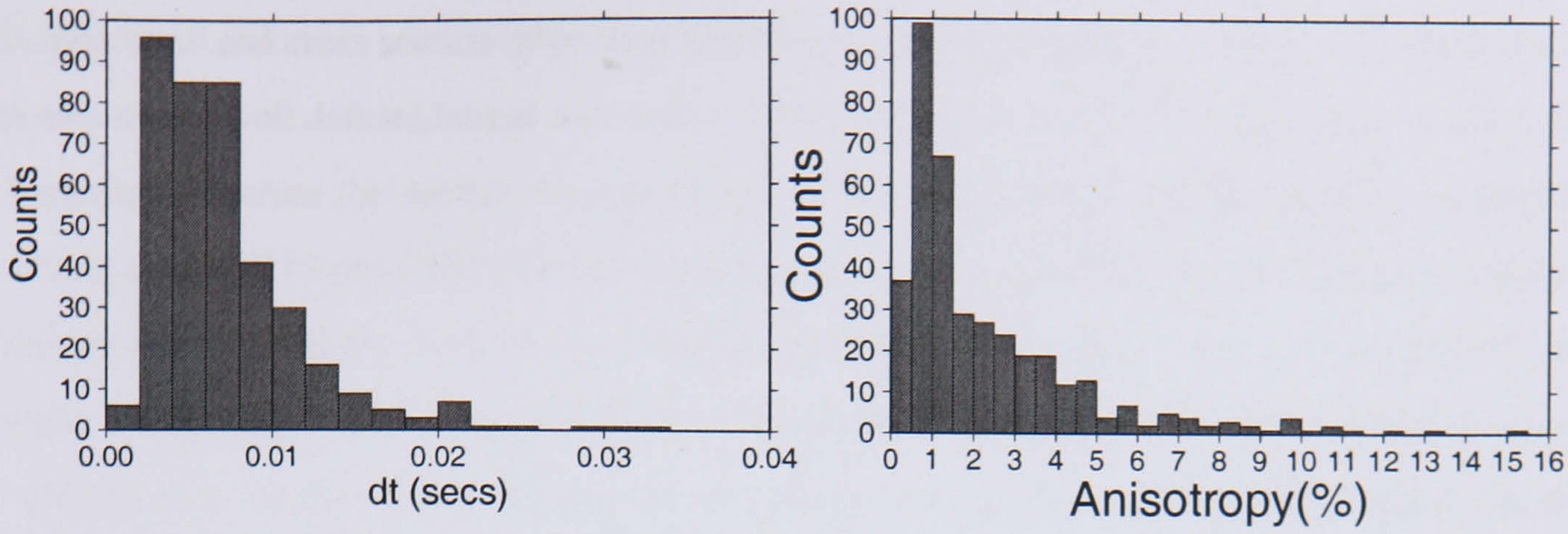

Figure 5.2 [**Left**] Lag-time and [**right**] percent anisotropy observed in the analysed data.

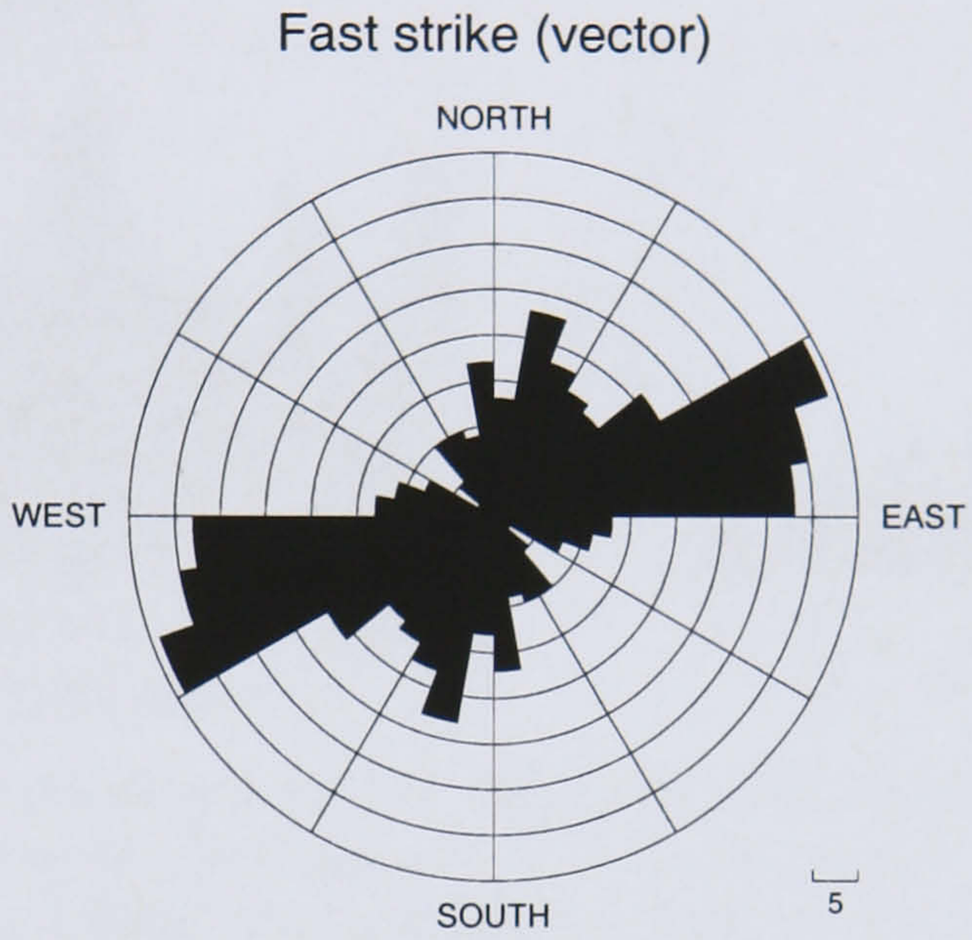

Figure 5.3 Rose diagram of the strike of the fast-shear polarisation vector for the entire dataset.

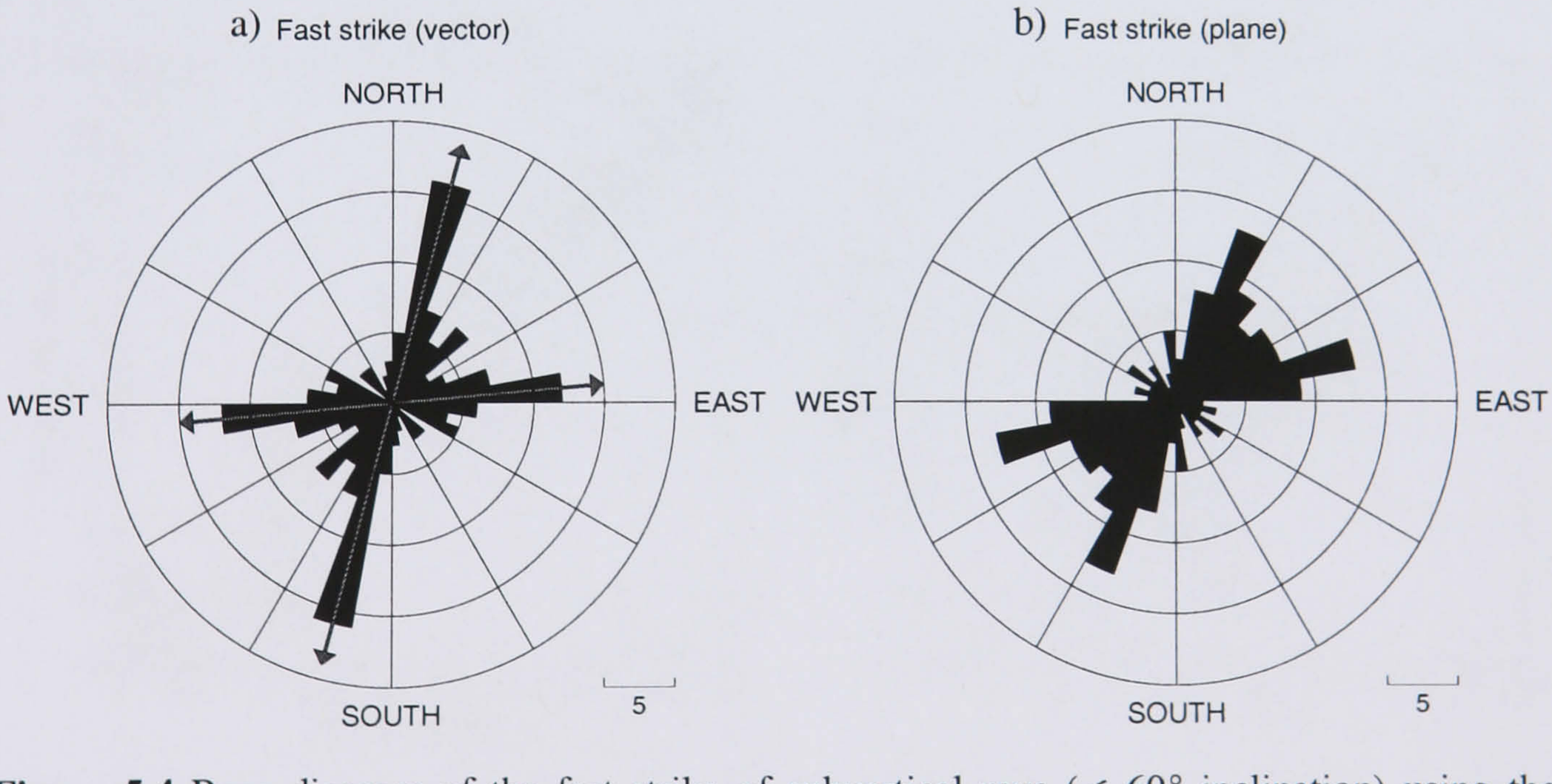

Figure 5.4 Rose diagram of the fast strike of subvertical rays (< 60° inclination) using the projection of the: [**a**] polarisation vector and [**b**] polarisation plane. The two average peak strikes of 15°±7° and 84°±7° are marked with arrows. A 30° bin size is used to estimate the standard deviation of the two peak values (i.e., the fast strike ranges 0°-30° and 70°-100°, respectively).

A map view and cross section of percent anisotropy (Figure 5.9) plotted at source-receiver mid-points shows well defined lateral and vertical variations in anisotropy. Percent anisotropy decays dramatically across the eastern-most graben fault from 6% (average) in the SE footwall to 1% (average) in NW blocks (NW footwall and hanging wall) (Figure 5.9a). Figure 5.9b shows strong anisotropy in the Natih A reservoir, moderate in Fiqa and Natih B-G1 and very weak (1%) in Natih B-G2. Figure 5.10 shows the percent anisotropy in the SE footwall and NW blocks separately in cross sections to remove the effect of lateral changes in anisotropy. They clearly show similar lateral and vertical variations in anisotropy.

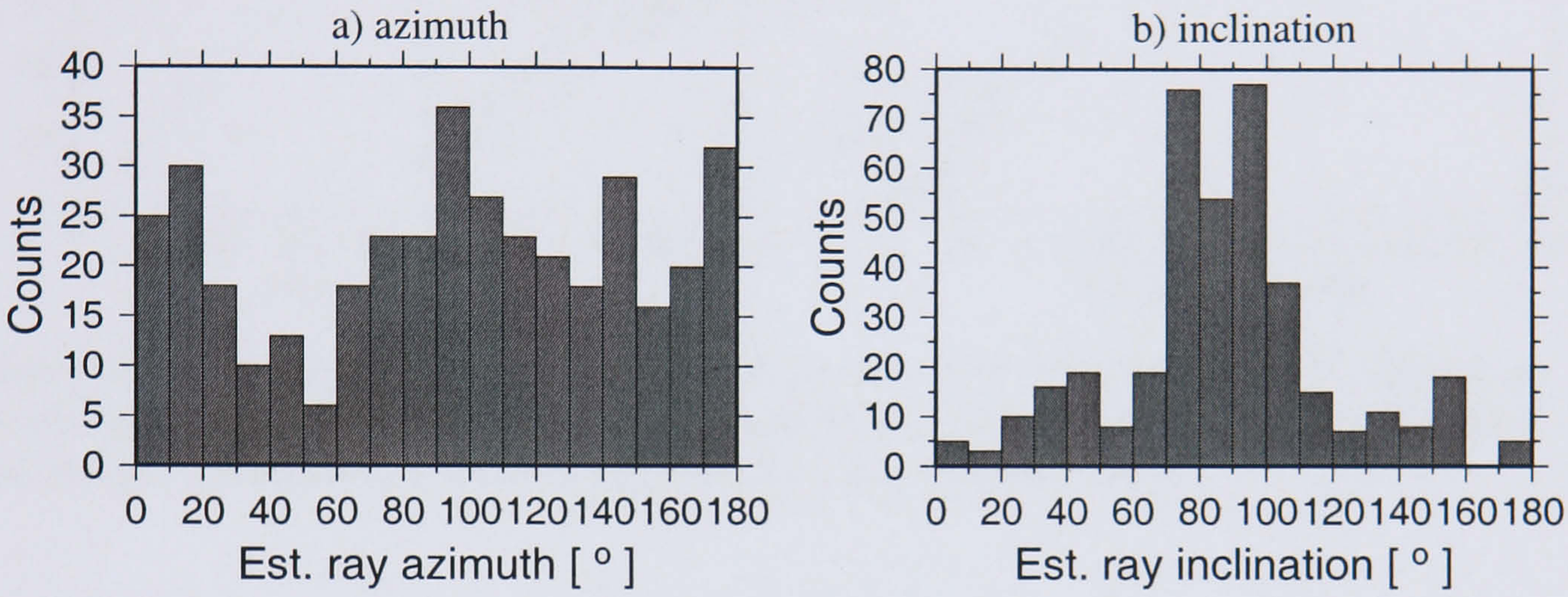

Figure 5.5 Ray coverage in horizontal and vertical planes based on estimated angles from particle motion analysis. [**a**] Ray azimuth defined by particle motion and [**b**] incidence angle from vertical-up. Note the good azimuthal coverage (a) and moderate vertical coverage (b). Most rays travel horizontally and fewer rays propagate vertically.

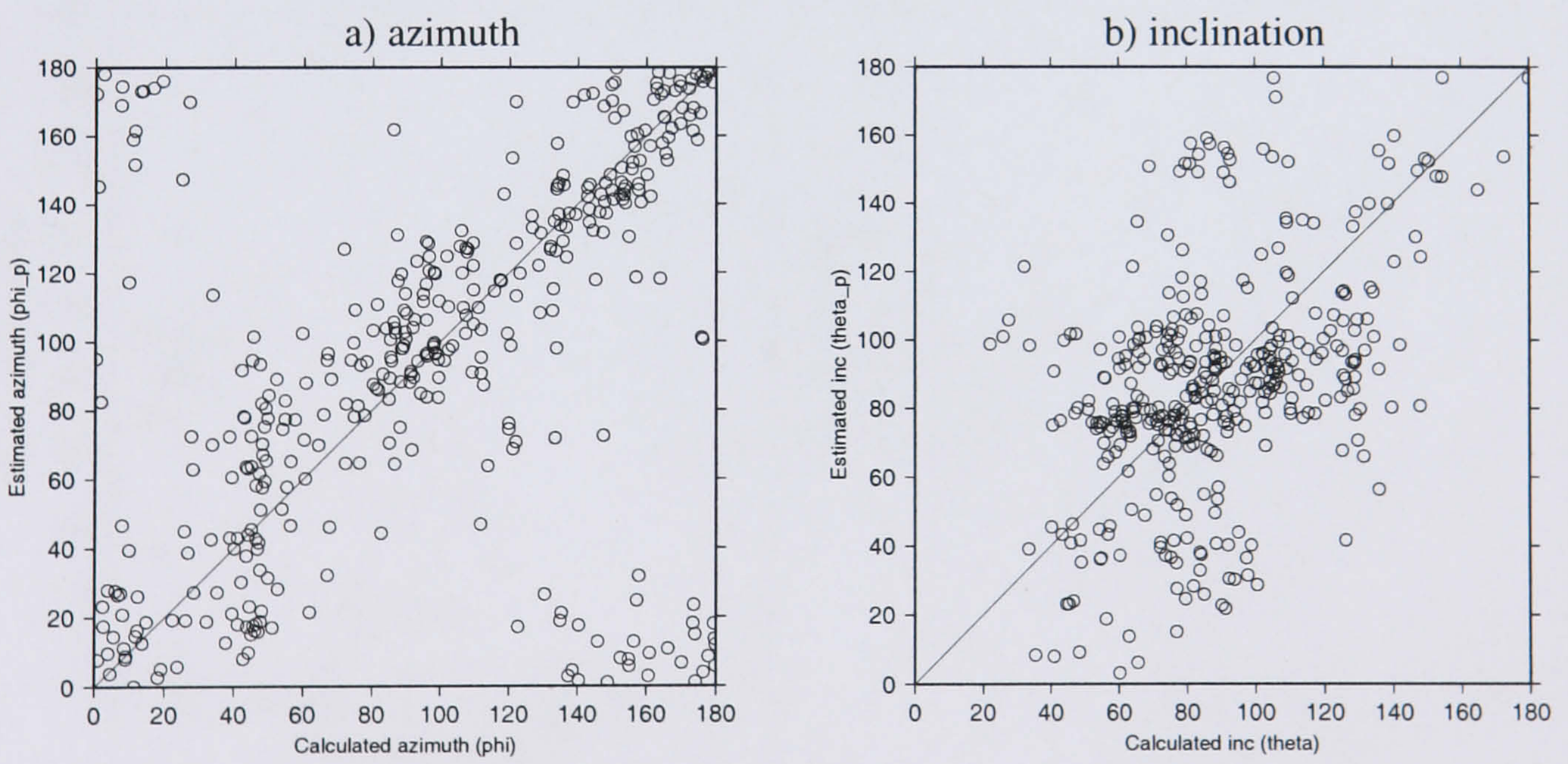

Figure 5.6 Quality control: [**a**] Estimated ray azimuth and [**b**] inclination versus calculated ones. Estimated values are derived by means of P-wave or S-wave particle motion analysis while calculated ones are based on a straight path from source to receiver. The match between estimated and calculated is good for the azimuth (a) and poorer for the inclination (b) due to neglecting ray bending effects in the straight source-receiver raypath approximation.

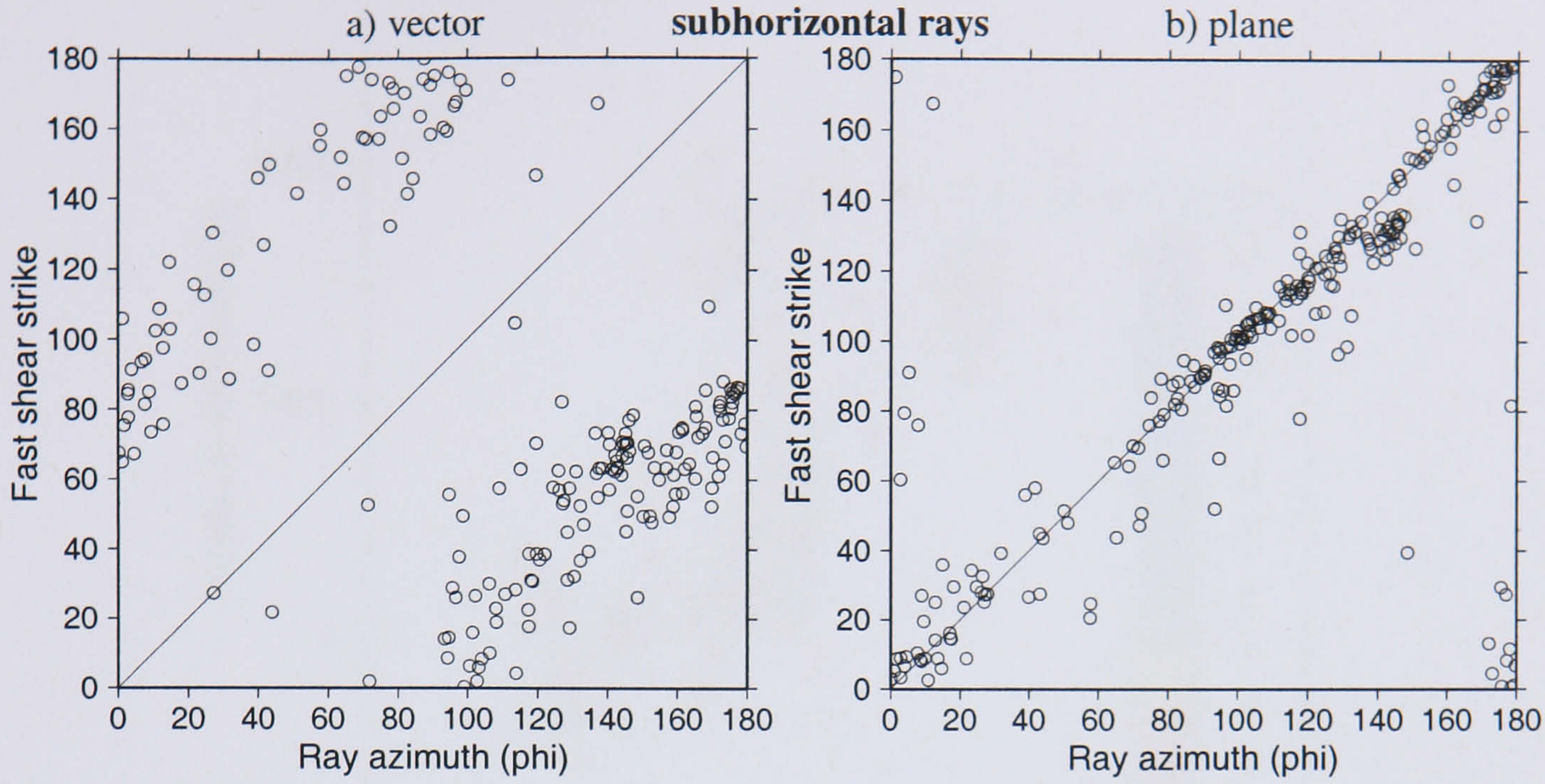

Figure 5.7 Fast shear strike versus ray azimuth for rays ±30° off horizontal. Estimated ray azimuth versus strike of [**a**] fast-shear polarisation vector and [**b**] fast-shear polarisation plane. Solid straight line represents points of identical fast strike and ray azimuth.

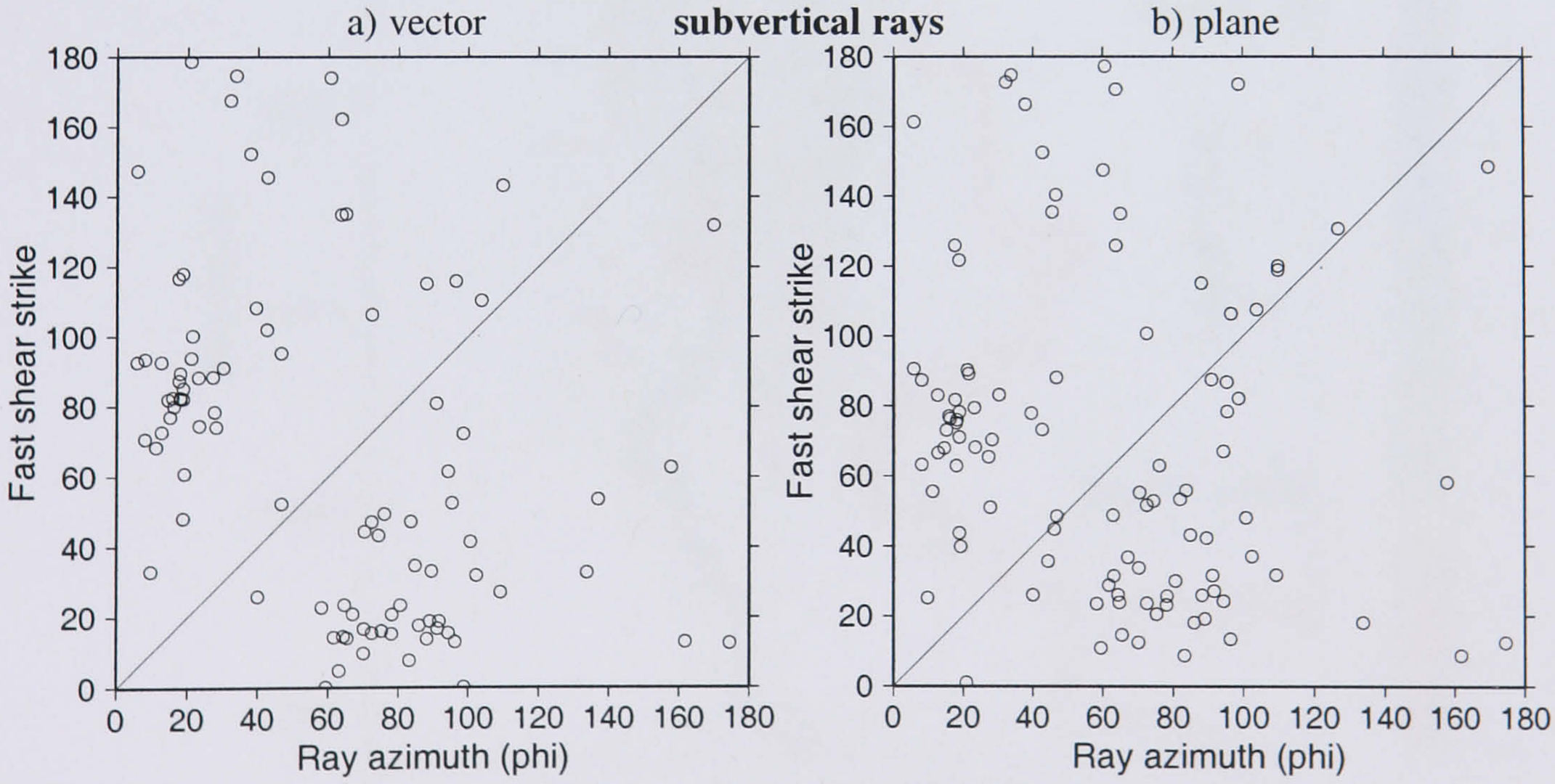

Figure 5.8 Fast shear strike versus ray azimuth for rays ±60° off vertical. Estimated ray azimuth versus strike of [**a**] fast-shear polarisation vector and [**b**] fast-shear polarisation plane. Solid straight line represents points of identical fast strike and ray azimuth.

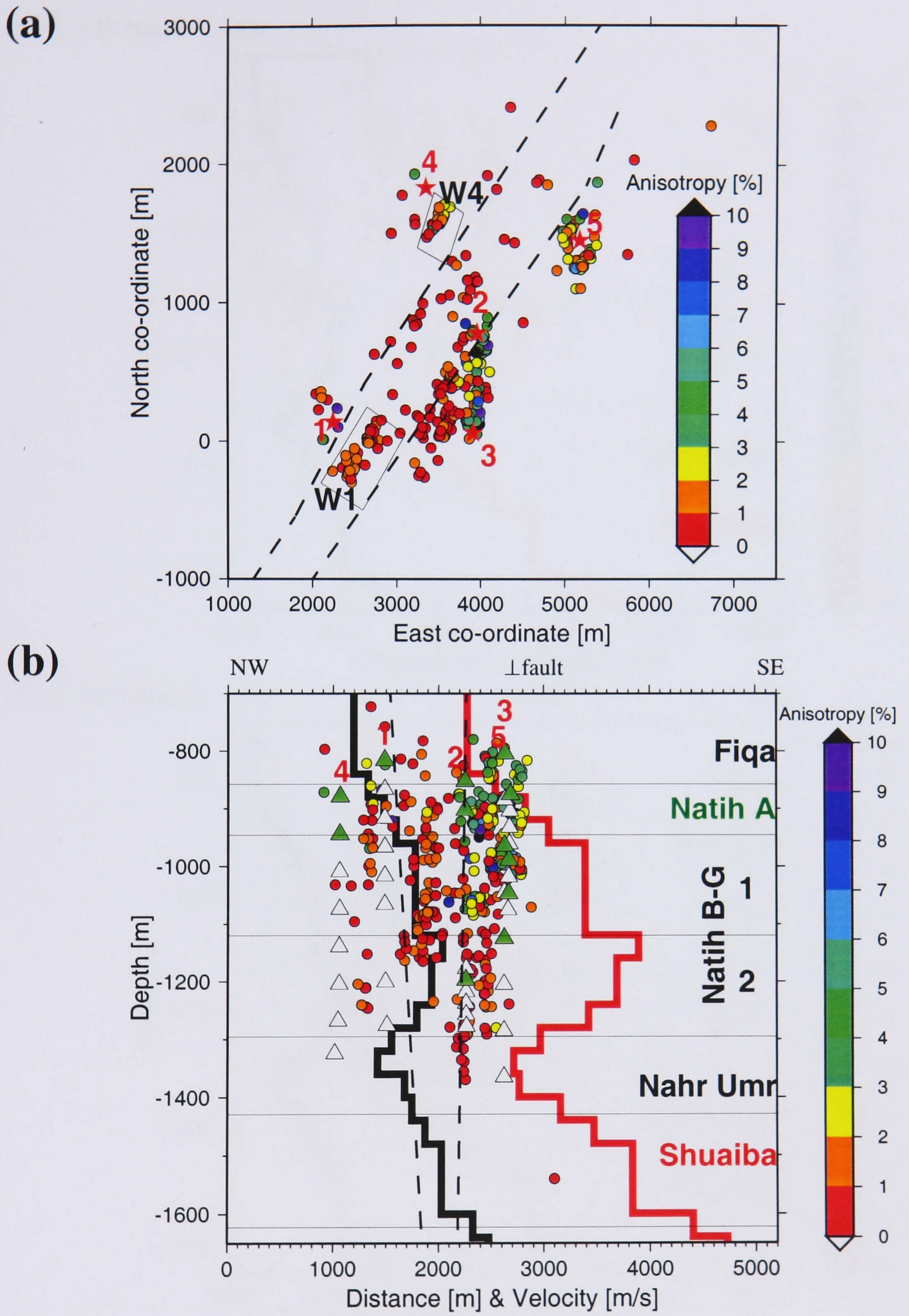

Figure 5.9 [**a**] A map view and [**b**] cross section of anisotropy distribution. The cross section runs perpendicular to the major faults (dashed lines). Circles are located at source-station mid-point. Sensor locations are shown by triangles, and green triangles mark the sensors used to measure S-wave splitting. The cross-sectional image is oriented at 45° clockwise from east. Note the sharp reduction in anisotropy across the eastern-most graben fault.

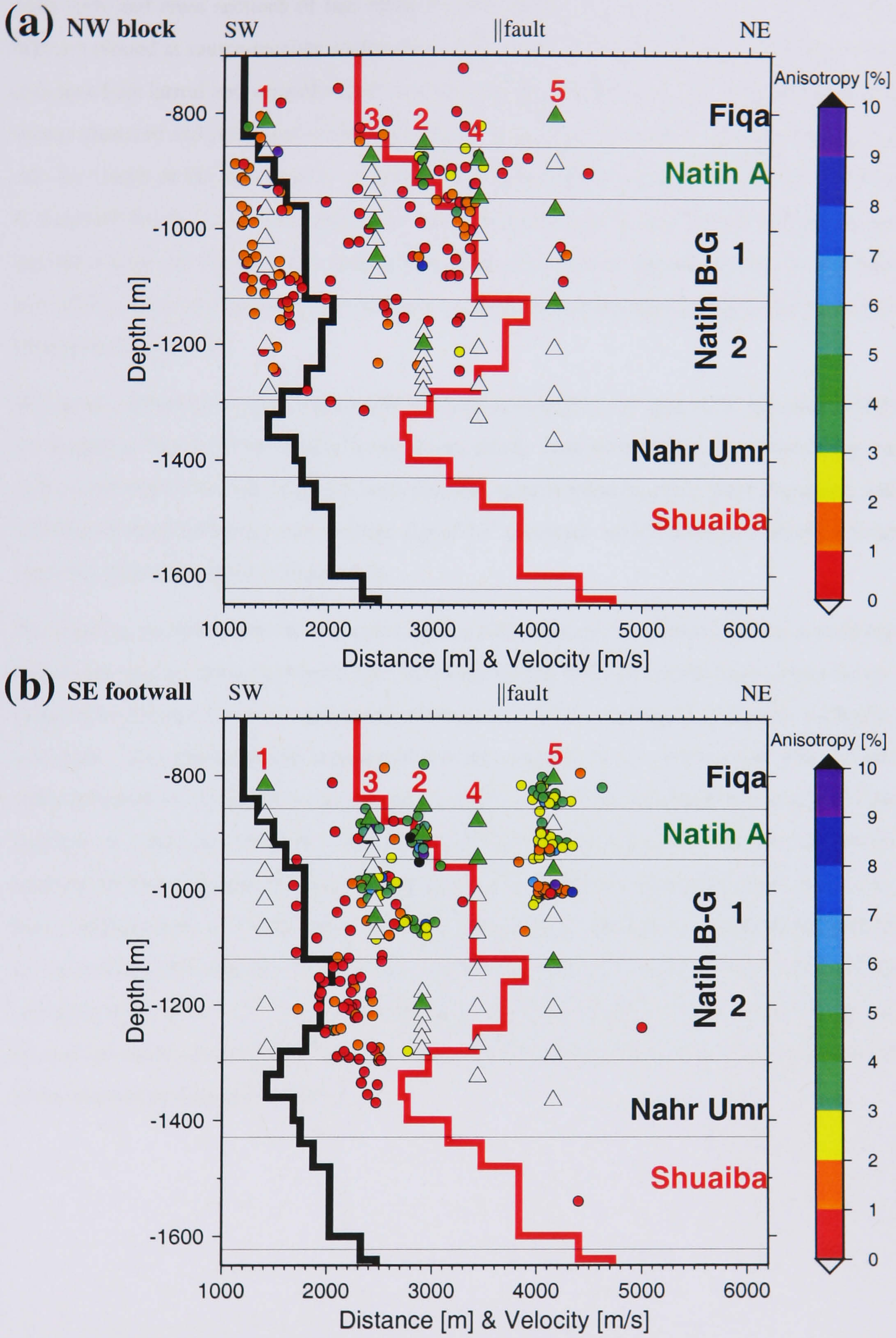

Figure 5.10 Cross sections of percent anisotropy parallel to the main graben faults showing [**a**] the NW block (NW footwall and hanging wall) and [**b**] SE footwall. The cross sections are oriented at 55° anticlockwise from east. Note the low and high amounts of anisotropy in the NW block (a) and SE footwall (b), respectively.

Map view and cross sections of fast strike for subvertical rays and fast dip for subhorizontal rays are plotted at source-receiver midpoints in Figures 5.11 and 5.12, respectively. Figure 5.11 indicates both lateral and vertical variation in the fast-shear-wave strike. The measurements also appear clustered and consistent within each cluster (e.g., Nahr Umr cluster indicates NNE trend and the cluster at the very bottom of Natih B-G1 shows NE trend in Figure 5.11b). NNE to E dominant trends occur across the whole rock column (Figure 5.11b). On the other hand, the fast-shear-wave dip (Figure 5.12) shows nearly vertically polarised fast-shear-waves at all depths and offsets. There are though a few subhorizontal fast-shear-wave dips mostly in the Natih B-G formation (Figure 5.13).

Histograms of fast-shear-wave dip for subhorizontal rays ($\pm 15°$, $\pm 5°$ and $\pm 2.5°$ from horizontal) are plotted in Figures 5.14. Figure 5.14a shows mostly near-vertical fast dips. Narrowing the cone of subhorizontal rays (Figure 5.14c), the near-vertical trend becomes more dominant, and indicates vertical fracturing with average dip of 73° (compare with fast-shear-wave dip for the vertically fractured model in Figure 4.2).

The splitting measurements for the entire data as a function of ray azimuth and for several ray inclination bins are shown in Figure 5.15. It reveals mainly NNE fast-shear-wave strikes for up-going rays (Figures 5.15(a,b)) and mostly E fast strikes for downgoing rays (Figures 5.15(e,f)). In Figure 5.15e, the azimuthal variation in fast dip suggests 80°E, which agrees with the fast strike information. In Figure 5.15e, the best fit spline (solid line) to percent anisotropy and the synthetic ψ (strike,dip) response (dashed lines) of buried porous unicrack medium with cracks trending 80°E are superimposed. Overall, Figure 5.15e suggests a unicrack medium with E oriented vertical cracks as: (1) the fast-shear-wave strike and dip correlate well with the predictions for such a medium, and (2) the maxima of the percent anisotropy suggests a 90° crack strike (compare with Figure 4.2c). This best fit model is only restricted to this subset (120° ray inclination) of the mother dataset. This further confirms the variability in the orientation and magnitude of the anisotropy throughout the field.

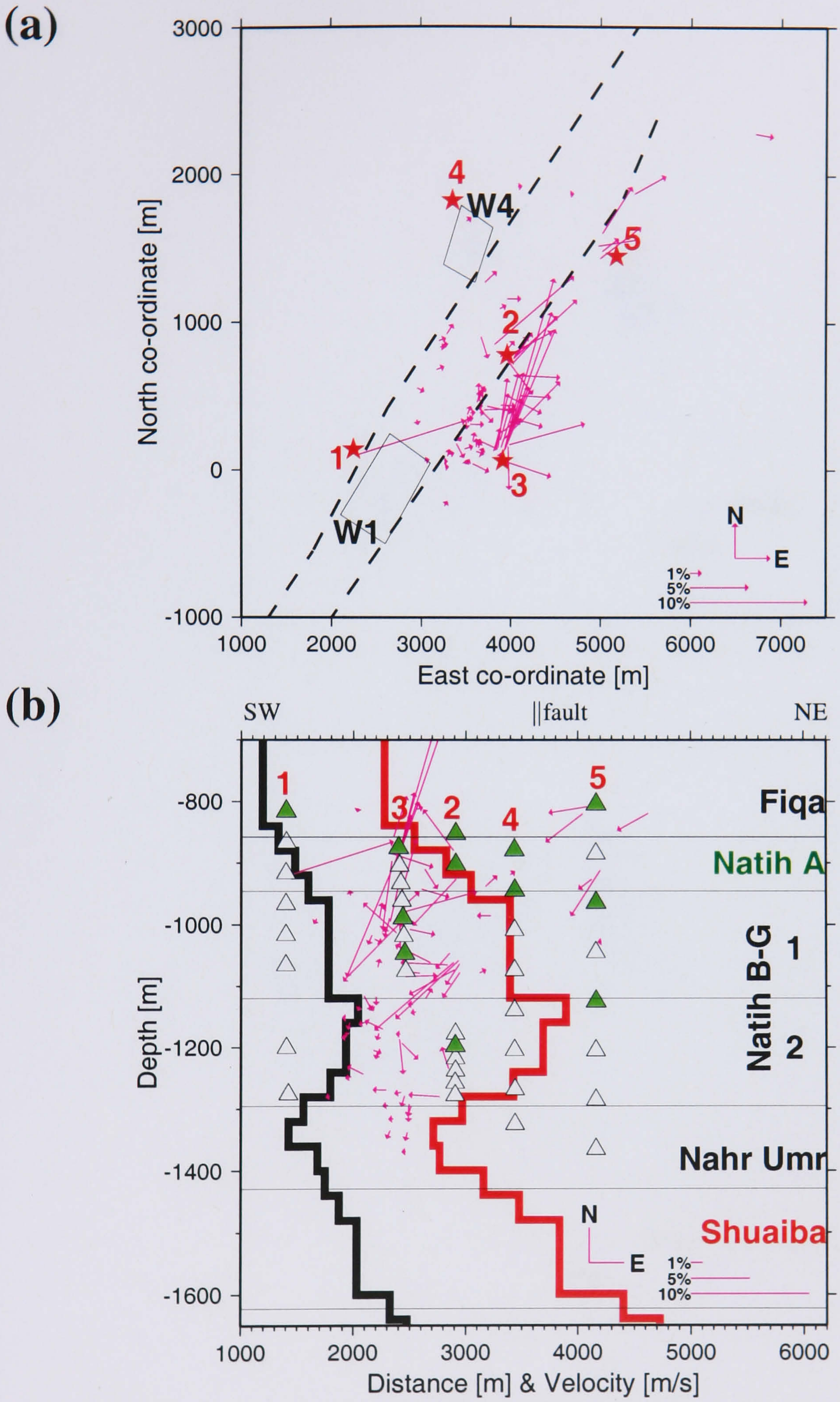

Figure 5.11 The strike of the fast-shear-wave determined from subvertically propagating rays (i.e., $< 60°$ from the vertical): [**a**] map view and [**b**] fault-parallel cross section. The pink vectors (starting at the source-receiver midpoints) mark the fast shear-wave strike and the length of the vector is proportional to the percent anisotropy. The vectors in the cross section shows the fast-shear-wave strike relative to north. Note the lateral variations in strength of anisotropy across the faults and the vertical variations. Also note the predominant NNE and E trends.

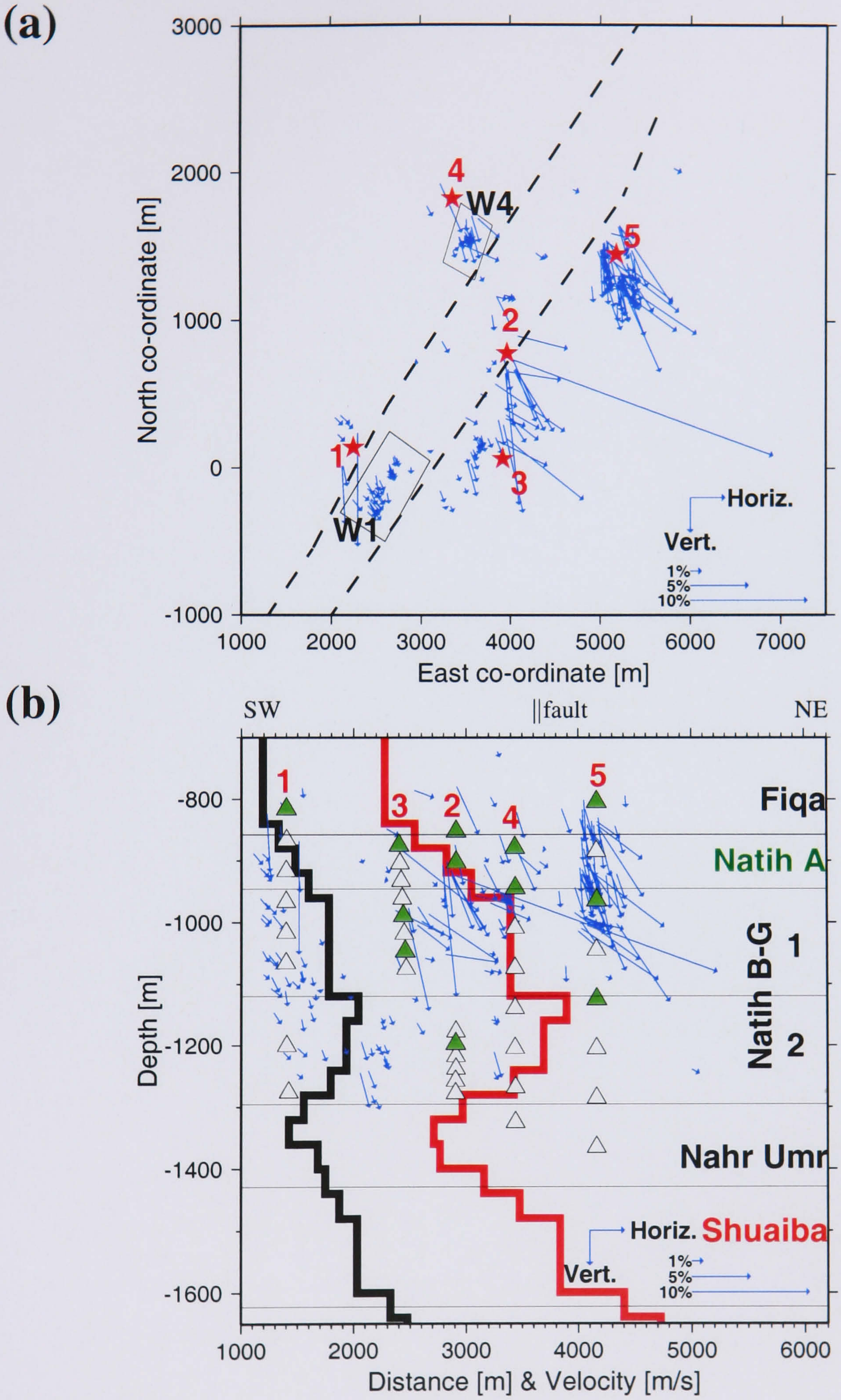

Figure 5.12 Fast-shear-wave dip (blue) for subhorizontal rays (inclination=90° ±15°) in [**a**] map view and [**b**] cross section. Vector length is proportional to percent anisotropy. The vectors start at source-receiver midpoints. Note that in (a) the vectors show the dip and not the strike (i.e., a N-S vector means vertical dip). The fast dips are mostly near vertical indicating vertical fracturing.

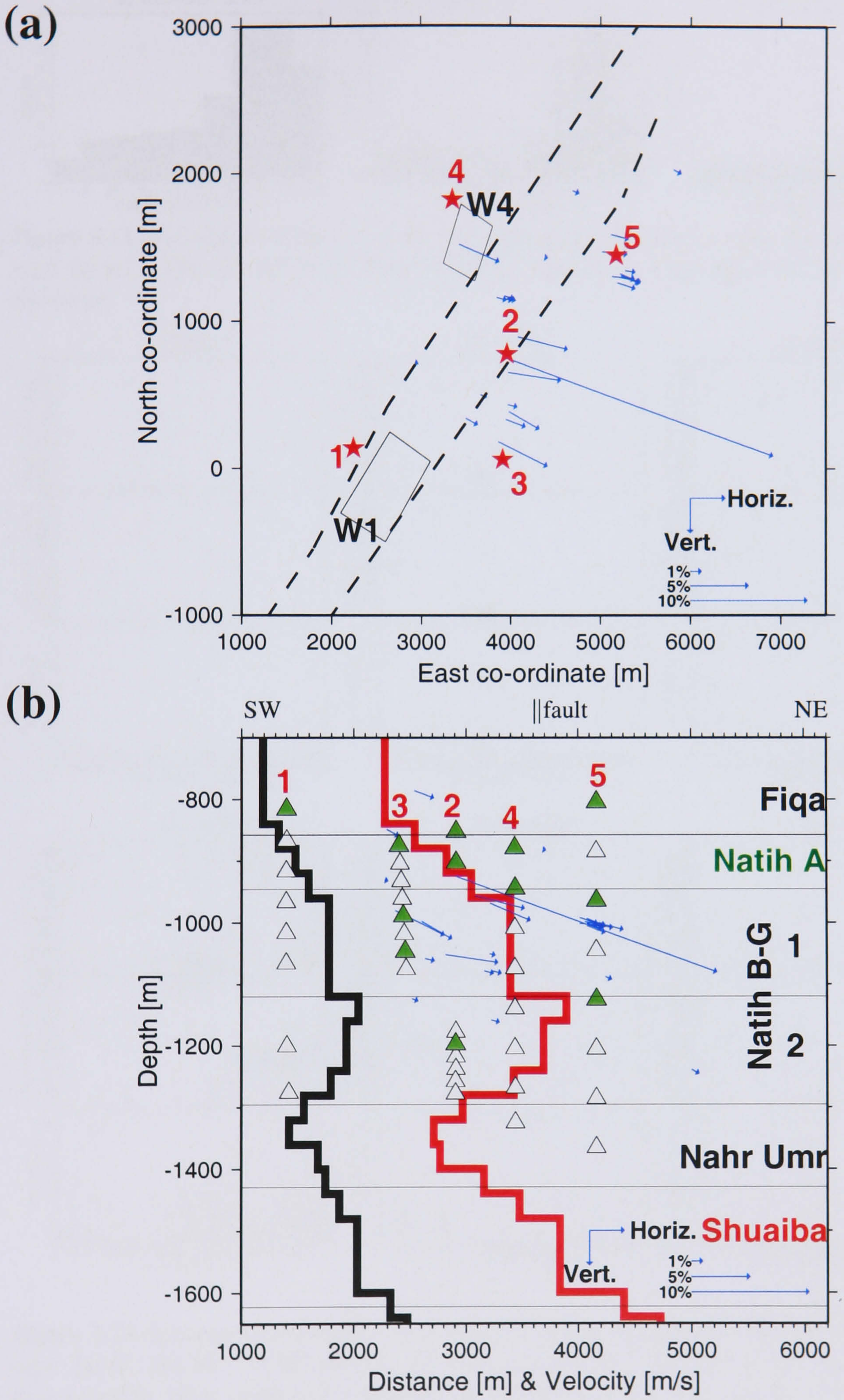

Figure 5.13 Same as Figure 5.12 with subhorizontal fast planes only (fast dip less than 30°). Note the subhorizontal fast dips are mainly clustered in Natih B-G formation.

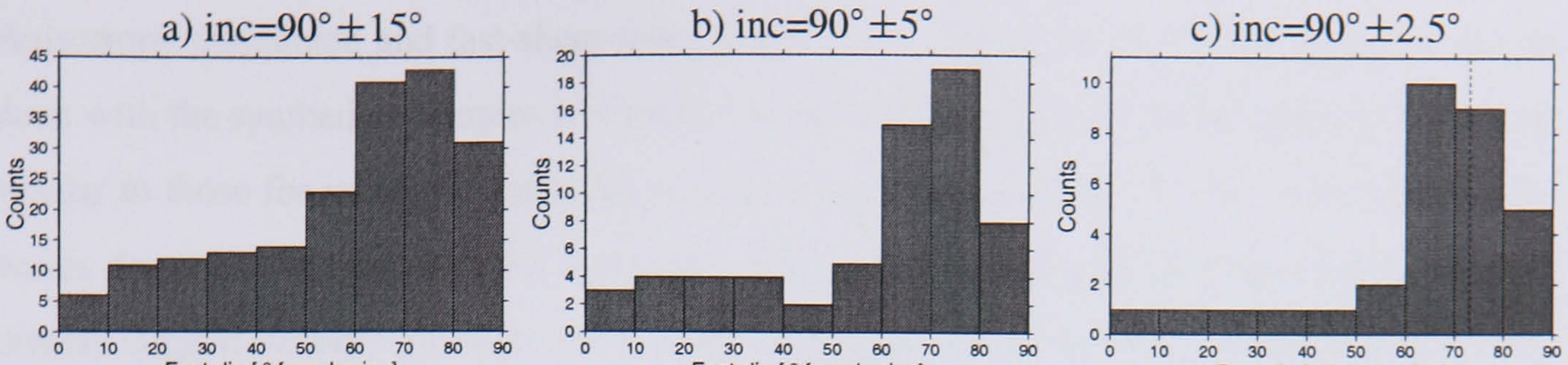

Figure 5.14 Histograms of the dip of the fast-shear-wave polarisation plane for subhorizontal rays: [**a**] ±15°, [**b**] ±5°, [**c**] ±2.5° from horizontal. In (c) the average dip is 73° for the 60°-90° dip range.

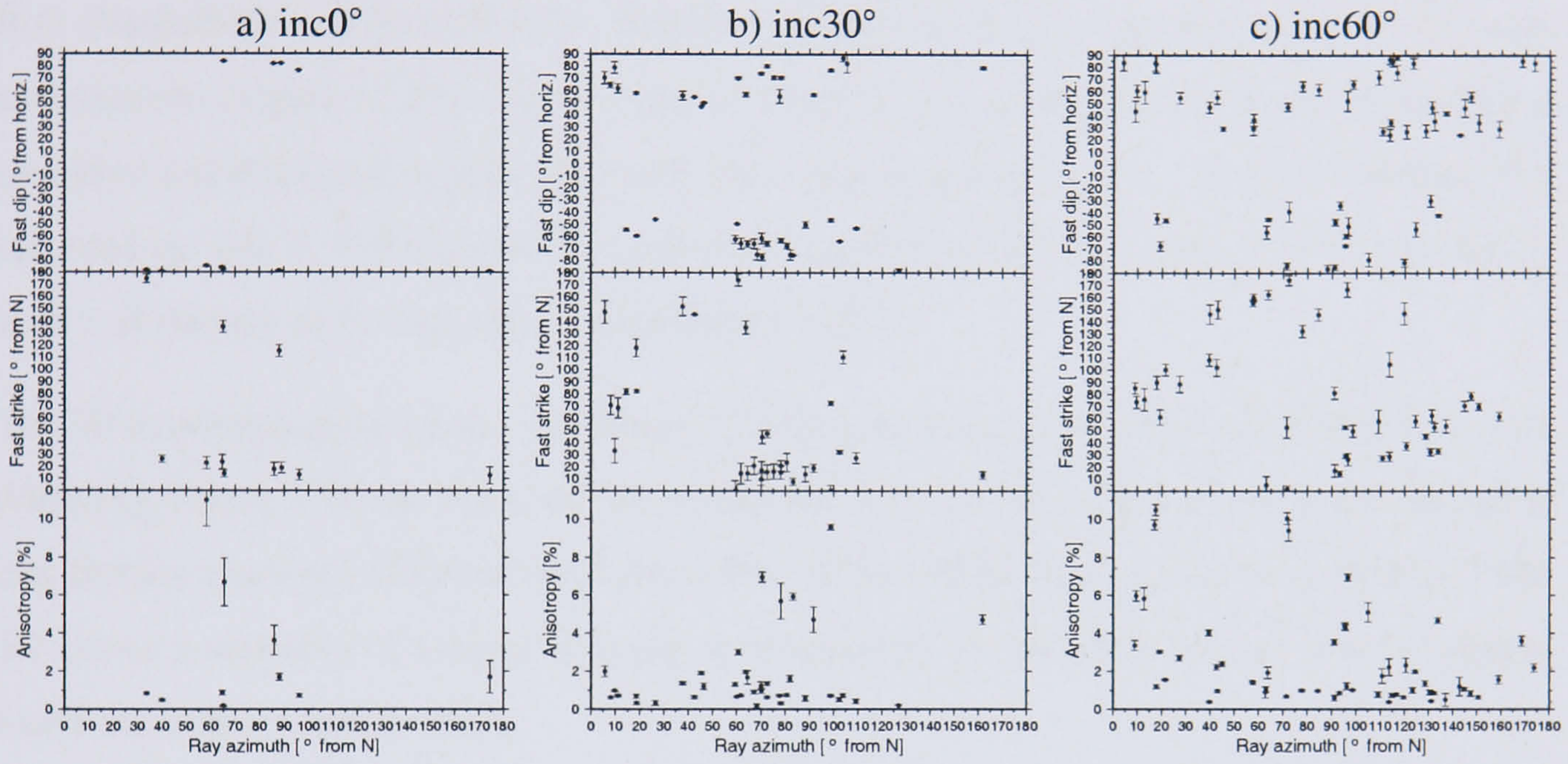

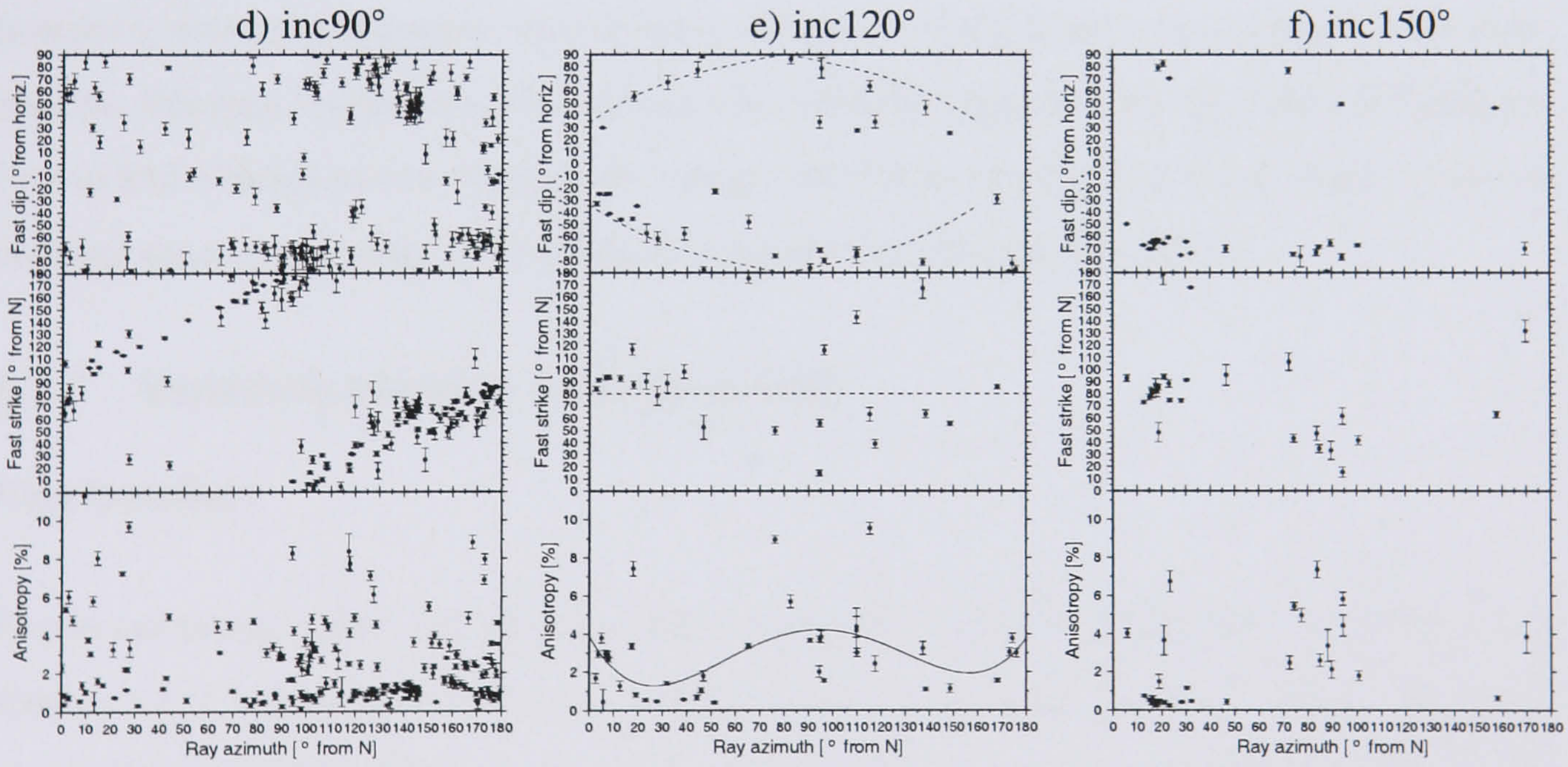

Figure 5.15 Splitting measurements as a function of ray azimuth for various ray inclination bins: [**a**] 0°, [**b**] 30°, [**c**] 60°,[**d**] 90°, [**e**] 120° and [**f**] 150°. Bin size is 30°. In (e), the 4th degree best-fit spline (solid line) and synthetic responses (dashed lines) for the 120° inclination bin for a buried porous unicrack model (gas and water have identical responses) with vertical cracks aligned 80°E are also shown (compare with the model in Figure 4.2c). Note the good fit of unicrack model in (e) indicating E trending near-vertical cracks. Upgoing vertical rays (a,b) indicate mainly NNE crack trends, while downgoing waves (e,f) imply mainly E trends.

Anisotropy magnitude and fast-shear-wave strike can be shown on 3D anisotropy plots as was done with the synthetic examples in Chapter 4. Results for the entire dataset (Figure 5.16a) are similar to those for vertically fractured models (compare with Figure 4.10c), where fast shear-waves for subhorizontal rays are vertically polarised. The fast strike of the subvertical rays display large variations. The data can be split into subsets where the fast strike is more uniform.

The data are subdivided into clusters based on lithology and location. On the basis of lithology, I consider rays that travelled purely within the individual formations of Fiqa, Natih A and Natih B-G (Natih B-G1 and Natih B-G2). These are chosen due to their good coverage with events and receivers (Figure 5.17b). On the basis of location, five clusters of microseismic events are identified and displayed in map view and cross section in Figure 5.17. These are named: W1 recorded by well 1; W4 recorded by well 4; G recorded by wells 2, 3 and 4; W3 recorded by well 3; H (known as the Horseshoe) recorded by well 5.

The 3D anisotropy plots for the individual lithologies and clusters are shown in Figure 5.16. Additionally, Figure 5.18 also shows the 3D anisotropy plots for the individual lithologies separated into clusters south east (SE) and north west (NW) of the eastern-most graben fault. Finally, Table 5.1 shows a summary of average splitting measurements for the entire dataset, and the subsets based on lithology and location.

In order to assist interpretation, various ways of sorting and plotting the data in terms of location, stations, lithology, inclination, and azimuth are considered. Drawing on the results of Chapter 4 I try to find a buried porous model with a single set of fractures that best fits the observations. A constant crack aspect ratio, η, of 0.001 , is assumed for all the tested models.

5.3.1 Variations between lithological units

Fiqa formation

Events occurring within the Fiqa formation (600-858 m depth range) and were recorded by stations 1.1, 2.1 and 5.1, yield 13 rays confined entirely to the Fiqa formation. The 3D anisotropy plot of the Fiqa subset (Figure 5.16b) shows percent anisotropy in the range 0–5% (time lag 0–10 ms) with an average of 3%. Figure 5.16b also shows that subhorizontal fast-shear-waves have a vertical polarisation with an average fast dip of 83°. This is indicative of a vertically fractured medium (compare with Figure 4.10c). The vertical ray coverage is poor (Figure 5.16b) and therefore crack strike estimation from subvertical rays is not possible. For subhorizontal rays (inclinations 70°-90°), the splitting observations as a function of ray azimuth (Figure 5.19a) show

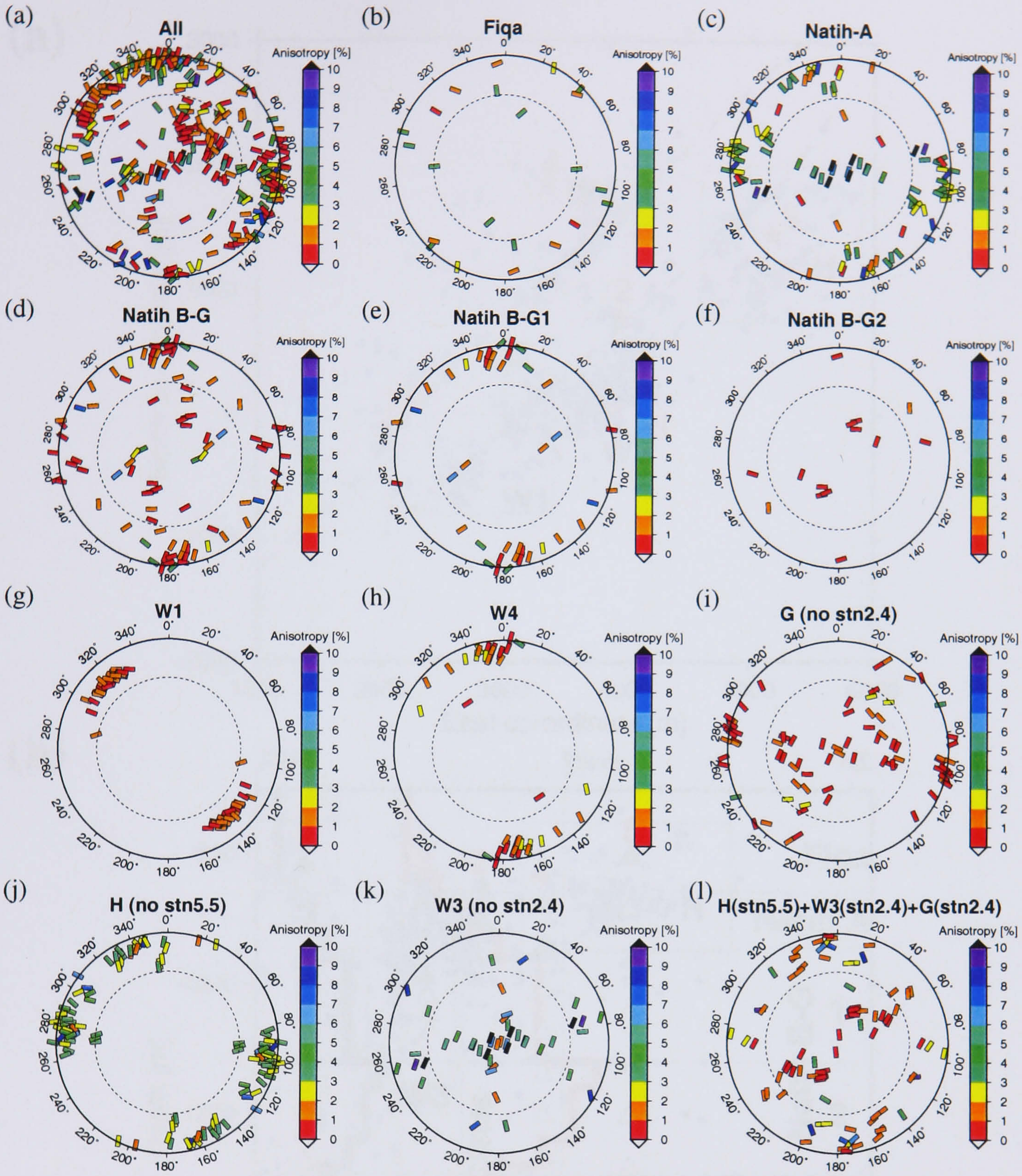

Figure 5.16 3D plots (lower hemisphere projection) of the Yibal anisotropy: horizontally propagating waves plot at the perimeter, whilst vertically propagating waves plot at the center. The magnitude of the anisotropy is indicated by the colour and the orientation of the fast shear-wave is indicated by the orientation of the long axis of the coloured rectangles. [**a**] Results for the entire dataset. Results confined entirely to [**b**] the Fiqa shale cap rock, [**c**] Natih-A carbonate reservoir, [**d**] Natih B-G formation, [**e**] upper part of Natih B-G, and [**f**] lower part of Natih B-G. Results for cluster [**g**] W1, [**h**] W4, [**i**] G (excluding the deepest station 2.4). [**j**] Cluster H, known as the Horseshoe (excluding those for the deepest station 5.5). [**k**] Cluster W3 (excluding the deepest station 2.4). [**l**] Results for only the deepest stations 2.4 and 5.5. In (b) through (i) the results are mirrored to the opposite hemisphere for illustration purposes. 60° inclination is shown as a dashed line. Note that in (a) through (j) sub-horizontally propagating fast shear-waves are vertically polarised, most probably indicating fractured media. In contrast, for sub-horizontal rays in (l) the fast shear-wave is horizontally polarised and the anisotropy is much weaker, thus suggesting anisotropy due to the background intrinsic anisotropy of the rock.

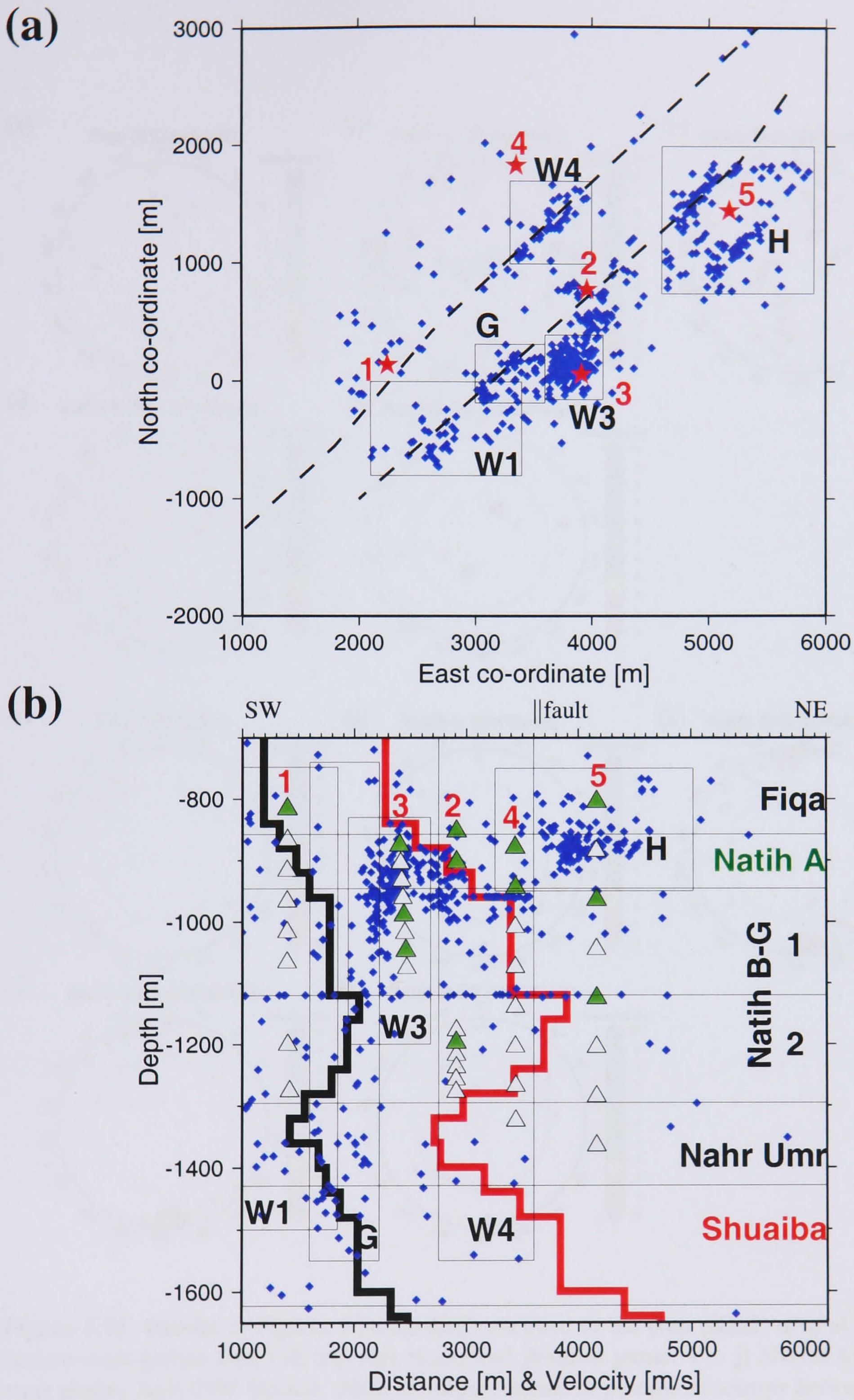

Figure 5.17 Event locations (blue) for the entire dataset (4-10/June02+19-26/Oct02) in [**a**] map view and [**b**] cross section. Clusters are also shown by open rectangles. Wells (stars), sensors (triangles), sensors used for anisotropy analysis (green triangles) and two main faults (dashed line) are also shown. The cross section is oriented SW→NE (55° anticlockwise from east), parallel to the main graben faults.

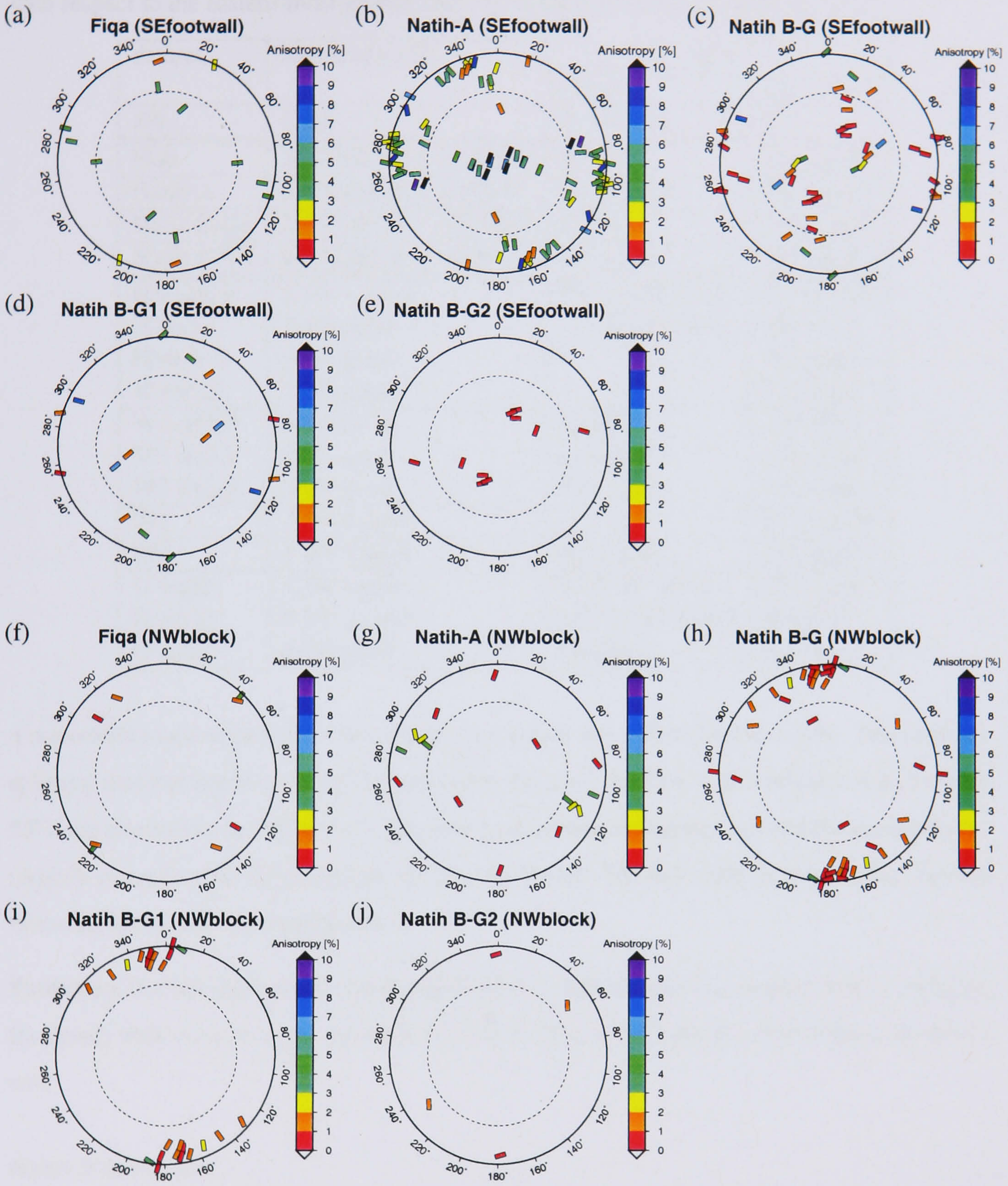

Figure 5.18 Results in Figures 5.16(b,c,d,e,f) confined to the [**top panel**: **a** to **e**] SE of the eastern-most graben fault (SE footwall block) and [**bottom panel**: **f** to **j**] NW of the eastern-most graben fault (NW blocks). Note the large contrast in percent anisotropy between the SE footwall and NW blocks.

Table 5.1 Summary of average percent anisotropy, fast-shear-wave strike and dip in clusters and formations. Confidence in results is indicated by very good to very low coverage. For a given lithology the percent anisotropy varies across the graben faults. SE and NE refer to the location with respect to the eastern-most graben fault. Note the anisotropy is higher to the SE.

dataset	anisotropy [%]	fast	
		strike	dip
All	2.4%	15° & 84°	73°
Fiqa	3.0%(SE) & 2.1%(NW)	90° low	83° good
Natih-A	4.7%(SE) & 1.8%(NW)	19° v.good	75° v.good
Natih B-G1	2.7%(SE) & 1.3%(NW)	45° low	63° v.good
Natih B-G2	0.9%(SE) & 1.1%(NW)	82° good	38° good
Horseshoe	3.1% v.good	52° & 80° v.low	71° v.good
H stn5.1	3.0% good	52° & 80° v.low	68° good
H stn5.3	3.4% good	-	72° good
H stn5.5	1.7% good	-	31° good
W3 stn3.7	4.3% good	variable	26° v.low
W3 stn3.1	8.2% good	17° good	38° v.low
W3 stn2.4	2.6% good	117° v.low	14° v.low
W1	1.1% v.good	-	59° v.good
W4	1.3% v.good	54° v.low	70° good
G well2	1.1% v.good	9° & 89° good	25° v.low
G well3	0.9% v.good	16° & 114° good	69 good°
G well4	0.7% good	variable	60° v.low

a noticeable trend, especially when the B class results are added (Figure 5.19b). The synthetic splitting measurements for a buried permeable unicrack medium with vertical cracks trending 85°E are also shown in Figure 5.19. The observed percent anisotropy and fast dip measurements roughly coincide with the predicted ones for the model. The fast strike is meaningless because of the subhorizontal ray propagation.

Summary The fast dip is vertical (average of 83°). A buried porous unicrack model (moderately fractured) with vertical cracks trending E (crack density = 0.07) fits the observations reasonably well.

Natih A formation

The Natih A dataset (59 results) comes from events that occurred within Natih A formation (858-946 m depth range) and were recorded by stations 2.1, 2.2, 3.1, 4.1, 4.2 and 5.3. Stations 2.1 and 5.3 are a little beyond the Natih A boundaries (Figure 5.17b), but are considered anyway because the raypath is mainly in the Natih A carbonate. The 3D anisotropy plot for Natih A (Figure 5.16c) displays high amounts of anisotropy, between 0–10% (time lag 0–20 ms) with an

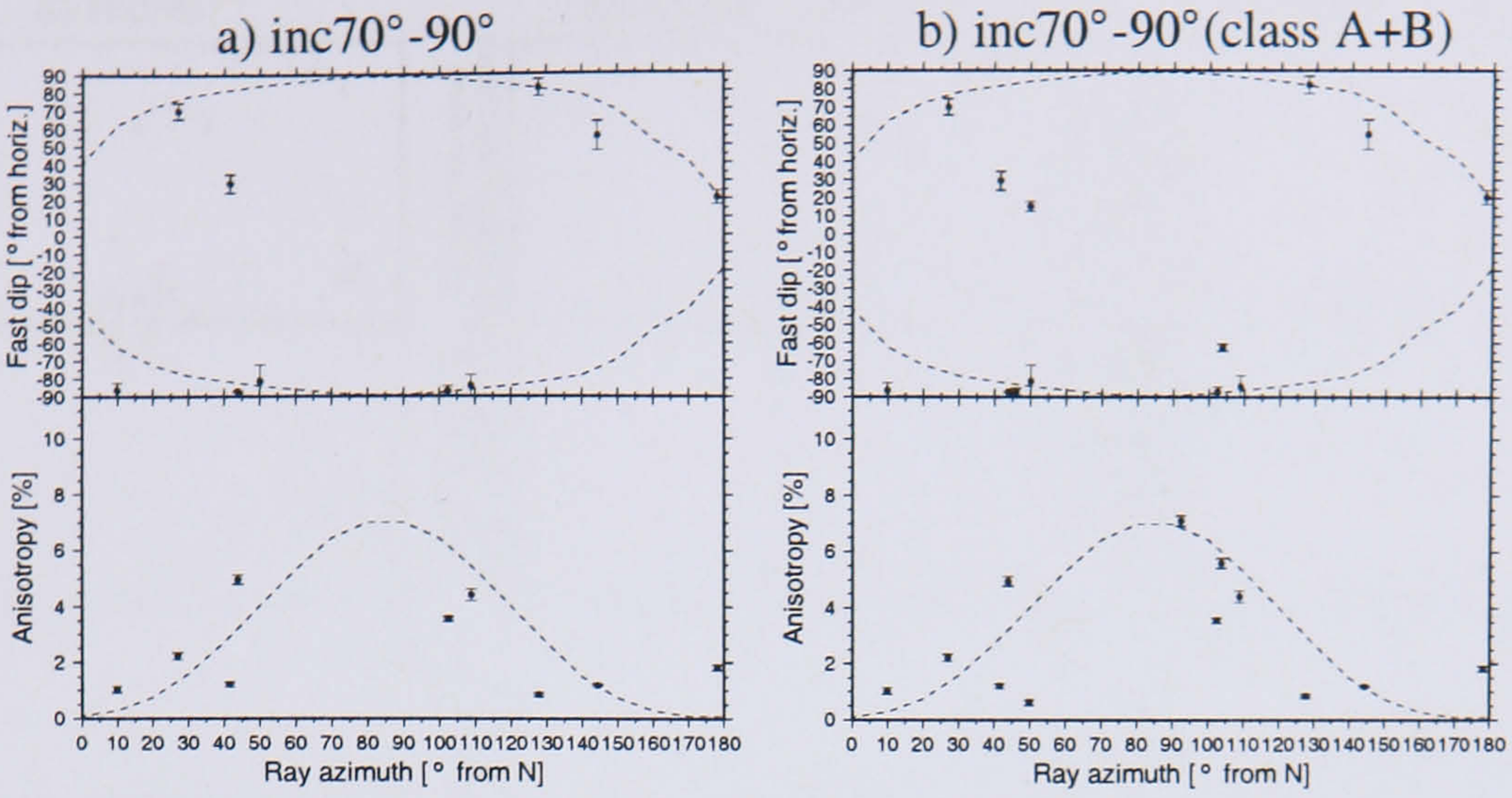

Figure 5.19 Splitting measurements in the Fiqa formation as a function of ray azimuth for the ray inclination range 70°–90° [**a**] A class results only and [**b**] A and B results. The synthetic response (dashed lines) of a ray propagating at a 80° inclination through a buried porous unicrack medium (gas and brine fill have identical responses) with vertical cracks trending 85°E (crack density = 0.07) is also shown. Although the fit between synthetics and real measurements is not perfect, the data show similar trends as the synthetic model in percent anisotropy and fast dip. Note that the fast strike data are not shown because they are meaningless in this case.

average of 4.7%. The fast-shear-wave strike for subvertical rays (Figure 5.16c) shows a NNE trend with an average of 19°. The fast dip for subhorizontal rays show a consistent vertical fast dip, with an average of 75°. This fits well with a buried porous unicrack medium with vertical cracks oriented NNE (compare with Figure 4.10c).

Splitting measurements are plotted as a function of azimuth (Figures 5.20(a,b,c)) for inclination bins of 90° and 60° (without and with B class results), respectively. The synthetic response (dashed lines) for a buried porous unicrack medium with vertical cracks trending 19°NNE are superimposed in Figure 5.20. Also overlain is the 4th degree best fit spline (solid line) to percent anisotropy in Figure 5.20(b,c). The model fit to fast dip (mostly subvertical) is good while the fit in percent anisotropy is poor (Figure 5.20). This may imply spatial variation in fracture density or may imply the model is not correct.

Summary The fast strike and dip are on average 19°NNE and near vertical (75°), respectively. The best fit model of Natih A is a buried porous unicrack medium (highly fractured) with vertical cracks with a dominant trend of 19°NNE (crack density = 0.1). Although the percent anisotropies differ from those predicted by the model, this model remains the best fit model that is consistent with the observed fast wave orientation (strike and dip). However, due to the scatter in anisotropy and low coverage, non porous brine-filled unicrack models and gas-filled bicrack models cannot be ruled out at this stage.

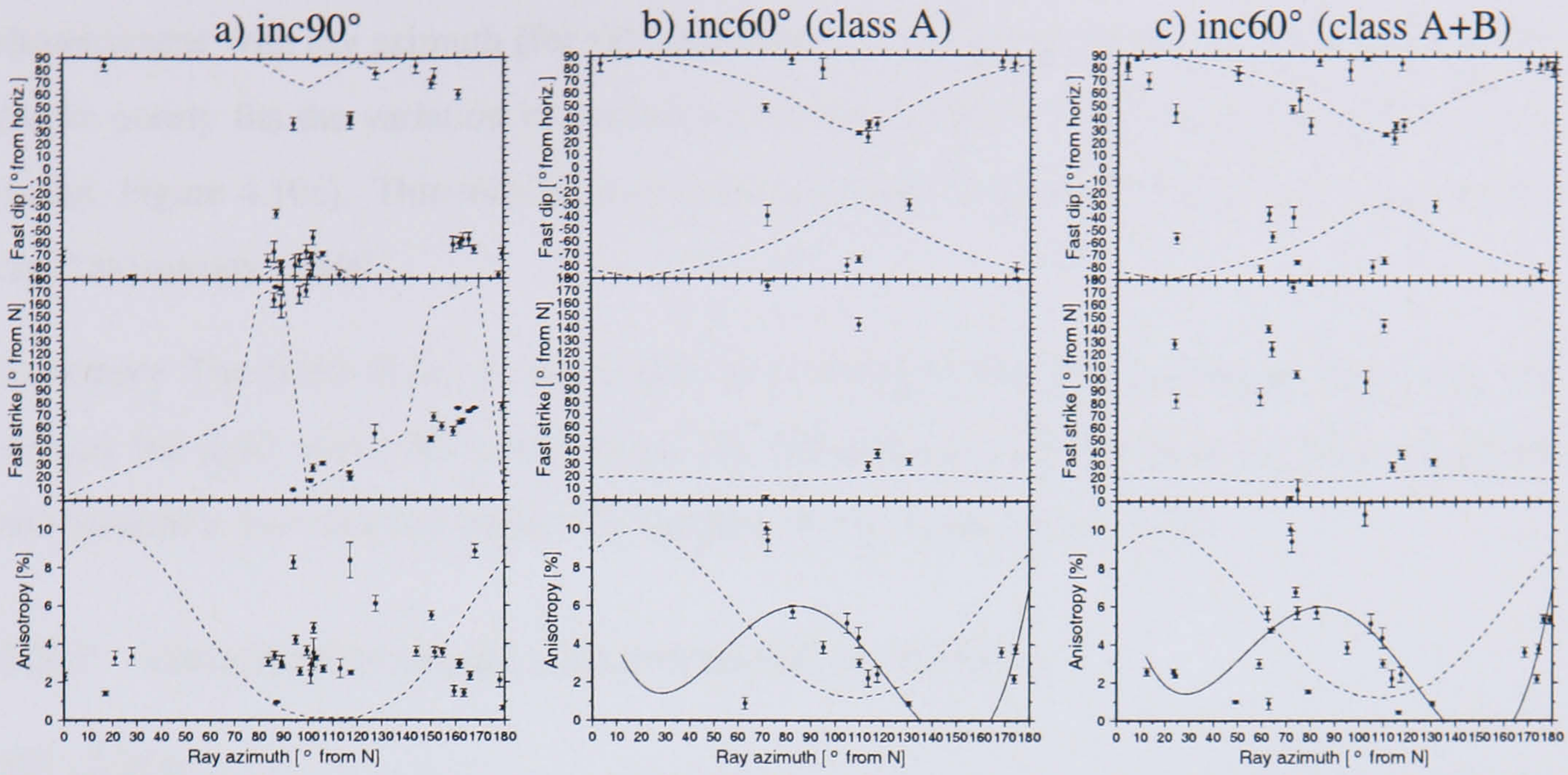

Figure 5.20 Splitting measurements in the Natih-A formation as a function of ray azimuth for ray inclination bins [**a**] 90°, [**b**] 60° for A class results only, [**c**] 60° for A and B class results. Inclination bin size is 30°. The synthetic response (dashed lines) for a buried porous unicrack medium with vertical cracks trending 19°NNE (crack density = 0.1) are superimposed. In (b and c) the 4th degree best-fit spline (solid line) to percent anisotropy in (c) is also shown. Note the fast strike is meaningless in (a). The real fast dip matches those of the model, whereas the percent anisotropy has an azimuthal shift from those predicted by the model.

Natih B-G formation

Events that occurred within the Natih B-G formation (946-1295 m depth range) and were recorded by stations 2.4, 3.5, 3.7, 4.2, 5.3 and 5.5 form the Natih B-G dataset (51 results). The corresponding rays are entirely confined within this formation. The upper and lower part of the Natih B-G (Natih B-G1 and Natih B-G2, respectively) are also separately investigated by considering rays that are entirely confined within each individual formation. This is done by considering that events within Natih B-G1 (946-1120 m depth range) recorded by stations 3.5, 3.7, 4.2, 5.3 and 5.5 form the Natih B-G1 subset (24 results). Similarly, events within Natih B-G2 (1120-1295 m depth range) recorded by stations 2.4 and 5.5 form the Natih B-G2 subset (7 results).

The 3D anisotropy plot for the entire Natih B-G formation (Figure 5.16d) shows that the subhorizontal rays are mainly vertically polarised, with an average of a 74° fast dip. The fast strike (of subvertical rays in Figure 5.16d) has two dominant trends, NE and E. The NE trend appears to be associated with the Natih B-G1 (Figure 5.16e), whereas the E trend is more associated with the lower Natih B-G2 (Figure 5.16f). Figure 5.16e also shows moderate anisotropy with mainly vertical fast dips, while Figure 5.16f shows weak anisotropy with horizontally polarised fast-shear-waves. This indicates the presence of vertical fractures and intrinsic VTI background in the upper and lower part of the Natih B-G formation, respectively. The percent anisotropy

shows scatter with ray azimuth (for subhorizontal rays in Figures 5.16(d,e)) and a model of NE cracks poorly fits the variation in percent anisotropy (compare with a buried porous unicrack model, Figure 4.10c). This may indicate heterogeneities in fracture density or a more complicated anisotropy model.

Summary The Natih B-G1 is moderately and vertically fractured (moderate anisotropy and vertical fast dips) with a NE crack strike. The Natih B-G2 is weakly fractured (low anisotropy and horizontal fast dips indicating VTI background) with an E crack trend.

5.3.2 Variations between clusters based on location

W1 cluster

The W1 events cluster along the eastern-most fault (Figure 5.17a) and are recorded by station 1.1. They sample the SW region bounded by the two large-scale faults (Figure 5.9a). The W1 subset consists of 34 results. Unfortunately, all these results fall into a very narrow ray orientation range (Figure 5.16g), rendering detailed analysis impossible. The lack of subvertical rays renders determination of crack strike unfeasible (Figure 5.16g). The subhorizontal rays show subvertical fast dips (Figure 5.16g) indicating vertical fracturing. The percent anisotropy (Figure 5.16g) is consistently low (average 1.1%).

Summary A weakly vertically fractured model (1% anisotropy) fits the W1 cluster, but there is no information on crack strike due to limited ray coverage.

W4 cluster

The W4 events cluster along the western-most fault (Figure 5.17a) and are recorded by well 4 stations (stations 4.1 and 4.2). They sample the region just west of the fault (Figure 5.9a). The W4 subset consists of 24 results. Similar to the W1 cluster distribution, all W4 results are limited to a narrow ray orientation range (Figure 5.16h). Therefore, a detailed analysis of the anisotropy is not possible. The subhorizontal rays (Figure 5.16h) indicate vertically polarised fast-shear-waves (average 70° fast dip) and hence vertical fracturing. Similar to the W1 subset, the poor coverage in subvertical rays (Figure 5.16h) renders confident estimation of crack strike impossible. The percent anisotropy (Figure 5.16h) is consistently low (average 1.3%).

Summary Similarly to the W1 cluster, a weakly vertically fractured model (1.3%) fits the W4 cluster, but there is no information on crack strike due to limited ray coverage.

G cluster

The G cluster lies along the eastern-most fault (Figure 5.17a). The events in the G cluster are located in a column between 740-1550 m depth (Figure 5.17b). The rays sample formations above Shuaiba. Recordings of events in the G cluster by wells 2 (26 results), 3 (28 results) and 4 (7 results) form the G subset (total 61 results). Wells 3 and 4 cover Fiqa, Natih A and Natih B-G1 (shallow) while well 2 also covers Natih B-G2 (deep). The 3D anisotropy plot of the G subset excluding the deepest station 2.4 (Figure 5.16i) shows that percent anisotropy is consistently low (average 1%). The fast dip for the subhorizontal rays (Figure 5.16i) is mainly vertical (average 64°) indicating subvertical fracturing. The fast strike of the subvertical rays (Figure 5.16i) shows two main trends, NNE and E (as seen in the entire dataset). This is due to the different lithologies sampled by the G subset.

Splitting measurements as a function of ray inclination are shown in Figure 5.21 for well 2. Also plotted is the response of pure VTI medium (dash line). The observations from well 2 correlate well with the model, particularly the fast dip. This favors the presence of intrinsic VTI background around well 2, which mostly samples the deeper part of the Natih B-G.

Summary Similarly to the W1 and W4 clusters, a weakly vertically fractured model (1%) fits the G cluster data (for wells 3 and 4, i.e., top part), with crack strike dominantly either NNE or E depending on the sampled lithology. For the deeper part of the Natih B-G (well 2), the most likely model is a VTI background anisotropy.

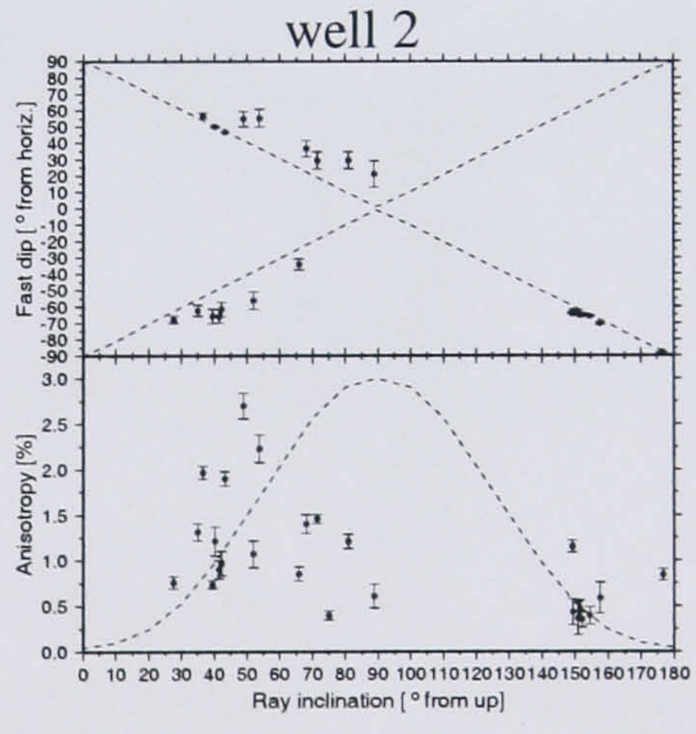

Figure 5.21 Splitting measurements as a function of ray inclination from the G data recorded in well 2. The synthetic response (dashed lines) of a VTI symmetry (3% anisotropy) is superimposed. The fast strike is meaningless for VTI symmetry because fast shear-waves are horizontally polarised. Note the good match between the VTI model and the data in well 2 indicating a VTI background.

Horseshoe (H) cluster

The Horseshoe cluster is located within the Natih A formation around well 5 (Figure 5.17). Recordings of H events by well 5 stations form the H dataset (88 results). The 3D anisotropy plot of the H cluster excluding results belonging to the deep station 5.5 (Figure 5.16j) shows relatively high values of anisotropy, 0-10% with an average of 3.1%. The vertical ray coverage is poor in the H cluster (Figure 5.16j) rendering estimation of crack strike difficult. The fast-shear-waves for subhorizontal rays (Figure 5.16j) are mainly polarised vertically (average 71° fast dip) indicating a subvertically fractured medium. The splitting observations at the shallow stations (mostly sampling Natih A) versus deeper station 5.5 (mostly sampling Natih B-G) are shown in Figures 5.22(a,b), respectively. The predicted response of a buried porous unicrack model (with a 90° crack strike) and a VTI symmetry model are also shown in Figure 5.22. The observations support a fractured model in the Natih A and a VTI background model (weaker anisotropy, average 1.7%, and horizontally polarised fast waves) in the deeper Natih B-G. Figure 5.22a shows considerable scatter in percent anisotropy around the model prediction. This is perhaps due to inhomogeneities in fracture intensity. Due to this large degree of scatter the crack strike is only roughly constrained to be E.

Summary The most likely model for the H cluster is a highly fractured medium (0-10%) for the Natih A formation (constrained by the top stations 5.1 and 5.3) and a weakly fractured medium with stronger VTI background for the Natih B-G formation (constrained by the deeper station 5.5).

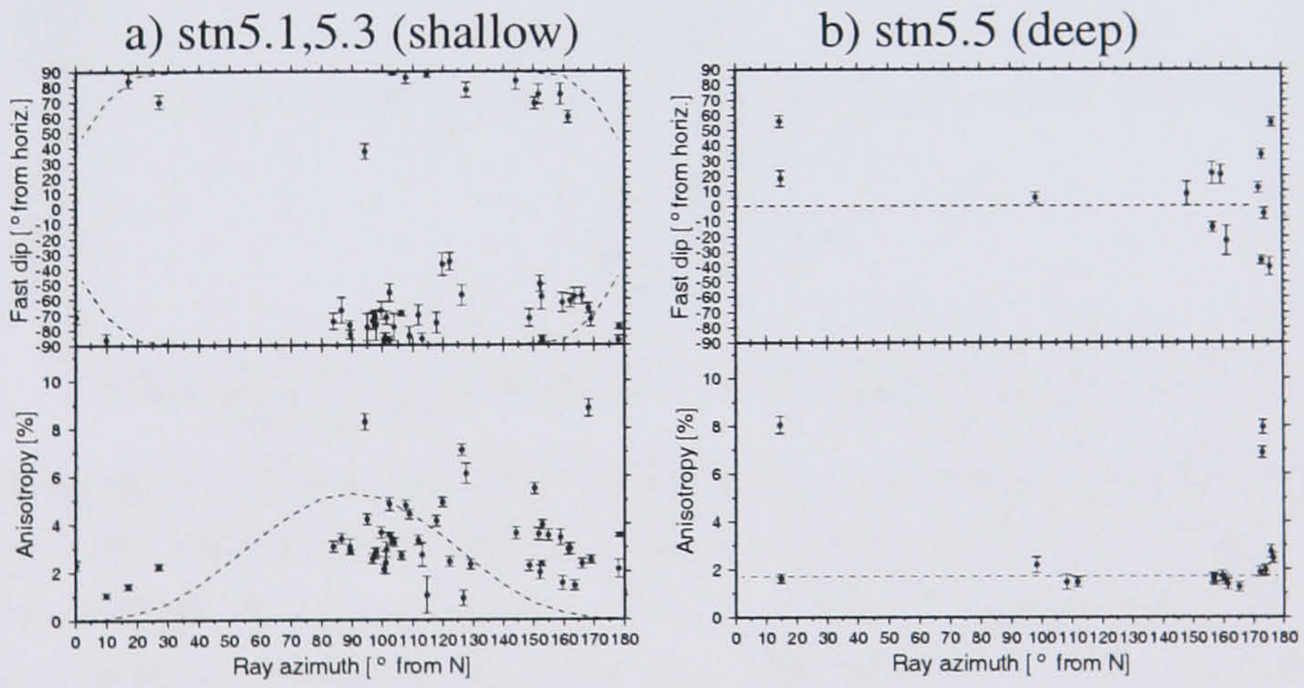

Figure 5.22 Splitting measurements for the Horseshoe cluster as a function of ray azimuth for subhorizontal rays (inclinations ±15° off horizontal) [**a**] shallow stations 5.1 and 5.3, and [**b**] deeper station 5.5. The synthetic response (dashed lines) for a buried porous unicrack medium (gas and brine fill have identical responses) with vertical cracks trending 90°E (crack density = 0.05) and a VTI symmetry (1.7% anisotropy) are superimposed in (a) and (b), respectively. Note the fit of vertical fracturing with high anisotropy in the shallow stations in (a) and intrinsic VTI background with low anisotropy for the deeper station in (b).

W3 cluster

An event cluster lies around well 3 (Figure 5.17a) and is therefore named the W3 subset. The W3 events are mostly located in the Natih A layer and are recorded by stations 3.7, 3.1 and 2.4. The 3D anisotropy plot (Figure 5.16k) shows significant (0-10%) anisotropy and a NNE fast strike for subvertical rays. This suggests a highly fractured medium with cracks trending NNE. The NNE trend is the same as that derived for the Natih A in general (compare with Figure 5.16c). A large part of the W3 subset samples the Natih A formation. The 3D anisotropy plot of the W3 subset (Figure 5.16k) is also very similar to that of a buried porous unicrack model (Figure 4.10c).

The splitting measurements as a function of ray inclination for the deeper station 2.4 are plotted in Figure 5.23. The response of a pure VTI medium (dashed line) is superimposed. The fast dip coincides well with the model predictions. Although the data ray coverage is low, the low anisotropy (2.6%) and the match between the model and observations are suggestive of a VTI background symmetry in the deeper parts of the Natih B-G.

Summary The most likely model for the W3 cluster is a highly fractured buried porous medium (0-10%) anisotropy for the upper part of the Yibal field. The dominant fracture trend is NNE. For the lower part of the Natih B-G (station 2.4), a VTI background fits the data quite well.

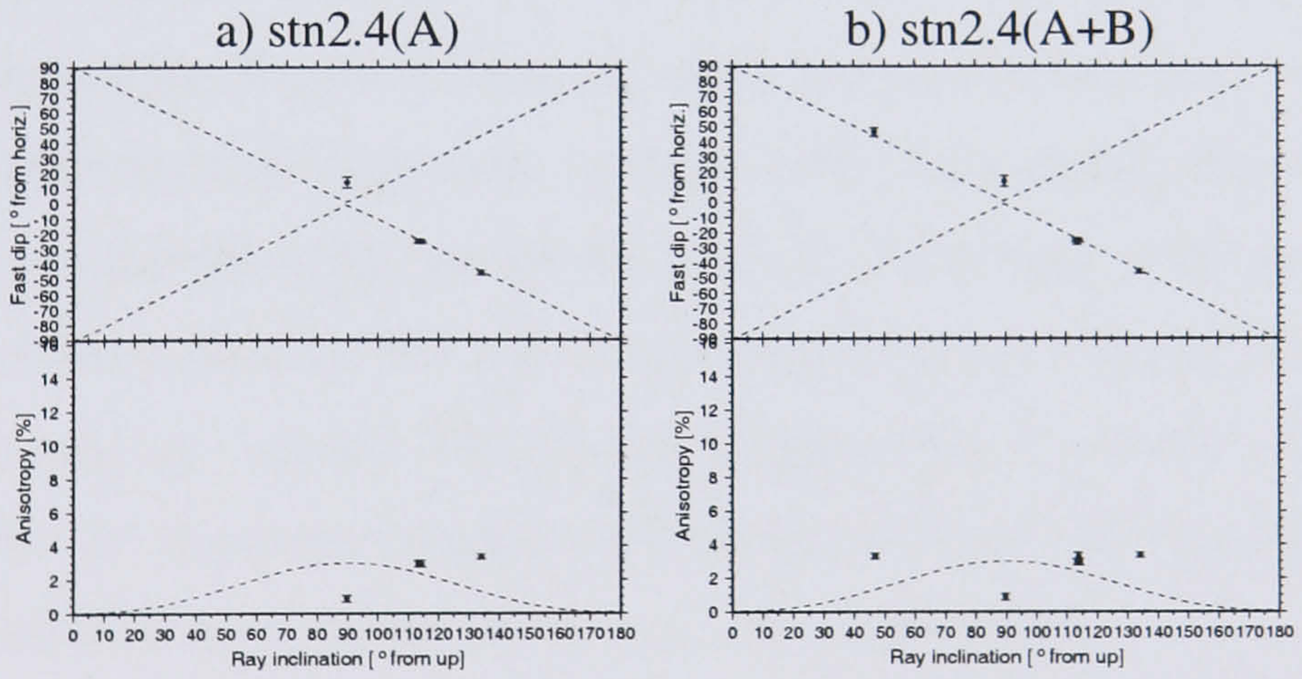

Figure 5.23 Splitting measurements for the W3 subset as a function of ray inclination for station 2.4 [**a**] without and [**b**] with B class results. The synthetic response (dashed lines) of a VTI symmetry (3% anisotropy) is superimposed. The fast strike is meaningless for VTI symmetry because fast shear-waves are horizontally polarised. The fit between the real and synthetic VTI values is considerable indicating elements of VTI background.

5.4 Summary of key observations

5.4.1 Lateral variation in fracture density

Figure 5.9 shows well defined fault-related lateral variations in the magnitude of the anisotropy. The percent anisotropy decays dramatically across the main graben faults from about 5-10% in the SE of the eastern-most fault, to about 1% on the other side. This reflects high and low fracture intensity in the SE footwall and NW block, respectively. The trend is even clearer in the cross sections of each block in Figure 5.10. The trend is also highlighted by the change from high anisotropy in the SE footwall clusters H (Figure 5.16j) and W3 (Figure 5.16k) to low anisotropy for the NW block clusters W1 and W4 (Figures 5.16(g,h), respectively).

This lateral variation in the magnitude of anisotropy is also manifested in Figure 5.18 where each of the studied lithological intervals in the SE footwall has higher anisotropy magnitude than in the NW block, except in the Natih B-G2. The Natih B-G2 formation exhibits similar weak anisotropy magnitude of about 1% in both blocks (Figures 5.9 and 5.18). A maximum anisotropy of 10% suggests fracture density on the order of 0.1.

5.4.2 Vertical variation in fracture density

The anisotropy also seems to correlate with the nature of the rock. In the SE footwall where the fracture density is high, Figures 5.18(a,b,d,e) show that percent anisotropy is highest (4.7% average) in the carbonate Natih-A reservoir, moderate (3%) in the capping Fiqa shale, moderate (2.7%) in the non-producing upper part of the Natih B-G carbonate, and low (0.9%) in the lowermost parts of the Natih B-G. This is also illustrated in Figures 5.9b and 5.10b. In contrast, these units in the hanging wall and NW footwall (Figures 5.9b, 5.10a and 5.18(f,g,i,j)) show much lower degrees of anisotropy, moderate in Natih-A and Fiqa (1.8% and 2.1%) and low in the upper and lower parts of Natih B-G (1.3% and 1.1%), respectively.

This vertical variation in anisotropy is also observed in the H, W3 and W4 subsets. For the H cluster, Figure 5.22 shows that the percent anisotropy for stations 5.1 and 5.3 (sampling Fiqa/Natih-A) is higher than station 5.5 (mostly sampling the deeper Natih B-G1) (see Figure 5.17b for event-station configuration). This agrees with the interpretation above. For the W3 cluster, the percent anisotropy decreases from station 3.1 (mainly sampling Natih A), to station 3.7 (Natih B-G1) and finally to station 2.4 (Natih B-G) (Table 5.1). This also agrees with the observed relative degree of anisotropy between lithological units.

5.4.3 Fracture strike

A guideline derived from the synthetic modelling is that subvertical rays recover the crack strike and subhorizontal rays retrieve the crack dip (vertically aligned fractures produce vertically polarised fast shear-waves). The subvertically propagating rays for the entire dataset (Figure 5.4) indicate two predominant fracture strikes, one oriented north-north-east (NNE) and the other east (E). As with the anisotropy magnitude, the fast strike also appears to correlate with the nature of the rock. In the more strongly anisotropic Natih-A gas reservoir (Figure 5.16c) and the Natih-A sampled by the W3 cluster by station 3.1 (Figure 5.16k), the fracture alignment is more purely NNE. The fast strikes in the moderately anisotropic Natih B-G1 and weakly anisotropic Natih B-G2 (Figures 5.16(e,f)) suggest NE and E crack trends, respectively. The observations in the moderately anisotropic Fiqa cap rock suggest an E crack trend (Figure 5.19).

5.4.4 Fracture dip

Subhorizontal rays propagating in the Fiqa, Natih-A reservoir, Natih B-G1, and the clusters W1, W4, G and cluster H, indicate near vertical fracturing with average dip of 73° from horizontal (Figures 5.16(b,c,e,g,h,i,j)). In contrast, results for the Natih B-G2 (Figure 5.16f) and the deep stations 2.4 and 5.5 of clusters G, H and W3 (Figures 5.16l, 5.21, 5.22 and 5.23) indicate horizontally polarised fast shear-waves and low anisotropy. These results are confined mainly to the deeper parts of the Natih B-G and comparisons with the VTI example (Figure 4.10k) suggests a weak VTI background anisotropy.

5.4.5 HTI and VTI model fit

The fit of HTI and VTI to the real data is considerable for the fast wave orientation. Occasionally, the real data are well represented by the model (e.g., compare the W3 subset results in Figure 5.16k with the unicrack model in Figure 4.10c). Similarly, the deeper parts of the field are reasonably well represented by a VTI model for subhorizontal rays (compare Figure 5.16l with 4.10k). However, the model agreements are less clear when considering azimuthal variations in percent anisotropy for subhorizontal rays. This may indicate non-uniform fracture density in the subsurface or it may indicate a more complicated fracture model. Unravelling the effects of heterogeneity versus anisotropy is a challenge even with good data coverage.

5.5 Discussion and interpretation

Spatial variation in fracture density— The vertical variations in anisotropy magnitude observed in the Yibal field are consistent with the observations of Potters et al. (1999) for the Natih Field (a nearby field that shares the same geological history, since both are part of the Fahud Salt Basin). Over the strongly anisotropic Natih A reservoir, our δt (0–20 ms) and percent anisotropy (0–10%) at Yibal agree with the Natih A results of Potters et al. (1999) (30 ms and 15%, respectively). Our results showing a moderately anisotropic Fiqa cap rock (0–10 ms time lag, 0-5% percent anisotropy) also agree with the Fiqa results of Potters et al. (1999) (0–8 ms) in the Natih field.

Our percent anisotropy results in the Fiqa (3%), Natih B-G1 (2.7%) and Natih B-G2 (1%) approximately match those inferred from dipole-shear logs (4%, 2% and 1%, respectively, see Chapter 2). In contrast, the Natih A reservoir (highest anisotropy of 5% average) is higher than that inferred from dipole-shear logs (2%). This may reflect larger-scale fractures in the Natih A that cannot be imaged by high frequency tools that probe short distances (often significantly shorter than the fracture spacing) and fine-scale fractures in the other formations. Additionally, the large amounts of anisotropy in the Natih A reservoir are consistent with the known geology, the reservoir is highly fractured (see Chapter 2).

An abrupt reduction in percent anisotropy is observed across the eastern-most graben fault from the south-east footwall (5–10%) to the north-west blocks (1%) in Fiqa, Natih A and Natih B-G1. No evidence of this is observed at deeper levels (e.g., the Natih B-G2). This fault-related lateral variation agrees with the geology where the crest and southern flank of the field is fractured more extensively than the northern flank. The absence of this lateral variation below Natih B-G1 agrees with the constant fracture density in the Shuaiba reservoir (deeper) inferred from FMI logs (Figure 2.7).

The poor fit of the fractured model to the observed percent anisotropy within each layer may imply significant spatial variations in fracture density. This agrees with the findings of Al-Busaidi (1997) where unevenly distributed zones of dense fractures were observed in FMI logs. Since the estimated percent anisotropy is a minimum value, it represents an average of highly fractured zones and unfractured zones that the ray may sample.

Fracture strike— The observed NNE trend in the Natih A reservoir roughly agrees with the regional maximum stress direction (NE) in Oman. The NNE trend also agrees with field data derived from Natih formation outcrops in the Salakh arch (130 km east of Yibal) where the

dominant fracture strike is NNE (after Mohammed Al-Kindi, Earth Sciences, Leeds Uni., pers. comm.). Moreover, the observed NNE fast strike is also similar to the fast strike results of Potters et al. (1999) (who reported a mainly NE orientation).

Fracture dip— In the Natih A reservoir, the observed subvertical fast dip (average 75°) is in good agreement with the fracture dip data (70°) from FMI logs in the Natih A (see Chapter 2). It also agrees with the field data of the Natih Formation outcrops in the Salakh arch conducted by Mercadier and Mäkel (1989). The observed subvertical fractures (75° dip in the reservoir) also support the idea of Sayers (2002) that non-vertical fractures may well be responsible for the observation of van der Kolk et al. (2001) of higher and lower shear-wave splitting anomaly in the gas and oil-filled parts, respectively, of the reservoir in the Natih field (i.e. shear-wave splitting is dependent on crack-fluid type).

5.6 Conclusions

Over 600 events are recorded by up to 10 downhole seismometers deployed in 5 boreholes, resulting in nearly 2500 shear-wave splitting measurements. Stringent quality control reduces the number of reliable measurements to 398. The microseismic experiment provided a unique resolution of anisotropy in the individual formations in the Yibal Field.

The results of the shear-wave splitting analysis were significantly useful in distinguishing between fracture-induced anisotropy and the intrinsic anisotropy of the rock. Specifically, percent anisotropy, and fast-shear-wave orientations (strike,dip) provide invaluable constraints on the relative density, strike and dip of fractures. The observations closely agree with the structural geology of the area.

Splitting magnitudes range from 0–20 ms, corresponding to 0–10% anisotropy. The largest anisotropy values lie to the SE (5–10%) and are bounded by a NE-trending major graben fault. Anisotropy is also observed to be depth-dependent. The highly fractured Natih A carbonate reservoir shows the highest percent anisotropy (5% average) compared to the moderately fractured capping Fiqa shale, the upper part of the Natih B-G carbonate (3%) and the weakly fractured lower part of the Natih B-G (1%). These values agree with anisotropy inferred from shear-dipole logs except in the Natih A where it is lower than 5% anisotropy, possibly reflecting larger fractures in the Natih A formation compared to smaller ones in the others. The fast-shear-wave orientations are interpreted in terms of a single set of aligned subvertical fractures trending north-north-east (NNE) in the Natih A; east (E) in the Fiqa and the lower part of Natih B-G; and

north-east (NE) in the upper part of Natih B-G. The vertical NNE fractures in Natih A agree with the known geology of the reservoir.

Shallow parts of the field show high anisotropy and subvertically polarised shear-waves that are attributed to fractures and cracks. In contrast, deeper parts of the field show low amounts of anisotropy and subhorizontally polarised fast-shear waves, which are attributed to the intrinsic anisotropy of the rock, rather than fractures or cracks. Collectively, our results suggest that the anisotropy is controlled by both rock-type and fault-related fracturing.

I also investigated temporal variations in shear-wave splitting measurements. However, no statistically significant variations were detected. For completeness they are included in the Appendix H.

Chapter 6

Frequency-dependent anisotropy

6.1 Introduction

In many reservoirs fracture orientations, densities and sizes control hydrocarbon production. In the previous chapter, the first two parameters (fracture orientations and density) were estimated using shear-wave splitting analysis. The only left unknown is the third parameter (fracture size) to fully determine the fracture geometry, which can be fed to a geomechanical model of Yibal. Liu et al. (2003b) estimated fracture size using the effective-medium theory of Chapman (2003) and observations of frequency-dependent shear-wave splitting. In this chapter, I follow their approach by using the Chapman crack model to estimate the fracture sizes in the Yibal and Valhall fields from microseismic data.

Mechanisms that are capable of producing frequency-dependent anisotropy are first outlined. The method used for filtering is introduced and the splitting analysis is then shown. The results are then compared with Chapman model predictions and the best fit fracture size is evaluated. Finally, filtering sensitivity tests are carried out to investigate the influence of filter parameters on the results.

6.2 Background

Recent shear-wave splitting studies have observed decreases in splitting lag time with increasing frequency (Chesnokov et al., 2001; Liu et al., 2001; Marson-Pidgeon and Savage, 1997). In some cases, fast shear strike ψ was also observed to vary with frequency (Liu et al., 2001; Fouch and Fischer, 1998). The observed frequency-dependent anisotropy can be explained by two mechanisms: scattering and fluid flow.

6.2.1 Mechanisms: Scattering versus fluid flow

Scattering by inhomogeneities

Scattering-induced anisotropy can only be observed when the seismic wavelength is longer than the size of the inhomogeneities. With decreasing wavelength (caused by increasing frequency) the propagating wave senses individual heterogeneities, which results in a decrease in anisotropy and propagation becomes better characterised by scattering (Tod and Liu, 2002). Mathematically anisotropy occurs when $\lambda \gg a_f$ where λ is seismic wavelength and a_f is scale length of fractures (Liu et al., 2003c) (in contrast scattering occurs when $\lambda \ll a_f$). For the Yibal dataset, anisotropy is expected to be caused by fractures smaller than 5–100 m (for an average S-wave velocity, v_s, of 2 km/s and frequency band 20-400 Hz). Larger fractures than 5–100 m will cause scattering. Similarly, for the Valhall dataset, fractures larger than 10–60 m (for v_s=0.6 km/s and frequency range 10–70 Hz) will cause scattering.

Fluid flow in fractured porous rock during seismic wave propagation

Seismic wave propagation induces pressure gradients that cause fluid exchange between inclusions (squirt-flow) to achieve pressure equalisation (Chapman, 2003). The time taken to achieve the latter is called the relaxation time (related to squirt-flow frequency). The relaxation time depends on fracture size (smaller times for grain-scale flow and larger times for macro-scale crack flow). The ratio of surface area to volume decreases with increasing fracture size resulting in more fluid having to move through an element of surface area to equalize the pressure, which requires more time (Maultzsch et al., 2003). For a given fracture size, perfect equalisation occurs in low frequencies and its degree decreases (over squirt-flow frequency) with increasing frequency where it is partly equalised. Fractured rock, therefore, causes dispersion over the seismic frequency band instead of in the sonic frequency band as is the case with unfractured rock (Chapman, 2003).

In porous media at low-frequencies, Brown and Gurevich (2004) modelled frequency-dependent anisotropy induced by penny-shaped aligned cracks based on a combination of anisotropic Gassmann fluid substitution and a dispersion relationship. They validated their model by using experimental measurements of angle-dependent wave velocities for a synthetic porous sandstone with aligned disc-shaped cracks. Their model agreed closely with experimental measurements.

6.2.2 Dependence of δt and ψ on fracture size

More important to our study, fracture size has been estimated in low porosity reservoirs by Liu et al. (2003b) and Maultzsch et al. (2003). Using an effective-medium theory that models frequency-dependent anisotropy and is sensitive to fracture length scale, they computed the frequency-dependent variation in shear-wave splitting as a function of fracture size, assuming random grain-scale cracks and aligned fractures. Their result is shown in Figure 6.1 which shows a transition frequency band where percent anisotropy decays with increasing frequency. The transition frequency band is dependent on the fracture size (Figure 6.1).

Liu et al. (2003a) extended the model of Chapman (2003) to incorporate both aligned micro-cracks and aligned fractures. They found that the fast-shear wave polarisation is strongly dependent on frequency and fracture size, and that also depends on the angle of incidence and azimuths relative to the fracture and crack orientations (as was also shown in Chapter 4). In general, the high frequency band gives the (small scale) macro-crack direction while low frequencies indicate the orientation of (larger scale) fractures. However this interpretation should be used with care because the fast-shear wave polarisation is also dependent on incidence angle and azimuth (Liu et al., 2003a).

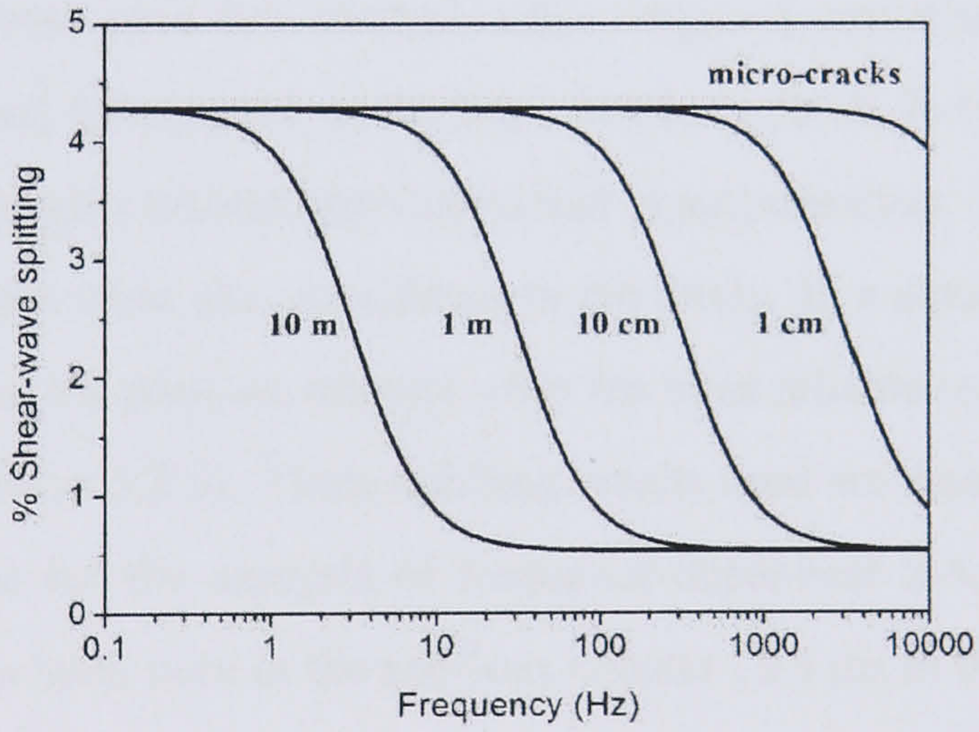

Figure 6.1 Percentage shear-wave splitting as a function of frequency for different fracture sizes. The waves are propagating at an angle of 60° measured from the fracture normal. For a given fracture size there is a transition frequency range where the anisotropy dies quickly with increasing frequency (after Chapman, 2003).

6.3 Method

As described in Section 1.9, the data recorded in the ENZ coordinate frame are rotated to ray coordinates before filtering. The data are filtered with a one octave passband (i.e., a constant

ratio of high to low frequencies of 2). Normally, ranges of 5–10 Hz, 10–20 Hz, 20–40 Hz, 30–60 Hz, etc, are considered but any intermediate frequency band (e.g., 7–14 Hz) can be used if necessary. The filtering stops at the frequency band where the signal is absent in the original signal spectrum. A Butterworth filter with 6 poles is used. A 1-pass filter is used instead of a 2-pass filter to avoid ringing effects that make splitting analysis difficult and result in higher uncertainties. A one pass filter can be used since the relative time is only desired, not the absolute time.

For each frequency-band, the shear-wave splitting analysis is performed (as described in Section 5.2) to estimate δt and ψ. Additionally, for each frequency-band, the dominant frequency (f_d) is calculated based on the definition of Barnes (1993),

$$f_d^2 = \frac{\int_0^\infty f^2 P(f) df}{\int_0^\infty P(f) df}, \tag{6.1}$$

where f and $P(f)$ are the frequency and power spectrum, respectively.

6.4 Results

The Yibal subset of microseismic data studied in this chapter is comprised of data with raypaths confined to the individual lithological units, Fiqa, Natih A, Natih B-G1 and Natih B-G2 (see Section 5.3.1). This is to gain insights into individual layer properties. Examples of the Valhall 1998 microseismic dataset were also considered in this study. In a similar manner to the shear-wave splitting analysis in the previous chapter, only the most reliable results are used (i.e., class A results, defined in Section 5.2.3). These splitting results used are listed in Appendix A (Table A.2). The error criteria for the analysis of frequency-dependent S-wave splitting is slightly increased from what has been used in the previous chapter ($\pm$3 ms in δt and $\pm 20°$ in angles of ψ(strike,dip)).

The S-wave frequency content for each carbonate and shale formation is illustrated in Figures 6.2(a,b), respectively (based on a representative example confined to these layers). The carbonate layers generally have broader bandwidth than the shales. This is due to the attenuation being higher in shales and lower in chalks (Sheriff and Geldart, 1994). The frequency bandwidth is broadest in the Natih A carbonate reservoir (10–500 Hz) and narrowest in the Valhall field (10–70 Hz). The best frequency band coverage for frequency-dependent splitting measurements is found in the Natih A reservoir.

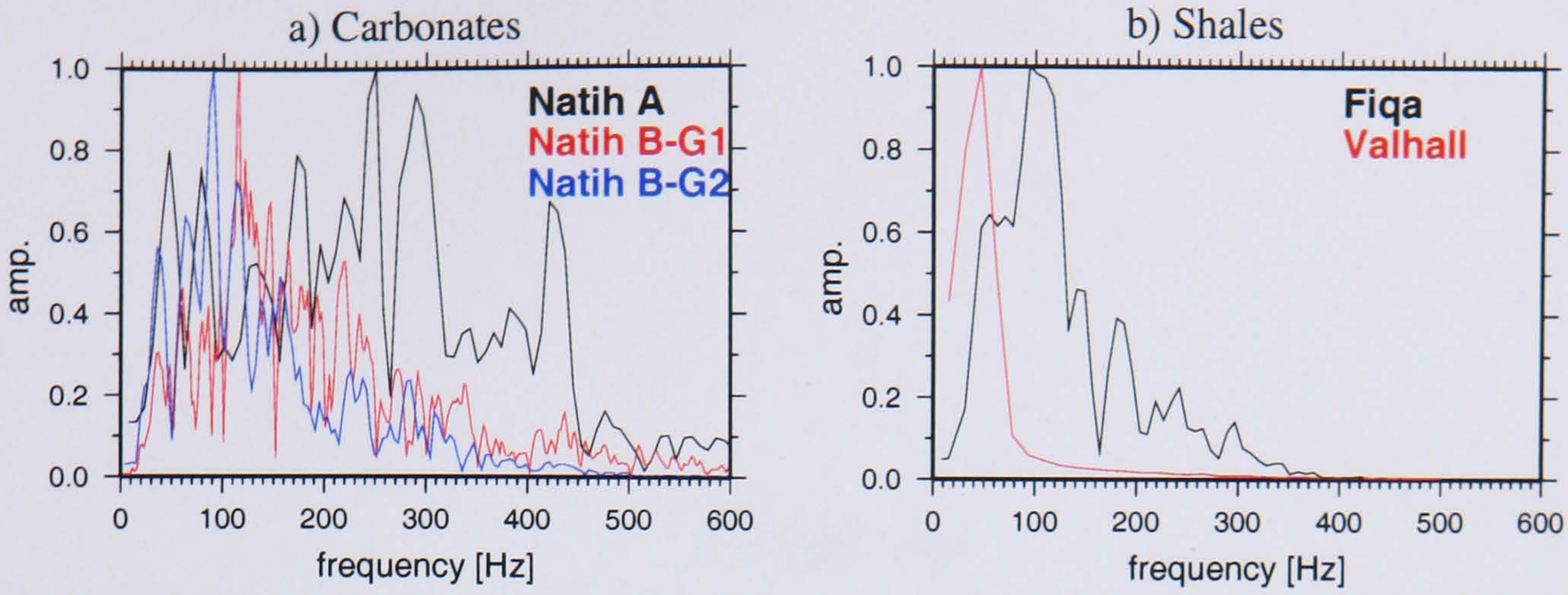

Figure 6.2 Normalised S-wave amplitude spectra for the analysed carbonate sequences (**a**) and shales (**b**) used in this study. The seismogram examples used for the Yibal field (Natih A, Natih B-G1, Natih B-G2, Fiqa) and the Valhall field are y020605.0216.5.3, y021021.0003.3.7, y021020.0001.2.4, y020608.0505.5.1 and v980605.0047.1.3, respectively. Note the narrow frequency band in the Valhall field (shale) and wide frequency band in the Yibal field (particularly in the Natih A reservoir).

6.4.1 Results for lithological units

Frequency-dependent S-wave splitting analysis was applied to: 10 event-receiver combinations entirely confined to the Fiqa formation; 17 to Natih A; 3 to Natih B-G1; 3 to Natih B-G2; and 12 events for the Valhall field. Of these only 5 Fiqa, 12 Natih A, 2 Natih B-G1, 0 Natih B-G2 and 8 Valhall examples gave results with good frequency coverage. In total 19 event-receiver combinations were considered in the Yibal field and 8 events were used in the Valhall field.

For each Valhall event, the analysis was performed on the top 3 stations. Since these stations are only 20 m vertically apart, the corresponding rays approximately sample the same rock with the same orientation. For better frequency coverage, therefore, results from the 3 top stations were calculated for each event. In addition, the bias of poorly clamped and rotating geophones with time in the Valhall microseismic experiment is accounted for by using the corrections of De Meersman (2005) when estimating the strike of the fast shear-wave.

The splitting measurements as a function of dominant frequency are presented in Figures 6.3, 6.4 and 6.5 for the Yibal formations, Fiqa, Natih A and Natih B-G1, respectively. Results for the Valhall field are shown in Figure 6.6. Each event-receiver combination in Yibal (or each event in Valhall) is illustrated with different colour to show the individual trends. The results show large variability in the recovery of reliable estimates of anisotropy. There are several frequency bands over which reliable estimates are not possible to obtain. This is highly dependent on the frequency content of the shear-waves.

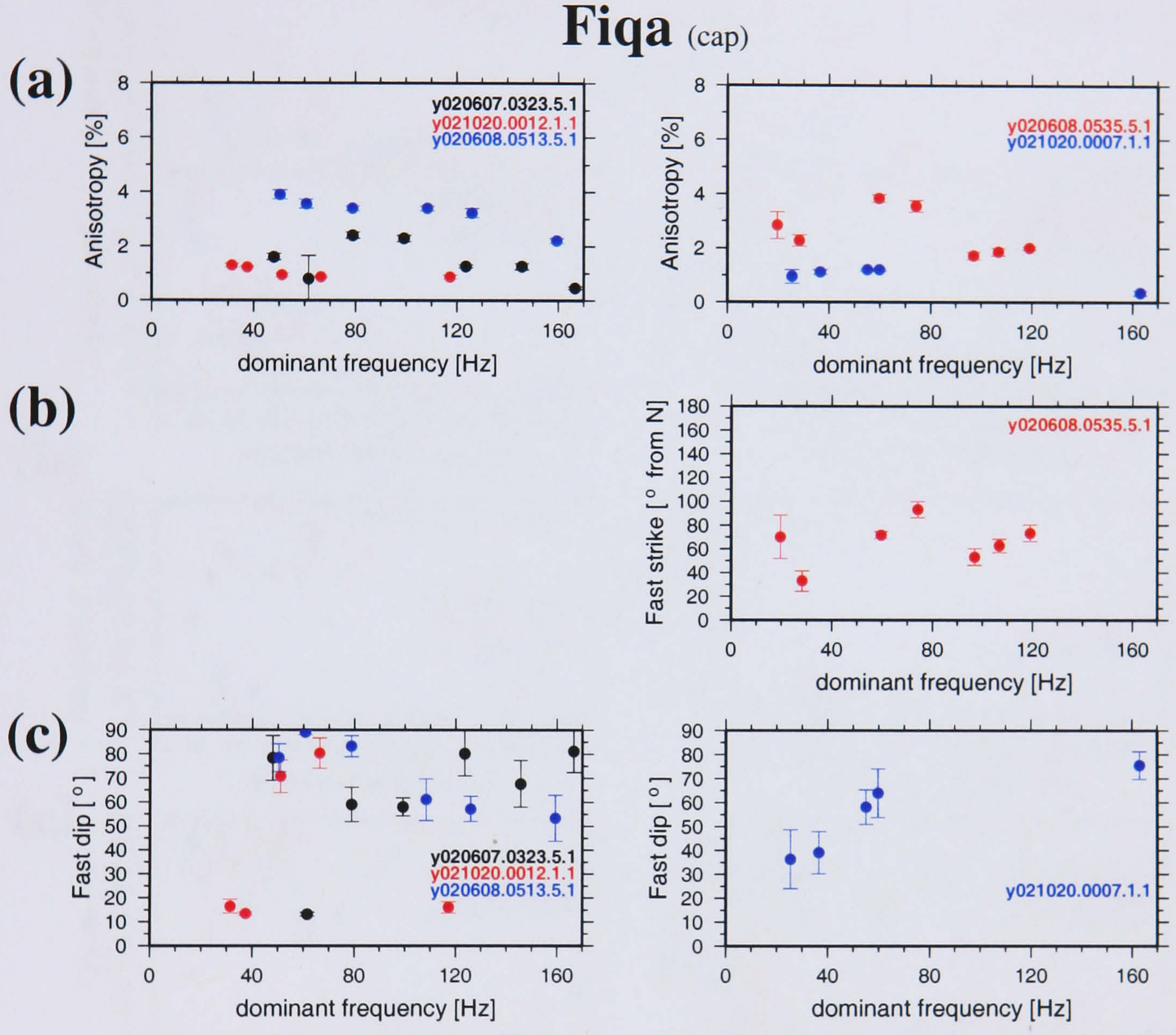

Figure 6.3 Splitting measurements as a function of dominant frequency for 5 event-station pairs where waves have propagated within the Fiqa formation. [**a**] Percent anisotropy, [**b**] fast-shear-wave strike for subvertical rays (±60° off vertical) and [**c**] fast-shear dip for subhorizontal rays (±15° off horizontal).

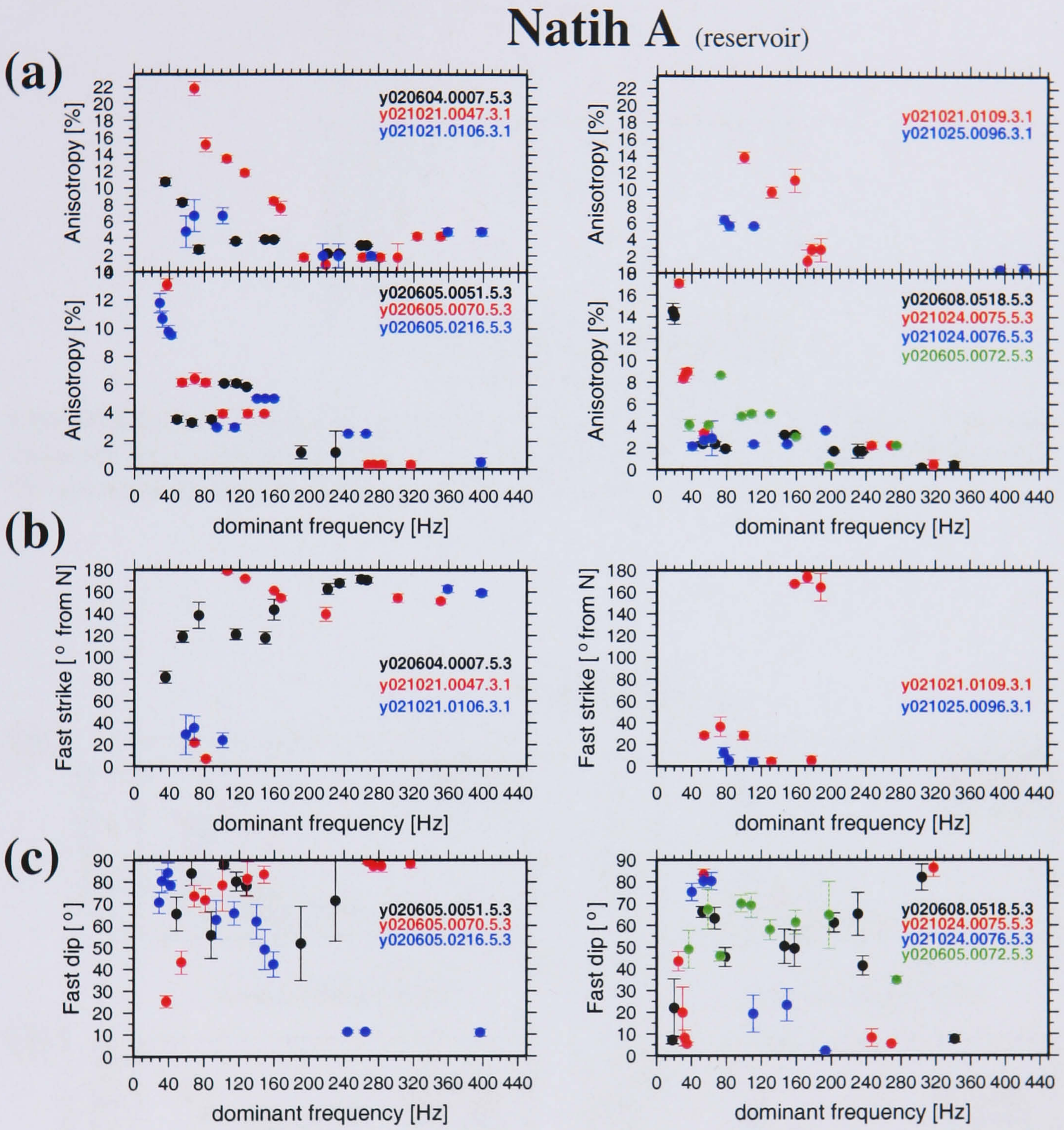

Figure 6.4 Splitting measurements as a function of dominant frequency for 12 event-station pairs where waves propagate within the Natih A formation. [**a**] Percent anisotropy (top-panels contain subvertical rays and bottom-panels contain subhorizontal rays), [**b**] fast-shear-wave strike for subvertical rays (±60° off vertical) and [**c**] fast-shear-wave dip for subhorizontal rays (±15° off horizontal).

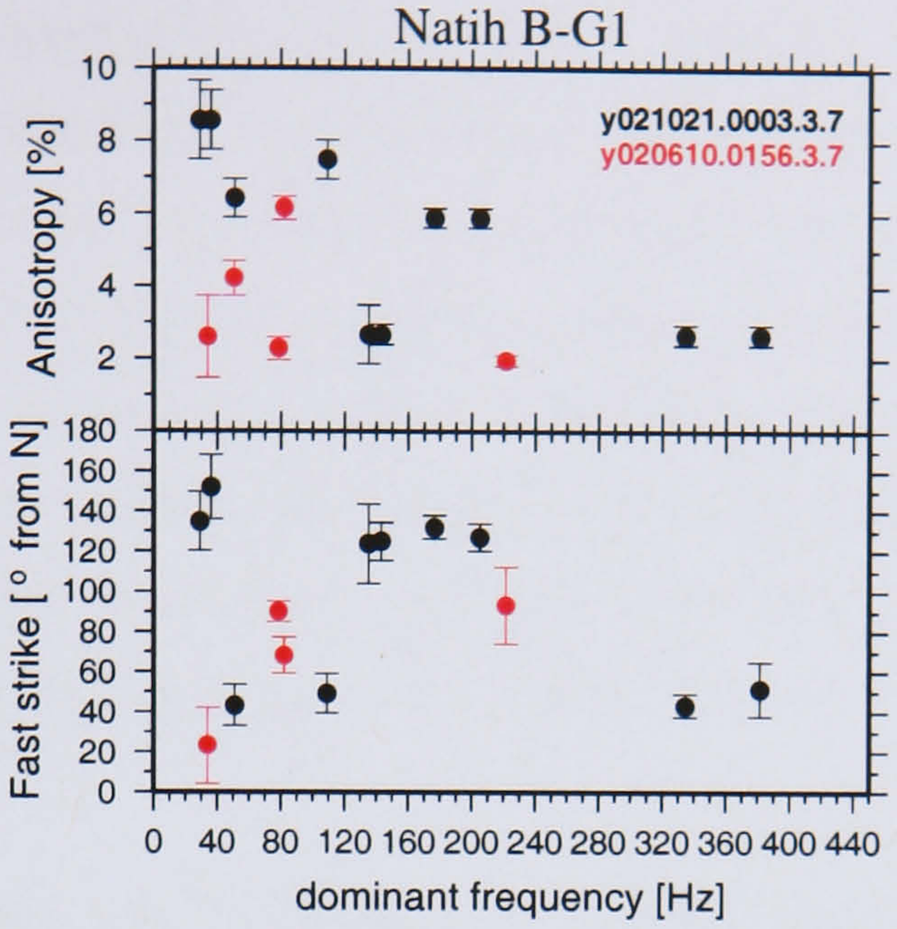

Figure 6.5 Splitting measurements (percent anisotropy and fast strike) as a function of dominant frequency for 2 event-station pairs where waves propagate within the Natih B-G1 formation. The examples are for subvertical rays (±60° off vertical).

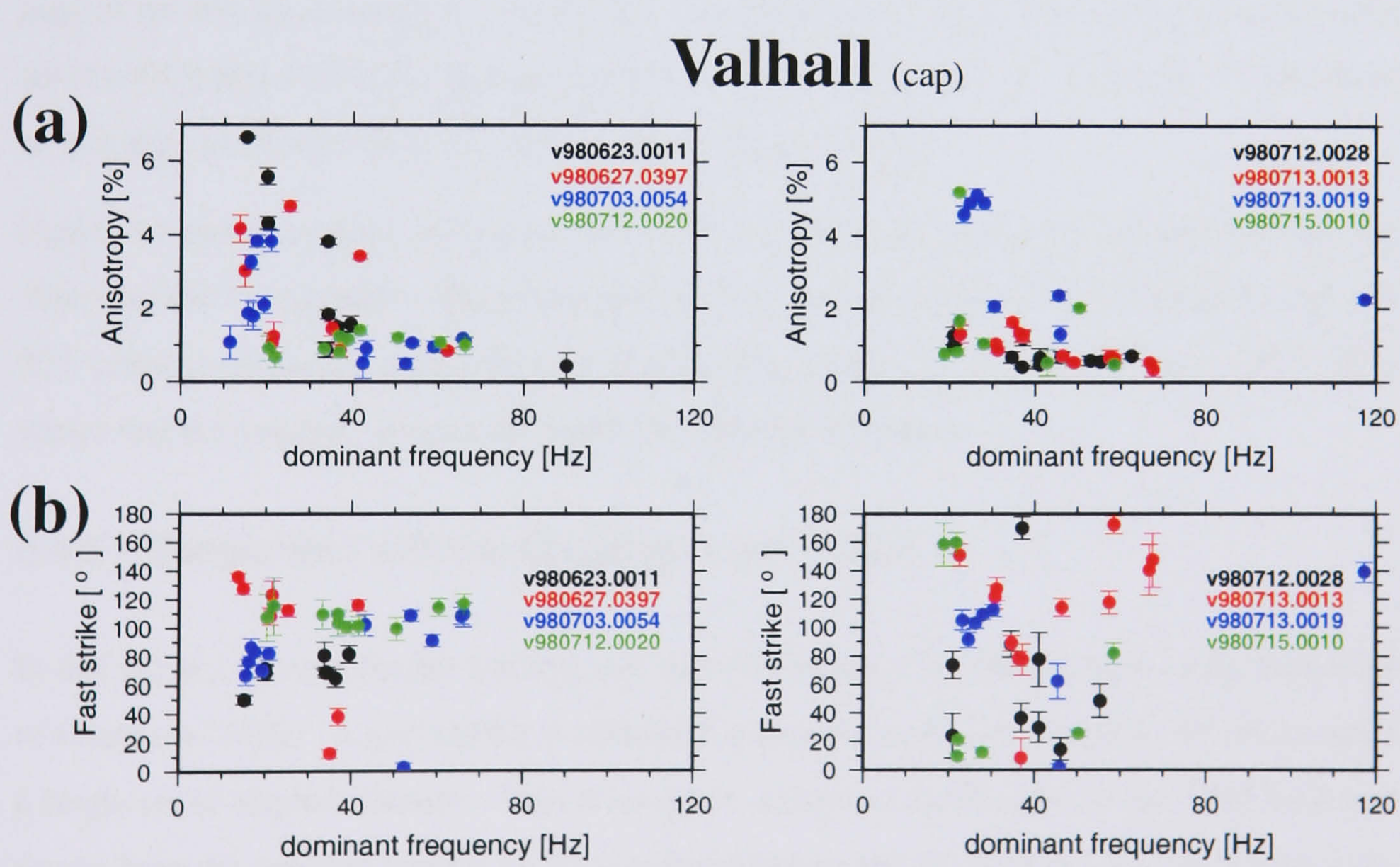

Figure 6.6 Splitting measurements as a function of dominant frequency for 8 events in the Valhall field. Results from the 3 top stations are shown for each event. [**a**] Percent anisotropy [**b**] fast-shear-wave strike. Note that fast-shear-wave dip is not shown because there are no horizontally propagating rays in the Valhall experiment.

The Fiqa results (Figure 6.3a) show little variation in anisotropy with frequency. This frequency-invariant splitting indicates tiny cracks (less than a centimeter scale) (compare with Figure 6.1). In contrast, the Natih A (Figure 6.4a) generally shows a decreasing percent anisotropy trend with increasing frequency. This trend is similar to the Chapman model predictions (Figure 6.1) indicating a fracture-induced anisotropy with fracture size in the order of centimeters. The Natih B-G1 formation (Figure 6.5) shows poor frequency coverage, but one example suggests a decreasing anisotropy trend with increasing frequency. For the Valhall data (Figure 6.6), some events (events v980712.0020, v980713.0028 and v980713.0019) show a similar behaviour to that of the Fiqa formation (i.e., no evidence of frequency-dependent S-wave splitting), but the others show variations in percent anisotropy with frequency (mostly in the frequency range 10–30 Hz).

The fast strike of the fast shear-wave is roughly constant with frequency for most examples, but few examples exhibit large scatter (Figures 6.3b, 6.4b, 6.5 and 6.6b). The fast strike is about 90° in Fiqa, mainly NNE in Natih A, variable in Natih B-G units and the Valhall field (consistent with those in Chapter 5).

The fast dip shows more variations with frequency (Figures 6.3c, 6.4c and 6.5). However, in general the fast dip is mainly subvertical in Fiqa, Natih A and Natih B-G1 (also consistent with results of Chapter 5). For the Valhall field, the fast dip information is not useful due to subvertical propagation of all rays (30°–45° incidence angles from vertical).

Figure 6.7 shows contour error plots for various dominant frequencies for examples from the Yibal and the Valhall fields. The results demonstrate the robustness of the solutions through the 95% confidence contour around the estimated splitting parameters (Silver and Chan, 1991). This shows that the measured frequency-dependent splitting is reliable.

6.4.2 Comparison with the Chapman crack model

In this section, I invert for the fracture size that best matches the observations using the model of Chapman (2003). A grid search is adopted for the inversion. The Chapman model assumes a single set of aligned fractures. This assumption appears to be satisfied in the Yibal field (see results from the previous chapter on shear-wave splitting) and the Valhall data (see Teanby et al. (2004b)). The model parameters used in the inversion are listed in Table 6.1.

In all computations of theoretical curves, I use: (1) vertical cracks (inferred from geology and S-wave splitting) , (2) the assumption of low crack aspect ratio, η (< 0.01), (3) the estimated

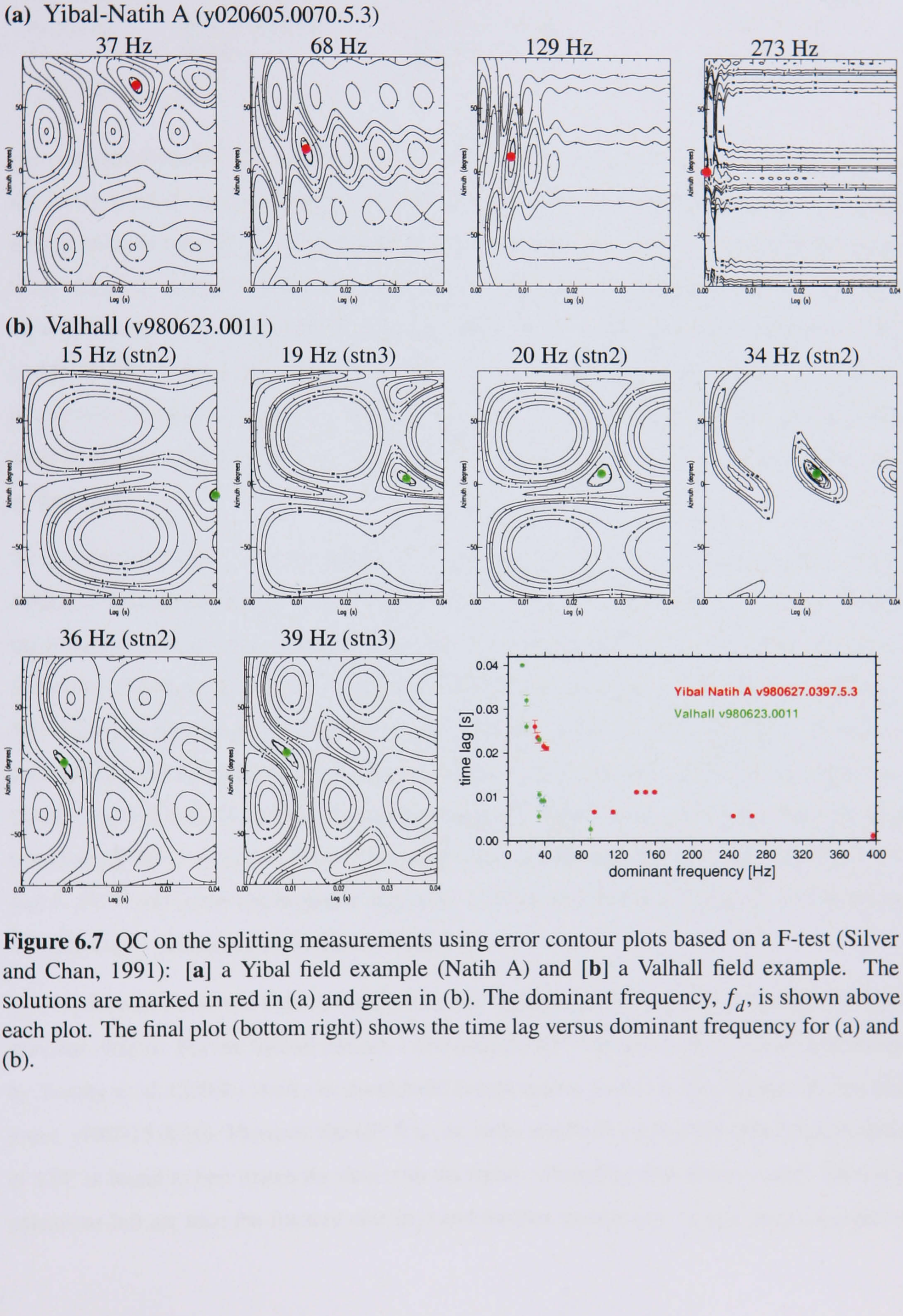

Figure 6.7 QC on the splitting measurements using error contour plots based on a F-test (Silver and Chan, 1991): [**a**] a Yibal field example (Natih A) and [**b**] a Valhall field example. The solutions are marked in red in (a) and green in (b). The dominant frequency, f_d, is shown above each plot. The final plot (bottom right) shows the time lag versus dominant frequency for (a) and (b).

Table 6.1 Model parameters used in the fracture size inversion [**left**] for the entire data and [**right**] for specific layers. τ_m is the relaxation time scale, k_f the fluid bulk modulus and η crack aspect ratio.

Crack dip	Vertical
η	< 0.01
Ray direction	P- or S-hodogram
v_p, v_s, ρ	21-layer model
f_0	40 Hz
Porosity	0.35

Layer	Crack strike [°]	τ_m [s]	k_f [GPa]
Fiqa	90	3	2.3
Natih A	19	4×10^{-7}	0.006
Natih B-G1	45	1×10^{-5}	2.3
Valhall	130	3	2.3

ray orientation based on P- or S-wave particle motions, (4) average v_p and v_s of the ray based on the 21-layer Yibal velocity model (for Yibal) and 5-layer Valhall model (for Valhall), (5) density estimated from average v_p using Gardner's rule (Gardner et al., 1974), (6) a relaxation time scale value, τ_m (related to microscale squirt flow), estimated by Chapman (2001b) and based on experiment, (7) f_0 frequency of 40 Hz at which v_p and v_s are measured, and (8) porosity and fluid bulk modulus (k_f) used in the shear-wave splitting modelling (see Table 4.5 and 4.3, respectively). Tests of various f_0 and porosities, and k_f (for gas, oil and brine in Table 4.3) showed that our results are not very sensitivity to these parameters whose final values are given in Table 6.1.

A τ_m value of 2×10^{-5} s is estimated by Chapman (2001b) based on experiment for water-saturated sandstone with high permeability (250 mD) and fluid viscosity (7.5×10^{-3} Pa.s). Since these fluid properties are significantly higher from our fluid parameters, a correction is required. Following Chapman (2001a), permeability and viscosity calibrations were performed using the fact that τ_m is proportional to the viscosity/permeability ratio. For the calibration: (1) the gas permeability and viscosity (Table 4.5 and 4.3) were used in the gas bearing Natih A reservoir, (2) the Fiqa, Natih B-G1 and the siltstone overburden in Valhall are assumed water-saturated and therefore the brine viscosity (Table 4.5) is used, and (3) a permeability of 25 mD in Natih B-G1 and 1×10^{-4} mD in the impermeable cap rocks in Yibal and Valhall is assumed. The resulting τ_m values after calibration are shown in Table 6.1.

The fracture strike is also known (Table 6.1) and depends on lithology as estimated from the previous chapter. For the Valhall dataset, I first used the 65° fracture strike in cluster 1 observed by Teanby et al. (2004b) since our considered events belong to this cluster (except for the last event, v980715.0010). However the 65° fracture strike resulted in a poor fit. The fracture strike of 130° is found to best match the data with the theory. Therefore, this value is used. The only unknowns left are then the fracture size (a_f) and fracture density (ε). A grid search is used to

find the pair of a_f and ε which yields the best fit between the Chapman (2003) model and the data. The solution with the minimum misfit is chosen. The misfit is defined by the average of the absolute perpendicular residuals (L1 norm) between the model curve and the data points. First, a coarse grid is used to roughly estimate the solution, followed by a fine grid search for an exact estimate.

The results are shown in Figures 6.8 and 6.9 for the Yibal and Valhall fields, respectively, and summarised in Table 6.2. The Chapman theory explains the trends very well. In the Fiqa cap rock (Figure 6.8a) the results suggest tiny fractures (less than 0.1 μm). The fracture size can not be determined exactly due to the absence of the transition zone.

Table 6.2 Inverted fracture size (a_f) and density (ε) for the Yibal field formations and the Valhall field. Stated are average values.

Layer	a_f	ε
Fiqa	<0.1 μm	0.03-0.05
Natih A	2 m	0.07-0.23
Natih B-G1	0.3 m	0.1
Valhall	<0.1 μm & 8 μm	0.02 & 0.29

In nearly all modelled examples for the Natih A reservoir (Figure 6.8b), the fracture size is around the 2 m average. Differences in the model curves in the Natih A are due to different ray orientations relative to the crack orientation. The single Natih B-G1 example suggests, but not conclusively, a fracture size of 0.3 m (Figure 6.8c). Determining the ray orientation from the P-wave particle motion was not possible for two cases for the Natih A formation (y021021.0047.3.1 and y020604.0007.5.3). In these cases the ray-orientation was determined using the straight source-receiver orientation as a starting point. The best-fit model was found with a ray orientation that was 20° away from this starting point, probably because the raypaths are not straight. Two other examples required a raypath deviation of 20° to explain the results (y020605.0070.5.3 and y020607.0323.5.1).

In the cap rock at Valhall, some frequency independent examples (e.g., Figure 6.9a) suggest tiny fractures (less than 0.1 μm). Frequency-dependent examples in Valhall (e.g., Figure 6.9b) suggest larger fractures (8 μm).

Figures 6.10 and 6.11(a,b) show the grid search contour plots of the misfit for the Natih A, Natih B-G1 and Valhall examples, respectively. They reflect the robustness of the meter scale fractures in the Natih A reservoir and the micrometer scale fractures for the frequency-dependent shear-wave splitting event in Valhall. The Natih B-G1 example (Figure 6.11a) shows a poorly

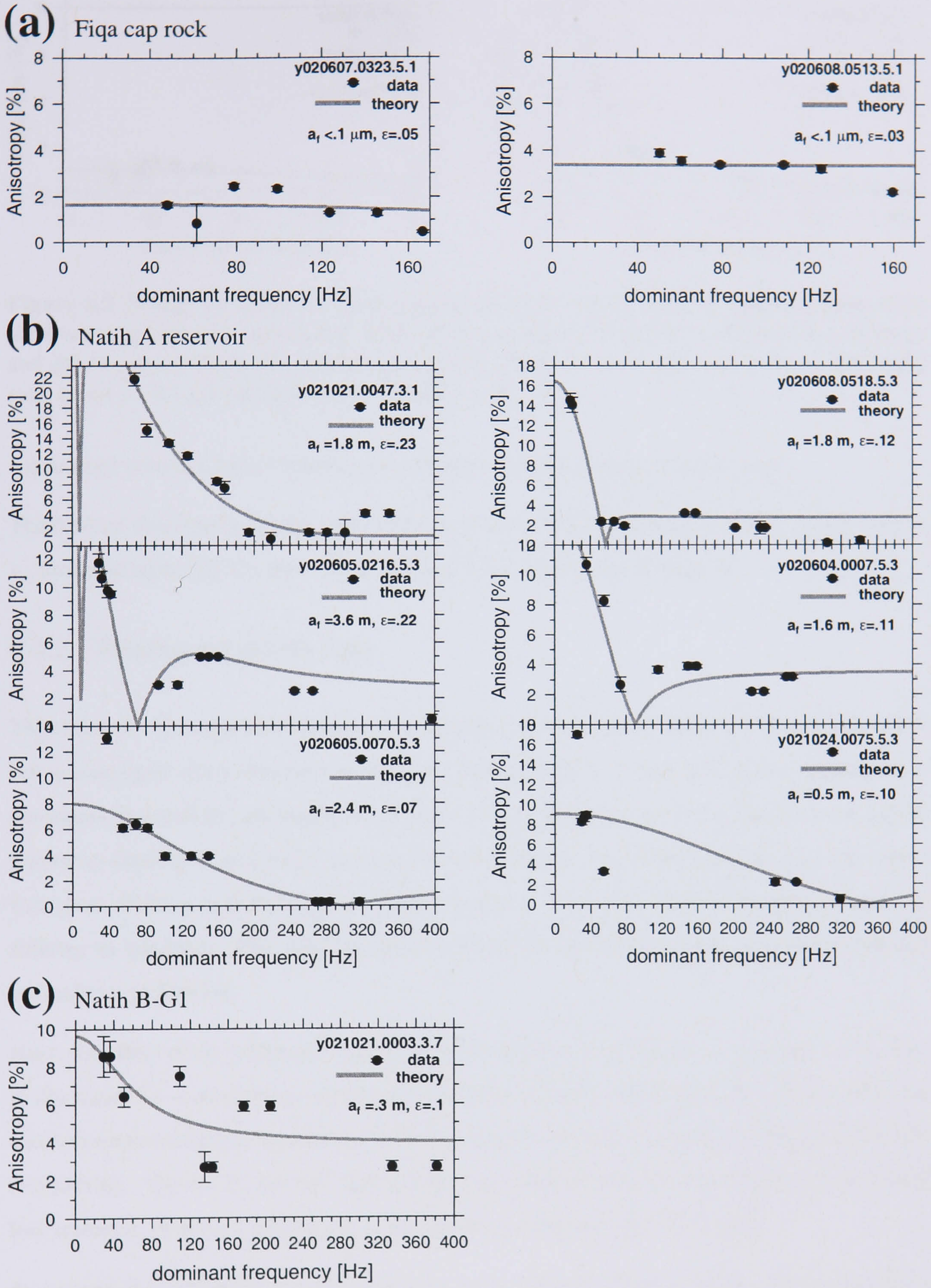

Figure 6.8 Fitting the Chapman (2003) crack model to observations of frequency-dependent shear-wave splitting for the Yibal formations: [**a**] the Fiqa cap rock, [**b**] the Natih A reservoir and [**c**] the Natih B-G1. Note the good match between data and the model. The best fit fracture length (a_f) and density (ε) are also shown.

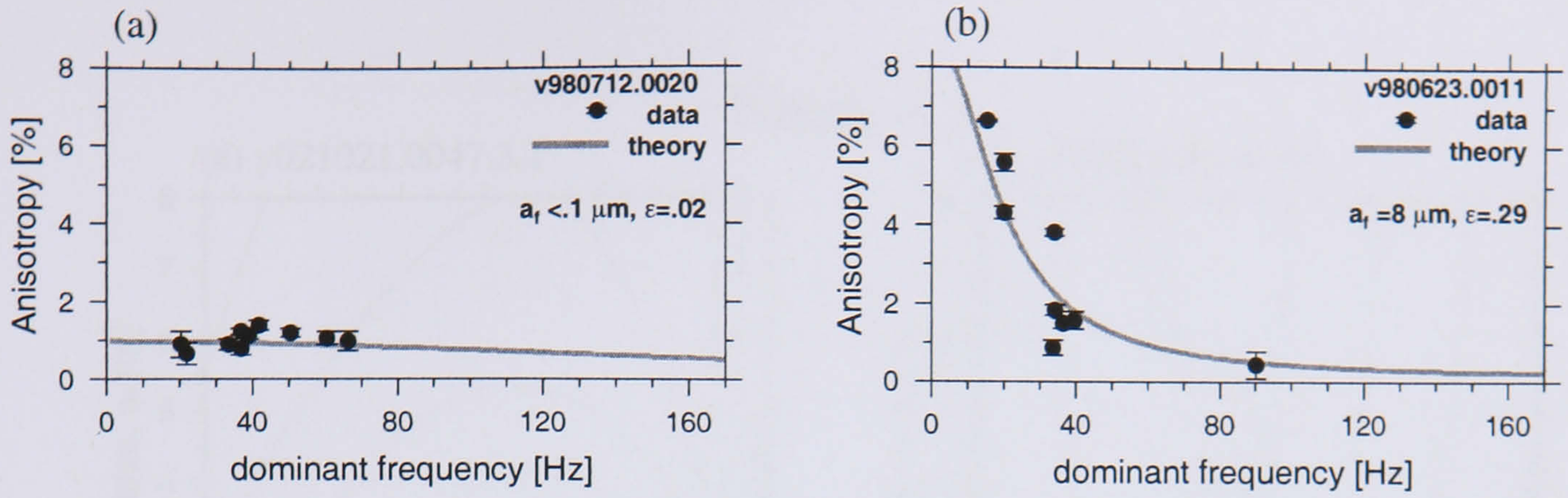

Figure 6.9 Fitting the Chapman (2003) crack model to observations of frequency-dependent shear-wave splitting for the Valhall field [**a**] an example of frequency-independent anisotropy and [**b**] frequency-dependent anisotropy example. Note the variability in the inverted fracture size: small (< 0.1 μm) in (a) and large (8 μm) in (b).

constrained solution, but it indicates a centimeter-to-meter range of fracture size.

The fracture size results are also very sensitive to the relaxation time scale, τ_m. A $\pm 20\%$ error in τ_m produces up to ∓ 0.5 m error in the inverted 2 m fracture size in Natih A.

6.4.3 Filtering sensitivity tests

The observed variations in anisotropy with frequency is attributed to fractures. Tests were carried out to investigate other explanations such as filtering artifacts. Figure 6.12 shows splitting measurements on synthetic seismograms generated by an anisotropic ray tracer that does not handle frequency-dependent anisotropy and processed in the same way as the real data (i.e., one octave band-pass filtering, followed by the splitting analysis). The results show the independence of splitting to frequency. This suggests that our frequency-dependent splitting results are real and not artifacts of filtering.

Next, the effect of the frequency bandwidth in the filter is investigated on real data. This effect is illustrated by a comparison between two octave and one octave band-pass filters. The one and two octave results for examples in the Fiqa and the Natih A are shown in Figures 6.13(a,b), respectively. The results for the higher larger passband (two octaves) are more smoothed and less scattered. However, differences in the splitting results are typically small.

An exception is the Natih A example shown in the top-left of Figure 6.13b, where differences between the two and one octave results are visible (although the same trend exists). This example is further examined with various pass bandwidths (0.7, 1, 1.5, 2 and 3 octaves) and is displayed in Figure 6.14. The results are still separated between the one octave (higher anisotropy) and two octave (lower anisotropy) results. This may indicate that mono-frequency waves (one octave

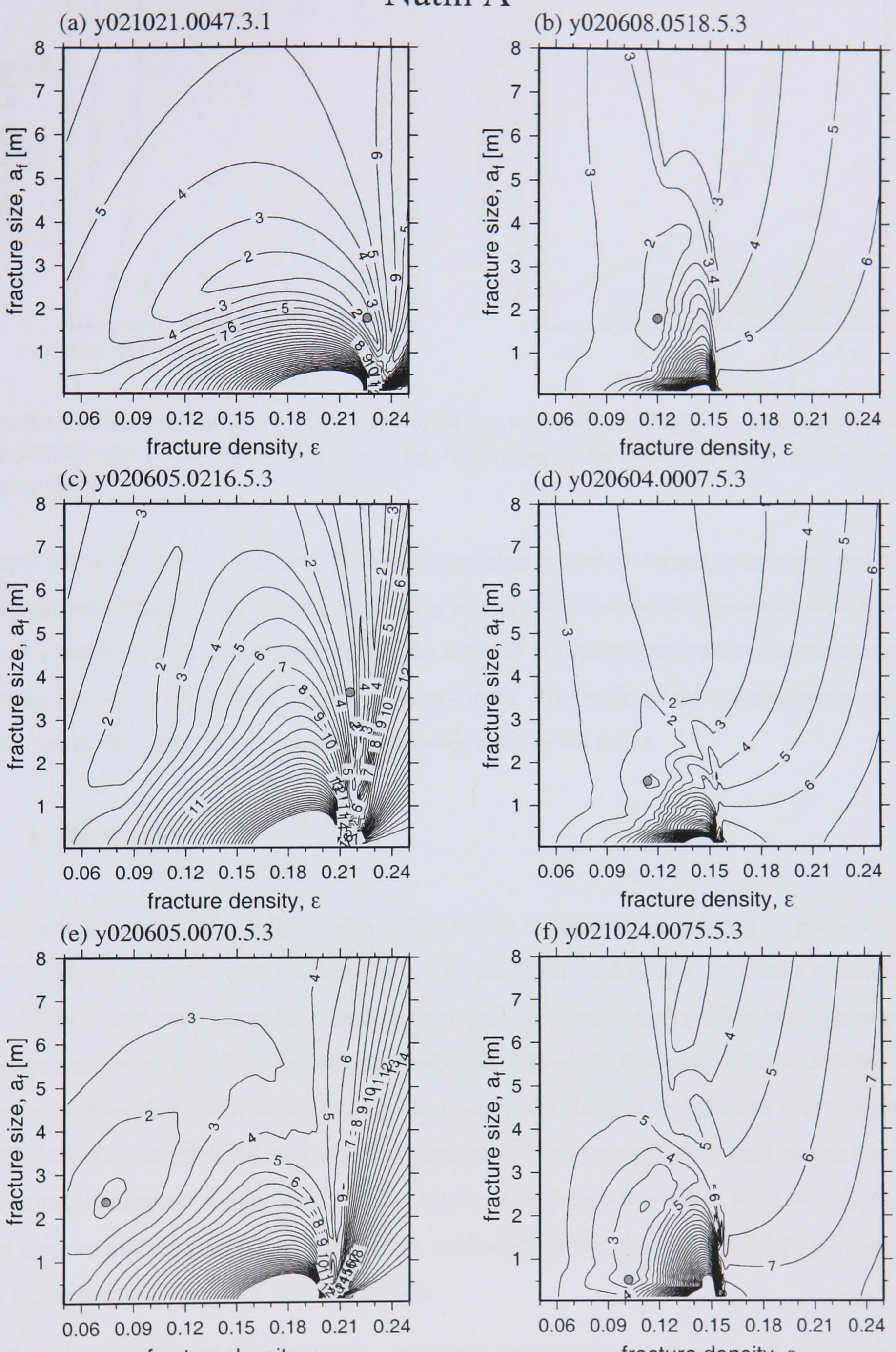

Figure 6.10 Misfit contour plots for the Natih A examples shown in Figure 6.8. Note the clear minimum misfit at the inverted a_f and ε values (marked by a grey circle).

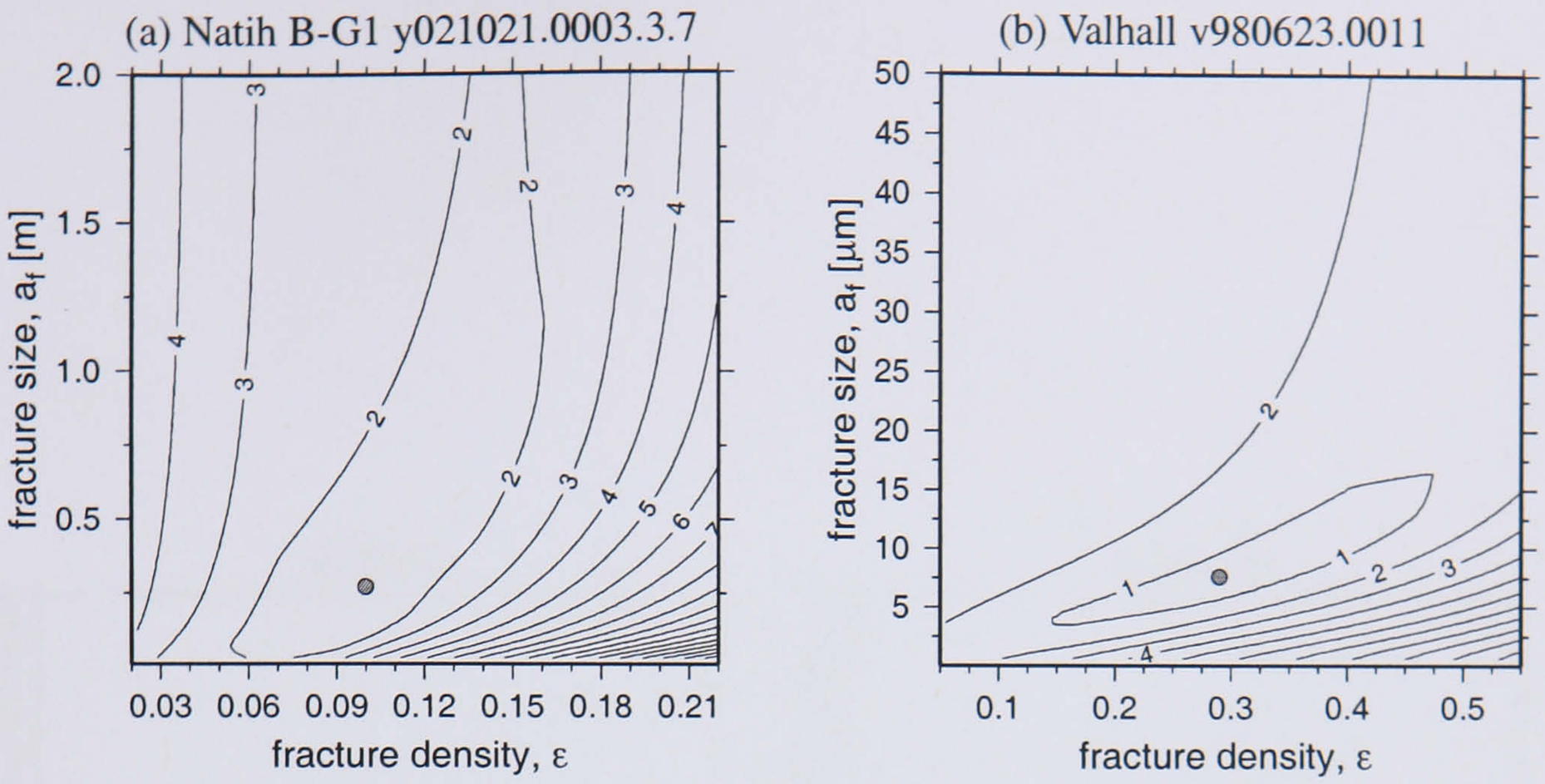

Figure 6.11 Misfit contour plot for the Natih B-G1 example y021021.0003.3.7 and Valhall example v980623.0011. The solutions a_f and ε (corresponding to the minimum misfit) are marked by a grey circle.

and less) are more accurate because the broader passbands tend to reduce anisotropy due to smoothing and averaging. I conclude that filtering using broader bandwidths produces smoother and less scattered results, but occasionally at the expense of reducing the true mono-frequency anisotropy due to averaging over larger frequency-bands. This trade-off between narrower and broader bandwidths deserves a more comprehensive study in the future.

6.5 Interpretation

This chapter examined the frequency-dependent nature of shear-wave splitting in microseismic events from the Yibal and Valhall fields. For the Yibal field results for events confined to the Natih A carbonate formation show a clear and fairly consistent pattern of frequency-dependent shear-wave splitting. Results confined to the Fiqa shale formation show no evidence of frequency-dependent shear-wave splitting. In general, the Natih A results show much larger anisotropy magnitudes than the Fiqa results. Events analysed from the Valhall field are confined to the primarily siltstone overburden. Measurements of frequency-dependent shear-wave splitting in these events show significant variability. It is worth noting that the Yibal data are much richer in frequency content than the Valhall data.

The Chapman (2003) model of frequency-dependent shear-wave splitting is used to interpret the measurements. The results for the Natih A formation suggest that the anisotropy is due to cracks or fractures that have an average length of 2 m and fracture density of 0.07–0.23. The

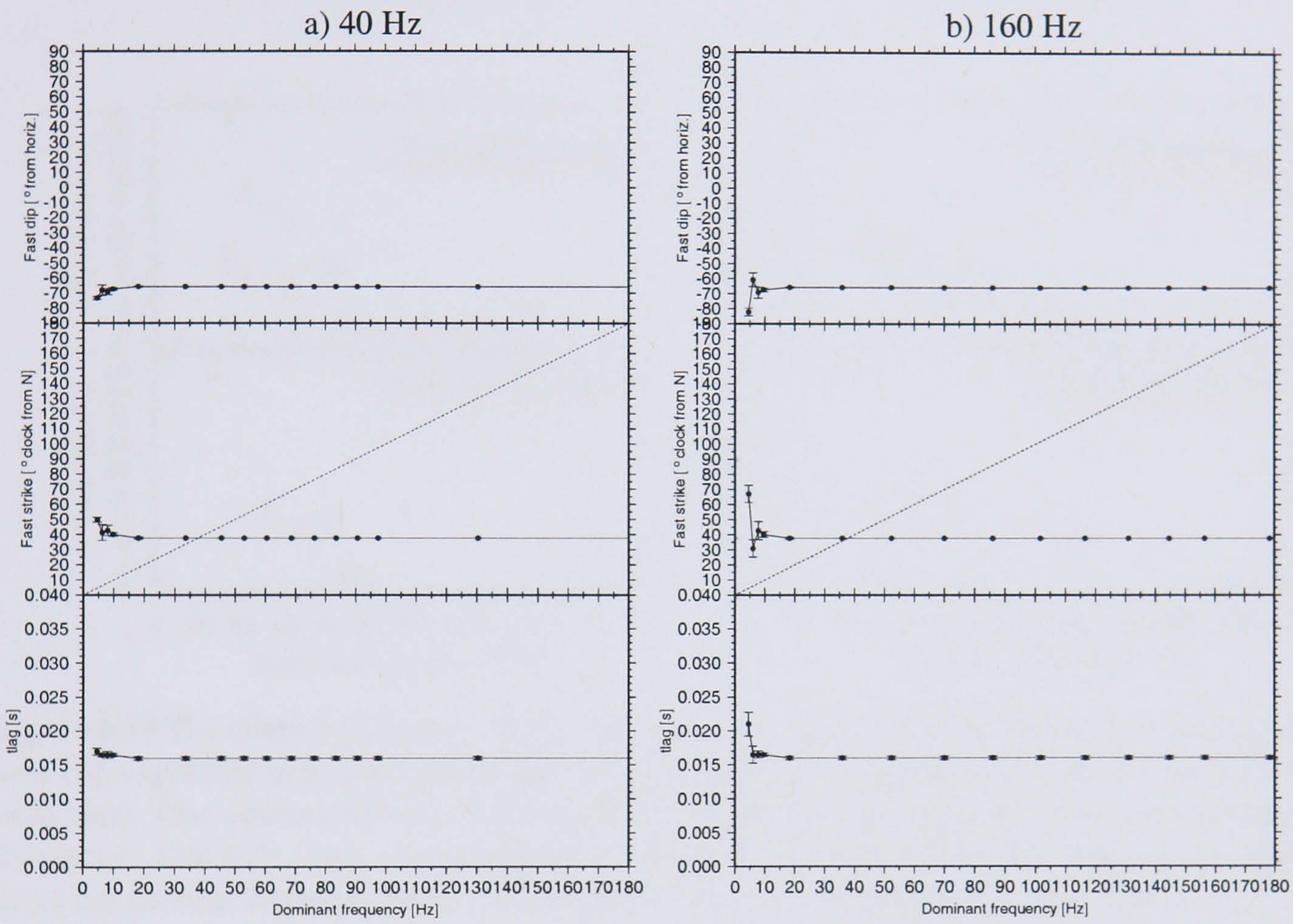

Figure 6.12 Filtering effects on splitting measurements using synthetic data and a Ricker source wavelet with a dominant frequency of [**a**] 40 Hz and [**b**] 160 Hz. The synthetic data are for a buried and porous medium with a single set of cracks (40° crack strike). The ray is shot at a 60° inclination towards the east. The data are generated using the anisotropic ray-tracer ATRAK Guest and Kendall (1993), which does not model frequency-dependent anisotropy. The filtering does not introduce erroneous estimates of the splitting parameters.

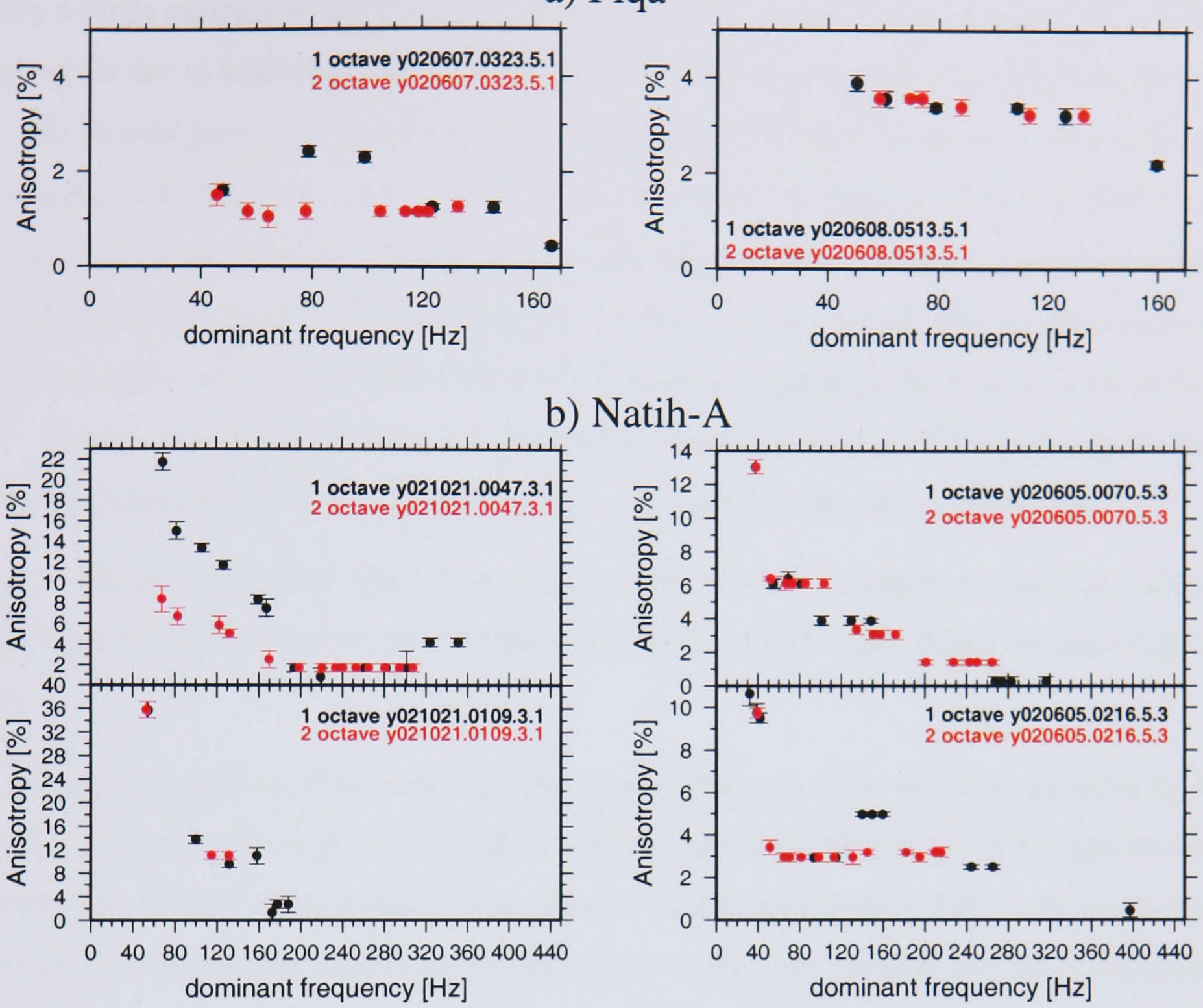

Figure 6.13 The effect of the length of the filter frequency interval on the splitting measurement time lag, expressed as percent anisotropy for [**a**] the Fiqa (two examples) and [**b**] the Natih A (4 examples). One octave refer to a frequency band where the end frequency is twice the starting frequency. Similarly, two octaves refer to a frequency band where the end frequency is four times the starting frequency. Note the smoother results with a broader band-pass filter.

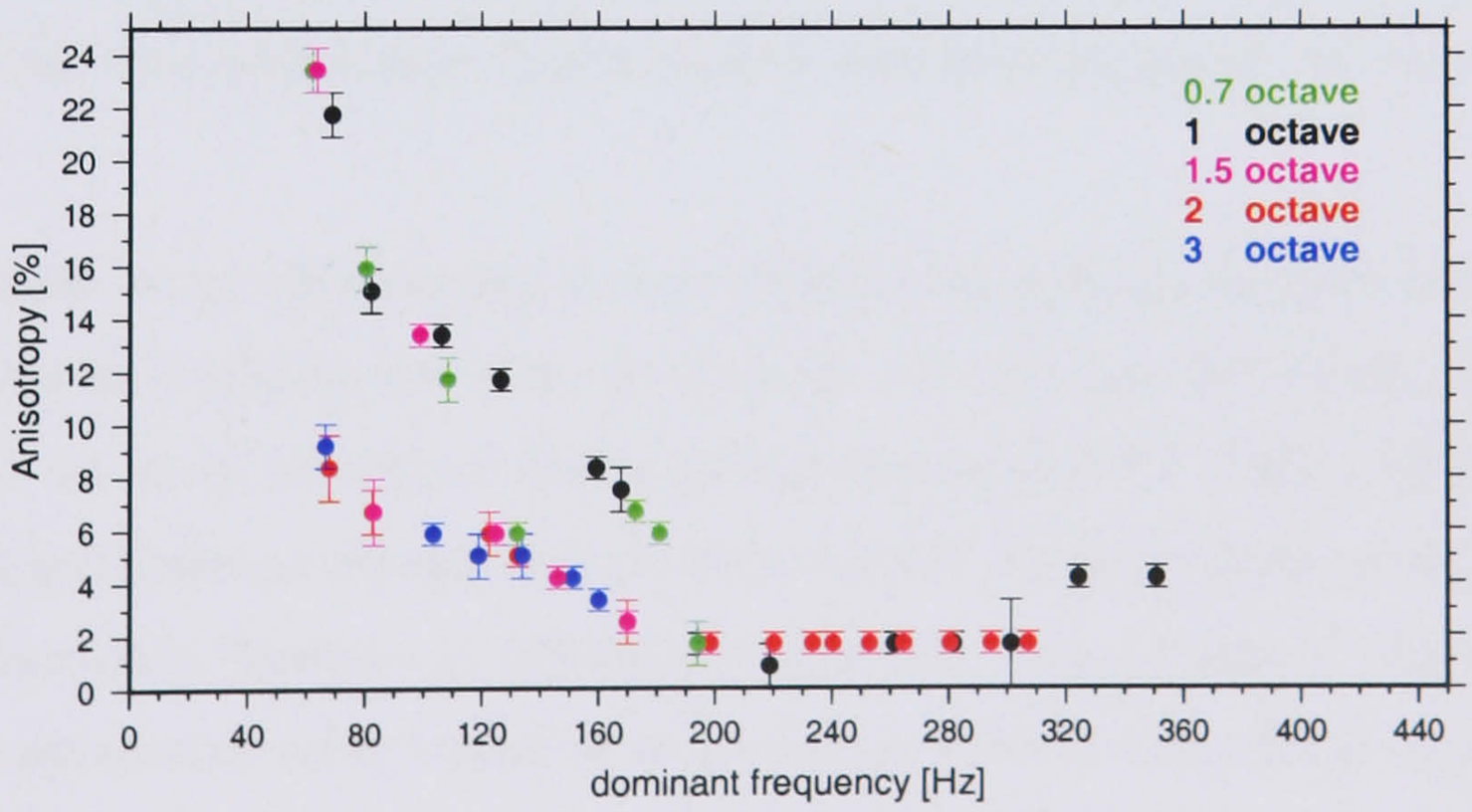

Figure 6.14 The effect of the length of the filter frequency interval on the estimated percent anisotropy for the Natih-A y021021.0047.3.1 example. *n* octave refers to a frequency band where the end frequency is 2^n times the starting frequency.

top part of the Natih B-G suggests a centimeter-to-meter fracture size. However, this is based on only a single example with noticeable scatter. In contrast, results for the Fiqa suggest that the anisotropy is due to scatterers that are less than 0.1 μm in size. The anisotropy could be due to fine-scale aligned pores or microcracks or crystal alignment (vertical alignment is evident from the observed fast-shear-wave dips). These results are somewhat intuitive. The Fiqa shale is a seal (cap rock to the Natih A), and therefore not expected to be fractured. Production from the Natih A formation is facilitated by secondary permeability due to fractures. The resulted fracture density is highest in the Natih A reservoir (0.07–0.23) and moderate in the Fiqa cap rock (0.03-0.05). These are consistent with the previous chapter findings. The high fracture density in the Natih A is expected to support production from a rock matrix of very low permeability.

The 2 m fracture size in the Natih A is approximately similar to mapped fractures in thinly-bedded units of Natih outcrops in the Salakh arch (130 km east of Yibal) (Mercadier and Mäkel, 1989).

The frequency-dependent shear-wave splitting measurements in Yibal are well modelled by a medium fractured with a single set of cracks using the Chapman (2003) theory. This supports the interpretation of shear-wave splitting observations in the previous chapter. Due to the sensitivity of the results to the relative ray direction to the fracture orientation, the good match between data and theory also reflects the accuracy of fracture dip and strike estimates from the S-wave splitting analysis in the previous chapter (steeply-dipping fractures oriented 19°NNE in the Natih A and 90°E in the Fiqa).

The frequency-dependent fast-strike measurements at Yibal are mainly constant and independent of frequency as expected by the Chapman (2003) model. However, the model does not explain the scatter in the observed fast-dips. Further work is required to investigate the variation in the fast dip.

The interpretation of the Valhall results is more difficult. Some results suggests no frequency-dependent shear-wave splitting and hence small cracks <0.1 μm (and low density 0.02), while others suggest cracks up to 8 μm in size (with high density of 0.29). This variability is due to: (1) the limited frequency content, and (2) stress-induced temporal variations in shear-wave splitting as observed by Teanby et al. (2004b) in the same microseismic dataset. These temporal variations are strongest in cluster 1 (most of our considered Valhall events). Teanby et al. (2004b) suggest that tidal loading or oil production may cause such variations in stress. The estimates of the fast-shear-wave strike are also much more variable than those for Yibal.

6.6 Conclusions

Fracture size is one of the main parameters that the reservoir engineers are interested in due to its importance in hydrocarbon production. I estimate the fracture size using the Chapman (2003) theory of frequency-dependent shear-wave splitting. The splitting analysis was carried out for microseismic data recorded in the Yibal and Valhall fields. Sensitivity tests suggest that filtering has little influence on the frequency-dependent S-wave splitting measurements. I therefore interpret detected variations in S-wave splitting with frequency in terms of different fracture sizes and densities.

The results of frequency-dependent S-wave splitting (and thereby, fracture size and density) are mainly controlled by lithology. The Natih A carbonate reservoir shows significant variations in the splitting magnitude over seismic frequencies. This reservoir demonstrates the largest fracture size and fracture density of 2 m and 0.07–0.23, respectively. The 2 m fracture size roughly coincides with that in thinly-bedded chalks in Natih outcrops in the Salakh arch, 130 km east of Yibal (Mercadier and Mäkel, 1989). The high fracture density agrees with the geology of a highly fractured reservoir.

The Fiqa shale cap rock has no frequency-dependent S-wave splitting over the recorded seismic frequencies. This corresponds to tiny fracture sizes (<0.1 μm) which is expected for a seal rock. The corresponding fracture densities are relatively moderate (0.03-0.05) which is consistent with those obtained in the previous chapter.

The Valhall results are variable and suggest two fracture scenarios: small cracks of <0.1 μm in size (with very low density of 0.02) and bigger cracks up to 8 μm in size (with high density of 0.29). The variability is attributed to the limited frequency content and temporal variations in the stress field (Teanby et al., 2004b).

Cumulatively, these results suggest that it is possible to use measurements of frequency-dependent shear-wave splitting in microseismic data to infer the size, density and orientation of cracks or fractures in rocks. Such information is useful for assessing the sealing potential of cap rocks and provides insight into fracture-induced production in reservoirs.

Chapter 7

Conclusions

This thesis presents a study of earthquake focal mechanisms, stress fields and seismic anisotropy in a hydrocarbon setting. The data used for the analysis come from a downhole microseismic survey in the Yibal Field, Oman. The key conclusions are summarised in Figure 7.1.

7.1 Overview of conclusions

Review of graben fault mechanisms and stress

Forty-three reliable fault plane solutions are determined for microseismic events in the Yibal field. They mostly fall along the eastern-most graben fault that trends NE through the field. The results indicate heterogeneities in the local stress field that are controlled by lithology and deformation (compaction). I observe strike-slip movements in the Fiqa and Nahr Umr shale cap rocks, thrust faulting in the compacting gas carbonate Natih-A reservoir, and normal faulting in the oil-bearing carbonate Shuaiba reservoir. The normal graben faults and the extensional regime in Yibal (Litsey et al., 1986), suggest that the normal faulting regime in the Shuaiba reservoir is expected. The observed thrusting regime is also perhaps an expected result for Fiqa and Natih A due to compaction.

Stress inversion results show variations in the maximum compressive stress direction with depth: horizontal east (E) in Fiqa, horizontal north-north-east (NNE) in Natih-A, sub-horizontal east (E) in Nahr Umr, and sub-vertical in Shuaiba. The local stress field controls the development of new structures such as fractures or dikes, and the opening or closing of preexisting fractures. For example, Nakamura (1977) estimated the stress directions in a volcanic chain based on the distribution of dikes using the fact that dikes open along the direction of least stress. Analogously, fractures open in the direction of least stress in the horizontal plane and thereby preferentially

align themselves in the direction of the maximum compressive stress in the horizontal plane (Al-Ruwaili and Chardac, 2003; Khan and Teufel, 2003).

Therefore, the estimated E direction of the maximum stress in Fiqa and Nahr Umr predicts E oriented open fractures. This agrees with the dominant E fracture trend inferred from shear-wave splitting analysis. Similarly, the NNE direction of the maximum stress in the Natih-A reservoir predicts NNE fractures, which agrees well with the NNE fast-shear strike inferred from shear-wave splitting in the Natih reservoir. The deduced stress field in the Natih reservoir is also consistent with the in-situ stress inferred from wellbore breakouts (Baker Atlas GEOScience, 1999).

Stress modelling based on a passive basin model suggests that the transition at each shale-cap-rock/carbonate-reservoir interface could be due to variations in fault friction angles across the interface. The estimated best fit friction angles are low in the shales (12° in Fiqa and 18° in Nahr Umr) and high in the chalks (39° in Natih A and Shuaiba). These agree well with typically reported values in the literature. The modelling also suggests a positive anomaly in Poisson's ratio (increasing by about 0.06), which is consistent with ongoing compaction in this unit. The modelling also predicts a regional thrusting system in the top reservoir and its cap rock and a normal system in the bottom reservoir and its cap rock. However, at this time, other possibilities cannot be ruled out (e.g., a regional strike-slip regime with a perturbation in Natih A (thrust) and Shuaiba (normal) due to hydrocarbon extraction).

Modelling shear-wave splitting in fractured anisotropic media

Good ray coverage in both azimuth and inclination is important to interpret the nature of anisotropic media. HTI (due to a single set of vertical cracks) and VTI (due to intrinsic anisotropy) symmetries can be discriminated using horizontally propagating rays, which will show vertically or horizontally polarised fast-shear-waves, respectively. In HTI media, the strike of the fast-shear-wave polarisation vector is a better representative of the crack strike than that of the polarisation plane. It is also easy to distinguish between brine and gas-saturated rocks in non-porous media, but hard to do so in porous media based on shear-wave splitting measurements only. Multiple sets of cracks can also be detected and the strikes of the crack sets can be estimated from the ray azimuths that show the maximum percent anisotropy.

Anisotropy from shear wave splitting

Splitting magnitudes range from 0–20 ms, corresponding to 0–10% anisotropy. The largest anisotropy values lie to the SE (5–10%) and are bounded by a NE-trending major graben fault.

This anisotropy varies between the Fiqa, Natih A and the upper part of the Natih B-G, and diminishes with depth. This is consistent with (1) the known geology, which shows extensive fracturing in the crest and southern flank, compared with the northern flank, and (2) laterally constant fracture density in the Shuaiba reservoir (deeper) as inferred from FMI logs.

The Natih A carbonate reservoir shows the highest percent anisotropy (5% average) as expected for a highly fractured reservoir. The Fiqa cap rock and the upper part of the Natih B-G carbonate exhibit moderate anisotropy (3%), while the lower part of the Natih B-G shows weak anisotropy (1%). These values agree with anisotropy inferred from shear-dipole logs except in the Natih A where it is lower than 5% anisotropy. This can be explained by larger fractures in the Natih A formation, compared with smaller fractures in the other formations. Our study of frequency-dependant shear-wave splitting suggests a fracture size of 2 m in the Natih A and fine-scale cracks (<0.1 μm) in the Fiqa cap rock. The fast-shear-wave orientation results show aligned near-vertical fracture sets trending NNE in the Natih A; E in the Fiqa and the lower part of Natih B-G; and NE in the upper part of Natih B-G. These fracture orientations agree with the structural geology of the area and the maximum stress orientations as estimated from the FPSs.

Shallow parts of the field (Fiqa, Natih A, the upper part of Natih B-G) show high amounts of anisotropy and subvertically polarised shear-waves, which I attribute to fractures and cracks. In contrast, deeper parts of the field (the lower part of Natih B-G) show low amounts of anisotropy and subhorizontally polarised fast-shear waves, which I attribute to the the intrinsic anisotropy of the rock rather than fractures or cracks. Collectively, the results suggest that the anisotropy is controlled by both rock-type and fault-related fracturing.

The off vertical cracks (75° dip in the Natih A reservoir) also provide a plausible cause for the shear-wave splitting sensitivity to the crack-fluid observed by van der Kolk et al. (2001) and explained by Sayers (2002) for vertical ray propagation.

Frequency-dependent anisotropy

Microseismic data in both the Yibal and Valhall fields show evidence of frequency-dependent S-wave splitting. The Chapman (2003) model (of a single set of cracks) fits the measurements, and is used to estimate crack size and density. In Yibal, the Natih A reservoir demonstrates the largest fracture size and density of 2 m and 0.07-0.23, respectively, as expected for a reservoir with hydrocarbon production promoted primarily by fractures. In contrast, the shale Fiqa cap rock demonstrates fine-scale cracks (<0.1 μm), as expected for a seal rock. This explains the anisotropy underestimated and correctly estimated by the dipole shear high-frequency tool in the

Natih A reservoir and Fiqa cap rock, respectively. The good fit between the Chapman (2003) model and the measurements is consistent with the fracture orientations estimated in our S-wave splitting study (near-vertical fractures trending 19°NNE in the Natih A and 90°E in the Fiqa).

The Valhall field measurements (primarily imaging siltstone) show variable results, one similar to that for the Natih A and the other similar to the Fiqa. I relate the variability to the limited frequency content of the Valhall microseismic dataset and temporal variations in stress also inferred from shear-wave splitting by Teanby et al. (2004b). Possible causes of temporal stress changes could be tidal loading and oil production (Teanby et al., 2004b).

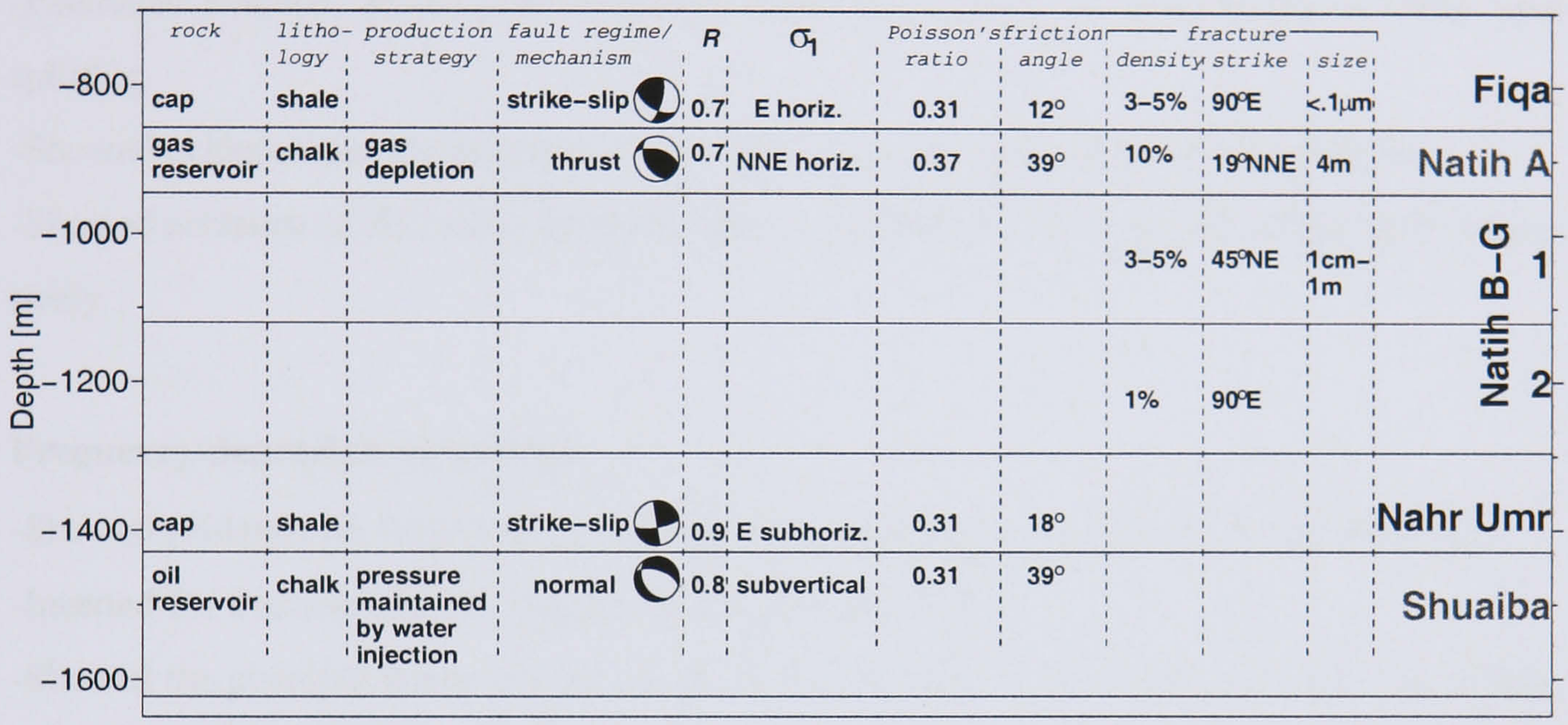

Figure 7.1 A diagram showing the key results of the PhD project. *R* is the relative stress magnitude and σ_1 is the maximum principal stress.

7.2 Thesis significant contributions

Focal mechanisms and Stress inversion

-Detailed synthetic testing of the suitability of the Yibal data for focal mechanism analysis.

-Estimating fault plane solutions for the Yibal field.

-Inversion for in-situ stress directions.

-Estimated stress magnitudes.

-Stress modelling based on a passive basin model.

-Developed a new method to estimate fault friction angles.

-Estimated friction angles.

Modelling shear-wave splitting in fractured anisotropic media

-Calculated the anisotropic elasticity of a shale sample based on the elasticity of the constituent

minerals.

-Showed that it is more accurate to use the projection of the fast-shear-wave polarisation vector rather than the projection of the fast-shear-wave polarisation plane to estimate fracture strike.

-Developed guidelines to interpret the real data and discriminate between HTI and VTI media.

-Tested the effect of burial and pore-crack fluid connectivity on shear-wave splitting measurements.

Anisotropy from shear-wave splitting in real data

-Estimated fracture density and orientation (strike,dip) based on observations of shear-wave splitting.

-Showed evidence that the fracturing is controlled by rock-type and proximity to faults.

-Showed evidence of HTI and VTI symmetries in the shallow and deep parts of the field, respectively.

Frequency-dependent anisotropy

-Showed evidence for frequency-dependent S-wave splitting in the Yibal and Valhall fields.

-Inverted for fracture size and fracture density in both fields.

-Showed the potential for assessing the quality of cap rocks seals and fracture-induced production in reservoirs.

Cumulatively, this thesis has contributed significantly to the understanding of the geomechanical properties (stress and fractures) in the cap rocks (Fiqa and Nahr Umr) and reservoirs (Natih A and Shuaiba) of the Yibal field.

7.3 Future directions

Focal mechanisms and Stress inversion

There are several potential directions for future work on this topic. The focal mechanisms in this study were determined from P-SV-SH polarity and amplitude ratio picks using the FOCMEC program. This is time consuming, requires intensive manual input and good coverage. Other disadvantages are that non double-couple components (compensated linear vector dipole, CLVD) are difficult to determine with accuracy from these picks only, and an anisotropic subsurface (like Yibal) cannot be handled by FOCMEC. The observed anisotropy (up to 10% in Yibal)

places ambiguities in the esimation of the full source mechanism (Rössler et al., 2004). Therefore, volumetric changes are obscured due to the presence of anisotropy (Vavryčuk, 2005).

Automated methods can analyse bigger datasets in relatively less time with less user intervention. A potential direction is therefore to use automated methods of a full waveform inversion that can handle anisotropy. This can be achieved by using a one-way wave equation method of Angus (2005), which has been developed for 3D anisotropic media. Usage of waveform inversion algorithms (e.g. Sileny and Panza, 1991; Sileny et al., 1992) can also recover the CLVD component for a CLVD source from the inverted moment tensor and source time function even with few records (Kravanja and Panza, 2005).

Doublets and triplets that occur successively in time have been recorded. Cross correlation analysis of all events in the microseismic dataset can be used to find temporally variant doublets and triplets. These can be further analysed for repeated slip mechanisms.

Anisotropy from shear wave splitting

The two weeks of data in this study were manually analysed to estimate the shear-wave splitting parameters. The main potential direction is to analyse bigger datasets of Yibal using the less user-intensive program developed by Teanby et al. (2004a). This performs automatic shear-wave splitting analysis, given an S-wave arrival time. These S-wave arrival times can be extracted from the proprietary software XMETAL.

Differential S-wave attenuation

Since the fast and slow shear-waves are determined by the splitting analysis, a follow up analysis of their differential attenuation is useful for estimating Q following the approach of Carter and Kendall (2004). Attenuation (1/Q) estimates are useful for a more accurate determination of focal mechanism from polarity and amplitude ratio picks and full wave inversion methods.

3D geomechanical modelling

A logical continuation of this work involves geomechanical modelling. The results from this thesis could be integrated into a 3D geological and geomechanical model of the field.

References

Addis, M. A., 1997, The stress-depletion response of reservoirs, SPE Annual Technical Conference and Exhibition, 5-8 October, San Antonio, Texas, SPE 38720.

Aki, K., and Richards, P. G., 1980, *Quantitative seismology: theory and methods*, W. H. Freeman, San Francisco.

Al-Abri, S. S. A., 2003, Fracture-induced anisotropy study using shear-wave splitting in the Yibal oil field, Oman, Master of Research thesis, The University of Leeds, Leeds, United Kingdom.

Al-Anboori, A., Kendall, M., Raymer, D., and Jones, R., 2005, Microseismic monitoring and spatial variations in anisotropy, an example from Oman, 67th EAGE Conference and Technical Exhibition, Madrid, Spain, Expanded Abstracts, Paper P094.

Al-Busaidi, R., 1997, The use of borehole imaging logs to optimize horizontal well completions in fractured water-flooded carbonate reservoirs, *GeoArabia*, **2**, 19–34.

Al-Ruwaili, S., and Chardac, O., 2003, 3D model for rock strength & in-situ stresses in the Khuff formation of Ghawar field, methodologies & applications, 2003 SPE 13th Middle East Oil Show and Conference held in Bahrain, SPE 81476.

Anderson, O. L., 1965, Determination and some uses of isotropic elastic constants of polycrystalline aggregates using single-crystal data, *in* Mason, W. P., Ed., *Physical Acoustics*, Academic press, 3B, 43–95.

Angus, D. A., 2005, A one-way wave equation for modelling seismic waveform variations due to elastic heterogeneity, *Geophys. J. Int.*, **162**, 882–898.

Arifin, Arta, P., and Castillo, D., 2003, A geomechanical modeling approach in deep horizontal well development designs, SPE International Improved Oil Recovery Conference in Asia Pacific, 20-21 October, Kuala Lumpur, Malaysia, SPE.

Avseth, P., Mukerji, T., and Mavko, G., 2005, *Quantitative seismic interpretation : applying rock physics tools to reduce interpretation risk*, Cambridge University Press, Cambridge.

Baker Atlas GEOScience, Karstic and tectonic fracture study, Natih-A reservoir, Yibal Gas Field, Northern Oman, Unpublished report, prepared by Baker Atlas GEOScience, Bahrain.

Baker Atlas GEOScience, 1999, In-situ stress analysis, Unpublished report, prepared by Baker Atlas GEOScience, Baker Hughes in July, 1999, Oman. Prepared for Petroleum Development Oman.

Barnes, A. E., 1993, Instantaneous spectral bandwidth and dominant frequency with applications to real seismic reflection data, *Geophysics*, **58**, 419–428.

Blyth, F. G. H., and de Freitas, M. H., 1984, *A geology for engineers*, Edward Arnold, London, 7th edition.

Bohnhoff, M., Baisch, S., and Harjes, H.-P., 2004, Fault mechanisms of induced seismicity at the superdeep German Continental Deep Drilling Program (KTB) borehole and their relation to fault structure and stress field, *J. Geophys. Res.*, **109**, B02309.

Bokelmann, G. H. R., and Harjes, H.-P., 2000, Evidence for temporal variation of seismic velocity within the upper continental crust, *J. Geophys. Res.*, **105**, 23879–23894.

Bouchon, M., 1981, A simple method to calculate Green's functions for elastic layered media, *Bull. Seism. Soc. Am.*, **71**, 959–971.

Brown, L., and Gurevich, B., 2004, Frequency-dependent seismic anisotropy of porous rocks with penny-shaped cracks, *Exploration Geophysics (Melbourne)*, **35**, 111–115.

Budiansky, B., and O'Connell, R. J., 1977, Elastic moduli of a cracked solid, *International Journal of Solids and structures*, **12**, 81–97.

Byerlee, J., 1978, Friction of rocks, *Pure Appl. Geophys.*, **116**, 615–626.

Caccamo, D., Neri, G., Sarao, A., and Wyss, M., 1996, Estimates of stress directions by inversion of earthquake fault-plane solutions in Sicily, *Geophys. J. Int.*, **125**, 857–868.

Caddick, J., Kendall, J.-M., and Raymer, D. G., 1998, Maslov shear-waveforms in highly anisotropic shales and implications for the shear-wave splitting analyses, *La Revue de l'IFP*, **53**, 64–71.

Carter, A., and Kendall, J.-M., 2004, Attenuation anisotropy and the relative frequency content of split shear-waves, *Eos Transactions of AGU, Fall Meeting, Supplement*, **85**(47).

Casey, M., 2004, Some elastic properties of shales, in *Leeds Microseismicity Project, phase 1 final report*, J-M. Kendall (ed.) The University of Leeds, Leeds, United Kingdom, 115-120.

Chapman, M., 2001a, The dynamic fluid substitution problem, 71st SEG Meet., San Antonio, Texas, USA, Expanded Abstr., Soc. Explor. Geophys., 1708–1711.

Chapman, M. 2001b, Modelling the wide-band laboratory response of rock samples to fluid pressure changes, Ph.D. thesis, University of Edinburgh, Edinburgh, United Kingdom.

Chapman, M., 2003, Frequency-dependent anisotropy due to meso-scale fractures in the presence of equant porosity, *Geophys. prospect.*, **51**, 369–379.

Chardac, O., Murray, D., Carnegie, A., and Marsden, J. R., 2005, A proposed data acquisition program for successful geomechanics projects, 2005 SPE 14th Middle East Oil and Gas Show and Conference held in Bahrain, SPE 93182.

Chesnokov, E. M., Queen, J. H., Vichorev, A., Lynn, H. B., Hoober, J., Bayuk, I., Castagna, J., and Roy, B., 2001, Frequency-dependent anisotropy, 71st SEG Meet., San Antonio, Texas, USA, Expanded Abstr., Soc. Explor. Geophys., 2120–2123.

Christova, C., 2004, Stress field in the Ryukyu-Kyushu Wadati-Benioff zone by inversion of earthquake focal mechanisms, *Tectonophysics*, **384**, 175–189.

Crampin, S., 1978, Seismic wave propagation through a cracked solid: polarization as a possible dilatancy diagnostic, *Geophys. J. Roy. Astr. Soc.*, **53**, 467–496.

Crampin, S., 1984, Effective anisotropic elastic-constants for wave propagation through cracked solids, *Geophys. J. Roy. Astr. Soc.*, **76**, 135–145.

De Meersman, K., 2005, Estimating signal polarisations in seismic array data: theory and applications, Ph.D. thesis, The University of Leeds, Leeds, United Kingdom.

Dietrich, M., 1988, Modeling of marine seismic profiles in the t-x and tau-p domains, *Geophysics*, **53**, 453–465.

Fanchi, J., 2003, Estimating geomechanical properties using an integrated flow model, *SPE Reservoir Evaluation & Engineering*, **6**, no. 83730, 108–116.

Filbrandt, J., Dhahab, S., Al-Habsy, A., Harris, K., Keating, J., Al-Mahruqi, S., Ozkaya, I., Richard, P., and Robertson, J. A., in press, Kinematic interpretation and structural evolution of Northern Oman, Block 6, since the Late Cretaceous, *GeoArabia*.

Fouch, M. J., and Fischer, K. M., 1998, Frequency-dependent shear-wave anisotropy in the Mariana subduction zone, *EOS Trans. AGU Suppl.*, 79, S212.

Garcia, J. G., and Teufel, L. W., 2005, Numerical simulation of fully coupled fluid-flow / geomechanical deformation in hydraulically fractured reservoirs, SPE Production Operations Symposium, Apr 16-19 April, Oklahoma City, Oklahoma, SPE 94062.

Gardner, G. H. F., Gardner, L. W., and Gregory, A. R., 1974, Formation velocity and density - The diagnostic basics for stratigraphic traps, *Geophysics*, **39**, 19–34.

Gephart, J. W., and Forsyth, D. W., 1984, An improved method for determining the regional stress tensor using earthquake focal mechanism data: application to the San Fernando earthquake sequence, *J. Geophys. Res.*, **89**, 9305–9320.

Gillard, D., Wyss, M., and Okubo, P., 1996, Type of faulting and orientation of stress and strain as a function of space and time in Kilauea's south flank, Hawaii, *J. Geophys. Res.*, **101**, 16025–16042.

Goodman, R. E., 1989, *Introduction to rock mechanics*, Wiley, New York, 2nd edition.

Guest, S., and Kendall, M., 1993, Modelling seismic waveforms in anisotropic inhomogeneous media using ray and maslov asymptotic theory: applications to exploration seismology, *Can. J. Expl. Geophys.*, **29**, 78–92.

Gutierrez, M., Lewis, R. W., and Masters, I., 2001, Petroleum reservoir simulation coupling fluid flow and geomechanis, *SPE Reservoir Evaluation & Engineering*, **4**, 164–172.

Hall, S. A., and Kendall, J.-M., 2000, Constraining the interpretation of AVOA for fracture characterisation, in *Anisotropy 2000: Fractures, Converted Waves, and Case Studies*, eds. L. Ikelle and A. Gangi, Soc. Explor. Geophys., Tulsa, USA, 107–144.

Hardebeck, J. L., and Hauksson, E., 2001, Stress orientations obtained from earthquake focal mechanisms: What are appropriate uncertainty estimates?, *Bull. Seism. Soc. Am.*, **91**, 250–262.

Hill, R. W., 1952, The elastic behaviour of a crystalline aggregate, *Proc. Phys. Soc. (London)*, **A65**, 349–354.

Hinzen, K.-G., 2003, Stress field in the Northern Rhine area, Central Europe, from earthquake fault plane solutions, *Tectonophysics*, **377**, 325–356.

Hitchings, V. H., and Potters, H., 2000, Production and geological implications of the Natih 9C3D seismic survey, *GeoArabia*, **5**, 511–524.

Hornby, B. E., Schwartz, L. M., and Hudson, J. A., 1994, Anisotropic effective-medium modeling of the elastic properties of shales, *Geophysics*, **59**, 1570–1583.

House, L., Flores, R., and Withers, R., 1996, Microearthquakes induced by a hydraulic injection in sedimentary rock, East Texas, 66th Annu. Meet., Ext. Abstr., Soc. Explor. Geophys., 110–113.

Hudson, J. A., and Crampin, S., 2003, Comment on: 'The 3D shear experiment over the Natih field in Oman: the effects of fracture-filling fluids on shear propagation' by C. M. Van der Kolk, W. S. Guest and J. H. H. M. Potters, *Geophys. prospect.*, **51**, 365–368.

Hudson, J. A., Liu, E., and Crampin, S., 1996, Mechanical properties of materials with interconnected cracks and pores, *Geophys. J. Int.*, **124**, 105–112.

Hudson, J. A., 1980, Overall properties of a cracked solid, *Mathematical Proceedings of the Cambridge Philosophical Society*, **88**, 371–384.

Hudson, J. A., 1981, Wave speeds and attenuation of elastic waves in material containing cracks, *Geophys. J. Roy. Astr. Soc.*, **64**, 133–150.

Jaeger, J. C., and Cook, N. G., 1989, *Fundamentals of rock mechanics*, Chapman and Hall, London, 3rd edition.

Jones, R., Raymer, D., Mueller, G., Rynja, H., Maron, K., and Hartung, M., 2004, Microseismic monitoring of the Yibal oilfield, Oman, 74th SEG Meet., Denver, Colorado, USA, Expanded Abstr., Soc. Explor. Geophys.

Jupe, A., Jones, R., Wilson, S., and Cowles, J., 2000, The role of microearthquake monitoring in hydrocarbon reservoir management, 2000 SPE Annual Technical Conference and Exhibition held in Dalllas, Texas, SPE/ISRM 63131.

Kanamori, H., 1977, The energy release in great earthquakes, *J. Geophys. Res.*, **82**, 2981–2987.

Kennett, B. L., and Kerry, N. J., 1979, Seismic waves in a stratified half-space, *Geophys. J. Roy. Astr. Soc.*, **57**, 557–583.

Khan, M., and Teufel, L. W., 2003, The effect of geological and geomechanical parameters on reservoir stress path and its importance in studying permeability anisotropy, *SPE Reservoir Evaluation & Engineering*, **3**, no. 66184, 394–400.

Kravanja, S., and Panza, G. F., 2005, Full moment tensor retrieval for two earthquake swarms at the alps-dinarides junction, *Geophys. J. Int.*, **160**, 683–694.

Kristiansen, T. G., Barkved, O., and Pattillo, P. D., 2000, Use of passive seismic monitoring in well and casing design in the compacting and subsiding Valhall field, North Sea, SPE European Petroleum Conference, 24-25 October, Paris, France, SPE 65134.

Litsey, L. R., MacBride Jr., W. L., Al-Hinai, K. M., and Dismukes, N. B., 1986, Shuaiba reservoir geological study, Yibal field, Oman, *Journal of Petroleum Technology*, pages 651–661.

Liu, K., Zhang, Z., Hu, J., and Teng, J., 2001, Frequency band dependence of S-wave splitting in China mainland and its implications, *Science in China (Series D)*, 44 (7),659-665 (in English).

Liu, E., Chapman, M., Queen, J. H., Maultzsch, S., and Li, X. Y., 2003a, Frequency-dependent anisotropy: effects of multi-fracture sets on shear-wave polarizations, EAGE 65th Conference and Exhibition, abst. P264, Stavanger, Norway, June 2-5.

Liu, E., Maultzsch, S., Chapman, M., and Li, X. 2003b, Frequency-dependent seismic anisotropy and its implication for estimating fracture size in low porosity reservoirs, *The Leading Edge*, **22**, 662–665.

Liu, E., Queen, J. H., Li, X. Y., Chapman, M., Maultzsch, S., Lynn, H. B., and Chesnokov, E. M. 2003c, Observation and analysis of frequency-dependent anisotropy from a multicomponent VSP at Bluebell-Altamont field, Utah, *J. Applied Geophys.*, **54**, 319–333.

Liu, Q., Stone, T., Han, G., Marsden, R., and Shaw, G., 2004, Coupled stress and fluid flow using a finite element method in a commercial reservoir simulator, SPE Asia Pacific Oil and Gas Conference and Exhibition, 18-20 October, Perth, Australia, SPE 88616.

Lu, Z., Wyss, M., and Pulpan, H., 1997, Details of stress directions in the Alaska subduction zone from fault plane solutions, *J. Geophys. Res.*, **102**, 5385–5402.

Madariaga, R., 1976, Dynamics of an expanding circular fault, *Bull. Seism. Soc. Am.*, **3**, 639–666.

Maddock, J. S., Fisher, Q. J., Kendall, J.-M., and Lloyd, G. E., 2004, Petrofabric analysis of seismic anisotropy in siliciclastic sedimentary rocks, 66th EAGE Conference and Technical Exhibition, Paris, France, Expanded Abstracts, Paper P348.

Mallick, S., and Frazer, L. N., 1987, Practical aspects of reflectivity modeling, *Geophysics*, **52**, 1355–1364.

Marson-Pidgeon, K., and Savage, M. K., 1997, Frequency-dependent anisotropy in Wellington, New Zealand, *J. Geophys. Res.*, **24**, 3297–3300.

Maultzsch, S., Chapman, M., Liu, E., and Li, X., 2003, Modelling frequency-dependent seismic anisotropy in fluid-saturated rock with aligned fractures: implication of fracture size estimation from anisotropic measurements, *Geophys. prospect.*, **51**, 381–392.

Maxwell, S. C., Young, R. P., Bossu, R., Jupe, A., and Dangerfield, J., 1998, Microseismic logging of the Ekofisk reservoir, Eurock '98, Trondheim, Norway, SPE/ISRM 47276, 387–393.

McKenzie, D. P., 1969, Relation between fault plane solutions for earthquakes and directions of principal stresses, *Bull. Seismol. Soc. Am.*, **59**, 591–601.

Mercadier, C. G. L., and Mäkel, G. H., 1989, Fracture pattern of Natih outcrops at jebels Nihayda, Qusaybah and Salakh, North Oman, relevance to the Natih field and development implications, Unpublished report PE/89/181, prepared by Petroleum Development Oman.

Nakamura, K., 1977, Volcanoes as possible indicators of tectonic stress orientation: principle and proposal, *Journal of volcanology and geothermal research*, **2**, 1–16.

Neri, G., Barberi, G., Olive, G., and Orecchio, B., 2005, Spatial variations of seismogenic stress orientations in Sicily, south Italy, *Physics of the earth and planetary interiors*, **148**, 175–191.

Osipov, V. I., Sokolov, V. N., and Eremeev, V. V., 2004, *Clay seals of oil and gas deposits*, Swets and Zeitlinger, Lisse, The Netherlands.

Parker, R. L., and McNutt, M. K., 1980, Statistics for the one-norm misfit measure, *J. Geophys. Res.*, **85**, 4429–4430.

Potters, J. H. H. M., Groenendaal, H. J. J., Oates, S. J., Hake, J. H., and Kalden, A. B., 1999, The 3D shear experiment over the Natih field in Oman. Reservoir geology, data acquisition and anisotropy analysis, *Geophys. prospect.*, **47**, 637–662.

Press, W. H., Flannery, B. P., Teukolsky, S. A., and Vetterling, W. T., 1989, *Numerical recipes*, Cambridge University Press, Cambridge, 2nd edition.

Reuss, A., 1929, Berechnung der fliessgrenze von mischkristallen auf grund der plastizitatsbedingung fur einkristalle, *Z. Angew. Math. Mech.*, **9**, 49–58.

Rössler, D., Rümpker, G., and Krüger, F., 2004, Ambiguous moment tensors and radiation patterns in anisotropic media with applications to the modeling of earthquake mechanisms in W-Bohemia, *Stud. Geophys. Geod.*, **48**, 233–250.

Rutledge, J. T., Phillips, W. S., and Schuessler, B. K., 1998, Reservoir characterization using oil-production-induced microseismicity, Clinton County, Kentucky, *Tectonophysics*, **289**, 129–152.

Sanchez, J. J., Wyss, M., and McNutt, S. R., 2004, Temporal-spatial variations of stress at Redoubt volcano, Alaska, inferred from inversion of fault plane solutions, *Journal of volcanology and geothermal research*, **130**, 1–30.

Sayers, C. M., and Kachanov, M., 1991, A simple technique for finding effective elastic constants of cracked solids for arbitrary crack orientation statistics, *International Journal of Solids and structures*, **27**, 671–680.

Sayers, C. M., 2002, Fluid-dependent shear-wave splitting in fractured media, *Geophys. prospect.*, **50**, 393–401.

Schoenberg, M., and Sayers, C. M., 1995, Seismic anisotropy of fractured rock, *Geophysics*, **60**, 204–211.

Schön, J. H., 1996, *Physical properties of rocks : fundamentals and principles of petrophysics*, Pergamon, New York.

Segall, P., 1989, Earthquakes Triggered by Fluid Extraction, *Geology*, **17**, 942–946.

Shearer, P. M., 1999, *Introduction to seismology*, Cambridge University Press, Cambridge.

Sheriff, R. E., and Geldart, L. P., 1994, *Exploration seismology*, Cambridge University Press, Cambridge, 2nd edition.

Sibson, R. H., 1974, Frictional constraints on thrust, wrench and normal faults, *Nature*, **249**, 542–544.

Sibson, R. H., 1985, A note on fault reactivation, *Journal of Structural Geology*, **7**, 751–754.

Sileny, J., and Panza, G. F., 1991, Inversion of seismograms to determine simultaneously the moment tensor components and source time function for a point source buried in a horizontally layered medium, *Stud. Geoph. Geod.*, **35**, 166–183.

Sileny, J., Panza, G. F., and Campus, P., 1992, Waveform inversion for point source moment tensor retrieval with variable hypocentral depth and structural model, *Geophys. J. Int.*, **109**, 259–274.

Silver, P. G., and Chan, W. W. J., 1991, Shear-wave splitting and subcontinental mantle deformation, *J. Geophys. Res.*, **96**, 16429–16454.

Snoke, J. A., Munsay, J. W., Teague, A. G., and Bollinger, G. A., 1984, A program for focal mechanism determination by combined use of polarity and SV-P amplitude ratio data, *Earthquake Notes*, **55**, 15.

Snoke, J. A., 2003, FOCal MEChanism determinations, *in* Lee, W. H. K., Kanamori, H., Jennings, P. C., and Kisslinger, C., Eds., *International Handbook of Earthquake and Engineering Seismology*, Academic Press, San Deigo, Chapter 85.12.

Teanby, N., Kenda, N. A., Kendall, J.-M., and Van der Baan, M., 2004a, Automation of shear-wave splitting measurements using cluster analysis, *Bull. Seism. Soc. Am.*, **94**, 453–463.

Teanby, N., Kendall, J.-M., Jones, R. H., and Barkved, O. 2004b, Stress-induced temporal variations in seismic anisotropy observed in microseismic data, *Geophys. J. Int.*, **156**, 459–466.

Thomas, L., Chin, L., Pierson, R., and Sylte, J., 2003, Coupled geomechanics and reservoir simulation, *SPE Journal*, **8**, no. 87339, 350–358.

Thomsen, L., 1995, Elastic anisotropy due to aligned cracks in porous rock, *Geophys. Prospect.*, **43**, 805–829.

Tod, S. R., and Liu, E., 2002, Frequency-dependent anisotropy due to fluid flow in bed limited cracks, *Geophys. Res. Lett.*, **29**, 01.

Tod, S. R., 2001, The effects on seismic waves of interconnected nearly aligned cracks, *Geophys. J. Int.*, **146**, 249–263.

Tran, D., Settari, A., and Nghiem, L., 2004, New iterative coupling between a reservoir simulator and a geomechanics module, *SPE Journal*, **9**, 362–369.

Valcke, S., Casey, M., Lloyd, G. E., Kendall, J.-M., and Fisher, Q., in press, Lattice preferred orientation and seismic anisotropy in sedimentary rocks, *Geophys. J. Int.*.

van der Kolk, C. M., Guest, W. S., and Potters, J. H. H. M., 2001, The 3D shear experiment over the Natih field in Oman: the effect of fracture-filling fluids on shear propagation, *Geophys. prospect.*, **49**, 179–197.

Vavryčuk, V., 2005, Focal mechanisms in anisotropic media, *Geophys. J. Int.*, **161**, 334–346.

Voigt, W., 1928, *Lehrbuch der Kristallphysik*, Teubner-Verlag, Leipzig.

Walters, D. A., Settari, A., and Kry, P. R., 2002, Coupled geomechanical and reservoir modeling investigating poroelastic effects of cyclic steam stimulation in the Cold Lake reservoir, *SPE Reservoir Evaluation & Engineering*, **5**, no. 80997, 507–516.

Warpinski, N. R., Branagan, P., and Wilmer, R., 1985, Insitu stress measurements at United-States DOE's multiwell experiment site, Mesaverde group, Rifle, Colorado, *J. Petrol. Technol.*, **37**, 527–536.

Williamson, J. H., 1968, Least-squares fitting of a straight line, *Can. J. Phys.*, **46**, 1845–1847.

Winterstein, D. F., 1990, Velocity anisotropy terminology for geophysicists, *Geophysics*, **55**, 1070–1088.

Woodland, D. C., and Bell, J. S., 1989, Insitu stress magnitudes from mini-frac records in western canada, *Journal of Canadian Petroleum Technology*, **28**, 22–31.

Woodland, D. C., 1990, Borehole instability in the western Canadian overthrust belt, *SPE Drilling Engineering*, **5**, 27–33.

Wu, B., Addis, M. A., and Last, N. C., 1998, Stress estimation in faulted regions: the effect of residual friction, SPE/ISRM Rock Mechanics in Petroleum Engineering, 8-10 July, Trondheim, Norway, SPE/ISRM 47210.

Wyss, M., Liang, B., Tanigawa, W. R., and Wu, X., 1992, Comparison of orientations of stress and strain tensors based on fault plane solutions in Kaoiki, Hawaii, *J. Geophys. Res.*, **97**, 4769–4790.

York, D., 1966, Least-squares fitting of a straight line, *Can. J. Phys.*, **44**, 1079–1086.

Zoback, M. D., and Zinke, J. C., 2002, Production-induced normal faulting in the Valhall and Ekofisk oil fields, *Pure appl. geophys.*, **159**, 403–420.

Appendix A

Codes and S-wave splitting results

Table A.1: FORTRAN codes, SAC macros, MATLAB and GMT scripts used in this thesis and written by A. Al-Anboori unless otherwise stated. A software copy of the Codes written by Abdullah Al-Anboori are in the attached CD at the back cover of the thesis.

Name	Task
	Data preparation and rotation
	FORTRAN codes
XMETAL	The **X**-windows version of the **M**icroseismic **E**vent **T**imig **A**nd **L**ocation program, developed by ABB (by Rob Jones and others)
fitl1perp.f	Solves iteratively for the best fit line through data points based on least absolute (L1 norm) perpendicular offsets
fitl2perp.f	Numerically fit the best line through data points based on least squared (L2) vertical offsets
srotate.f	Rotate 3-C data to the ray direction. The ray direction is estimated via means of S-wave particle motion
lsrotate.f	Rotate 3-C data to the ray direction out of the source. The ray direction is estimated via means of S-wave polarisation and event location
protate.f[1]	Rotate 3-C data to ray direction estimated from P-wave hodogram
lprotate.f	Rotate 3-C data to ray direction out of the source via means of P-wave particle motion and the source location
lrotate.f	Rotate 3-C data to ray direction assuming a straight source-receiver raypath
urotate.f	Rotate 3-C data based on user rotation angles
	SAC macros
srotate.m	Executes srotate FORTRAN program and displays the S-wave particle motion
lsrotate.m	Executes lsrotate FORTRAN program and displays the S-wave particle motion
protate.m[2]	Executes protate FORTRAN program and displays the P-wave particle motion
lprotate.m	Executes lprotate FORTRAN program and displays the P-wave particle motion
lrotate.m	Executes lrotate FORTRAN program
urotate.m	Executes urotate FORTRAN program

continued on next page

[1] Written by N. Teanby.
[2] Written by N. Teanby.

Table A.1: *continued*

Name	Task
	C-shells
datprep.csh[3]	Prepare and convert the data exported from XMETAL to SAC format
	Focal mechanisms and stress inversion
	FORTRAN codes
FOCMEC [4]	Determines focal mechanisms
FMSI [5]	Performs focal mechanism stress inversion
axitra[6]	Reflectivity modelling code to simulate synthetic seismograms
skb[7]	Reflectivity modelling code
surefl psvsh[8]	Reflectivity modelling code
wfps.f	Prepares polarity picks, amplitude ratios, ray azimuth and takeoff angles in a suitable format for the FOCMEC program
	SAC macros
calcpsvsh.m	Rotates ENZ data to ray frame and pick polarity and amplitudes of P- and SV- and SH-waves
	C-shells
fps.csh	Runs *wfps* FORTRAN program
fmp.sh	Run the FOCMEC program and plot the possible fault plane solution together with the input P polarities
fmpr.sh	Does *fmp.sh* but also plots S polarities
fmprs.sh	Does *fmp.sh* but also plots S polarities and amplitude ratios
fmep.sh	Does *fmp.sh* but also plots emergent P-arrivals
fmepr.sh	Does *fmpr.sh* but also plots emergent P-arrivals
fmeprs.sh	Does *fmprs.sh* but also plots emergent P-arrivals
	S-wave splitting modelling
	FORTRAN codes
CIJSTAN	Evaluate elastic constants of fractured media by Hall and Kendall (2000)
ATRAK	Anisotropic ray-tracer by (Guest and Kendall, 1993)
EMATRIX	Calculates slownesses and group velocities over the whole hemisphere for propagating plane waves in anisotropic crystals. The program is developed by David Mainprice (LABORATOIRE DE TECTONOPHYSIQUE, France)
ani_scale_VR	Calculate elastic constants of an entire rock based on the elasticity of the constituent anisotropic mineral using an average of Voigt and Reuss methods
log2azpv	Extract group velocities from SLWVEL (part of the ATRAK package) output for 2D group-velocity plots as a function of the ray azimuth
log2incpv	Extract group velocities from SLWVEL (part of the ATRAK package) output for 2D group-velocity plots as a function of the ray inclination

continued on next page

[3]Actually accompanies several C shells executed individually, initially written by Nick Teanby, that are modifi ed to the current single fi le.

[4]Developed by Snoke et al. (1984), free program, downloaded from http://www.geol.vt.edu/outreach/vtso/focmec/

[5]Developed by Gephart and Forsyth (1984), downloaded from ftp://www.geo.cornell.edu/pub/FMSI/FMSI_for_IBM with slight modifi cations.

[6]A free code for local-distance seismograms based on Kennett and Kerry (1979) and Bouchon (1981), written by Olivier Coutant (LGIT-IRIGM BP 53X 38041 Grenoble cedex, coutant@lgit.observ-gr.fr), available on http://orfeus.knmi.nl/other.services/software.links.shtml.

[7]Written by Michel Dietrich, (Dietrich, 1988), provided by Mirko Van der Baan, Leeds University, UK.

[8]Part of Seismic Unix (SU) package.

Table A.1: *continued*

Name	Task
ilog2enz_hyb	Computes the strike of fast-shear-wave vector rather than of fast-shear polarisation plane
	SAC macros
split_oman.m	Splitting macro that calls the splitting FORTRAN code shear_ms based on the method of Silver and Chan (1991). Both are written by N. Teanby
	MATLAB scripts
plot_vpg.m	Uses EMATRIX output to plot phase velocities of P-waves, S-wave anisotropy and fast-shear-wave polarisations in a hemisphere projection, written by J. Wookey
plot_az.m	Uses EMATRIX output to plot fast-shear vector strike as a function of ray azimuth
plot_crstr.m	Uses EMATRIX output to plot fast-shear vector strike as a function of crack strike
	C-shells
aseis2asc	prepare the ATRAK output for SAC
	Windows programs
P3	(Free) Windows program, version 1.60, that calculates petroleum properties based on Gassmann theory, developed by Malkewicz Hueni Associates, Colorado, USA
	Anisotropy from S-wave splitting
	FORTRAN codes
ani_vis.f	Calculate percent anisotropy from splitting measurements, the S-velocity model and source and receiver locations
ilog2enz_hyb_c	Does the same as *ilog2enz_hyb* but for multiple splitting measurement sets at one go. *abc2ilog.csh* C-shell file runs the code
abc2ilog.csh	Runs the FORTRAN *ilog2enz_hybrid_c.f* code
	SAC macros
filterabc.m	100 Hz low pass filter a-,b- and c-components with 6 poles and 2 passes
split_oman.m	See above
	GMT scripts
sphani.gmt	Uses *ani_vis.f* output to plot the magnitude of the S-wave splitting and the associated fast-shear-wave polarisations in 3D (upper hemisphere projection)
	Frequency-dependent anisotropy
	FORTRAN codes
dmnntfreq.f	Calculates the mean and dominant frequency of shear-waves
split_oman.m	See above
ybfda.f	Calculates percent anisotropy in Yibal from splitting measurements of various S-wave frequency bands, the S-velocity model and source and receiver locations
vhfda.f	Calculates percent anisotropy in Valhall from splitting measurements of various S-wave frequency bands, the S-velocity model and source and receiver locations

continued on next page

Table A.1: *continued*

Name	Task
chapman.f[9]	Calculates the frequency-dependent S-wave splitting based on the Chapman (2003) theory
misfitperp.f	Estimates fracture size and density from observations of frequency-dependent S-wave splitting. The estimation is based on a grid search to minimise the misfit (average perpendicular residuals) between the Chapman (2003) model and the data
	GMT scripts
misfit.gmt	Uses *misfitperp.f* output to plot the misfit results of the grid search on contour plots

Table A.2: Shear-wave splitting results stored in the attached CD at the back cover of the thesis.

File name	Content description
	Data preparation and rotation
	S-wave splitting
split_fastplane_A.dat	Class A splitting results of the Yibal data with fast-shear-wave strike and dip of the fast-wave polarisation plane
split_fastplane_B.dat	Class B splitting results of the Yibal data with fast-shear-wave strike and dip of the fast-wave polarisation plane
split_fastvector_A.dat	Class A splitting results of the Yibal data with fast-shear-wave strike and dip of the fast-wave vector
split_fastvector_B.dat	Class B splitting results of the Yibal data with fast-shear-wave strike and dip of the fast-wave vector
split_hybrid_A.dat	Class A splitting results of the Yibal data with fast-shear-wave strike and dip of the fast-wave vector and the fast-wave polarisation plane, respectively
split_hybrid_B.dat	Class B splitting results of the Yibal data with fast-shear-wave strike and dip of the fast-wave vector and the fast-wave polarisation plane, respectively
	Frequency-dependent S-wave splitting
yb02.dat	Class A splitting results of various frequency bands of the Yibal microseismicity
vh98.dat	Class A splitting results of various frequency bands of the Valhall microseismicity

[9]Written by Mark Chapman, (Chapman, 2003), British Geological Survey, Edinburgh.

Appendix B

Station locations

Table B.1 Local easting (x), northing (y) and depth (z) of the 8-level, 4C receiver array in the five boreholes. The local x and y coordinates are offset from the Universal Transverse Mercator (UTM) coordinates (x_{UTM},y_{UTM}) by: x=x_{UTM}-395000 and y=y_{UTM}-2448000.

well	level	x[m]	y[m]	z[m]
1	1	2243.281250	138.500000	-816.200012
1	2	2242.968750	138.250000	-866.200012
1	3	2242.812500	137.750000	-916.200012
1	4	2242.593750	137.750000	-966.200012
1	5	2242.281250	138.000000	-1016.200012
1	6	2242.125000	138.000000	-1066.199951
1	7	2251.343750	137.000000	-1200.300049
1	8	2278.406250	141.000000	-1275.400024
2	1	3964.125000	777.500000	-852.500000
2	2	3964.593750	776.750000	-902.400024
2	3	3968.656250	771.000000	-1177.400024
2	4	3969.062500	770.500000	-1197.300049
2	5	3969.500000	770.000000	-1217.300049
2	6	3969.968750	769.500000	-1237.300049
2	7	3970.468750	768.750000	-1257.300049
2	8	3971.000000	768.250000	-1277.300049
3	1	3955.656250	162.500000	-875.599976
3	2	3959.812500	170.750000	-904.200012
3	3	3964.093750	179.000000	-932.700012
3	4	3968.406250	187.250000	-961.200012
3	5	3972.687500	195.500000	-989.700012
3	6	3976.906250	203.500000	-1018.299988
3	7	3981.156250	211.750000	-1046.800049
3	8	3985.500000	219.750000	-1075.400024
4	1	3350.593750	1847.250000	-879.200012
4	2	3349.906250	1848.750000	-944.200012
4	3	3349.187500	1850.000000	-1009.200012
4	4	3347.968750	1851.000000	-1074.199951
4	5	3346.812500	1852.000000	-1139.099976
4	6	3345.656250	1852.500000	-1204.099976
4	7	3337.375000	1860.250000	-1267.800049
4	8	3311.406250	1878.750000	-1324.099976
5	1	5175.312500	1455.500000	-804.799988
5	2	5174.281250	1456.250000	-884.799988
5	3	5173.156250	1456.750000	-964.799988
5	4	5172.000000	1457.250000	-1044.800049
5	5	5170.875000	1458.000000	-1124.800049
5	6	5169.843750	1458.750000	-1204.800049
5	7	5168.906250	1459.750000	-1284.800049
5	8	5168.093750	1460.750000	-1364.800049

Appendix C

Event locations

Table C.1: Easting (x), northing (y), depth (z), event number (EV), root mean square of time error (RMS), magnitude (MAG) and origin time (yymmddhhmm: year, month, day, hour and minute), time in seconds from midnight 00:00:00 (TIME) of data recorded in the 4-10/June2002 and 19-26/Oct2002 periods. A -10.00 magnitude is a null result (i.e., XMETAL failed to estimate the event magnitude).

x [m]	y [m]	z [m]	EV	RMS [ms]	MAG	yymmddhhmm	TIME [s]
3831.822	46.723	-937.192	3	2.5	-1.82	0206041307	47269
4867.679	1499.811	-883.838	7	5.3	-1.86	0206041626	59167
5243.293	1139.219	-866.513	8	3.7	-10.00	0206041641	60061
5220.328	1114.063	-885.460	9	4.3	-1.82	0206041641	60109
5217.102	1117.280	-796.598	10	2.5	-10.00	0206041642	60158
5220.701	1055.645	-875.052	11	4.7	-10.00	0206041732	63169
5475.979	1333.576	-891.841	15	13.3	-0.77	0206041831	66683
5293.720	1175.587	-862.722	28	2.9	-1.91	0206042016	73000
5303.729	1168.360	-886.420	42	4.2	-10.00	0206042213	80025
5251.650	1075.643	-896.409	44	4.3	-10.00	0206042231	81068
4927.790	1624.021	-839.071	45	3.8	-1.78	0206042306	83192
4971.894	1663.439	-876.249	46	3.4	-1.55	0206042314	83686
5234.727	1117.101	-876.214	48	1.3	-0.62	0206042335	84926
5284.317	1187.358	-886.011	49	3.3	-1.76	0206042343	85417
5251.168	1155.153	-871.687	51	3.1	-10.00	0206050035	2152
5280.581	1093.359	-897.268	57	3.1	-10.00	0206050049	2988
5221.608	1094.368	-899.846	58	1.1	-1.36	0206050100	3626
5198.503	1040.490	-905.042	59	5.3	-10.00	0206050105	3957
3937.776	776.635	-951.492	63	8.6	-1.58	0206050139	5940
5276.877	1153.231	-880.562	67	4.9	-10.00	0206050158	7122
5243.020	1115.434	-897.542	68	4.4	-1.30	0206050227	8854
5246.888	1154.455	-903.578	69	5.3	-10.00	0206050228	8930
4970.686	1638.878	-894.400	70	2.8	-1.59	0206050229	8941

continued on next page

Table C.1: *continued*

x [m]	y [m]	z [m]	EV	RMS [ms]	MAG	yymmddhhmm	TIME [s]
5225.447	1131.157	-900.154	71	4.0	-10.00	0206050229	8959
4919.917	1534.872	-867.382	72	3.3	-1.86	0206050241	9678
5246.699	1134.854	-881.114	73	5.2	-1.37	0206050304	11082
4975.897	1256.686	-872.575	202	13.7	-1.76	0206050442	16928
5240.213	1113.593	-902.362	203	4.7	-1.51	0206050519	19143
5264.857	1383.750	-948.614	207	6.1	-1.16	0206050601	21677
5225.936	1115.946	-901.589	211	4.6	-1.48	0206050631	23513
3367.305	1059.425	-960.013	212	6.0	-10.00	0206050653	24835
5115.997	2742.591	-771.295	213	7.9	-10.00	0206050732	27167
5212.223	1127.396	-880.180	216	5.7	-1.72	0206050807	29237
3155.637	982.849	-1433.499	217	4.2	-0.95	0206050813	29606
4942.421	1639.837	-885.443	220	3.6	-1.66	0206050905	32747
3569.128	180.956	-960.175	1001	7.2	-1.40	0206051040	38407
3524.139	-83.697	-1054.193	1002	2.9	-10.00	0206051040	38429
3564.822	203.795	-870.416	1004	3.9	-10.00	0206051049	38988
5331.579	1166.060	-892.739	1005	3.2	-10.00	0206051054	39253
3416.446	1075.573	-983.599	1006	14.1	-1.51	0206051054	39257
3933.494	39.232	-1017.656	1008	4.2	-1.97	0206051154	42858
3763.936	82.375	-957.341	1009	2.6	-1.74	0206051246	45962
3743.136	259.285	-960.055	1011	3.0	-10.00	0206051248	46090
3855.459	-23.261	-983.801	1012	3.1	-1.89	0206051248	46095
3703.036	133.060	-928.770	1014	4.7	-1.64	0206051249	46143
7039.764	3253.947	-1800.466	1015	27.3	-10.00	0206051258	46735
2171.686	158.159	-1003.212	1017	8.5	-1.82	0206051309	47366
3808.454	112.785	-960.994	1018	10.0	-1.17	0206051314	47644
3768.351	89.607	-934.021	1020	5.8	-1.65	0206051316	47792
3801.538	109.581	-917.750	1022	1.3	-1.96	0206051316	47818
5265.485	1080.529	-865.622	1025	2.2	-1.59	0206051325	48324
5226.859	1145.323	-887.566	1026	3.8	-1.62	0206051338	49081
5225.173	1093.954	-902.696	1027	1.8	-10.00	0206051338	49122
3740.398	78.381	-1051.296	1029	7.8	-1.51	0206051353	49992
3711.424	28.274	-1012.115	1030	7.6	-1.23	0206051353	50027
3338.718	1.205	-1176.865	1032	21.9	-10.00	0206051430	52241
5097.605	1730.827	-875.441	1033	2.2	-10.00	0206051452	53544
1833.557	-2.773	-869.507	1035	7.2	-10.00	0206051518	55098
3650.185	95.647	-1012.175	1036	3.8	-10.00	0206051538	56315
4178.053	-98.482	-696.281	1042	3.2	-10.00	0206051620	58836
3458.690	170.103	-883.624	1045	6.7	-10.00	0206051627	59229
3366.893	-174.135	-1005.361	1046	6.0	-10.00	0206051628	59333
3637.882	-109.580	-1142.961	1050	4.5	-10.00	0206051655	60944
5213.040	1093.908	-887.539	1059	3.5	-10.00	0206051808	65319
5116.601	1170.289	-880.730	1060	4.8	-1.55	0206051832	66732
3469.850	174.702	-999.240	1062	14.7	-1.39	0206051847	67669
3418.710	-307.551	-1118.758	1063	10.3	-10.00	0206051854	68067
5267.419	1200.746	-878.309	1065	4.9	-10.00	0206051901	68487

continued on next page

Table C.1: *continued*

x [m]	y [m]	z [m]	EV	RMS [ms]	MAG	yymmddhhmm	TIME [s]
3683.905	54.130	-1059.131	1067	2.8	-10.00	0206051923	69821
3679.946	256.377	-947.051	1069	4.8	-10.00	0206051942	70934
5084.851	1167.741	-879.185	1070	0.6	-10.00	0206051948	71314
3820.167	488.084	-936.076	1071	6.3	-10.00	0206051950	71446
5449.600	1524.315	-885.218	1072	6.7	-1.47	0206052021	73292
5125.084	1124.988	-894.058	1074	5.5	-1.83	0206052048	74883
5074.449	1736.803	-884.932	1075	4.3	-1.92	0206052048	74900
3887.680	712.794	-1260.720	1076	3.6	-0.95	0206052049	74983
4989.046	1655.833	-877.888	1079	9.0	-1.73	0206052055	75337
4782.907	1371.331	-808.353	1083	6.1	-10.00	0206052144	78249
5223.157	1827.211	-884.541	1084	2.6	-10.00	0206052149	78565
5008.972	1732.411	-818.235	1085	12.3	-0.75	0206052150	78633
5356.384	1241.582	-882.442	1088	4.3	-1.49	0206052151	78691
4995.594	1626.519	-887.941	1089	6.0	-1.70	0206052152	78750
5316.619	1236.338	-889.546	1094	6.0	-1.40	0206052219	80369
5321.869	1235.271	-882.619	1098	5.3	-1.43	0206052242	81743
5047.165	1703.948	-846.312	1103	5.0	-1.41	0206052340	85232
3760.107	-58.910	-960.030	108	10.0	-10.00	0206060136	5789
3340.343	-121.125	-1120.061	109	11.2	-0.96	0206060148	6503
3665.001	55.726	-1194.225	110	4.1	-10.00	0206060148	6534
3881.088	33.252	-1007.422	114	6.8	-10.00	0206060231	9091
4863.500	1766.651	-1021.024	116	3.0	-1.56	0206060236	9379
5388.383	1800.759	-788.544	122	3.8	-10.00	0206060319	11947
3863.787	-1.479	-910.302	129	6.3	-1.76	0206060412	15177
5194.216	1757.419	-1014.586	130	21.0	-1.27	0206060427	16061
3754.646	57.581	-949.750	131	7.3	-1.55	0206060430	16238
3666.411	166.151	-1048.377	132	6.0	-1.40	0206060432	16334
3645.158	231.157	-960.021	134	4.1	-10.00	0206060459	17955
3849.018	263.187	-842.107	135	3.6	-10.00	0206060536	20173
3784.314	-63.352	-1134.935	136	2.8	-10.00	0206060543	20598
5232.625	1797.971	-887.363	137	2.6	-1.55	0206060607	22059
5309.184	2860.776	-1637.353	138	56.7	-10.00	0206060654	24878
3850.445	219.809	-851.659	143	3.0	-10.00	0206060852	31926
4960.480	1656.435	-880.282	146	7.3	-10.00	0206061050	39034
5036.333	1684.846	-867.603	148	4.2	-1.66	0206061136	41783
4960.032	1642.332	-885.588	150	4.1	-10.00	0206061251	46303
4888.855	1569.799	-898.325	153	2.9	-10.00	0206061504	54297
3799.753	32.608	-957.742	154	2.0	-1.98	0206061610	58220
3742.816	206.375	-961.593	156	4.1	-10.00	0206061649	60586
3732.754	307.646	-960.028	159	5.4	-1.76	0206061740	63640
3745.595	297.663	-945.890	160	16.0	-1.20	0206061753	64415
3871.877	244.194	-960.000	161	2.1	-2.21	0206061815	65710
3878.850	-13.315	-960.500	167	4.6	-2.02	0206061848	67721
4869.998	1425.867	-880.224	168	2.7	-1.69	0206061852	67932
5482.523	652.305	-1123.718	184	19.9	-1.42	0206062105	75925

continued on next page

Table C.1: *continued*

x [m]	y [m]	z [m]	EV	RMS [ms]	MAG	yymmddhhmm	TIME [s]
3915.846	96.518	-945.059	186	2.5	-10.00	0206062110	76247
5247.892	1835.924	-834.930	189	12.7	-0.18	0206062128	77331
5260.343	1810.285	-876.476	191	2.4	-10.00	0206062130	77453
4057.765	159.094	-957.926	199	5.6	-10.00	0206070110	4255
3808.720	61.691	-916.525	202	5.3	-1.79	0206070116	4617
3794.907	92.674	-917.564	203	4.9	-1.51	0206070207	7625
3699.495	150.751	-960.031	204	5.5	-1.91	0206070207	7637
3780.561	363.645	-940.997	206	5.3	-0.83	0206070257	10674
3958.886	412.786	-960.001	221	4.2	-1.90	0206070411	15071
4639.584	1104.816	-677.482	222	1.2	-10.00	0206070411	15085
3309.012	-396.041	-1205.098	223	9.9	-0.97	0206070417	15461
3225.154	150.317	-1006.975	226	4.2	-10.00	0206070426	15991
5257.757	1155.199	-873.454	231	2.7	-10.00	0206070443	17025
5227.774	1773.544	-893.837	232	7.2	-1.67	0206070452	17539
3708.162	122.646	-936.204	233	3.3	-1.93	0206070517	19047
3965.258	565.255	-957.477	234	22.1	-10.00	0206070532	19950
5018.364	1674.873	-867.021	235	4.0	-1.53	0206070539	20378
2362.832	68.499	-1025.246	237	8.1	-1.66	0206070603	21815
3908.795	76.914	-952.416	239	1.7	-10.00	0206070722	26528
3931.539	88.039	-938.593	240	6.1	-1.97	0206070731	27096
3964.564	771.844	-1423.190	243	3.0	-10.00	0206070935	34538
3859.040	-18.993	-1020.551	245	1.6	-10.00	0206070942	34959
3917.363	89.025	-928.453	252	3.5	-2.11	0206071155	42946
2521.609	276.755	-727.940	256	1.2	-10.00	0206071302	46944
5133.510	972.031	-847.773	261	4.3	-10.00	0206071419	51582
3813.311	82.913	-917.723	262	5.1	-10.00	0206071450	53458
3711.830	179.558	-960.005	263	2.7	-10.00	0206071451	53466
3799.544	49.544	-960.059	266	3.2	-1.81	0206071514	54842
3759.140	134.392	-958.470	267	3.4	-1.08	0206071515	54900
4239.027	112.305	-681.823	268	20.6	-0.92	0206071515	54901
4996.998	1107.578	-854.176	272	3.5	-1.72	0206071537	56250
3934.829	230.086	-920.164	275	2.6	-1.26	0206071657	61060
3776.656	93.996	-958.543	276	15.9	-1.79	0206071703	61384
3751.240	133.026	-957.569	277	4.2	-10.00	0206071704	61479
3888.397	37.110	-866.732	278	1.7	-10.00	0206071710	61840
3727.388	94.852	-965.098	279	4.1	-1.63	0206071711	61913
3669.670	-167.824	-1092.091	282	2.6	-1.28	0206071735	63301
3725.537	229.748	-954.191	284	14.5	-10.00	0206071743	63835
3880.623	84.931	-1059.409	287	2.2	-10.00	0206071820	66027
3762.108	47.692	-960.176	288	2.8	-10.00	0206071840	67216
5463.992	1824.278	-851.611	289	6.0	-10.00	0206071856	68196
3755.756	44.947	-975.472	290	4.4	-1.67	0206071908	68937
5093.409	964.859	-863.534	292	6.4	-10.00	0206071945	71121
3914.889	82.504	-973.269	293	4.0	-1.94	0206071955	71754
5001.817	982.846	-838.213	299	12.5	-10.00	0206072042	74550

continued on next page

Table C.1: *continued*

x [m]	y [m]	z [m]	EV	RMS [ms]	MAG	yymmddhhmm	TIME [s]
5321.281	853.511	-1120.024	300	20.5	-1.15	0206072045	74711
3944.509	244.717	-927.356	304	8.4	-1.19	0206072117	76657
3779.048	157.556	-916.623	307	17.4	-1.75	0206072139	77962
4759.653	905.479	-960.184	312	1.1	-10.00	0206072241	81680
5453.764	1727.290	-872.570	314	14.1	-1.40	0206072252	82339
5001.565	932.830	-792.797	315	5.6	-10.00	0206072252	82350
3718.903	9.652	-886.869	316	1.5	-10.00	0206072302	82971
5618.594	810.453	-1123.210	317	27.3	-1.33	0206072306	83177
5601.451	955.669	-1120.233	318	18.6	-10.00	0206072306	83206
4680.596	980.271	-857.184	319	9.6	-1.17	0206072308	83331
5760.247	1798.388	-1210.506	321	11.2	-10.00	0206072317	83847
5593.246	1730.198	-768.778	322	3.3	-10.00	0206072318	83938
5537.763	1827.406	-785.088	323	3.3	-10.00	0206072320	84036
5060.997	951.885	-808.157	324	8.5	-1.80	0206072321	84086
5039.079	1065.020	-877.888	325	7.7	-1.25	0206072329	84580
5673.606	1609.109	-784.401	326	15.3	-10.00	0206072339	85141
4860.688	1089.571	-839.281	327	12.5	-10.00	0206072347	85641
5714.898	1652.716	-1200.071	328	7.2	-1.57	0206072347	85644
3782.552	320.806	-954.754	329	15.9	-2.04	0206072353	86039
3627.796	30.915	-935.925	330	6.7	-10.00	0206072357	86247
4634.316	1022.925	-936.053	331	4.4	-1.15	0206080113	4396
3782.822	131.765	-965.286	332	12.1	-1.16	0206080153	6795
3775.492	0.743	-992.713	334	15.1	-1.51	0206080156	6960
4655.774	857.751	-1120.279	335	23.1	-10.00	0206080156	6996
4652.888	798.043	-1120.113	337	12.5	-1.29	0206080201	7268
5048.627	879.959	-936.652	339	3.7	-10.00	0206080308	11285
4363.222	113.043	-1411.318	340	7.0	-1.41	0206080405	14735
5100.564	911.746	-1021.508	440	7.3	-1.64	0206080416	15394
3455.581	-342.142	-1120.176	449	33.4	-10.00	0206080421	15699
3784.393	82.298	-915.528	451	3.0	-1.88	0206080514	18849
3897.659	141.764	-925.514	452	1.7	-2.20	0206080520	19222
3716.953	31.358	-950.008	453	6.0	-10.00	0206080603	21799
3865.595	-14.900	-991.311	456	3.7	-10.00	0206080631	23499
5650.233	1839.804	-995.502	460	3.5	-10.00	0206080734	27297
5077.963	1053.027	-845.634	461	2.5	-10.00	0206080751	28262
3582.708	-4.669	-1208.981	462	7.2	-10.00	0206080755	28523
4989.932	805.930	-965.218	463	4.5	-10.00	0206080755	28549
5076.729	973.728	-882.600	465	4.5	-10.00	0206080908	32939
4963.405	695.237	-926.486	469	5.4	-0.79	0206080953	35633
4447.878	726.229	-1209.776	470	6.2	-10.00	0206080954	35652
5716.252	1842.849	-1121.530	471	10.0	-0.46	0206080954	35657
3773.632	181.427	-899.447	475	5.4	-10.00	0206081027	37623
3661.469	93.982	-905.948	476	4.6	-1.50	0206081104	39881
3859.438	219.526	-919.969	481	2.3	-10.00	0206081155	42932
5383.288	1800.257	-767.591	482	1.5	-10.00	0206081200	43251

continued on next page

Table C.1: *continued*

x [m]	y [m]	z [m]	EV	RMS [ms]	MAG	yymmddhhmm	TIME [s]
3644.897	-64.856	-960.001	485	8.1	-1.62	0206081255	46546
3658.538	124.653	-960.025	488	16.8	-1.74	0206081257	46636
5527.855	1790.161	-853.873	490	2.4	-10.00	0206081327	48430
5107.786	809.287	-979.124	491	5.0	-10.00	0206081327	48432
3016.236	-74.370	-1455.091	493	12.4	-1.03	0206081348	49694
2999.162	61.343	-1428.943	494	12.4	-1.02	0206081348	49696
3427.476	609.645	-857.206	495	8.8	-10.00	0206081353	50019
3742.659	14.943	-951.748	496	5.6	-1.92	0206081404	50653
3640.805	-144.861	-1080.898	497	3.7	-1.52	0206081441	52900
3667.607	36.526	-1030.214	498	7.7	-1.46	0206081454	53645
3746.705	253.522	-960.035	499	9.1	-10.00	0206081455	53708
3872.448	566.410	-923.942	502	7.9	-1.43	0206081621	58910
5085.695	763.719	-828.328	505	3.2	-1.32	0206081639	59980
3726.339	215.215	-966.058	508	3.7	-1.84	0206081719	62360
3863.480	-9.937	-982.157	509	5.1	-1.90	0206081719	62360
3858.828	-27.612	-960.320	510	2.5	-1.80	0206081719	62366
5144.363	1155.490	-881.484	512	3.6	-1.64	0206081722	62579
4824.861	1435.204	-798.935	513	6.6	-1.55	0206081723	62603
5029.066	1515.750	-992.815	514	13.2	-0.65	0206081724	62666
4867.199	1591.438	-859.294	517	13.5	-0.88	0206081724	62675
4821.192	1507.667	-886.457	518	5.0	-1.62	0206081724	62680
3843.554	75.503	-921.109	519	5.1	-1.24	0206081732	63145
5437.983	1246.394	-880.016	520	9.7	-1.63	0206081733	63184
4823.211	1514.671	-840.014	521	11.2	-1.77	0206081737	63456
4854.832	1525.834	-844.472	522	6.3	-1.77	0206081741	63711
4900.021	1187.968	-924.660	523	0.1	-1.29	0206081744	63849
4859.568	1581.309	-863.191	524	16.4	-1.25	0206081746	64009
4963.191	1650.569	-855.839	525	18.2	-1.00	0206081747	64074
4704.966	1596.516	-916.313	527	2.8	-10.00	0206081749	64162
4861.845	1454.444	-883.160	528	5.5	-1.74	0206081755	64521
4943.486	1215.831	-880.065	529	4.7	-1.82	0206081803	65023
4359.602	1219.914	-845.859	530	2.4	-10.00	0206081806	65203
4989.391	1751.841	-849.040	531	12.7	-0.96	0206081819	65953
4777.864	1592.876	-813.047	535	12.0	-1.51	0206081830	66630
4864.663	1473.928	-860.167	536	11.5	-1.51	0206081834	66878
3781.575	102.160	-941.031	537	3.3	-10.00	0206081835	66922
5442.520	1198.942	-847.811	539	16.3	-1.50	0206081842	67374
5045.587	953.238	-855.657	2	6.6	-1.04	0206090842	31344
4055.137	379.089	-981.683	3	10.2	-1.23	0206090848	31728
3905.474	54.875	-914.685	5	5.0	-1.50	0206090849	31765
4954.974	1640.523	-888.130	7	1.3	-10.00	0206090906	32806
3965.623	137.037	-911.619	9	3.2	-1.66	0206090953	35615
3957.750	101.752	-907.923	10	3.5	-1.87	0206090953	35625
5853.230	1781.039	-1335.407	11	12.6	-0.65	0206091004	36272
3845.900	84.270	-919.356	13	7.5	-10.00	0206091009	36590

continued on next page

Table C.1: *continued*

x [m]	y [m]	z [m]	EV	RMS [ms]	MAG	yymmddhhmm	TIME [s]
5519.657	1511.036	-874.737	15	7.5	-1.62	0206091021	37284
4895.082	1092.710	-860.842	19	11.2	-1.21	0206091100	39611
6292.239	2352.805	-1227.409	20	19.6	-0.57	0206091100	39629
4828.912	1492.384	-885.336	23	5.0	-1.58	0206091113	40392
4964.208	1556.325	-881.987	24	6.3	-1.68	0206091118	40709
3924.355	103.691	-926.376	25	2.2	-2.14	0206091120	40822
5350.211	1053.093	-870.539	27	8.8	-1.60	0206091155	42940
3861.497	382.962	-954.256	28	3.8	-10.00	0206091214	44077
3429.088	-79.753	-1305.181	32	8.2	-1.17	0206091345	49546
3928.160	141.351	-929.760	33	12.5	-10.00	0206091355	50128
3895.345	182.871	-920.001	38	2.0	-1.91	0206091640	60043
4180.405	904.401	-913.325	39	7.5	-1.44	0206091642	60159
3968.402	217.494	-884.785	40	2.8	-2.22	0206091652	60727
3360.270	165.353	-919.020	47	9.6	-10.00	0206091729	62960
4676.820	1048.655	-959.992	48	7.9	-0.94	0206091730	63039
4858.997	1484.160	-870.930	50	3.3	-1.72	0206091735	63315
3289.814	1350.065	-1119.118	51	1.5	-1.08	0206091745	63926
5241.252	1122.734	-904.708	55	7.8	-1.85	0206091757	64666
4322.752	1180.067	-1110.293	61	14.2	-10.00	0206091827	66437
4807.772	917.670	-981.299	62	3.7	-1.42	0206091831	66699
3756.233	109.465	-959.765	64	5.3	-1.88	0206091836	67013
3973.508	219.082	-883.132	81	3.9	-2.19	0206091849	67779
3977.909	242.085	-880.489	82	3.2	-10.00	0206091853	68009
3842.035	198.302	-883.039	84	2.2	-2.14	0206091905	68706
5197.951	1115.990	-920.018	85	11.0	-1.13	0206091906	68812
5199.751	769.493	-1177.886	102	15.7	-10.00	0206091930	70259
3450.630	46.259	-1268.031	105	7.1	-1.09	0206091942	70947
5174.314	1768.049	-868.674	106	5.2	-1.54	0206091956	71778
5428.430	1250.190	-887.182	107	6.5	-1.70	0206092002	72126
3970.624	249.817	-862.073	127	10.3	-0.95	0206092032	73969
3926.176	299.004	-784.891	128	10.2	-2.01	0206092032	73973
3803.119	290.662	-960.267	129	1.8	-2.05	0206092032	73978
3769.086	-8.357	-943.611	132	6.4	-1.79	0206092033	74029
3933.760	124.931	-923.331	136	1.1	-2.42	0206092111	76309
3829.744	-61.425	-892.030	139	5.5	-10.00	0206092151	78661
3814.553	181.406	-981.599	142	3.1	-1.63	0206092219	80350
5412.750	1333.243	-895.671	145	3.9	-10.00	0206092327	84465
4272.750	956.501	-1171.517	146	29.2	-1.47	0206092331	84675
3806.379	122.777	-942.657	147	5.3	-1.41	0206092332	84754
3523.022	74.780	-912.325	148	4.1	-1.58	0206092332	84756
5425.987	1292.457	-880.042	154	8.8	-1.72	0206100111	4287
4920.228	1614.036	-875.249	155	5.8	-1.68	0206100111	4294
3780.119	29.832	-996.702	156	3.5	-1.65	0206100118	4725
3674.294	939.896	-927.000	159	6.1	-1.67	0206100213	8025
3735.782	261.944	-955.073	160	6.2	-1.93	0206100216	8216

continued on next page

Table C.1: *continued*

x [m]	y [m]	z [m]	EV	RMS [ms]	MAG	yymmddhhmm	TIME [s]
5378.990	1245.919	-884.602	161	4.8	-1.51	0206100319	11997
4959.473	1627.114	-870.309	274	4.4	-10.00	0206100434	16493
3713.030	-11.617	-960.060	296	9.9	-10.00	0206100904	32690
4105.358	555.635	-888.872	318	17.8	-1.81	0206100932	34326
4784.136	1270.286	-852.541	336	10.5	-10.00	0206101029	37751
4049.360	-194.884	-960.049	2	11.0	-10.00	0210190032	1966
3641.205	4.974	-959.825	15	14.8	-0.99	0210190226	8815
4086.834	517.670	-935.011	17	20.0	-0.91	0210190256	10564
3958.653	484.141	-960.014	20	12.6	-10.00	0210190310	11407
4245.161	240.175	-1363.324	23	37.3	0.31	0210190316	11818
4007.815	488.920	-959.962	31	14.8	-0.80	0210190322	12164
3851.232	840.969	-897.297	35	5.2	-1.17	0210190329	12594
4141.586	576.061	-1001.297	36	17.0	-1.06	0210190349	13763
4045.481	542.249	-976.890	37	15.4	-1.36	0210190352	13923
4132.981	573.586	-998.209	38	16.1	-1.12	0210190353	13986
4132.749	502.026	-896.489	41	18.0	-1.31	0210190430	16209
4003.241	279.528	-899.922	42	5.6	-1.81	0210190451	17490
3810.658	177.394	-919.243	43	3.5	-1.43	0210190455	17731
3967.143	573.303	-922.622	44	12.1	-1.12	0210190456	17795
4041.647	600.483	-966.107	45	16.4	-0.99	0210190501	18071
3677.241	1408.593	-1120.080	46	23.3	-0.83	0210190822	30167
4109.163	563.340	-980.495	55	17.7	-1.26	0210190856	32196
3216.958	1925.046	-1426.817	57	161.8	-10.00	0210190902	32533
3925.396	-63.485	-989.704	59	11.9	-1.18	0210190911	33079
4368.587	914.729	-870.245	72	26.7	0.15	0210191017	37053
3848.649	2936.639	1397.941	83	11.3	-10.00	0210191104	39878
3330.446	224.755	-1450.771	90	6.5	-1.39	0210191135	41739
3649.240	1024.515	-1033.634	103	20.8	-0.64	0210191226	44791
4190.958	3074.103	-3230.071	105	92.5	0.46	0210191249	46141
3696.213	102.893	-960.085	162	21.5	-0.80	0210191329	48557
3955.978	503.307	-920.052	205	11.2	-1.36	0210191434	52454
4177.246	546.111	-999.373	207	16.4	-0.84	0210191436	52599
3960.393	527.758	-975.570	210	33.4	-1.15	0210191514	54860
3879.187	744.173	-797.973	212	6.2	-1.09	0210191524	55483
4030.272	456.688	-903.133	214	14.7	-1.23	0210191535	56158
4171.105	567.240	-882.601	215	17.3	-1.21	0210191538	56310
4205.540	622.543	-970.424	218	18.4	-1.33	0210191601	57718
4223.102	480.099	1.714	220	9.7	-1.38	0210191632	59522
4580.641	4103.048	-1801.632	223	108.7	0.01	0210191708	61709
3992.440	739.206	-648.467	228	17.6	-1.06	0210192029	73778
3662.671	1663.430	-1548.241	230	114.2	-10.00	0210192058	75527
3943.239	137.335	-776.553	231	0.4	-1.27	0210192101	75665
3858.819	1628.446	-1013.513	232	25.3	-0.40	0210192117	76623
2718.676	-572.848	-1289.345	234	23.4	0.52	0210192122	76955
4053.611	586.719	-933.886	235	13.5	-1.14	0210192131	77475

continued on next page

Table C.1: *continued*

x [m]	y [m]	z [m]	EV	RMS [ms]	MAG	yymmddhhmm	TIME [s]
4045.968	565.260	-979.251	237	15.3	-1.38	0210192141	78069
3981.758	761.784	-845.782	240	9.2	-1.50	0210192242	81776
4002.678	215.438	-891.758	241	7.3	-2.04	0210192244	81883
3761.685	1383.274	-960.054	242	37.9	-1.28	0210192257	82678
3807.392	1469.105	-960.006	243	42.4	-0.53	0210192313	83581
2626.345	-637.331	-1277.265	245	51.0	-0.58	0210192353	86020
2568.937	-733.682	-1121.040	1	9.9	-0.35	0210200020	1214
2685.816	-729.709	-1007.769	2	20.5	0.10	0210200021	1293
2837.419	-301.607	-1360.550	3	8.1	0.19	0210200021	1300
2829.610	-417.924	-1381.594	5	17.3	-0.80	0210200023	1392
2697.013	-458.069	-1162.616	6	15.2	-1.06	0210200024	1442
2749.566	-346.753	-794.980	7	7.8	-1.01	0210200024	1464
3274.573	-266.899	-897.779	8	13.1	-10.00	0210200025	1512
3003.737	-481.141	-1120.016	9	32.6	-1.27	0210200025	1529
2744.504	-445.766	-1280.436	10	5.0	-10.00	0210200027	1665
3049.085	-84.614	-748.789	12	12.7	-0.65	0210200037	2248
2427.491	-632.950	-1410.444	13	22.6	-0.74	0210200037	2265
2643.914	-663.318	-1159.407	26	14.1	-0.71	0210200241	9694
3924.669	95.749	-1126.496	28	4.9	-10.00	0210200247	10065
2622.120	-581.603	-1120.719	31	22.1	-10.00	0210200317	11848
3235.464	-361.179	-1120.028	35	26.7	-10.00	0210200400	14446
3731.376	117.387	-1303.244	39	5.6	-10.00	0210200434	16470
2488.930	-207.626	-1593.778	40	6.4	-10.00	0210200450	17407
3340.807	902.416	-1879.846	41	158.3	-10.00	0210200522	19336
2919.178	69.274	-1438.985	42	25.0	-10.00	0210200538	20285
2519.694	979.228	-1161.313	43	9.7	-10.00	0210200538	20297
2819.487	-488.798	-1125.891	44	21.5	-10.00	0210200538	20321
3893.315	162.509	-930.962	46	3.4	-1.66	0210200602	21753
3100.086	-251.398	-1449.351	47	5.8	-10.00	0210200609	22146
3872.043	320.889	-886.328	49	3.9	-10.00	0210200653	24789
2469.001	-516.449	-1352.577	50	21.2	-1.31	0210200721	26497
3939.106	110.133	-1091.093	51	2.0	-10.00	0210200737	27430
3981.137	211.603	-899.415	54	9.2	-1.68	0210200748	28134
3968.201	236.796	-893.105	55	2.6	-2.20	0210200753	28415
2755.424	-535.130	-1240.979	66	5.4	-10.00	0210200903	32635
2604.459	-433.936	-1361.808	67	17.7	-1.35	0210200915	33335
3085.012	2013.868	-798.523	71	3.2	-10.00	0210200951	35489
2568.186	-419.694	-1398.866	75	5.7	-10.00	0210201100	39637
3348.440	1850.120	-962.248	79	46.5	-10.00	0210201319	47971
3784.574	1429.494	-960.981	80	24.0	-1.01	0210201321	48067
3058.449	-96.907	-1498.037	82	9.1	-10.00	0210201328	48515
3704.496	28.332	-919.881	84	10.0	-10.00	0210201452	53575
2795.864	1708.687	-649.088	89	3.7	-10.00	0210201628	59333
3979.164	544.392	-907.292	90	8.0	-2.22	0210201640	60052
3980.478	573.888	-950.064	92	8.3	-10.00	0210201656	60979

continued on next page

Table C.1: *continued*

x [m]	y [m]	z [m]	EV	RMS [ms]	MAG	yymmddhhmm	TIME [s]
2232.284	-571.787	-960.521	95	29.5	-10.00	0210201752	64330
2752.719	-240.361	-1405.783	96	19.9	-10.00	0210201805	65106
3994.676	540.241	-910.999	98	10.5	-10.00	0210201813	65595
2543.095	-339.542	-1476.377	99	23.6	-10.00	0210201837	67078
2118.323	463.796	-1627.424	104	6.3	-1.33	0210202001	72093
3389.070	1324.566	-806.958	105	10.8	-10.00	0210202005	72355
3562.920	1243.291	-960.011	113	11.9	-10.00	0210202024	73472
2608.344	1678.286	-959.432	119	13.7	-10.00	0210202038	74307
3833.673	144.674	-840.066	142	4.8	-1.89	0210202123	77012
3976.767	539.291	-909.507	149	10.2	-10.00	0210202217	80228
3966.473	108.394	-919.884	150	5.9	-0.74	0210202220	80441
3968.458	-58.039	-888.871	153	8.4	-1.82	0210202232	81132
1980.548	26.095	-915.483	2	3.7	-0.55	0210210038	2308
3849.392	200.191	-949.826	3	1.9	-1.12	0210210050	3012
3363.054	1082.269	-1032.446	4	8.7	-0.34	0210210112	4371
3432.146	1117.959	-1120.081	8	8.1	-0.55	0210210144	6278
3535.613	-129.094	-1416.981	14	11.8	-0.13	0210210317	11828
3792.812	248.797	-865.950	18	1.2	-1.50	0210210427	16066
3953.948	38.122	-919.709	21	2.6	-1.20	0210210512	18741
4013.686	109.748	-931.932	41	3.3	-1.41	0210210827	30465
3895.509	69.566	-1053.528	43	3.1	-1.50	0210210831	30691
3649.814	1316.546	-841.399	44	8.6	-0.45	0210210902	32557
3500.645	1293.162	-1542.193	45	8.4	-0.70	0210210903	32613
3929.435	132.654	-922.780	46	4.4	-1.03	0210210926	34010
3911.000	123.934	-943.739	47	1.6	-1.57	0210210927	34033
3860.594	1420.034	-979.940	49	13.6	-0.64	0210210939	34751
3934.806	-111.224	-1082.907	51	3.5	-1.11	0210211026	37617
3192.852	-422.183	-967.898	53	7.1	-0.64	0210211030	37849
3803.815	146.352	-917.000	55	4.4	-1.16	0210211040	38415
3948.044	130.845	-927.897	56	7.2	-0.90	0210211041	38466
3179.339	-126.532	-1440.119	57	8.0	-1.07	0210211131	41492
3730.219	1309.701	-865.268	59	7.9	-1.20	0210211200	43207
3946.697	151.918	-932.023	63	1.7	-1.76	0210211258	46694
4008.773	222.758	-910.678	64	0.9	-1.61	0210211258	46713
3788.636	1371.985	-1119.613	65	17.0	-0.48	0210211259	46760
3682.999	1298.501	-960.002	67	8.7	-0.70	0210211315	47700
4028.428	93.726	-940.941	71	2.8	-1.03	0210211349	49755
3166.539	33.140	-1476.388	72	12.6	0.32	0210211500	54040
3910.035	131.218	-935.875	73	3.1	-1.66	0210211512	54728
3519.164	1285.655	-1359.814	75	12.3	-0.26	0210211517	55028
3654.624	1297.635	-1074.607	77	7.1	-0.95	0210211522	55365
3989.723	135.273	-915.799	84	1.7	-0.72	0210211709	61789
2547.609	268.651	-1005.969	89	4.2	-0.74	0210211839	67166
3514.237	93.216	-1114.151	91	11.0	-0.61	0210211852	67979
3917.856	107.010	-977.023	94	2.4	-1.62	0210211912	69174

continued on next page

Table C.1: *continued*

x [m]	y [m]	z [m]	EV	RMS [ms]	MAG	yymmddhhmm	TIME [s]
3916.298	127.957	-927.225	96	3.4	-1.23	0210211920	69628
3278.092	91.327	-1534.471	97	22.2	-0.52	0210211927	70042
3894.728	95.135	-940.086	99	1.4	-1.52	0210211940	70851
3929.235	121.454	-938.521	100	2.5	-1.70	0210211941	70894
3917.125	120.722	-929.208	106	3.0	-1.61	0210212116	76609
3933.629	145.385	-914.801	107	3.9	-1.10	0210212126	77196
3926.957	135.132	-910.881	109	2.6	-1.45	0210212135	77704
4035.825	262.832	-901.478	111	1.7	-1.29	0210212145	78359
2528.534	1158.666	-1120.079	112	8.6	-0.36	0210212156	78981
3135.401	41.228	-1454.221	113	7.9	0.30	0210212200	79213
3118.470	-123.245	-1383.097	114	6.6	-0.41	0210212200	79224
3092.903	-474.118	-1120.246	123	8.9	-0.62	0210212331	84715
1842.375	552.074	-1374.845	129	3.2	-0.75	0210212357	86220
1905.811	320.354	-1605.881	130	5.6	-10.00	0210212357	86246
3947.865	528.902	-928.121	2	7.7	-1.84	0210220010	620
3908.326	519.075	-962.414	4	11.0	-1.77	0210220010	620
3923.255	520.821	-962.401	5	10.4	-1.62	0210220010	620
2033.042	-114.056	-839.553	8	1.3	-10.00	0210220050	3022
2027.090	-109.571	-975.699	9	3.3	-0.75	0210220010	620
2544.925	488.794	-974.537	10	6.9	-0.60	0210220010	620
1939.986	-86.727	-709.419	11	14.3	-0.41	0210220010	620
3506.799	1209.905	-994.412	12	14.8	-10.00	0210220100	3612
2001.803	-111.719	-832.315	21	5.3	-10.00	0210220233	9235
3623.031	1306.601	-1045.907	22	11.1	-0.95	0210220010	620
3373.675	1106.346	-943.807	24	9.1	-10.00	0210220350	13831
2604.212	-560.767	-1303.943	25	1.5	-10.00	0210220501	18091
2038.514	-117.446	-823.509	27	2.9	-10.00	0210220536	20167
3638.515	1446.636	-960.036	28	8.0	-10.00	0210220540	20437
1963.113	-253.551	-960.163	33	10.4	-1.09	0210220010	620
3724.150	1288.798	-944.254	36	6.9	-10.00	0210220746	27984
3339.470	206.128	-1351.628	37	15.2	-0.80	0210220010	619
3199.095	237.105	-1263.564	38	3.9	-1.56	0210220010	619
2123.283	-584.218	-570.887	39	39.5	-10.00	0210220829	30593
3279.549	152.609	-1359.966	42	11.5	-0.59	0210220010	619
3260.294	87.080	-1348.876	43	16.4	-1.11	0210220010	619
3328.632	142.382	-1541.545	44	5.8	-10.00	0210220902	32567
3325.182	175.730	-1478.966	45	6.8	-10.00	0210220904	32643
3320.632	204.764	-1396.387	46	6.9	-10.00	0210220911	33078
3393.294	172.009	-1386.637	52	20.0	-1.13	0210220010	619
3369.140	235.478	-1395.046	53	13.7	-1.05	0210220010	619
3793.386	197.291	-892.646	54	6.0	-1.93	0210220010	620
3926.949	-99.235	-720.168	55	9.4	-0.56	0210220010	620
5251.154	1842.703	-880.289	57	17.8	-0.34	0210220010	620
3718.066	1336.730	-960.306	70	16.7	-10.00	0210221650	60625
3632.630	1364.148	-960.086	71	16.8	-10.00	0210221725	62748

continued on next page

Table C.1: *continued*

x [m]	y [m]	z [m]	EV	RMS [ms]	MAG	yymmddhhmm	TIME [s]
3952.760	328.191	-901.482	74	9.0	-2.07	0210220010	620
3293.167	-81.762	-1220.748	75	13.5	-10.00	0210221757	64644
8258.333	3106.443	-3367.534	80	12.6	-10.00	0210221918	69507
3977.561	581.029	-969.347	81	8.1	-1.86	0210220010	620
2778.478	-590.456	-993.479	84	8.1	-1.18	0210220010	619
5210.647	1081.634	-860.007	86	7.8	-1.16	0210220010	619
6032.504	1939.681	-1296.862	87	17.9	-0.78	0210220010	619
3929.307	1544.348	-904.701	90	7.1	-1.30	0210220010	619
3791.804	1575.059	-698.692	1	23.0	-0.73	0210230052	3168
3913.998	79.176	-981.058	4	1.7	-1.29	0210230106	3994
5589.786	2301.143	-835.381	5	25.7	-0.24	0210230109	4145
3898.242	55.715	-985.239	6	2.7	-1.52	0210230114	4446
3948.207	366.661	-920.081	7	5.7	-1.05	0210230115	4500
3807.074	164.066	-942.928	8	3.6	-1.54	0210230116	4593
3956.752	139.613	-930.631	13	0.7	-1.60	0210230142	6163
4039.789	361.651	-904.075	16	5.4	-0.48	0210230236	9414
3962.118	377.503	-908.467	18	4.7	-0.42	0210230240	9622
3894.038	28.527	-999.954	20	3.3	-1.64	0210230333	12803
3035.872	-82.973	-845.754	21	19.9	-0.74	0210230406	14784
3737.198	1357.694	-991.424	23	16.2	-0.71	0210230443	17017
3790.615	142.319	-917.480	54	1.6	-1.52	0210230507	18435
3793.801	111.281	-919.869	62	2.0	-1.06	0210230508	18500
3937.907	375.989	-912.738	66	5.2	-0.30	0210230512	18726
3768.752	-118.200	-1101.145	67	3.5	-0.83	0210230523	19386
2114.355	462.111	-1676.244	69	1.2	-10.00	0210230636	23790
3846.421	-33.541	-1030.847	70	1.8	-1.43	0210230658	25113
3278.591	949.104	-1119.194	77	11.0	-10.00	0210230749	28190
4053.300	437.101	-926.145	78	4.1	-0.84	0210230802	28935
3956.520	354.875	-920.000	81	5.4	-1.30	0210230913	33231
3062.718	-14.282	-1473.608	83	8.8	-10.00	0210231008	36539
5357.574	2978.063	-859.860	87	23.4	0.40	0210231052	39169
3093.291	1294.390	-1123.572	91	28.5	-0.53	0210231223	44615
3985.393	429.442	-886.367	96	6.0	-0.57	0210231351	49880
3942.298	147.370	-939.604	102	2.1	-1.96	0210231704	61490
3345.422	14.045	-1159.934	104	22.1	-0.67	0210231721	62517
3810.087	216.247	-919.998	111	1.0	-1.42	0210231804	65067
3751.340	162.118	-913.994	115	1.4	-1.15	0210231855	68141
1970.114	579.713	-1592.287	119	0.7	-10.00	0210232008	72513
3668.505	1536.255	-959.994	122	24.3	-0.42	0210232103	75811
300.655	-367.115	-840.787	123	65.3	-10.00	0210232114	76455
3792.359	-70.132	-971.665	124	1.9	-1.16	0210232134	77684
3553.538	1208.950	-1051.573	125	12.0	-0.81	0210232135	77735
3813.880	163.410	-943.026	128	0.7	-1.60	0210232215	80123
3622.990	1445.272	-960.031	129	27.2	-1.07	0210232219	80346
2569.173	-651.482	-1107.347	130	24.1	0.34	0210232225	80745

continued on next page

Table C.1: *continued*

x [m]	y [m]	z [m]	EV	RMS [ms]	MAG	yymmddhhmm	TIME [s]
2451.506	-521.653	-1366.776	131	19.3	-0.45	0210232227	80871
3840.222	155.674	-920.318	132	3.4	-1.43	0210232249	82189
3691.600	146.544	-1105.824	136	12.4	-0.28	0210232358	86337
3713.652	776.651	-954.064	5	13.8	-0.82	0210240145	6304
4184.781	984.935	-998.744	6	25.6	-10.00	0210240145	6314
4078.530	706.308	-997.932	11	20.2	-0.59	0210240302	10924
6234.321	2734.035	-2565.717	12	44.6	0.09	0210240356	14198
2611.236	-606.383	-1016.998	18	17.2	-0.70	0210240506	18372
3161.486	903.810	-1614.041	22	8.0	0.04	0210240524	19488
3952.361	378.090	-909.685	29	3.9	-0.75	0210240654	24899
3476.543	1062.428	-960.067	31	15.2	-10.00	0210240739	27556
4095.767	697.747	-657.748	32	12.6	-10.00	0210240753	28411
5241.219	1084.162	-893.403	35	4.9	-0.78	0210240904	32678
2779.966	1286.655	-1479.977	39	4.6	-10.00	0210241031	37877
4413.233	2261.328	-1120.489	40	38.6	-0.43	0210241150	42600
1977.823	494.875	-1664.369	42	1.6	-10.00	0210241310	47412
3311.841	-239.306	-1121.281	46	51.7	-10.00	0210241556	57364
5959.493	2361.815	-1423.494	49	9.8	-10.00	0210241618	58689
2351.911	338.978	-918.983	50	1.3	-10.00	0210241644	60248
4865.696	1517.725	-813.435	51	19.0	0.16	0210241708	61708
2666.297	-677.418	-961.615	52	30.5	-10.00	0210241718	62316
4518.124	283.823	-960.001	53	18.0	-0.72	0210241745	63958
4891.100	1422.253	-670.531	57	20.8	-0.75	0210241904	68684
3422.000	1152.496	-119.983	58	11.7	0.22	0210241907	68861
4895.931	1344.988	-670.708	59	17.9	-0.39	0210241912	69136
3297.808	137.452	-1443.076	61	6.5	0.26	0210242025	73505
4301.187	844.285	-699.737	65	6.8	-0.22	0210242056	75411
6458.857	2619.098	-1352.757	67	20.8	-10.00	0210242108	76096
5812.930	1735.292	-956.524	69	12.9	-0.65	0210242155	78901
3625.396	1423.331	-960.493	71	12.6	-0.31	0210242245	81927
3890.925	1588.826	-959.574	72	8.3	0.70	0210242251	82309
4816.568	1426.301	-906.513	75	4.2	0.24	0210242330	84622
5571.730	1391.078	-884.765	76	7.1	-10.00	0210242333	84812
3181.649	46.631	-1514.105	1	10.5	-0.96	0210250022	1364
8164.341	3260.456	-997.181	7	20.6	0.17	0210250046	2787
2783.587	612.650	-1570.437	12	12.8	-10.00	0210250139	5979
4197.795	1023.738	-1062.157	17	15.2	-0.90	0210250231	9095
2109.421	-649.416	-1360.328	18	31.9	-0.22	0210250303	11020
2238.377	1255.049	-104.764	20	6.8	-10.00	0210250338	13119
3614.519	1282.916	-500.784	22	4.3	-0.64	0210250345	13508
4090.317	1433.185	-1387.250	27	11.5	-0.06	0210250527	19635
3567.670	161.529	-770.305	32	3.0	-10.00	0210250701	25287
3373.857	1037.931	-1616.965	41	15.3	-0.09	0210251046	38814
3942.873	139.801	-935.073	43	0.2	-1.90	0210251052	39142
2887.795	1438.572	-504.514	46	32.9	-1.05	0210251058	39531

continued on next page

Table C.1: *continued*

x [m]	y [m]	z [m]	EV	RMS [ms]	MAG	yymmddhhmm	TIME [s]
7508.294	1941.729	-1882.727	49	18.0	-0.19	0210251127	41223
2279.528	317.984	-1220.937	50	2.3	-0.77	0210251135	41753
3341.859	118.270	-1379.106	51	15.8	-0.89	0210251155	42953
3994.706	1992.956	-1025.068	53	20.5	-0.66	0210251244	45892
7984.052	3488.740	-3669.591	56	17.0	-10.00	0210251329	48586
3929.794	114.566	-946.083	58	0.5	-1.65	0210251343	49402
3858.885	237.891	-919.995	61	3.1	-1.39	0210251401	50475
3786.562	1523.131	-939.029	64	9.2	-0.75	0210251406	50764
3961.444	147.497	-925.022	65	0.5	-1.44	0210251406	50786
2804.550	-386.944	-870.626	66	6.4	-0.45	0210251412	51152
4191.131	224.437	-879.244	69	10.9	0.53	0210251458	53905
3718.770	145.854	-1116.387	72	8.1	-0.71	0210251518	55114
3825.987	262.418	-959.828	75	3.1	-1.54	0210251541	56465
3397.225	76.480	-1362.526	76	24.8	-0.66	0210251543	56599
2646.842	904.944	-546.621	84	9.9	-0.99	0210251706	61602
4120.487	759.686	-959.767	86	17.8	-0.76	0210251720	62427
2640.650	-559.663	-1298.220	87	11.1	-0.53	0210251731	63119
3404.196	1053.354	-3215.771	88	19.0	-0.23	0210251736	63373
2545.155	-319.505	-1382.804	95	18.2	-0.71	0210252002	72125
3764.401	145.353	-920.033	96	2.5	-1.34	0210252006	72375
3801.102	820.139	-848.357	97	8.3	-0.98	0210252011	72700
3129.692	-516.150	-1120.010	98	10.0	-0.46	0210252018	73126
4099.432	749.259	-921.352	101	8.0	-0.74	0210252038	74319
3799.635	769.776	-896.855	105	6.4	-0.70	0210252053	75189
3078.040	782.555	-1120.260	108	14.7	-0.84	0210252100	75653
3661.397	311.645	-1183.807	112	20.1	-0.90	0210252206	79594
3722.153	1563.350	-960.631	113	52.8	-0.02	0210252220	80420
3739.226	310.183	-1118.466	114	15.3	-0.95	0210252221	80509
3865.033	-14.724	-1002.700	115	4.9	-1.42	0210252226	80815
3224.385	2.445	-1361.448	116	20.9	-0.38	0210252235	81332
3678.830	-361.834	-510.972	117	0.6	-10.00	0210252239	81553
3742.563	-524.018	-1120.057	120	9.6	-0.83	0210252311	83515
3517.757	110.415	-1120.053	125	10.2	-0.80	0210252343	85403
3955.801	1554.437	-1120.001	5	6.8	-10.00	0210260226	8788
3133.826	9.609	-1435.360	19	7.1	-0.15	0210260807	29237
3137.859	-148.831	-1340.912	20	10.7	0.13	0210260814	29697
3090.998	-123.082	-1057.271	21	10.0	-10.00	0210260901	32506
4119.078	441.124	-887.852	26	18.8	-10.00	0210260943	34993
4104.433	765.654	-932.181	36	19.9	-0.66	0210261054	39269
3684.111	211.082	-1059.045	44	3.6	-10.00	0210261150	42628
3765.558	776.651	-1102.889	45	21.1	-10.00	0210261207	43646
4076.988	737.796	-923.945	46	3.2	-1.41	0210261216	44193
4096.590	686.423	-861.829	48	1.1	-10.00	0210261223	44606
4107.725	736.172	-904.724	49	4.2	-1.42	0210261242	45779
3881.965	808.879	-992.680	51	3.8	-10.00	0210261250	46217

continued on next page

Table C.1: *continued*

x [m]	y [m]	z [m]	EV	RMS [ms]	MAG	yymmddhhmm	TIME [s]
3512.049	199.324	-1256.147	55	7.4	-10.00	0210261339	49183
3763.811	290.275	-758.474	59	5.8	-10.00	0210261409	50950
3769.695	123.334	-941.668	61	8.3	-10.00	0210261438	52725
4740.335	1370.624	-877.932	63	7.8	-10.00	0210261540	56440
3072.471	-124.086	-1296.931	64	9.6	-0.15	0210261618	58707
3058.022	-148.052	-1051.295	65	7.7	-0.08	0210261619	58761
3081.775	-74.218	-1390.666	66	10.7	-0.10	0210261624	59050
3096.029	-160.664	-1343.505	67	12.5	0.32	0210261624	59089
3074.873	-173.845	-1317.723	68	14.7	0.42	0210261624	59097
3827.178	804.490	-928.048	69	4.1	-1.19	0210261626	59191
4739.684	1481.195	-862.646	72	3.6	-10.00	0210261636	59807
3068.597	-53.072	-1449.889	73	6.5	-10.00	0210261639	59974
4734.486	1476.228	-869.313	74	5.9	-10.00	0210261640	60002
4741.940	1313.537	-844.708	75	7.6	-10.00	0210261643	60237
4761.416	1498.491	-870.022	76	1.6	-10.00	0210261645	60358
3070.216	-53.049	-1029.888	77	3.8	-10.00	0210261652	60744
4697.280	1388.757	-883.280	78	4.8	-0.81	0210261653	60790
4062.643	730.181	-926.398	80	3.4	-1.40	0210261744	63891
4810.196	1432.788	-854.056	82	6.7	-10.00	0210261814	65648
4360.532	2041.069	-950.921	83	7.4	-10.00	0210261836	67014
4806.524	1322.188	-914.793	84	21.2	-10.00	0210261852	67950
4310.315	935.275	-980.939	86	26.5	-0.76	0210261911	69115
3861.748	134.985	-983.549	90	4.0	-10.00	0210261931	70279
3926.578	150.275	-931.511	91	3.1	-1.12	0210261944	71063
4696.075	1389.400	-883.404	92	5.0	-10.00	0210262047	74876
2234.946	26.240	-1196.294	93	3.8	0.51	0210262115	76504
5322.535	1159.228	-898.645	94	5.8	-10.00	0210262143	78188
4403.652	644.535	-1122.758	95	24.6	-10.00	0210262211	79861
5047.105	1848.829	-853.943	97	5.3	-10.00	0210262253	82403
3980.002	73.704	-947.031	98	5.7	-10.00	0210262307	83244
3956.577	388.483	-931.062	100	6.9	-0.55	0210262335	84952
3853.127	810.137	-908.407	102	1.9	-10.00	0210262350	85829
4788.002	1501.196	-881.321	103	7.2	-10.00	0210270002	157

Table C.2: Easting (x), northing (y), depth (z), event number (EVENT), root mean square of time error (RMS), magnitude (MAG) and origin time (YEAR, MONTH, DAY, TIME (seconds from midnight 00:00:00) and YYMMDDHHMM) of high-magnitude Shuaiba 26 events (selected from the 30/Aug-1/Sep2002 and 21-24/Sep2002 periods). A -10.00 magnitude is a null result (i.e., XMETAL failed to estimate the event magnitude).

x [m]	y [m]	z [m]	EV	RMS [ms]	MAG	yymmddhhmm	TIME [s]
3164.621	-251.544	-1319.914	67	22.2	-0.12	0208302350	85807
3072.292	-311.315	-1327.882	81	14.2	0.38	0208310329	12543
3099.708	-74.151	-1371.805	86	8.5	-0.22	0208310332	12724
3109.639	-16.170	-1397.333	88	7.9	-0.33	0208310333	12834
3080.197	-37.389	-1432.884	91	6.7	-0.73	0208310419	15577
3493.951	10.774	-1411.494	93	12.6	-0.28	0208310441	16881
3065.045	-91.332	-1504.202	94	8.6	-0.70	0208310459	17985
3105.422	-442.686	-1350.456	142	16.0	0.23	0208311916	69414
3050.431	-355.283	-1380.129	147	14.0	-0.09	0208312002	72133
3240.705	83.075	-1346.332	184	9.6	-0.29	0209011749	64171
3244.009	55.295	-1432.885	186	12.7	0.33	0209011814	65664
3272.700	114.853	-1348.307	191	8.2	-0.55	0209011814	65676
3291.801	161.005	-1467.489	193	10.9	-0.70	0209011814	65690
3375.450	254.009	-1424.624	437	13.0	-0.95	0209211128	41297
3377.347	16.326	-1358.729	438	20.5	-0.51	0209211144	42251
3359.996	95.236	-1312.827	439	18.9	-0.58	0209211150	42629
3402.566	91.925	-1332.543	440	17.0	-0.51	0209211150	42640
3108.123	-59.923	-1453.612	4	8.5	-0.62	0209211620	58819
3268.724	114.003	-1452.030	23	6.1	-0.40	0209212258	82691
3215.085	-69.019	-1317.127	36	15.3	-0.33	0209220537	20233
3300.708	-367.161	-1470.570	249	8.2	-0.74	0209221455	53725
3329.487	164.183	-1521.923	279	3.9	-1.05	0209222040	74402
3068.009	-122.233	-1496.889	340	6.4	-0.93	0209231643	60230
3394.271	-262.197	-1449.873	352	8.7	-0.42	0209232033	73992
2502.488	-334.174	-1411.700	387	18.0	-0.35	0209240647	24477
3091.472	-382.886	-1404.329	389	16.5	-0.73	0209240702	25326

Appendix D

Rotations based on P- and S-wave polarisations

This Appendix describes the methods used to estimate the ray orientation angles from the P- and S-wave particle motions. First, the P-wave method is described, and its advantages over other methods are outlined through real data examples. Finally, the S-wave method is described.

D.1 Rotation based on P-wave polarisation

Rotation angles were initially estimated by least absolute (L1 norm) vertical residuals. This is based on fitting a straight line through data points that brings the sum of absolute vertical residuals between the fitted line and data points to minimum. Figure D.1a shows the application of the L1 norm of vertical residuals on real data for near eastward propagation. It shows that the method is successful in recovering the ray azimuth for near eastward propagation. This is also true for recovering the ray inclination for subhorizontal wave propagation. However, the L1 norm of vertical residuals assumes no error in the horizontal component. Therefore, the resulting rotation angles of northward or vertically propagating waves (contaminated by low-background noise in the x-component) can be far from the true angle. Figure D.2b illustrates with real data how the L1 norm of vertical deviations can fail to best fit a straight line through particle motion. Similar undesired fitting results using least squared (L2) vertical residuals (Figure D.2a). Thus L1 or L2 vertical residuals should not be used for vertical or north-south propagation.

To solve the problem, I estimate the rotation angles based on least absolute (L1 norm) perpendicular residuals, rather than vertical or horizontal residuals. Figure D.3 presents a graphical illustration of the difference between perpendicular and vertical residuals.

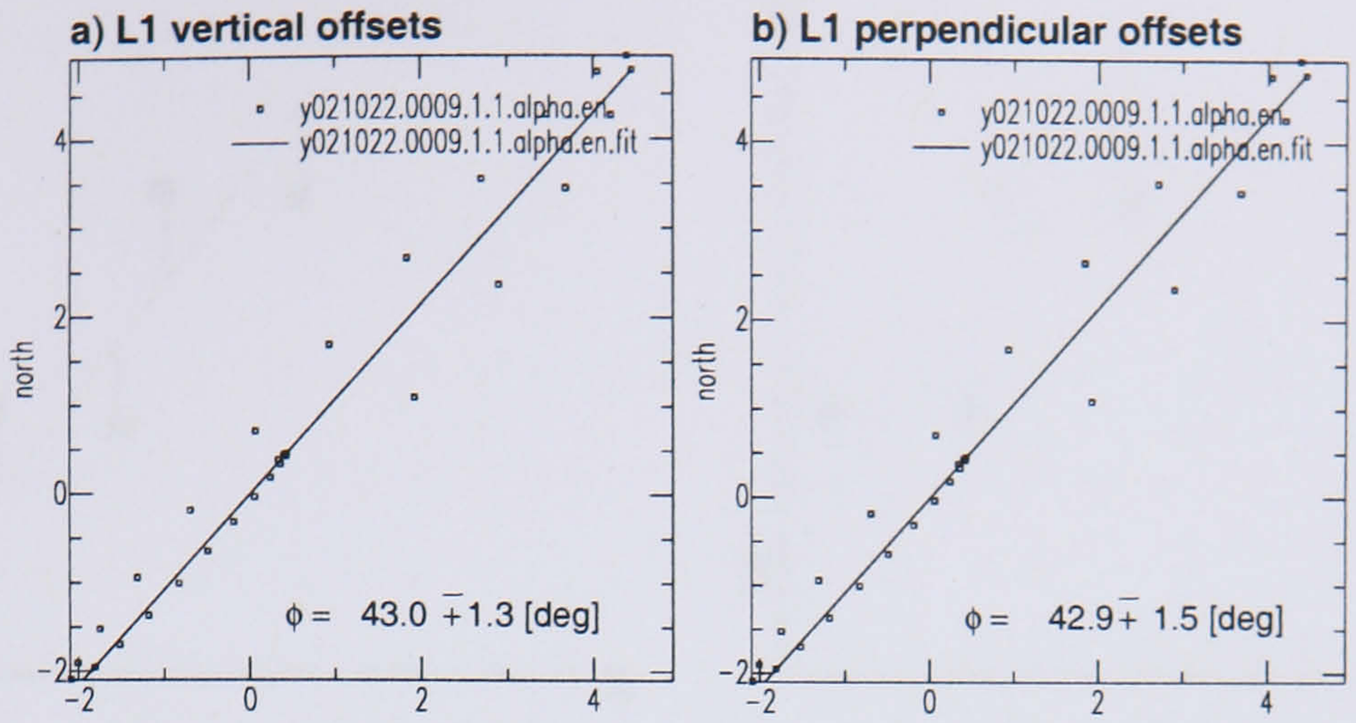

Figure D.1 Comparison of L1 fitting methods to obtain the particle motion in the case of sub-eastward wave propagation. P-wave particle motion is in the E-N plane and the best-fit straight line is found using [**a**] least absolute vertical residuals and [**b**] least absolute perpendicular residuals. Note both methods recover similar particle motion directions. The data are for event yb021022.0009.1.1 with low pass filter of 100Hz.

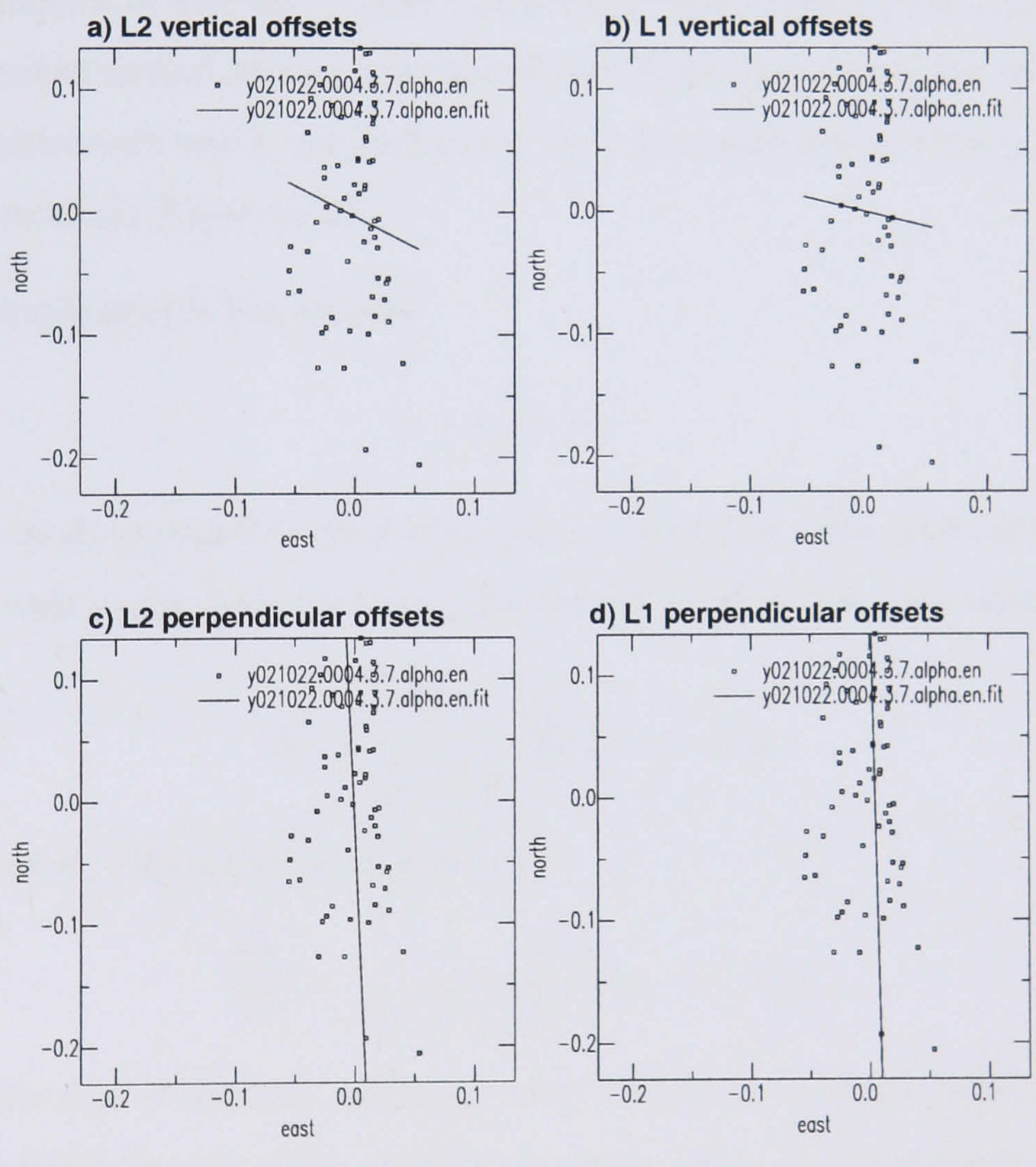

Figure D.2 Comparison of L1 and L2 fitting methods: perpendicular and vertical residuals for estimating the ray direction for northward P-wave propagation. P-wave particle motion is in the E-N plane and the best-fit straight line are calculated using [**a**] least squared vertical residuals, [**b**] least absolute vertical residuals, [**c**] least squared perpendicular residuals and [**d**] least absolute perpendicular residuals. Note the failure of the L1 and L2 vertical residual methods in recovering the true particle motion for near-vertical slopes due to noise in the east and north components. The data are for event yb021022.0004.3.7 with low pass filter of 400Hz.

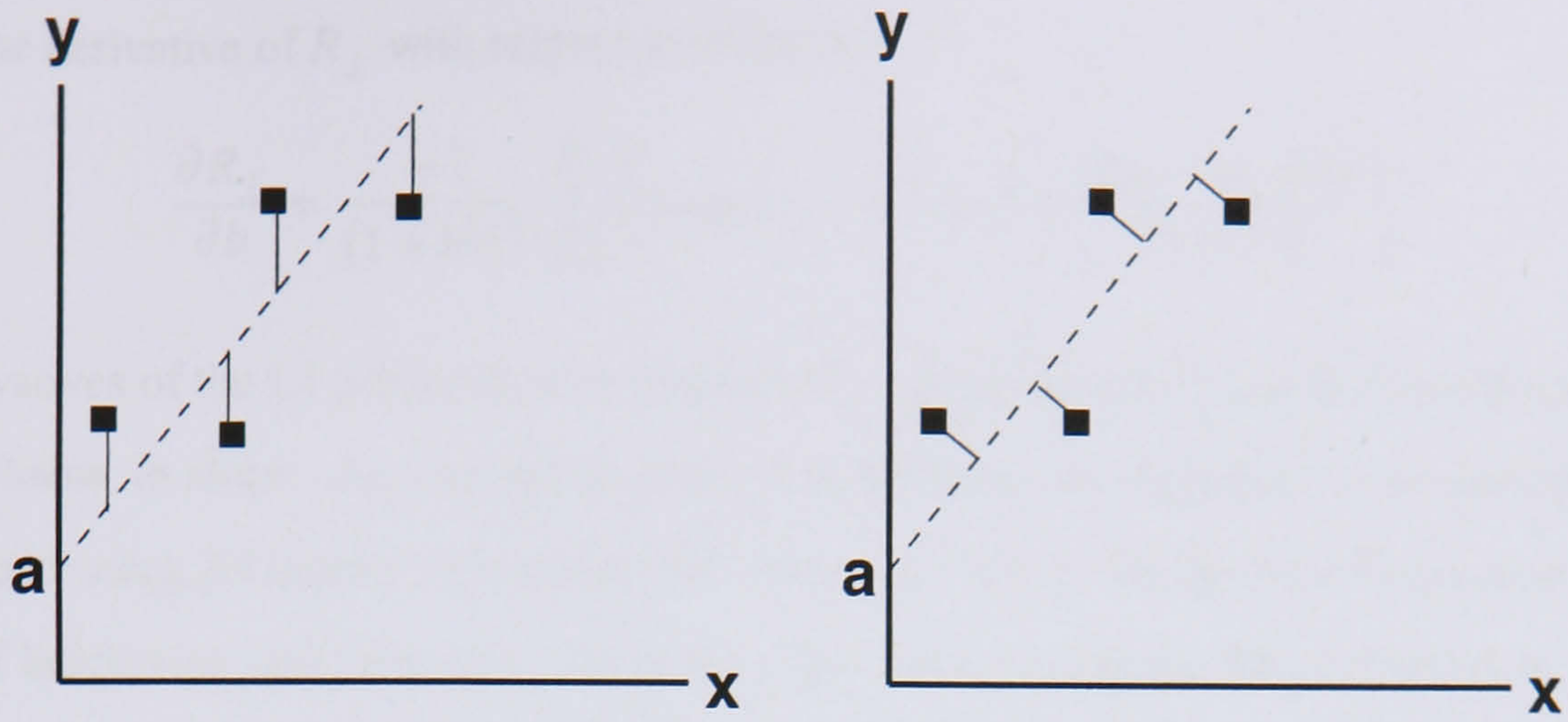

(a) Vertical residuals **(b) Perpendicular residuals**

Figure D.3 A simplified diagram of [**a**] vertical versus [**b**] perpendicular deviations minimised for best fit line through the data points.

Under the assumption of accurate x values (noise-free x measurements), fitting a straight line by minimising absolute vertical deviations is valid (Figure D.3a). In reality, both x and y coordinates are often associated with errors. For such cases, we seek a solution that minimises the absolute perpendicular residuals (Figure D.3b).

Consider the simple straight line equation

$$y = a + bx, \tag{D.1}$$

where a and b are the intersection point at the y-axis and the line slope, respectively. Therefore, for a set of N x and y measurements (x_i, y_i), the absolute residual (L1) error function $(R_\perp)$ to be minimised is

$$R_\perp = \frac{1}{(1+b^2)^{\frac{1}{2}}} \sum_{i=1}^{N} |y_i - a - bx_i|. \tag{D.2}$$

The derivative of $R_\perp$ with respect to intercept a is

$$\frac{\partial R_\perp}{\partial a} = \frac{-1}{(1+b^2)^{\frac{1}{2}}} \sum_{i=1}^{N} sgn(y_i - a - bx_i), \tag{D.3}$$

where sgn is the sign of the term between bracket. The fact that the median c_M of a set of numbers c_i minimises the sum of the absolute deviations $\sum_i |c_i - c_M|$ significantly simplifies our problem (Press et al., 1989). Hence, for fixed b the value of a that minimizes $R_\perp$ is

$$a = \text{median}\{y_i - bx_i\}. \tag{D.4}$$

While, the derivative of $R_\perp$ with respect to slope b is

$$\frac{\partial R_\perp}{\partial b} = \frac{-1}{(1+b^2)^{\frac{1}{2}}} \sum_{i=1}^{N} \left(x_i sgn(y_i - a - bx_i) + \frac{b|y_i - a - bx_i|}{(1+b^2)} \right). \tag{D.5}$$

The derivatives of the L1 perpendicular residual, $R_\perp$, (Equations D.3 and D.5) are discontinuous and non linear in slope. An analytical solution is therefore not feasible. A numerical solution is estimated using *fitl1perp.f* subroutine that iteratively solves for the best fit rotation angle by means of bracketing and bisection. Since the slope tends to infinity for northward or vertically aligned points, the trick lies in the bracketing and bisection of the rotation angle, rather than finding the slope by root-finding. For quick convergence the subroutine *fitl1perp.f* uses the least squared (L2) perpendicular residual solution[1] as a first guess for the polarisation angle.

The application of calculating the L1 norm of the perpendicular residual on real data with a northward propagation direction (Figure D.2d) shows a successful fit (compare with the failed fitting of the L1 norm of vertical residuals in Figure D.2b). A similar desired result is shown using L2 perpendicular residuals (Figure D.2c). The successful application of L1 norm of perpendicular residuals for near eastward propagation (Figure D.1b) shows that the method can also be applied for east-west or subhorizontal propagation directions. Unlike methods of least vertical residuals, no directional limitations are related to methods of least perpendicular residuals. Therefore, I use the method of L1 perpendicular deviations to estimate the rotation angles in this thesis. I use L1 norm method over L2 method of perpendicular deviation because non robust schemes such as L2 can have undesired sensitivity to outliers such as noise.

D.2 Rotation based on S-wave polarisation

The S-wave ray orientation is determined by means of S-wave particle motion. Similar to P-wave particle motion analysis, an S-wave window is picked and the covariance matrix (of size 3×3) is given by:

$$\mathbf{C}_{cov} = \mathbf{D}^{\mathbf{T}}\mathbf{D} = \begin{pmatrix} \mathbf{xx} & \mathbf{xy} & \mathbf{xz} \\ \mathbf{yx} & \mathbf{yy} & \mathbf{yz} \\ \mathbf{zx} & \mathbf{zy} & \mathbf{zz} \end{pmatrix}, \qquad \mathbf{D} = \begin{pmatrix} x_1 & y_1 & z_1 \\ x_2 & y_2 & z_2 \\ \vdots & \vdots & \vdots \\ x_{n-1} & y_{n-1} & z_{n-1} \\ x_n & y_n & z_n \end{pmatrix}, \tag{D.6}$$

where the multi-component data x, y and z form column vectors in the data matrix **D**. The covariance matrix is symmetric and therefore has real positive eigenvalues $\lambda_{1,2,3}$ (λ_1: largest,

[1] The L2 perpendicular residual solution is analytical and reviewed by York (1966) and Williamson (1968).

λ_2: intermediate, λ_3: smallest). S-wave ellipticity in the polarisation plane λ_2/λ_1 and out of the plane λ_3/λ_2 can also be calculated. If the S-wave motion is elliptic enough and confined within the S-wave polarisation plane, the eigenvector associated with the smallest eigenvalue λ_3 points towards the S-ray direction. Next, rotation angles in the horizontal and vertical planes are estimated. The *srotate* program determines the S-wave polarisation and then rotates to the S-wave ray frame. Application of the S-wave rotation method on synthetic data for a medium with little anisotropy (0.5 ms time lag and 0.06% anisotropy) showed a successfully retrieved ray orientation.

Appendix E

The VRH scheme

In this section I show how the isotropic elastic properties of a polycrystalline medium can be obtained from the single crystal elastic properties. The two classical methods of Voigt (1928) and Reuss (1929) are upper and lower limits for such averages. The commonly used method of Hill (1952) approximately accounts for this by averaging the two methods from single-crystal data. Below is a description of how the bulk modulus (k) and shear modulus (μ) for each method are evaluated. The aggregate P- and S-wave velocities, v_p and v_s, respectively, are then defined as a function of k, μ and density (ρ):

$$v_p = \sqrt{(k + \frac{4}{3}\mu)/\rho}, \tag{E.1}$$

$$v_s = \sqrt{\mu/\rho}. \tag{E.2}$$

E.1 Voigt method

Voigt's approximation of constant strain in a polycrystalline medium yields bulk modulus, k_V, and shear modulus, μ_V, as an arithmetic mean of the single crystal elastic constants, c_{ij}, as follow:

$$k_V = \frac{1}{9}[(c_{11} + c_{22} + c_{33}) + 2(c_{12} + c_{23} + c_{31})], \tag{E.3}$$

$$\mu_V = \frac{1}{15}[(c_{11} + c_{22} + c_{33}) - (c_{12} + c_{23} + c_{31}) + 3(c_{44} + c_{55} + c_{66})]. \tag{E.4}$$

If one has more than one crystal orientation or many crystal types the elastic stiffness matrices (c_{ij}) are simply averaged before constructing the isotropic parameters.

E.2 Reuss method

Reuss's approximation of constant stress in a polycrystalline medium yields bulk modulus, k_R, and shear modulus, μ_R, as a function of compliance constants, s_{ij}. That is,

$$\frac{1}{k_R} = \frac{1}{1}[(s_{11}+s_{22}+s_{33})+2(s_{12}+s_{23}+s_{31})], \tag{E.5}$$

$$\frac{1}{\mu_R} = \frac{1}{15}[4(s_{11}+s_{22}+s_{33})-4(s_{12}+s_{23}+s_{31})+3(s_{44}+s_{55}+s_{66})]. \tag{E.6}$$

E.3 Hill method

The expressions for Hill's average bulk modulus (k_H) and shear modulus (μ_H) are

$$k_H = (k_V+k_R)/2, \tag{E.7}$$

$$\mu_H = (\mu_V+\mu_R)/2. \tag{E.8}$$

Appendix F

VTI elastic constants from XRTG measurements

Elastic constants for the muscovite and chlorite crystal preferred orientations measured from X-ray texture goniometry, XRTG, on shale chippings from the Valhall borehole by M. Casey. Units are 10 GPa (after Casey, 2004).

chlorite 002 for specimen CH

1.2107	0.4874	0.4829	0.0000	0.0000	0.0000
0.4874	1.2106	0.4829	0.0000	0.0000	0.0000
0.4829	0.4829	0.9982	0.0000	0.0000	0.0000
0.0000	0.0000	0.0000	0.2971	0.0000	0.0000
0.0000	0.0000	0.0000	0.0000	0.2971	0.0000
0.0000	0.0000	0.0000	0.0000	0.0000	0.3616

muscovite 001 for specimen CH

1.1569	0.3543	0.3432	0.0000	0.0000	0.0000
0.3543	1.1569	0.3432	0.0000	0.0000	0.0000
0.3432	0.3432	0.8735	0.0000	0.0000	0.0000
0.0000	0.0000	0.0000	0.3302	0.0000	0.0000
0.0000	0.0000	0.0000	0.0000	0.3302	0.0000
0.0000	0.0000	0.0000	0.0000	0.0000	0.4013

chlorite 002 for specimen OCT

1.2049	0.4874	0.4843	0.0000	0.0000	0.0000
0.4874	1.2049	0.4844	0.0000	0.0000	0.0000
0.4843	0.4844	1.0034	0.0000	0.0000	0.0000
0.0000	0.0000	0.0000	0.2995	0.0000	0.0000
0.0000	0.0000	0.0000	0.0000	0.2995	0.0000
0.0000	0.0000	0.0000	0.0000	0.0000	0.3588

muscovite 001 for specimen OCT

1.1713	0.3555	0.3424	0.0000	0.0000	0.0000
0.3555	1.1713	0.3424	0.0000	0.0000	0.0000
0.3424	0.3424	0.8535	0.0000	0.0000	0.0000
0.0000	0.0000	0.0000	0.3266	0.0000	0.0000
0.0000	0.0000	0.0000	0.0000	0.3266	0.0000
0.0000	0.0000	0.0000	0.0000	0.0000	0.4079

Elastic constants of the mica crystal (10% anisotropy) calculated by averaging the 4 sets of elastic constants in the left.

1.1860	0.4211	0.4132	0.0000	0.0000	0.0000
0.4211	1.1859	0.4132	0.0000	0.0000	0.0000
0.4132	0.4132	0.9321	0.0000	0.0000	0.0000
0.0000	0.0000	0.0000	0.3133	0.0000	0.0000
0.0000	0.0000	0.0000	0.0000	0.3133	0.0000
0.0000	0.0000	0.0000	0.0000	0.0000	0.3824

Elastic constants of the used VTI shale medium (3% anisotropy) by diluting the above by 70% as described in Section 4.2.2.

1.1169	0.4175	0.4144	0.0000	0.0000	0.0000
0.4175	1.1169	0.4144	0.0000	0.0000	0.0000
0.4144	0.4144	1.0388	0.0000	0.0000	0.0000
0.0000	0.0000	0.0000	0.3295	0.0000	0.0000
0.0000	0.0000	0.0000	0.0000	0.3295	0.0000
0.0000	0.0000	0.0000	0.0000	0.0000	0.3497

Appendix G

Interesting features encountered during S-wave splitting analysis

In this section, I report some of the interesting features that were encountered whilst performing the splitting analysis on the real data. Some of these were important in the guidance of accurate splitting correction of similar later examples. Figure G.1 shows a successful splitting correction obtained by excluding an S-P conversion from the S-wave analysis window. Including this S-P conversion into the analysis window makes the splitting unsuccessful. This was used to guide the splitting analysis on similar examples for successful splitting and accurate measurements.

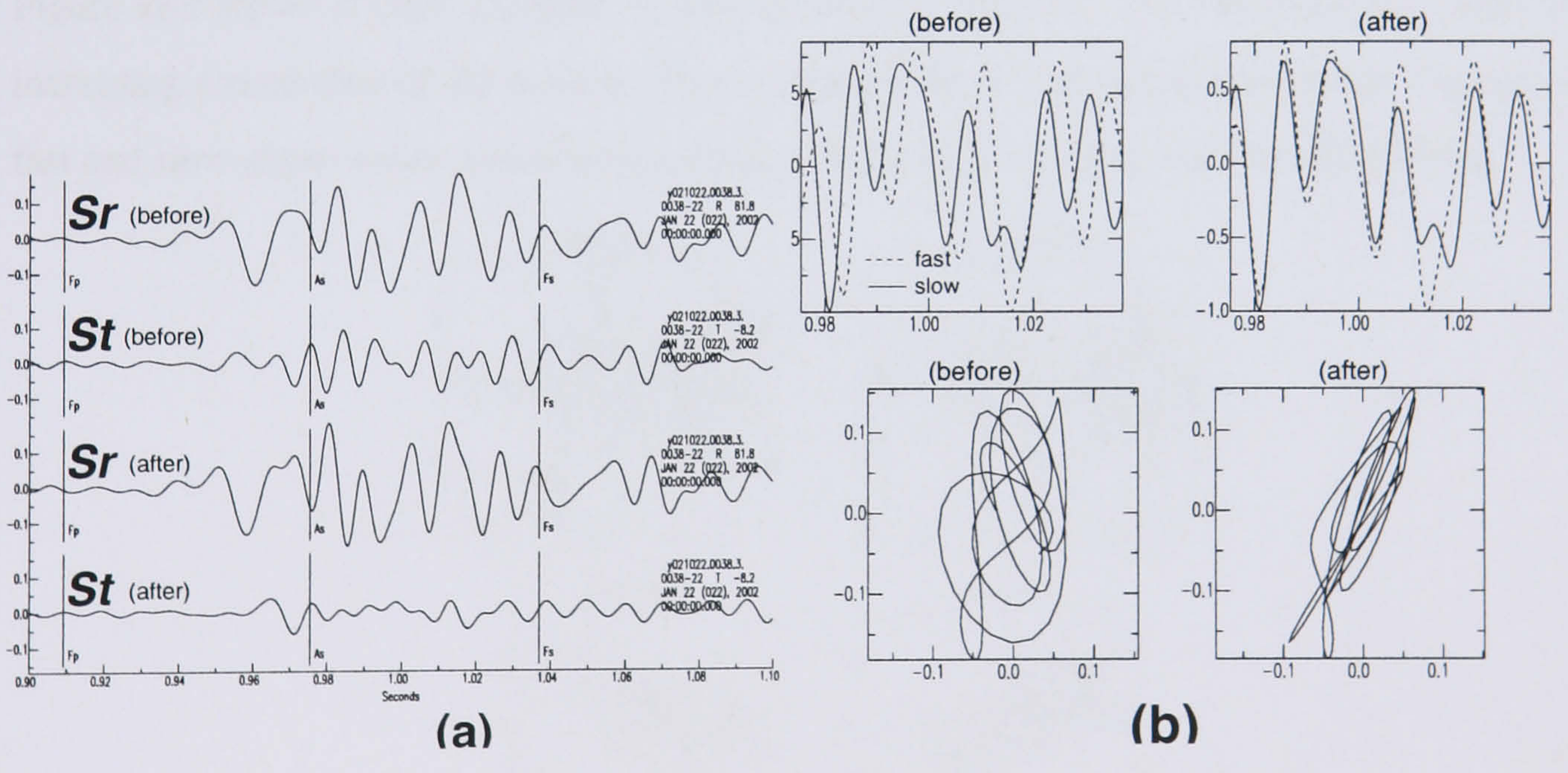

Figure G.1 The effect of P-wave contamination (most likely S-P conversions) on splitting analysis of a real data example of class A: event yb021022.0038 recorded on station 3.7. [**a**] *Sr*, *St* before and after splitting correction. [**b**] [**top panel**] Fast and slow shear waves before and after correction and [**bottom panel**] S-wave particle motion before and after correction. Note the shifted S-wave window to skip the S-P contaminant wave for accurate measurements. Also note the S-P contaminant wave being unminimised in the S_t component after correction.

Figure G.2 displays an unusual example of well defined perpendicular fast and slow shear waves. Before the splitting correction is applied, the S-wave particle motion shows clearly the orthogonality of fast and slow shear-waves. The anisotropy must be strong to completely separate the fast and slow shear-wave.

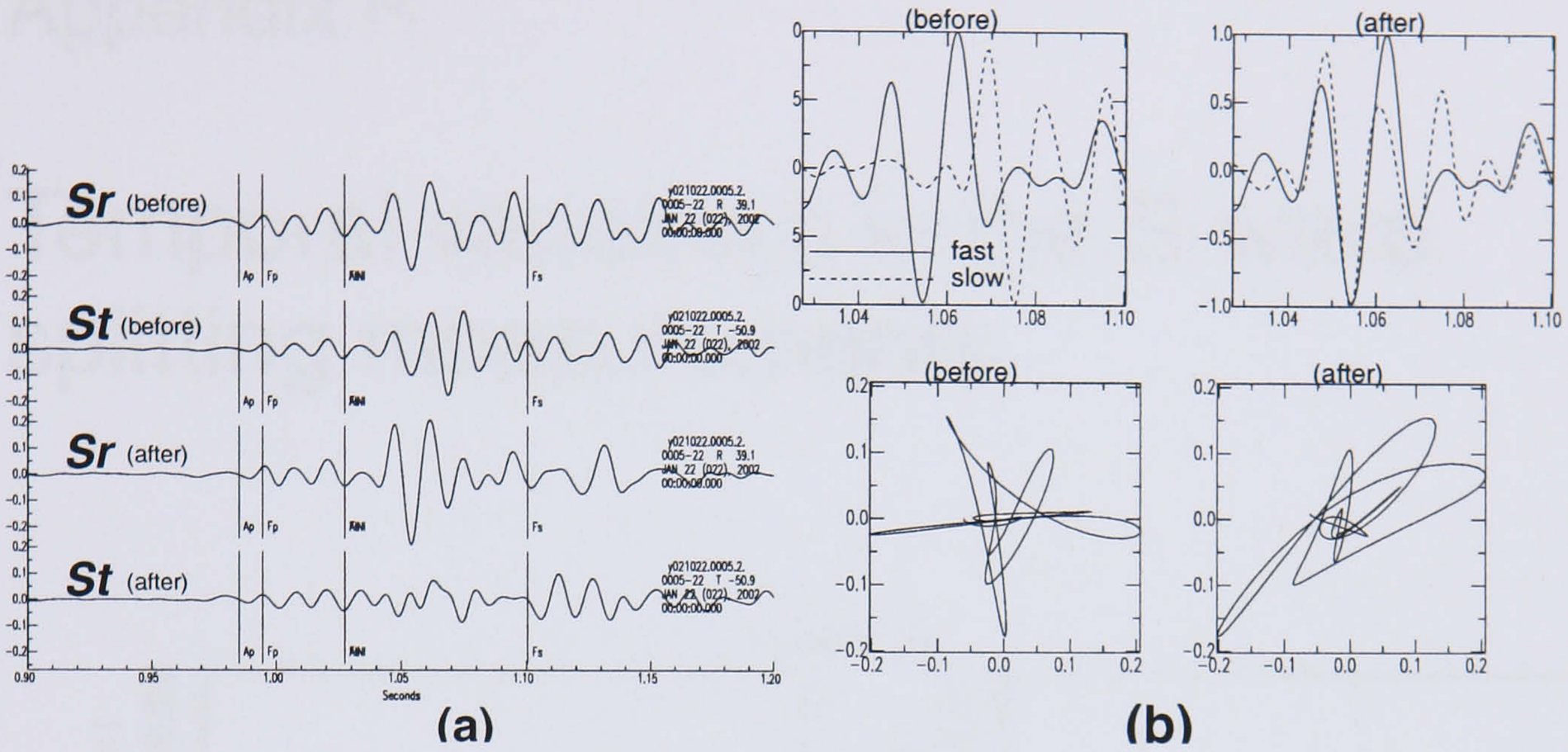

Figure G.2 A well defined perpendicular fast and slow shear waves of a real data example of class B: event yb021022.0005 recorded on station 2.2. [**a**] *Sr*, *St* before and after splitting correction. [**b**] [**top panel**] Fast and slow shear waves before and after correction and [**bottom panel**] S-wave particle motion before and after correction.

Figure G.3 shows a clear example of time-dependent time lag. The time lag increases with increasing arrival time of the S-wave. This is perhaps due to differential attenuation between the fast and slow shear-waves and deserves further attention (see Carter and Kendall (2004)).

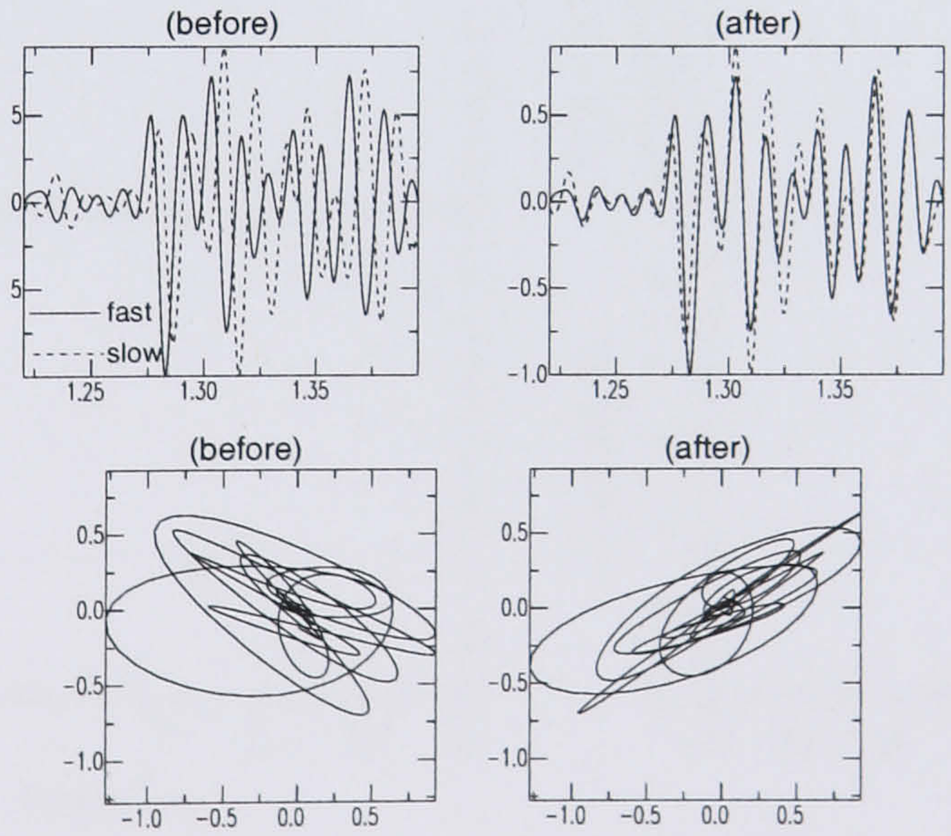

Figure G.3 Lag time dependence on S-wave arrival time on a real data example of class A: event yb021020.0050 recorded on station 1.1. [**Top panel**] Fast and slow shear waves before and after correction and [**bottom panel**] S-wave particle motion before and after correction. Note lag time increase with increasing time and subsequently undercorrected early arrivals and over corrected late arrivals.

Appendix H

Temporal variations in the S-wave splitting measurements

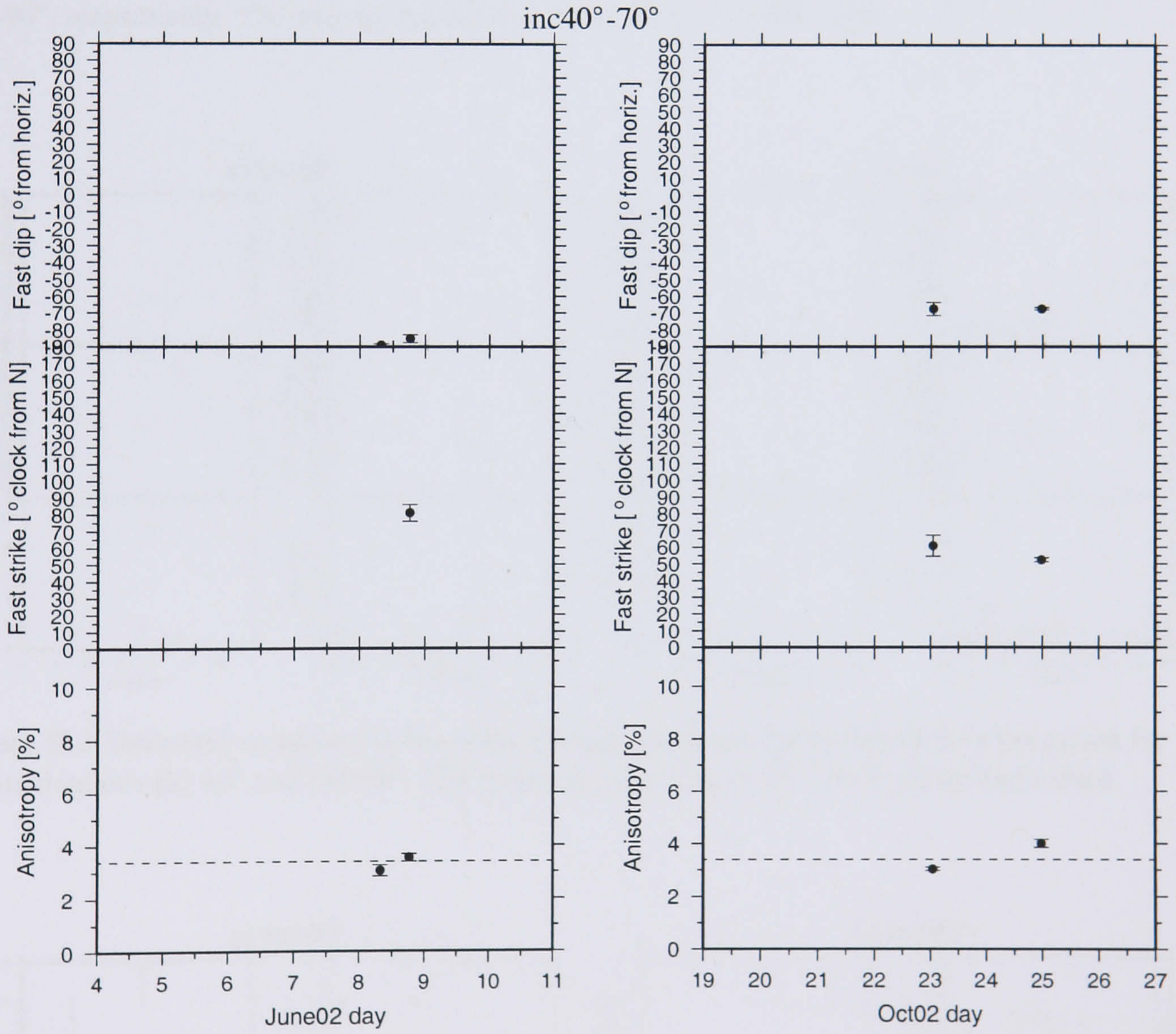

Figure H.1 Temporal variations in the splitting measurements for the Fiqa formation in the SE footwall for ray inclination range 40°–70°. The average anisotropy (dashed line) is 3.4%.

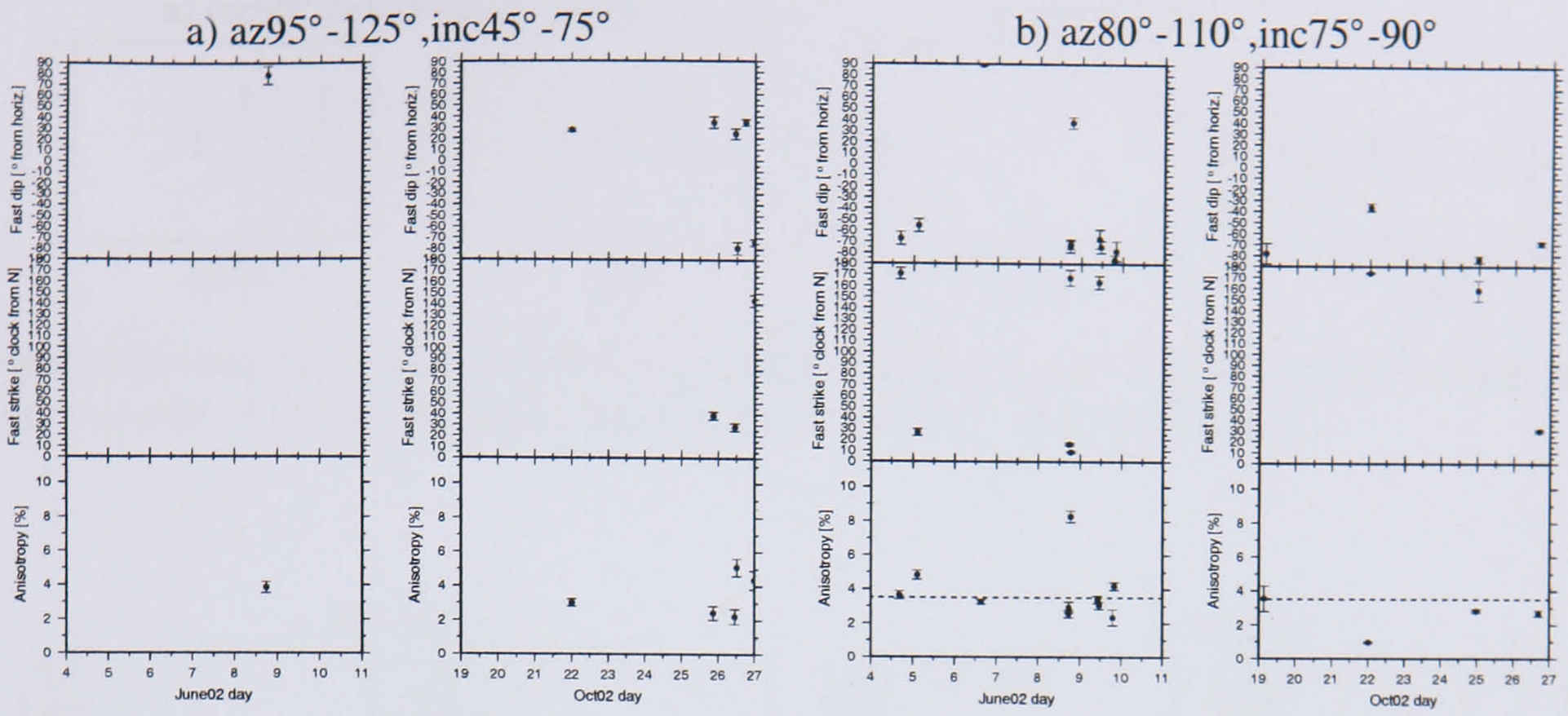

Figure H.2 Temporal variations in the splitting measurements for the Natih-A formation for ray azimuth and inclination ranges of [**a**] 95°-125° and 45°-75°, respectively, and [**b**] 80°-110° and 75°-90°, respectively. The average anisotropy, dashed line, is 3.5% in (b).

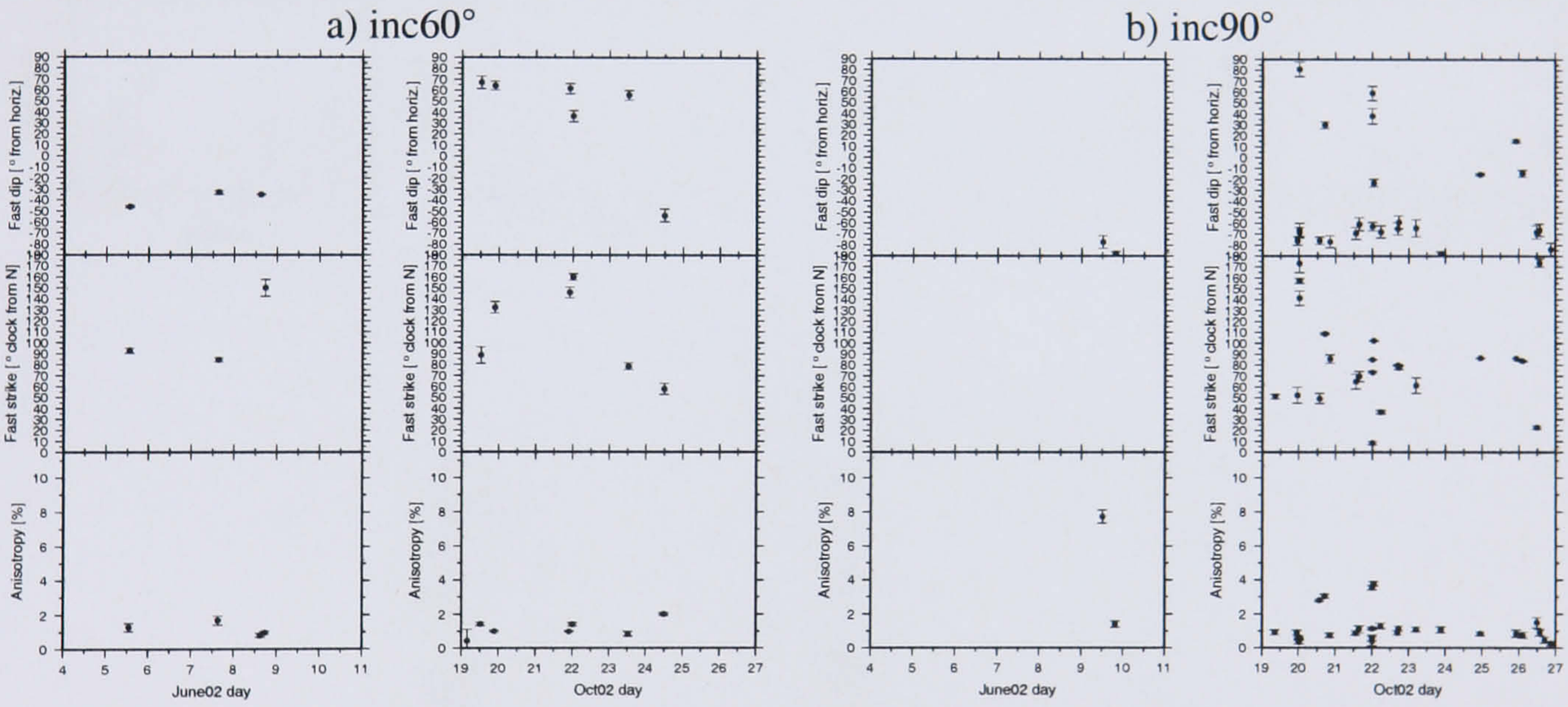

Figure H.3 Temporal variations in the splitting measurements for the Natih B-G formation for ray inclinations [**a**] 60° and [**b**] 90°. The inclination bin size is 30° (±15° about mid value).

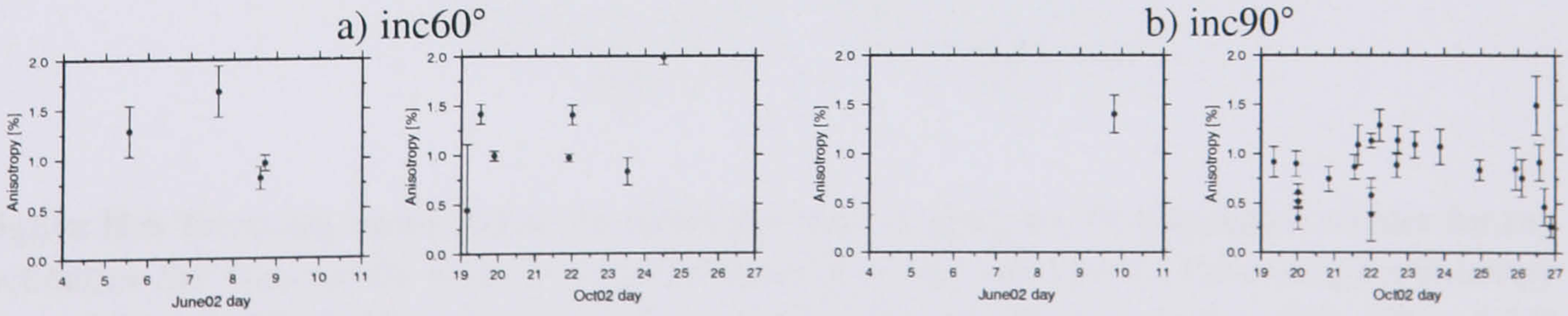

Figure H.4 A zoom in the 0-2% percent anisotropy plot in Figure H.3.

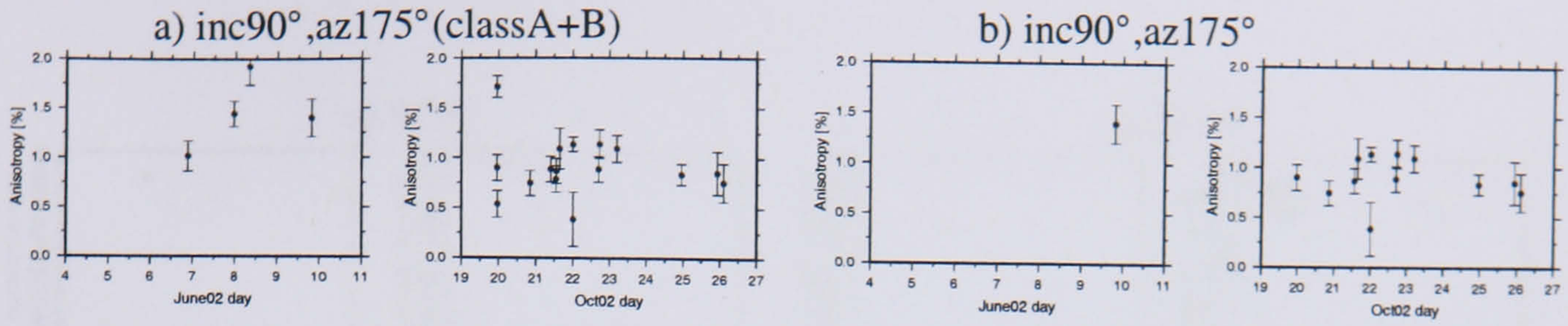

Figure H.5 Same as Figure H.4b with ray azimuth confined to 175° bin [**a**] with class A and B results and [**b**] only class A results. The bin size is 30° (±15° about mid value).

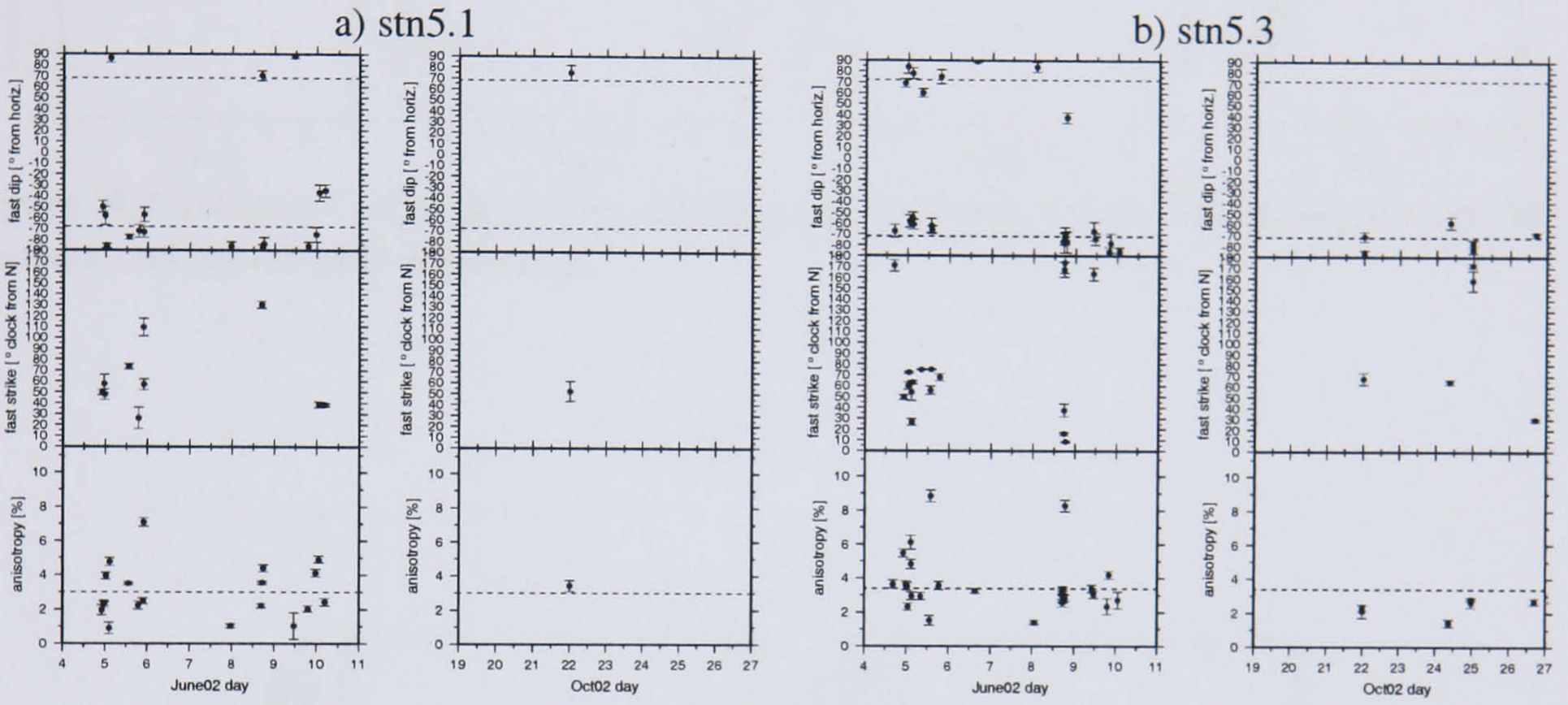

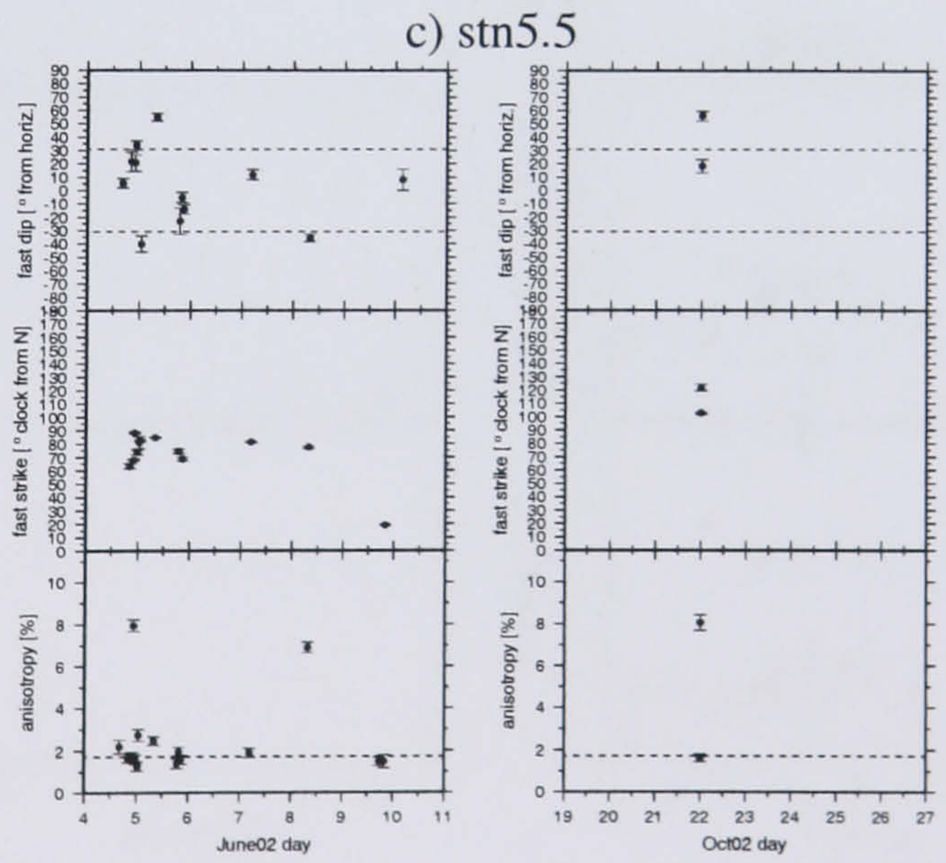

Figure H.6 Temporal variations in the splitting measurements for the Horseshoe cluster for ray inclination 90° bin and for well 5 stations of level [**a**] 1, [**b**] 3 and [**c**] 5. The average anisotropy (dashed line) is 3%, 3.4% and 1.7% and the average fast dip (dashed line) is 68°, 72° and 31° for stations 5.1, 5.3 and 5.5, respectively.

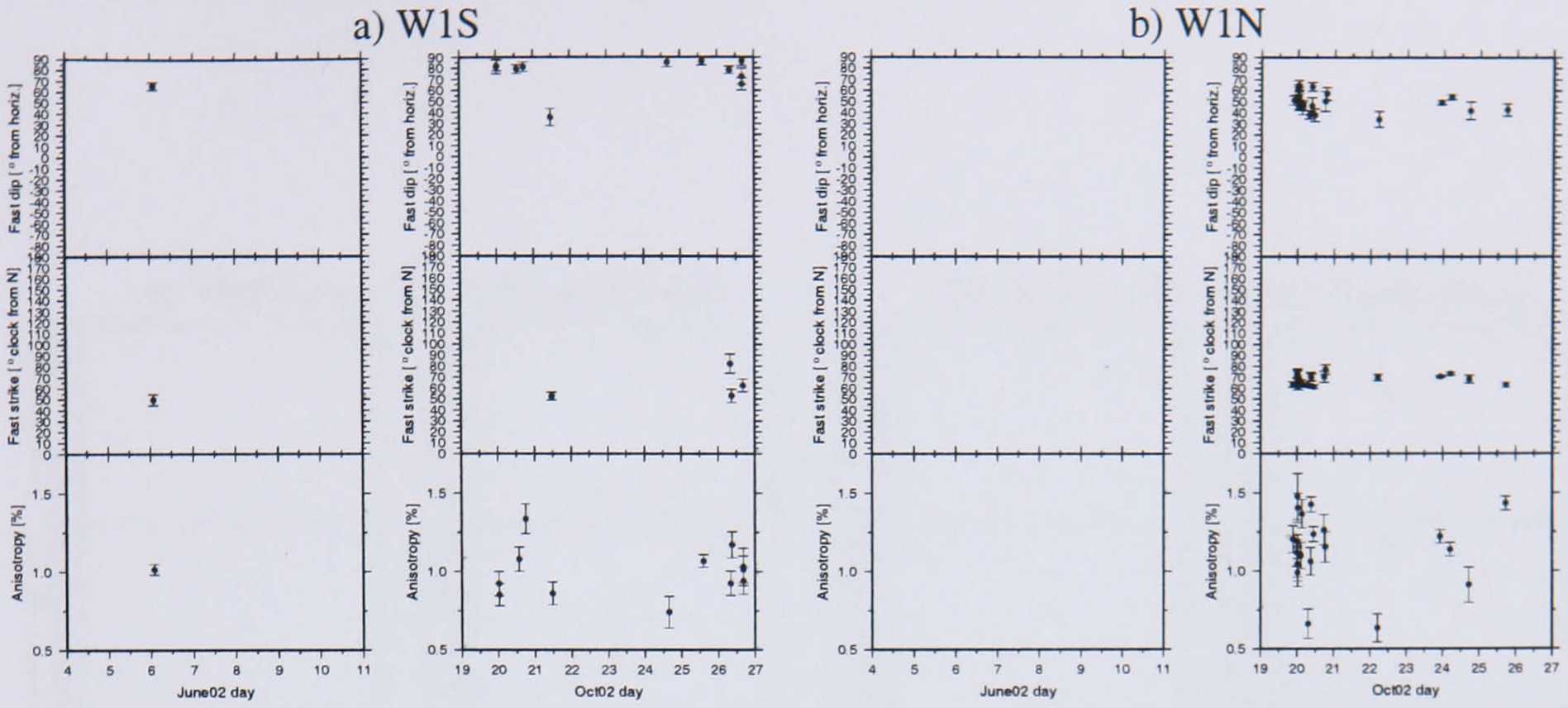

Figure H.7 Temporal variations in the splitting measurements for the W1 cluster for (**a**) the southern and (**b**) northern populations.

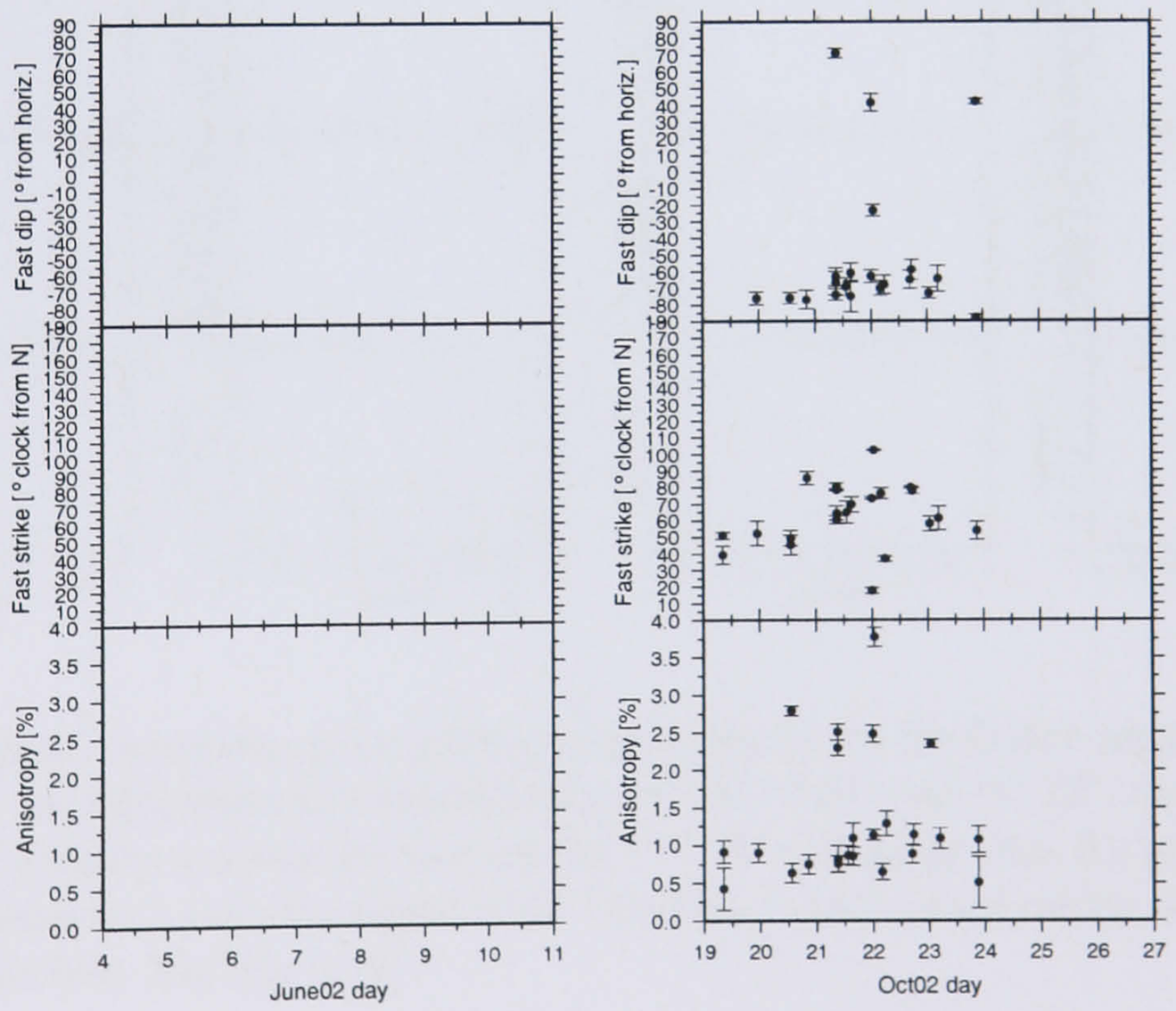

Figure H.8 Temporal variations in the splitting measurements for the W4 cluster. The average anisotropy of the low (0.9%) and high (2.5%) anisotropy populations are shown as dashed lines.

a) Well2 inc145°-160°, az15°-22°

b) Well2 inc75°,az45°(A+B class)

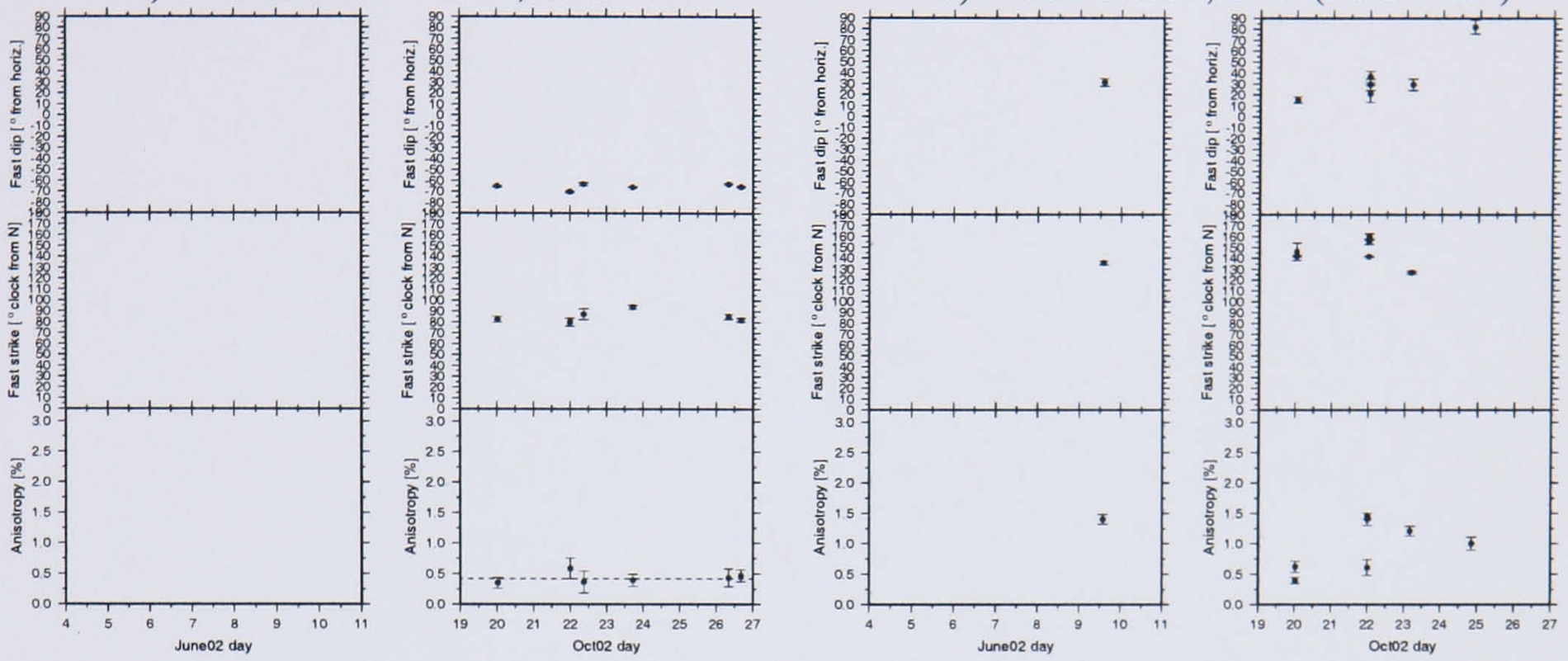

c) Well3 inc95°, az95°

d) Well3 inc95°, az95°(A+B class)

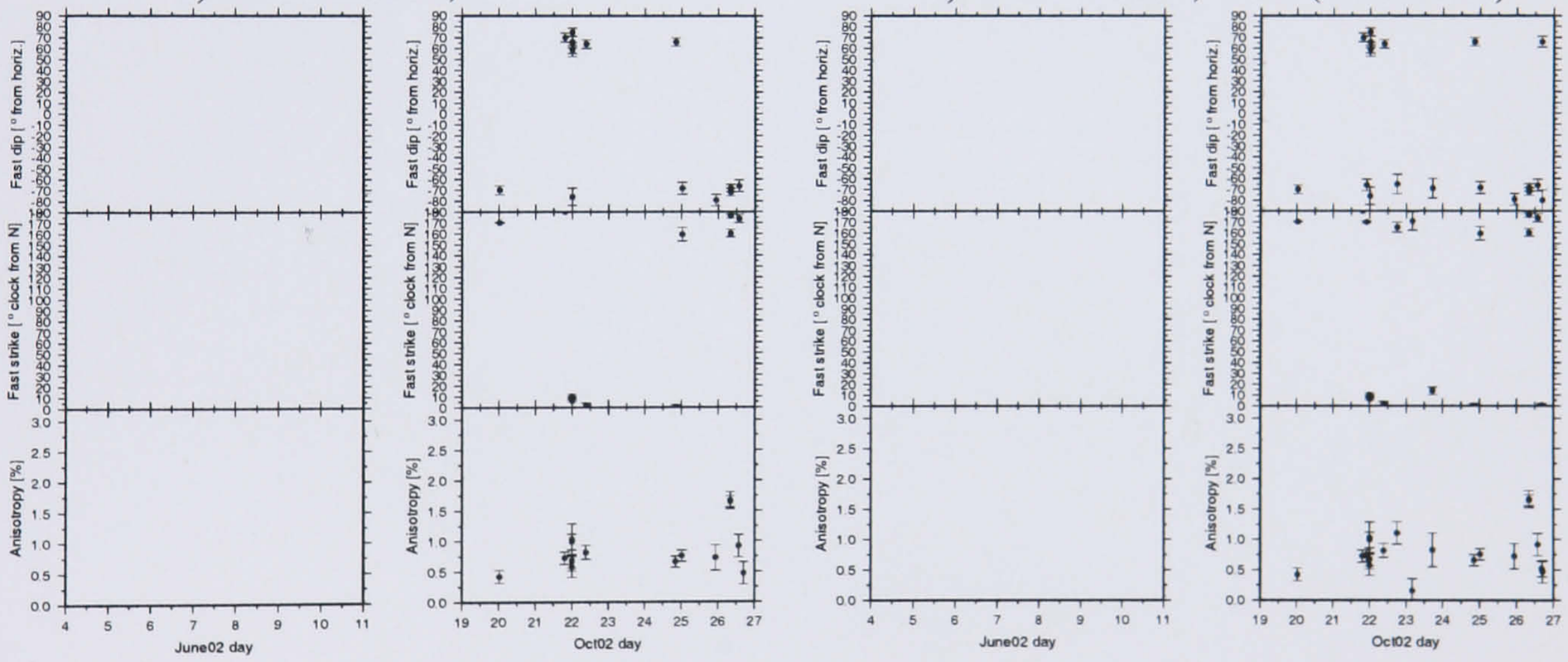

Figure H.9 Temporal variations in the splitting measurements for the G data recorded in well 2 (**a,b**) and 3 (**c,d**). [**a**] Inclination and azimuth range of 145°-160° and 15°-22°, respectively. For the next plots, inclination and azimuth bins are [**b**] 75°, 45° (including class B); [**c**] 95°, 95° and [**d**] 95° and 95°(including class B), respectively. The best fit percent anisotropy (0.42%) for (a) is shown as dashed line. Bin size is 30°.